

CRANFIELD UNIVERSITY

Ricardo Manuel Santos da Silva Cruz

TiB<sub>2</sub> CERAMIC AND DLC MULTILAYERED PVD  
COATINGS

SCHOOL OF APPLIED SCIENCES

PhD THESIS

CRANFIELD UNIVERSITY

SCHOOL OF APPLIED SCIENCES

PhD THESIS

Academic Year 2006-2007

Ricardo Manuel Santos da Silva Cruz

TiB<sub>2</sub> ceramic and DLC Multilayered PVD coatings

Supervisors: Prof. J. R. Nicholls  
Mr. Ken J. Lawson

This thesis is submitted in partial fulfilment of the requirements  
for the degree of Doctor of Philosophy

© Cranfield University 2007. All rights reserved. No part of this  
publication may be reproduced without the written permission of  
the copyright owner.

## CONTENTS

ABSTRACT .....	4
ACKNOWLEDGEMENTS.....	5
LIST OF FIGURES.....	6
LIST OF TABLES .....	13
THESIS INTRODUCTION .....	14
1. Types of Atomistic Deposition Processes .....	17
1.1. Physical Vapour Deposition .....	18
1.2. What is Sputtering?.....	19
1.2.1. Sputtering Threshold.....	20
1.2.2. Sputtering Yield.....	22
1.2.3. Sputtering theoretical models.....	25
1.2.4. Sputtering Advantages and Drawbacks [3-5, 7, 9, 17, 22]. .....	28
1.3. Sputtering techniques .....	28
1.3.1. DC – Direct Current .....	28
1.3.2. RF – Radio Frequency.....	30
1.3.3. Pulsed DC.....	31
1.4. Reactive Sputtering Deposition.....	33
1.4.1. Sputtering Target .....	35
1.4.2. Ion Bombardment .....	35
1.4.3. Gas Incorporation .....	36
1.5. Thin Film Growth.....	36
1.5.1. Thin film growth modes.....	37
2. Multilayer Concepts.....	46
2.1.1. Multilayer Advantages.....	49
3. Titanium Diboride .....	51
3.1.1. Practical Applications for Titanium Diboride.....	58
4. Diamond and DLC films .....	63
4.1.1. Deposition conditions.....	66
5. Nanoindentation .....	73
5.1. Theoretical Indentation Models .....	75
5.2. Analysing the Coatings .....	83

5.2.1.	Soft coating.....	83
5.2.2.	Hard Coating.....	85
5.2.3.	$H^3/E^2$ .....	86
6.	Scratch Test – Introduction .....	88
6.1.	Scratch testing .....	88
6.1.1.	Testing modes .....	89
6.1.2.	Failure Modes in Scratch Test .....	91
6.1.3.	Acoustic emissions .....	95
6.1.4.	Good practice guide to identifying critical loads .....	96
6.2.	Summary of Literature.....	97
7.	Experimental Work.....	100
7.1.	The Sputtering System.....	100
7.2.	Process conditions .....	104
7.2.1.	Set-up the of conditions for Multilayer Coatings.....	104
7.2.2.	Nanoindentation.....	107
7.2.3.	Tribological testing .....	110
7.3.	Substrates.....	111
7.3.1.	Tool Steel.....	111
7.3.2.	Powder processed Al Alloys substrates .....	112
7.4.	Focused Ion Beam .....	113
7.4.1.	Applications:.....	116
7.5.	Raman Spectroscopy .....	118
7.5.1.	Applications of Raman spectroscopy .....	119
8.	Results and Discussion .....	121
8.1.	Tribological characteristics of pulsed-DC, DC-sputtered and RF-sputtered titanium diboride ( $TiB_2$ ) thin film coatings .....	121
8.1.1.	Introduction .....	121
8.1.2.	Results and discussion .....	122
8.1.3.	Tribological testing of $TiB_2$ .....	129
8.1.4.	Conclusions .....	141
8.2.	$TiB_2/C$ Multilayer Films.....	144
8.2.1.	Introduction .....	144

8.2.2.	Results and discussion .....	145
8.2.3.	Conclusions .....	160
8.3.	(TiB <sub>2</sub> /DLC, CH <sub>4</sub> ) Reactive atmosphere .....	162
8.3.1.	Introduction .....	162
8.3.2.	Results and Discussion.....	163
8.3.3.	Conclusions .....	180
8.4.	TiB <sub>2</sub> monoliths on powder processed Aluminium (Al) alloys .....	181
8.4.1.	Introduction .....	181
8.5.	TiB <sub>2</sub> /DLC by Pulsed DC in Ar +7.5% CH <sub>4</sub> .....	197
8.5.1.	Introduction .....	197
8.5.2.	Results and discussion .....	198
8.5.3.	Conclusions .....	217
8.6.	Summary Discussion .....	219
9.	Conclusions and Further work.....	232
9.1.	Conclusions .....	232
9.2.	Further work.....	235
	REFERENCE LIST.....	236

## ABSTRACT

Titanium diboride ( $\text{TiB}_2$ ) has been investigated as a potential candidate for several industrial applications, such as: cutting tools, electric devices, wear parts and many more fields of application. The main drawback of  $\text{TiB}_2$  is its brittle nature, which has limited its range of applications.

Diamond-like Carbon (DLC) has been used in industrial applications, mainly for wear resistant parts. However, the application of DLC films has been limited by the level of internal stress accumulated during deposition.

This thesis investigates the deposition of  $\text{TiB}_2$ /DLC multilayer wear resistant coatings to overcome these limitations. The thesis focuses on the tribological effects caused by different deposition techniques on  $\text{TiB}_2$  ceramic used by the coatings industry today, in order to overcome the brittle nature of  $\text{TiB}_2$  and the lack of adhesion of DLC films.

The multilayer coatings consisted of 25 bi-layers of  $\text{TiB}_2$ /DLC. These  $\text{TiB}_2$ /DLC coatings were fabricated, maintaining a constant composition wavelength (sum of two layers  $\lambda = 200$  nm) for an array of ceramic fractions ranging from 25% to 95% by volume using as substrates, tool steel AISI 1095 and powder metallurgy aluminium alloys, type 2618. The effect of the DLC content on the structure and performance (hardness, adhesion and wear) of the films was investigated. The bi-layer thickness influences the failure patterns observed in the scratch testing. These observations have been used to optimise the multilayered coating structure.

Multilayer coatings have been manufactured to increase surface hardness and wear resistance as applied to a commercial powder metallurgy Al alloys (Al 2618) used in the automotive industry. Optimum coatings have found hardness values of 27.8 GPa, with a critical load of 20 N and a friction coefficient of 0.47. As a result of wear tests the multilayer with 10% of DLC was found to be best compromise between high hardness (23.8 GPa), good adhesion (critical load higher than 20 N), low friction and low wear rate.

## **ACKNOWLEDGEMENTS**

I would like to express my deepest gratitude to all the people that contributed for this project being possible. In particular I would like to express my gratitude to:

My supervisors, Prof. John Nicholls and Mr Ken Lawson, for their advice, useful discussions and dedication that helped put together this thesis.

To all the staff in building 57, for their help and advice in all the situations of this process.

To all the PhD students in the office who made a big contribution to an excellent working environment, a big thanks to all of them.

To all the Portuguese students at Cranfield University over the years, especially to Gil Lopes and his wife, to Rui Pires and his family, for their support, encouragement, understanding and guidance.

To my close friends, for their encouragement and friendship.

To my wonderful girlfriend, Marta for her love, never ending patience and understanding during this difficult period of our lives.

Finally this thesis is especially dedicated to my parents and my sister who probably suffered more than I did, for their constant support of every aspect of my life.

## LIST OF FIGURES

Figure 1 - PVD Overview [12].	19
Figure 2 - Variations of sputter yield with incident ion energy [16].	20
Figure 3 - Variation of sputtering yield with ion energy for Ar ions at normal	23
Figure 4 – Sputtering [21].	26
Figure 5 - Magnetron sputtering overview [12].	27
Figure 6 – Section view through vacuum chamber [12].	29
Figure 7- Average negative voltage in RF Sputtering [23].	30
Figure 8- RF Magnetron Sputtering [23].	31
Figure 9 - Generic hysteresis curve for system pressure	34
Figure 10- Sputtering Targets [36].	35
Figure 11 - Three modes of thin film growth processes [14].	38
Figure 12 – Film Growth [43].	39
Figure 13 – Mochvan and Demchishin Model [19].	40
Figure 14 – Thornton’s Model [19].	41
Figure 15 - Dislocation in a crystal lattice [37].	42
Figure 16 - Void in crystal structure [37].	43
Figure 17 – Nodules in a Multilayer coating.	44
Figure 18 – Thermal Barrier Coating cross section	45
Figure 19 – Cross-section of a TiB <sub>2</sub> /W Multilayer Coating	46
Figure 20 - The hexagonal unit cell of single crystal TiB <sub>2</sub>	56
Figure 21 – Pulsed Laser Deposition Overview [103].	57
Figure 22 – Three different bonding configurations of carbon [123].	65
Figure 23 – Illustration of elastic and plastic deformation during nanoindentation.	78
Figure 24 - Representation of a cross-section of an indentation.	79
Figure 25 – Effect of the substrate roughness in nanoindentation [148].	82
Figure 26 - Indentation of a soft coating [12].	84
Figure 27 - Coating yields before the substrate[154].	85
Figure 28 - Indentation of a hard coating,	85
Figure 29 - The substrate yields before the coating	86
Figure 30 – a) Adhesive vs. b) Cohesive failure [195]	88
Figure 31 - Schematic illustration of the scratch.	89
Figure 32 - Schematic of a scratch tester.	90
Figure 33 - The surface cracks generated in a scratch test track	90

Figure 34 – Brittle failure modes in scratch testing .....	92
Figure 35 – Ductile failure modes during scratch testing. ....	93
Figure 36 – AE signal curves during scratch testing.....	95
Figure 37 – Overview of the Sputtering system.....	100
Figure 38 – Overview of the Sputtering chamber. ....	101
Figure 39 – Leybold Box coater L560 .....	103
Figure 40 – 3” Magnetrons details.....	104
Figure 41 – Parameters for Multilayer Coating .....	105
Figure 42 – Berkovitch Diamond Tip [12] .....	107
Figure 43 – Drawing of the basic geometry of a Berkovich diamond tip[12] .....	108
Figure 44 – Nanotest pendulum[12] .....	109
Figure 45– Nanoindentation Loading and Unloading Curves[12] .....	109
Figure 46 - FIB system detail [206] .....	114
Figure 47 - FEI 200XP FIB Microscope.....	115
Figure 48 - FIB system Overview [12].....	115
Figure 49 - FIB Image of milling capabilities.....	116
Figure 50 –FIB Micrograph of TiB <sub>2</sub> Multilayer with a Pt protective layer .....	117
Figure 51 – Delaminated TiB <sub>2</sub> /W multilayer .....	117
Figure 52 - Grain contrast by FIB techniques .....	118
Figure 53 - Basic hardware components for Raman spectroscopy.....	119
Figure 54 - The Load-Displacement curves for the TiB <sub>2</sub> films.....	122
Figure 55 – Remnant depth for the of the coatings manufactured for this section .....	123
Figure 56 – FIB cross section of the RF 300W sample .....	124
Figure 57 – FIB section of the DC 200W samples.....	125
Figure 58 – FiB cross section if the samples manufactured with Pulsed-DC at 300W.....	125
Figure 59 - The variation in hardness as a function of indentation depth.....	126
Figure 60 - The variation of the reduced modulus as a function of indentation depth into the film.....	127
Figure 61 - Variation of H <sup>3</sup> /E <sup>2</sup> versus hardness for all the TiB <sub>2</sub> films.....	127
Figure 62 – AFM topography of Pulsed DC sample 200W. ....	128
Figure 63 – AFM topography of RF sample 300W. ‘ .....	129
Figure 64 – RF 200W, single pass scratch test with increasing load from 10N to 60N. ....	130
Figure 65 – RF 200W scratch testing with increasing load.....	130

Figure 66 - RF 300W, single pass scratch test with increasing load from 10N to 60N. .....	131
Figure 67 - RF 300W scratch testing with increasing load.....	132
Figure 68 - DC 200W, single pass scratch test with increasing load from 10N to 60N .....	132
Figure 69 - DC 200W scratch testing with increasing load .....	133
Figure 70 - DC 300W, single pass scratch test with increasing load from 10N to 60N .....	133
Figure 71 - DC 300W scratch testing with increasing load .....	134
Figure 72 – Pulsed-DC 200W, single pass scratch test with increasing load.....	135
Figure 73 – Pulsed-DC 200W scratch testing with increasing load.....	135
Figure 74 – Pulsed-DC- 300W, single pass scratch test with increasing load from 10N to 60N.....	136
Figure 75 – Pulsed-DC 300W scratch testing with increasing load.....	137
Figure 76 - Bidirectional Wear testing of 18 cycles at 10N load.....	138
Figure 77 - The wear volume of the DC, RF and pulsed-DC magnetron films fabricated .....	139
Figure 78 – Bidirectional wear test on Pulsed DC 200W .....	140
Figure 79 - Bidirectional wear test on DC 300W.....	140
Figure 80 - Bidirectional wear test on RF 200W .....	141
Figure 81 - Raman spectra from a carbon film fabricated as part of this study. ....	145
Figure 82 – FIB micrograph TiB <sub>2</sub> /C multilayer stack.....	146
Figure 83 – Surface topography of TiB <sub>2</sub> /C.....	147
Figure 84 - FIB micrograph TiB <sub>2</sub> /C multilayer stack showing some carrot like defects .....	148
Figure 85 – The variation of the hardness as a function of indentation depth. ....	149
Figure 86 - The variation in Reduced Modulus as a function of indent depth. ....	150
Figure 87 - The variation of hardness with % of carbon in coating. ....	151
Figure 88 – Variation of H <sup>3</sup> /E <sup>2</sup> versus hardness for all the TiB <sub>2</sub> /C.....	152
Figure 89 – Single pass scratch test with increasing load from 10N to 60N .....	153
Figure 90 – Spallation ahead of the indenter.....	153
Figure 91 – Spallation ahead of the indenter.....	154
Figure 92 – Single pass scratch test with increasing load from 10N to 60N .....	154
Figure 93 – Spallation ahead of the indenter with coating. ....	155
Figure 94 – Single pass scratch test with increasing load from 10N to 60N .....	156

Figure 95 – Critical failure point marked in blue .....	156
Figure 96 – Recovery spallation marked in blue.....	156
Figure 97- Bidirectional Wear test at 10N load of the TiB <sub>2</sub> /C multilayers .....	157
Figure 98- Wear Scar of the bidirectional wear test.....	158
Figure 99 - Bidirectional Wear test at 20N load of the TiB <sub>2</sub> /C multilayers .....	158
Figure 100 – Wear Scar of the bidirectional wear test.....	159
Figure 101 – Wear Scar of the bidirectional wear test.....	159
Figure 102 – Wear scar volume for two different loads during the bidirectional wear test .....	160
Figure 103 - Plot showing the Raman spectra of carbon and TiB <sub>2</sub> sputtered in Ar + 7.5 % CH <sub>4</sub> .....	164
Figure 104 - The Hardness of the multilayer films as a function of indentation depth.	165
Figure 105 – Hardness of the TiB <sub>2</sub> /DLC multilayer coatings vs the DLC volume fraction .....	167
Figure 106 - Schematic of the interfacial zones.....	168
Figure 107 – Variation of H <sup>3</sup> /E <sup>2</sup> versus hardness for all the carbon multilayer. ....	168
Figure 108 - Bulk Carbon adhesion testing on Ti sputtered in Ar 7.5% CH <sub>4</sub> .....	169
Figure 109 – Sputtered carbon in reactive atmosphere.....	170
Figure 110 – Single pass scratch test from 10N to 60N .....	171
Figure 111 – First failure point of 25%C containing multilayer coating .....	172
Figure 112 – Critical load of 25%C containing multilayer coating .....	172
Figure 113 – Increasing load scratch test with increasing load of the multilayer containing 50% Carbon.....	173
Figure 114 – Optical micrograph of the multilayer containing 50% Carbon. ....	173
Figure 115 – Scratch test with increasing load for the multilayer with 75% C .....	174
Figure 116 – Scratch test scar with increasing load, from 10N to 60N .....	174
Figure 117 - The variation of the friction coefficient against the number of cycles. ....	175
Figure 118 – Bulk Carbon sputtered in Ar + 7.5%CH <sub>4</sub> fabricated for this study .....	176
Figure 119 – Bulk TiB <sub>2</sub> sputtered in a Ar + 7.5%CH <sub>4</sub> fabricated for this study.. ....	176
Figure 120 - Multilayer films wear test over 20 cycles .....	177
Figure 121 – Multilayer coating containing 25%C highlighted in blue is a region with signs of coating removal. ....	178
Figure 122 – Multilayer containing 50% C.....	178
Figure 123 – Optical micrograph of the wear scar surface of the multilayer containing 75%C.....	179

Figure 124 – Wear scar volume for the bulk coatings of TiB <sub>2</sub> and Carbon.....	179
Figure 125 – Showing the variation of the friction coefficient of the TiB <sub>2</sub> monolayers	182
Figure 126 – Micrograph of a wear scar with signs of visible hertzian cracking .....	183
Figure 127 – SEM micrograph and EDX spectra of wear scar in the TiB <sub>2</sub> coating. ....	184
Figure 128- Showing the variation of the friction coefficient against the number of cycles with a constant 20N load.....	185
Figure 129 – Wear scar at 20N load showing debris in the middle of the test scar. ...	186
Figure 130 – FIB micrograph of 2 N constant load scratch of TiB <sub>2</sub> sputtered in Ar + 7.5 % CH <sub>4</sub> .....	187
Figure 131 – Optical micrograph of 5N constant load scratch of pure TiB <sub>2</sub> sputtered in pure Ar.....	187
Figure 132 – FIB micrographs of 5 N constant load scratch of TiB <sub>2</sub> sputtered in pure Ar .....	188
Figure 133 – FIB micrographs of 5 N constant load scratch of TiB <sub>2</sub> sputtered in Ar + 7.5 % CH <sub>4</sub> .....	188
Figure 134 - Optical micrograph of a 7 N constant load scratch presenting signs of recovery spallation .....	189
Figure 135 - FIB micrographs of a 7N constant load scratch of TiB <sub>2</sub> sputtered in pure Ar .....	189
Figure 136 – Optical micrograph of 7N constant load scratch of pure TiB <sub>2</sub> sputtered in Ar + 7.5 % CH <sub>4</sub> .....	190
Figure 137 - FIB micrographs of 7N constant load scratch of TiB <sub>2</sub> sputtered in Ar + 7.5 % CH <sub>4</sub> .....	190
Figure 138 - Optical micrograph of 10N constant load scratch .....	191
Figure 139 - FIB micrographs of 10N constant load scratch of TiB <sub>2</sub> sputtered in pure Ar .....	191
Figure 140 - FIB micrograph of 10N constant load scratch of TiB <sub>2</sub> sputtered in Ar 7.5%CH <sub>4</sub> .....	192
Figure 141 - Optical micrograph of 15 N constant load scratch presenting signs of cracking inside the scratch scar .....	192
Figure 142 - FIB micrographs of 15 N constant load scratch of TiB <sub>2</sub> sputtered in pure Ar .....	193
Figure 143 - FIB micrograph of 15N constant load scratch of TiB <sub>2</sub> sputtered in Ar + 7.5 % CH <sub>4</sub> .....	193
Figure 144 - Optical micrograph of 20 N constant load scratch .....	194

Figure 145 - FIB micrographs of 20 N constant load scratch of TiB <sub>2</sub> .....	194
Figure 146 - FIB micrograph of 20N constant load scratch of TiB <sub>2</sub> sputtered in Ar + 7.5 % CH <sub>4</sub> .....	195
Figure 147 – SEM micrograph and EDX spectra of the 20N constant load scratch scar .....	196
Figure 148 - The hardness of the multilayer films as a function of indentation depth. ....	198
Figure 149 - The reduced modulus of the multilayer films as a function of indentation depth .....	199
Figure 150 – The calculated H <sup>3</sup> /E <sup>2</sup> ratio for the multilayers fabricated in this section. ....	200
Figure 151– Plot showing the Raman spectra of carbon sputtered in Ar 7.5 %CH <sub>4</sub> ... ..	201
Figure 152 – 2 N constant load scratch friction curve.....	202
Figure 153 – 2N constant load scratch test of 95% ceramic with a FIB milling inside the scratch scar .....	203
Figure 154 – Multilayer cross-section of 2N constant load scratch.....	204
Figure 155 – 5 N constant load scratch friction curve with failure occurring .....	205
Figure 156 – 5 N constant load scratch of 95 % ceramic .....	205
Figure 157 – Acoustic emission 7 N constant load scratch .....	206
Figure 158 – 7 N constant load scratch of 75 % ceramic .....	207
Figure 159 –AE 15 N with failure occurring in all the coatings.....	208
Figure 160 – 15 N constant load scratch of 75 % ceramic .....	208
Figure 161 – Constant load scratch of 85% ceramic at 15N load .....	209
Figure 162 – 15N constant load scratch where there are visible pieces detached from the substrate.....	210
Figure 163 – Friction curve of 20N constant load scratch.....	210
Figure 164 – 20N constant load scratch where the coating is detached from the substrate.....	211
Figure 165 – 20N constant load scratch of 85% ceramic .....	211
Figure 166 – Failure on the edge of the scratch from a 20N constant load scratch ...	212
Figure 167 – Bidirectional Wear testing of 50 cycles at 10 N loads. ....	213
Figure 168 – FIB milling inside a 10N bidirectional friction test.....	214
Figure 169 – Bidirectional wear scar of 85 % ceramic content at 10N load .....	215
Figure 170 – SEM micrograph and EDX spectra of wear scar in the multilayer with 85% ceramic content .....	216
Figure 171 – Wear scar volume for during the bidirectional wear test at 10N load ....	217
Figure 172 – Hardness comparison all the Multilayers produced in Ar atmosphere. .	219

Figure 173 - Hardness comparison between all the multilayers with carbon produced. .....	220
Figure 174 – Reduced modulus comparison of all the multilayers produced.....	221
Figure 175 – Calculated $H^3/E^2$ ratio from the Nanoindentation data .....	222
Figure 176 – FIB cross section of the multilayers manufactured in section 8.5.....	223
Figure 177 – Average friction coefficient of the Multilayer coatings .....	224
Figure 178 – Calculated Wear Scar Volume of the Multilayer coatings. ....	225
Figure 179 – Nanolayer schematic of the reaction zones created by the deposition of DLC with $TiB_2$ ceramic.....	227
Figure 180 – High resolution FIB micrograph of $TiB_2$ /DLC multilayers.....	228
Figure 181 – Illustration of the reaction zones by the observation of Figure 180. ....	229
Figure 182 - Hardness comparison between all the multilayers with carbon produced. .....	231

## LIST OF TABLES

Table 1 – Atomistic Deposition Processes [3-7].	18
Table 2- Sputtering Threshold Data for Various Target Materials [4].	21
Table 3 - Titanium Diboride Properties [9, 12, 97-99].	55
Table 4 – Comparison of Graphite, Diamond and DLC [42, 45, 95, 120, 122].	66
Table 5 – Properties of DLC and CVD Diamond Coatings [42, 45, 95, 120, 122, 127].	67
Table 6 – Thickness variations of the ceramic and metal layers.	106
Table 7 - The experiments conducted in this part of the study	106
Table 8 – Properties of the substrate AISI 1095.	111
Table 9 - Calculated and measured values of the properties of the TiB <sub>2</sub> films fabricated and tested in this section	137
Table 10 - Calculated and measured values of the properties of the TiB <sub>2</sub> /C multilayered films fabricated in this section	157
Table 11 – Summary results of the different TiB <sub>2</sub> multilayers with DLC.	226
Table 12 – Average thickness of reaction zones calculated from Figure 180 a) and b).	229
Table 13 – Experimental ceramic layer, experimental composition wavelength ( $\lambda$ ) and Experimental ceramic fraction	230

## THESIS INTRODUCTION

Surface engineering has been responsible for the introduction of numerous high performance materials in many industrial applications. The use of advanced coating systems to enhance surface properties of components that until now have had a very limited life-time, has allowed a new generation of materials to have a widespread application in different industrial areas.

The use of ceramic coatings has brought enormous commercial potential for different applications, including: thermal barriers, wear resistant coatings, corrosion protection, erosion resistance, and many more.

Titanium diboride is a transition metal based, hard refractory ceramic that has unique properties including high hardness, high melting point, good wear and corrosion resistance, high temperature stability and electrical conductivity. These properties make titanium diboride a fascinating material. Although its brittle nature is a drawback in many industrial applications, multi-layering has offered a solution to this problem.

In recent times diamond-like carbon (DLC) coatings have been an active element in the thin film market. Due to a set of outstanding properties like high hardness, low coefficient of friction, high thermal conductivity and chemical inertness, DLC coatings have been an ideal candidate for many industrial applications. However, these outstanding properties have a severe drawback; the internal stress accumulated during deposition of a DLC film, and this has limited the use of DLC films to thicknesses up to 5 $\mu$ m. Multi-layering can once again offered a solution, enabling the production of high quality, high adhesion and long-life DLC films in industrial applications.

In the last years the automotive industry has increased the number of components manufactured from aluminium alloys. These alloys have desirable properties like: high stiffness, low weight and inertia [1]. The use of such light

components can have a direct impact on vehicle performance and therefore fuel economy [2]. The advantage of using such alloys is that they are cheap and easy to obtain. They can be manufactured by casting and by powder metallurgy. The main disadvantage of such alloys is their mechanical properties, they are soft and lack of wear resistance. Due to these conditions there is need to develop hard, high quality and well adherent lubricant coatings for these alloys.

The objective of this thesis is to study the deposition of  $TiB_2$  using all the main sputtering techniques, thus comparing Radio Frequency (RF), Direct Current (DC) and Pulsed DC deposition, and then explore the influence of the deposition conditions on the tribological properties of the coating.

A further aim is to produce a range of  $TiB_2$  /DLC multi-layers deposited by magnetron sputtering, once again, using all the main sputtering techniques: RF, DC and Pulsed-DC, under both reactive and non-reactive deposition conditions. The hardness and reduced modulus of these coatings are tested using nanoindentation. The tribological performance is also evaluated using a tribotester, capable of performing scratch testing, to measure the critical loads, and a range of wear tests to evaluate friction coefficient of the multilayer stacks produced. Focused Ion Beam (FIB) was used to provide high resolution micrographs of the multilayers.

This thesis is divided into 9 chapters which cover the following aspects:

- Types of deposition processes and a review of the state of the art of methods of magnetron sputtering techniques.
- Deposition of  $TiB_2$  and DLC coatings
- Multi-layer coatings concepts.
- Materials used in the experimental section of the thesis.
- Nano-indentation and methodology used to assess and evaluate thin films and multi-layers.
- Review of scratch testing and examination of failure modes

- Experimental methodology used to deposit and characterize these multilayer thin films.
- Experimental results
- Discussion and comparison for TiB<sub>2</sub> deposition under a range of conditions and for a range of TiB<sub>2</sub>/DLC multilayers.
- Concluding remarks and suggestions for future development.

# 1. Types of Atomistic Deposition Processes

In the Coatings Industry there are 4 groups of atomistic deposition processes. These groups can be divided into: evaporative, glow discharge, gas-phase chemical and liquid-phase chemical processes. The generic names of the processes are: Evaporative Methods, Chemical Vapour Deposition (CVD), Physical Vapour Deposition (PVD) and Liquid and Gas -Phase Chemical Techniques, showed in Table 1 [3-7].

CVD and PVD processes were first used in industrial applications in the 1980's because these deposition technologies introduced significant improvements in many tooling applications. These new coatings provided tools that would work harder, faster and longer than before.

In the 1990's these deposition methods have accompanied the technical evolution of the semiconductor industry. These four thin-film deposition technologies are used throughout the coatings industry worldwide. These methods present variations as variations as listed in the table below [3-7]:

## Evaporative Methods

<ul style="list-style-type: none"> <li>Vacuum Evaporation</li> </ul> Conventional vacuum evaporation; Electron-beam evaporation;	Molecular-beam epitaxy (MBE); Reactive Evaporation;
---	--

## Liquid-Phase Chemical Techniques

<ul style="list-style-type: none"> <li>Electro Deposition Processes</li> </ul> Electroplating; Electroless Plating; Electrolytic anodization;	Chemical reduction plating; Chemical displacement plating; Electrophoretic deposition;
---	--

## Glow-Discharge Processes

<ul style="list-style-type: none"> <li>Sputtering</li> </ul> Planar Diode sputtering; Sputtering ion plating; Magnetron sputtering; Reactive ion plating; Ion beam deposition; Ion beam sputter deposition; Cluster beam deposition (CBD);	<ul style="list-style-type: none"> <li>Plasma Processes</li> </ul> Plasma-enhanced CVD; Plasma oxidation; Plasma anodization; Plasma polymerization; Plasma nitridation; Plasma reduction; Microwave ECR plasma CVD;
--	--

### Gas-Phase Chemical Processes

<ul style="list-style-type: none"><li>• Chemical Vapour Deposition (CVD)</li></ul> Atmospheric Pressure CVD (APCVD); Low Pressure CVD (LPCVD); Metal-Organic CVD (MOCVD); Photo-enhanced CVD (PE-CVD) Laser-induced CVD (LCVD); Electron-enhanced CVD (E-CVD) Hot Filament CVD (HFCVD); Chemical Vapour Infiltration (CVI); Chemical Beam Epitaxy (CBE);	<ul style="list-style-type: none"><li>• Thermal Forming Processes</li></ul> Thermal oxidation; Thermal nitridation; Thermal polymerization;
--	---

**Table 1 – Atomistic Deposition Processes [3-7].**

## 1.1. Physical Vapour Deposition

Physical Vapour Deposition (PVD) processes are used for the deposition of: metals, ceramics, ionic materials, various hard coatings, high melting compounds and in the last years even polymers. They are used as well for the deposition of ternary and quaternary compound coatings like (Ti,Cr)N, (Ti,Al,Cr)N or (TiAl)BN and (Ti,B)N. PVD offers a wide range of possibilities for modification of the deposition parameters. The main difference between PVD and CVD is that the precursors are solid. The material to be deposited is vaporised from a solid target and deposited onto the substrate [3-12].

During PVD processes the film is grown by the deposition of atomic species. The species taking part in the growth are: atoms, molecules, radicals and/or ions which are deposited from the vapour phase. The most used PVD techniques available are: Thermal Evaporation, Ion Plating, Magnetron Sputtering and Pulsed Laser Deposition (PLD) [5, 13, 14]. The microstructure of the growing film can be amorphous, polycrystalline or single crystal, while the growth mode can be “layer-by-layer” or “nucleation and growth”. The growth and microstructure can be modified by the temperature of the substrate, the flux and energy of the atomic species hitting the growing film [6].

These growth parameters can be chosen using the various PVD techniques. When a specific microstructure is required only one of the available PVD

techniques may be applicable. The same film microstructure can be reproduced by several PVD techniques. In recent times there have been some hybrid-processes developed for example, CVD with magnetron sputtering may also be incorporated in the chamber [15]. When depositing films by thermal evaporation, the material is placed in an evaporation boat or crucible and heated by resistive heating or an electron beam.

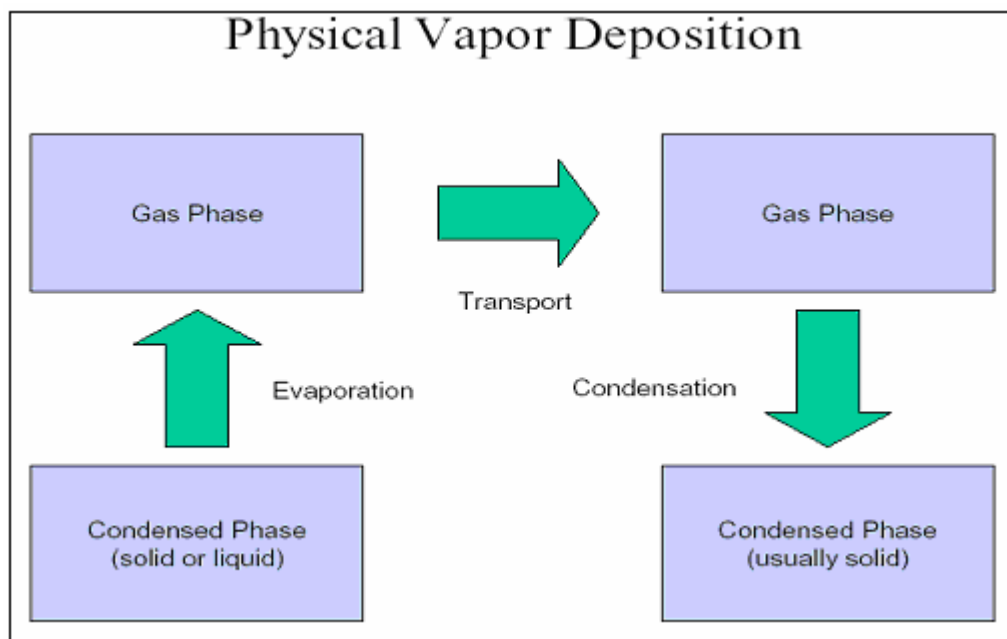


Figure 1 - PVD Overview [12].

In this thesis all multilayered coatings will be deposited using sputter deposition; therefore the sputter deposition based processes will be reviewed in detail in section 1.2.

## 1.2. What is Sputtering?

Sputtering was first described by W. Grove over 150 years ago. He described the first recorded observation of the ejection of atoms from a given material which results from its bombardment by positive ions, this is known by sputtering. The paper was reported in the Philosophical Transactions, volume 142, page 87 in 1852 [5].

The working gas is usually argon (Ar) and the process is based on momentum transfer from impacting positively charged gas ions, and it can deposit many materials, whether metallic, intermetallic, ceramic refractory, ionic and, to a limited extent, polymeric. The rate of deposition is a function of the sputtering yield.

### 1.2.1. Sputtering Threshold

In Figure 2 [16], the graph indicates that in a low energy region threshold energy exists for sputtering. The sputter yield shows a maximum value in a high-energy region.

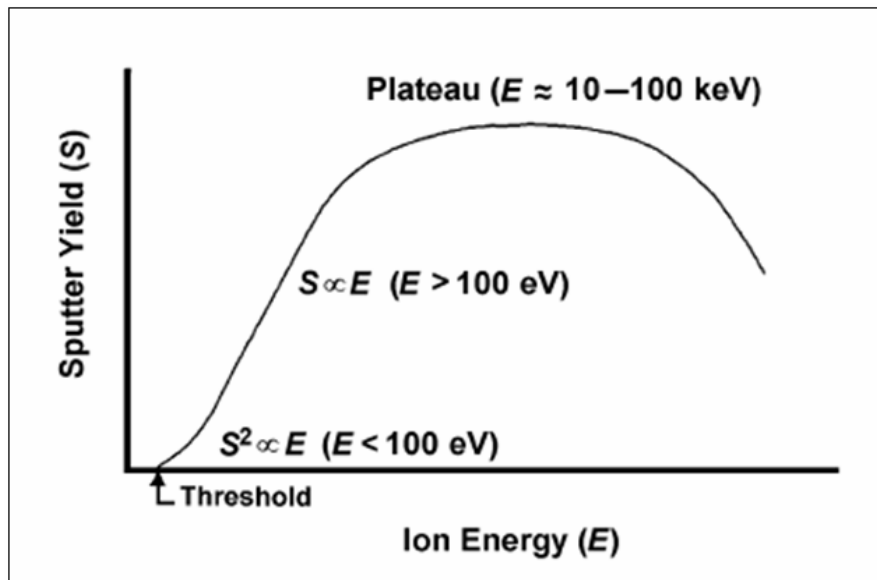


Figure 2 - Variations of sputter yield with incident ion energy [16].

The sputtering threshold has been connected with the mechanism of sputtering. The definition of sputtering threshold was reported when the Th-W (thorium-tungsten) thermionic cathode in gas rectifier tubes was damaged by bombardment with ions when the bombarding ion energy exceeded a critical value, which was between 20 to 30 eV [8, 16].

The threshold energy can be changed by the incident angle of ions and the crystal orientation of cathode materials. Therefore the threshold energy is very sensitive to contamination of the cathode surface.

Table 2 [4] summarizes the sputtering threshold energy measured by the spectroscopic method for various target materials.

Target Material	Bombarding Ions					Heat of sublimation (eV)
	Ne	Ar	Kr	Xe	Hg	
Be	12	15	15	15	-	-
Al	13	13	15	18	18	-
Ti	22	20	17	18	25	4.40
V	21	23	25	28	25	5.28
Cr	22	22	18	20	23	4.03
Fe	22	20	25	23	25	4.12
Co	20	25	23	22	-	4.40
Ni	23	21	25	20	-	4.41
Cu	17	17	16	15	20	3.53
Ge	23	25	22	18	25	4.07
Zr	23	22	18	25	30	6.14
Nb	27	25	26	32	-	7.71
Mo	24	24	28	27	32	6.15
Rh	25	24	25	25	-	5.98
Pd	20	20	20	15	20	4.08
Ag	12	15	15	17	-	3.35
Ta	25	26	30	30	30	8.02
W	35	33	30	30	30	8.80
Re	35	35	25	30	35	-
Pt	27	25	22	22	25	5.60
Au	20	20	20	18	-	3.90
Th	20	24	25	25	-	7.07
U	20	23	25	22	27	9.57
Ir		8				5.22

**Table 2- Sputtering Threshold Data for Various Target Materials [4]**

When the incident ions collide with the surface atoms of the target of the material to be deposited, therefore working in the low-energy near the

threshold, a proportion is established between the number of displaced atoms due to collisions and incident energy. During deposition, when working with higher ion energies (10 to 100 eV) the incident ions travel under the surface, the sputter yields are not influenced by surface scattering, but its influenced by the scattering inside the target. Above 20 keV, the sputter yields will decrease due to energy dissipation of the incident ions deep in the target [3-5, 16].

### 1.2.2. Sputtering Yield

The sputtering process is quantified by the sputtering yield, S. The sputtering yield is the rate of atoms removed from the surface by the ion bombardment. It can be defined as the average atom number removed form the target surface per incident ion and can be calculated by [6]:

$$S \approx \frac{\text{Mass of atoms removed}}{\text{Incident ion flux}}$$

The sputtering yield can be influenced by the following factors [6]:

- Energy of incident particles
- Surface topography
- Target materials
- Incident angles of particles
- Crystal structure of the target surface
- Deposition temperatures

During sputtering ions are used because they are easier to produce and to accelerate during a glow discharge process. At the bombarding energies used for sputter deposition, molecular bombarding species behave as if the atoms of the molecule arrive separately with the same velocity as the molecule and initiate their own sputtering events. With high energy bombardment, when

working in the spike regime, it can induce nonlinear behaviour and a sputtering yield that is higher than twice the single particle yield [6, 17, 18].

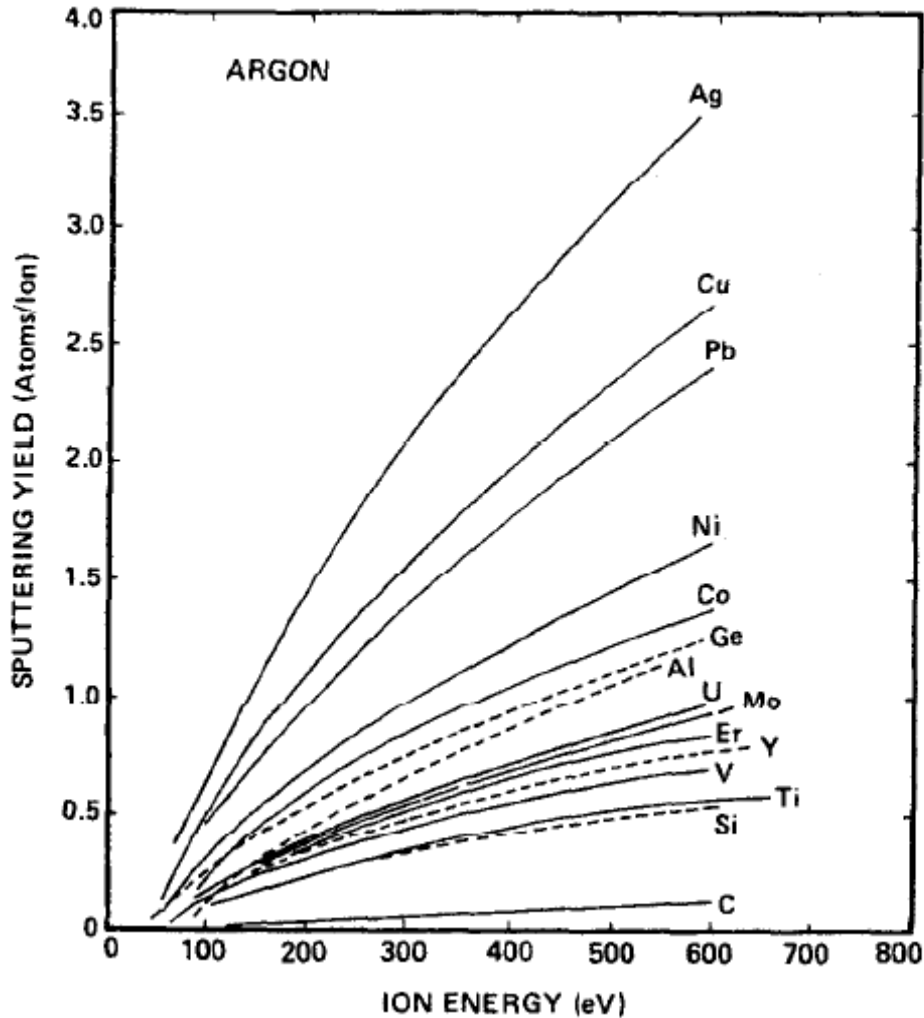


Figure 3 - Variation of sputtering yield with ion energy for Ar ions at normal angle of incidence [17].

Figure 3 shows the sputtering measured experimentally [17] versus the ion energy of several materials sputtered with Ar ions. The sputtering yield depends on the bombarding ion energy which exhibits a threshold of about 20-40 eV, which increases in linear way and can reach energies of around 600 eV [17]. When using high bombarding energies the curves of the sputtering yield begins to saturate and sputtering is more efficient when the ion energies are within the linear part of the chart [4, 17-19].

The sputtering yield, can be measured by the following methods [4, 17-20]:

- Weight loss of target
- Decrease of target thickness
- Collection of the sputtered materials
- Detection of sputtered particles in flight

Sputtering processes are calibrated to determine the deposition rate under a given process conditions. However, yield data of the type described above are often used in predicting deposition rate changes when the materials compositions are modified. An advantage of the sputtering process is that the composition of a sputtered film tends to be the same as that of the target, providing that [4, 6, 17, 18]:

- Effective cooling of the target is provided to avoid diffusion of the materials,
- The target material does not decompose,
- Reactive contaminants are not present,
- The target-to-substrate transfer is the same for all of the materials,
- The sticking coefficients at the substrate are the same for all of the materials.

Many applications require a very accurate control in the film composition, which has led to the wide use of sputtering in numerous industrial processes. When sputtering alloyed materials, the different components are sputtered at different rates due to the different sputtering yields. This creates a surface or altered layer which has a different composition from the bulk material [4, 7, 17-19]. If these conditions are satisfied, conservation of mass requires that sooner or later the process reaches a situation where the sputtered flux leaving the target has the same composition as the bulk material. Equilibrium is reached when the composition of the layer is such that the sputtering yield and the surface concentration for each material is proportional to the target composition.

The thickness and composition of the deposited layer will depend on the target material and sputtering conditions [4, 7, 17-19].

When depositing compounds materials the sputtering yield of the alloy will not be the same as the individual component materials. The change in sputtering yield is caused by the binding energies and the modification of the atomic masses involved during the deposition of the compound material[4, 18, 19].

Targets of compound such as: borides, carbides and silicides should behave as single phase alloys as soon as an equilibrated altered layer is formed in the surface. Powder-pressed targets sometimes present contaminants because of the raw materials from which they have been formed [18].

### **1.2.3. Sputtering theoretical models**

Since its discovery two theoretical models were originally proposed for sputtering [5]:

- The thermal-vaporization theory: where the surface of the target is heated sufficiently to be vaporized due to the bombardment of energetic ions.
- The momentum-transfer theory: the surface atoms of the target are emitted when kinetic moments of incident particles are transferred to target surface atoms.

In the sputtering process gas ions, are accelerated towards a target, which consists of the material to be deposited. Material is detached ('sputtered') from the target and deposited on a substrate placed in the vicinity. The process occurs in a contained chamber, which is pumped down to a vacuum base pressure before deposition [4, 5].

Plasma ignition is possible because of an inert gas is used. The most common inert gases used in PVD processes are Argon (Ar) Helium (He) and Krypton (Kr).

The gas purity is an important parameter to consider because film purity depends directly on the quality of the gas used. Argon is the most used because it is cheap and easy to obtain. In sputtering processes the gas is used as an ion source. It's easier to ionize atoms when they are in a gaseous state. In sputtering, ions are used because it is easier to accelerate ions rather than neutral atoms. Argon is fed into the chamber up to a certain pressure and flow. Sputtering starts when a negative charge is applied to the target material (material to be deposited), causing a plasma or glow discharge to be formed. Ignition occurs due to some ionised  $\text{Ar}^+$  ions available when an applied potential is presented across the electrodes. Further ionisation leads to a stable glow discharge plasma [4, 7, 17-19].

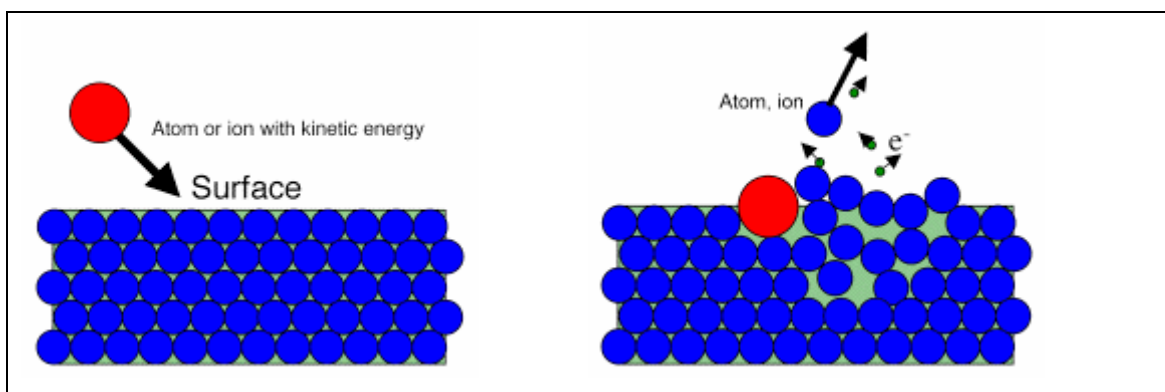


Figure 4 – Sputtering [21].

The Ar ions are then accelerated in the applied potential field. The high energy incident particles impact the surface or near-surface atoms of the target. In the plasma, the ions have sufficient energy to break bonds and dislodge atoms, Figure 4. The impact of an atom or ion with a surface produces sputtering from the surface, as a result of the momentum transfer from the in-coming particle. Unlike many other vapour phase techniques there is no melting of the material [5, 8, 18, 19].

In magnetron sputtering, the magnetron electrode is placed in a chamber with an inert gas, with a pressure of about 0.3 Pa. A negative current is applied to the target mounted on the magnetron electrode, from which a plasma or glow discharge is formed [6, 18].

The intensity of the plasma is amplified by a magnetic field created by the permanent magnets in the magnetron as we can see in Figure 5 [12]. The magnets are employed to trap electrons close to the cathode surface causing further ionization and promote plasma densification [3-7].

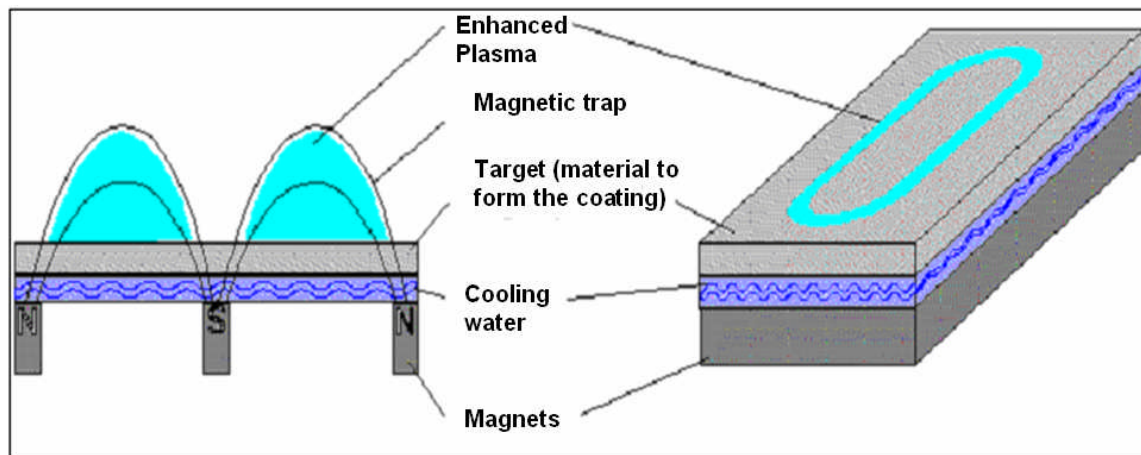


Figure 5 - Magnetron sputtering overview [12].

As electrons in the plasma are pushed away from the target and an electric field is formed, which accelerates positive ions towards the cathode. This ion bombardment of the cathode results in sputtering of the target. The atoms leave the target and hit the substrate with energy of a few eV [3-7].

Substrate ion bombardment is beneficial during film growth as we will see in section 1.4.2. It can be obtained by applying a negative voltage to the substrate by an independent power supply. The plasma is sustained between two electrodes when a sufficiently high negatively charged cathode and positively charged anode are placed in a gaseous environment [3-8].

#### **1.2.4. Sputtering Advantages and Drawbacks [3-5, 7, 9, 17, 22].**

##### **Advantages**

- Film thickness can be easily controlled and repeated;
- Coating uniformity;
- Can be fully automatic;
- Good adherence between the coating and substrate;
- Extremely versatile - A wide range of materials can be sputtered, insulators, metals, polymers;
- It can produce high purity coatings, dependent on the vacuum.

##### **Drawbacks**

- Energy inefficient compared with other processes;
- Depending on the process, the cost can be very high due to the incorporation of non-standard equipment (D.C. sources, R.F. sources):
- System requires complex cooling systems.

### **1.3. Sputtering techniques**

#### **1.3.1. DC – Direct Current**

In DC-sputtering a negative potential is applied to the target, usually a few hundred volts are sufficient to start the process. As discussed before the Ar-ions are accelerated towards the target and set the material free, causing secondary electrons to be produced and being responsible for further ionization of the working gas [3-6]. The gas pressure is an essential parameter during sputtering; it controls the ionization probability, which rises with an increase in pressure, meaning a higher number of ions and enhance the gas conductivity. The gas pressure and the electrode distance determine a break-through voltage from which a self-sustaining glow discharge starts. A sufficient ionisation rate means a stable plasma. For this reason, a sufficient number of ions is available for sputtering of the material [3-6, 11]. In sputtering the apparatus a magnetron is

placed below the source material (target) is used, as we can see in Figure 6 [12].

The secondary electrons in the magnetic field are trapped in cycloids and circulate over the target surface. It is also possible to form a plasma at a pressure some hundred times smaller than the ones used in conventional sputtering [3-6]. Another effect is that higher deposition rates can be achieved. On the other hand fewer collisions occur for the sputtered material on the way to the substrate, this happens because of the lower pressure and kinetic energy at the moment of impact. The electron density and the number of generated ions are higher where the B-field (magnetic) is parallel to the substrate surface. The highest sputter yield happens on the target area right below this region. An erosion zone is formed which follows the form of the magnetic field [3-8].

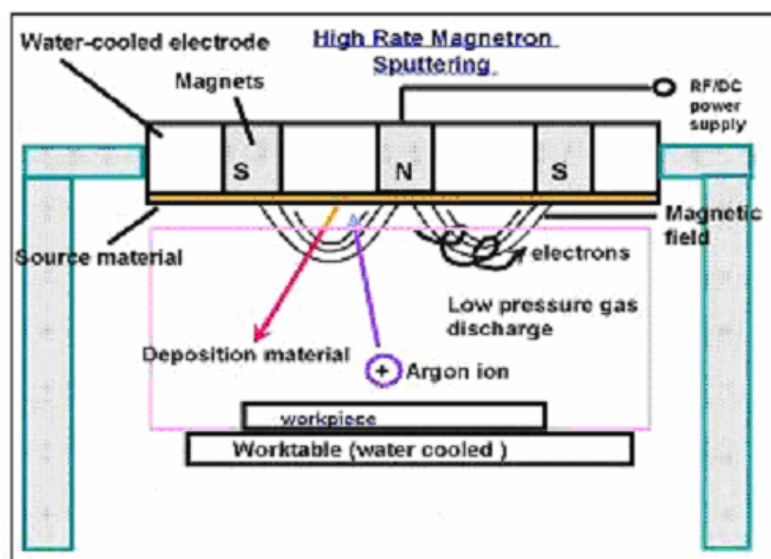


Figure 6 – Section view through vacuum chamber [12].

The bombardment of an insulating target with positive ions would lead to a charging of the surface and subsequently to a shielding of the electrical field. Therefore dc-sputtering is restricted to conducting materials like metals or doped semiconductors [3-8, 18].

But there are some strong limitations of the DC sputtering process [3-9, 12]:

- If an insulating coating is deposited or the substrate is an insulator DC sputtering can not be used;
- If an insulating coating is deposited by a DC reactive process, the growing insulating film on the substrate and anode area may charge up, which then generates arcs;

### 1.3.2. RF – Radio Frequency

When sputtering with an insulating target, the material will block any DC current and the current will build up on the target surface. By alternating the polarity of the target electrode (Figure 7), charge build up can be eliminated. Such sputtering is usually performed at 13.56 MHz, a frequency set by the Federal Communication Commission for Industrial-Scientific-Medical for plasma processing, at this frequency, and frequencies above 50 kHz.

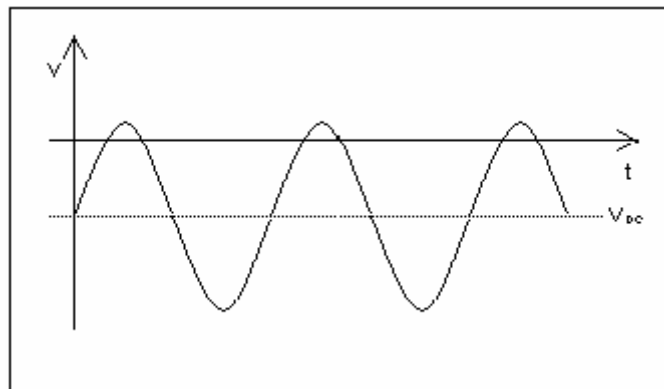


Figure 7- Average negative voltage in RF Sputtering [23].

A standard RF sputtering system is constituted by an RF source, matching circuit and a grounded or “directly coupled” electrode where the substrate is usually placed, and a capacitive-coupled driven electrode, as we can see in Figure 8 [3, 6, 8, 9, 16] . The plasma is generated when the alternating signal is applied to the cathode, acting as a rectifier. It generates an average negative voltage that is connected to the electrode, which is the target [5, 6].

It is important to note that the target is not directly coupled to the RF source. The potential at the target electrode does not have to have a time averaged potential of zero relative to ground. If the target were directly coupled, it would be flooded by the mobile electrons during the positive half of the cycle [3-6]. During the negative half, however, the positive ions would produce a small current (they have large inertia, and the flux of positive ions is limited by the diffusive flux to the plasma boundary). Since there cannot be a net current through the capacitor, the target develops a negative self-bias. The time spent at positive potential is just long enough to collect the electrons necessary to neutralise the charge collected during the negative portion of the cycle. Since the average bias is negative, it is reasonable to call the capacitive-coupled electrode a cathode [3-6, 8, 11].

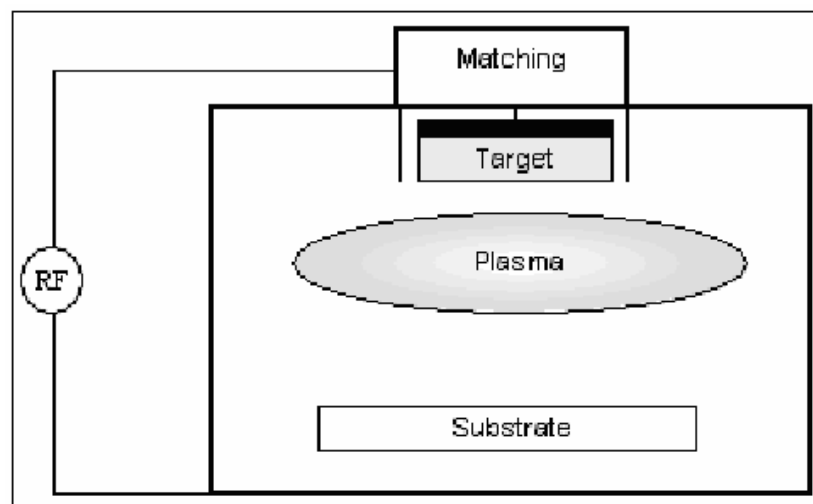


Figure 8- RF Magnetron Sputtering [23].

### 1.3.3. Pulsed DC

During the 1970's DC sputtering was the well known coating technique, but in the beginning of the 1980's with the introduction of reactive depositions for oxides this technique was further developed [24, 25]. Some of the major problems with the reactive DC magnetron sputtering were the low plasma density near the substrate and the complete coverage of the sputtering targets with an insulating layer resulting from the sputtering process. As a consequence

the process became unstable, with a tendency to arcing. With the development of process engineering, and the increasing demand for the industrial deposition of highly insulating materials, the need to deposit oxide films like: ITO (Indium tin oxide),  $\text{TiO}_2$ ,  $\text{Al}_2\text{O}_3$ ,  $\text{ZnO}$  became apparent and resulted in many more processes that are still used today [24-28].

With conventional DC magnetron sputtering the low plasma density near the substrate is a well documented fact [29]. The magnetic field of the magnetron concentrates ionization in the region near the target surface and only in this region is material removed by the sputtering process [25].

Pulsed DC processes suppress arcing during the deposition of reactive material and with this assure long term process stability [24-27]. If the surface potential is negative, ions are accelerated out of the plasma to bombard the surface and in this situation sputtering occurs, while electron bombardment causes mainly heating [24-27]. Secondary electron emission is less than the ion bombardment and the surface then builds up a positive charge and the bombardment energy will decrease. This build up of positive charge eventually causes an arc. Reverse bias during the pulsed DC process helps eliminate such charge build up [24-27].

Pulsed DC uses a potential with a variable frequency which can have an operating range from 50-300 kHz. Some of the process variables are: voltage, pulse width, shut off time, and pulse polarity [24-27]. The voltage increase and decrease is very rapid during the pulse. The pulse can be bipolar or unipolar [27, 30]. The bipolar pulse is symmetric, where the positive and negative heights are equal and the duration of the pulse can be varied [27, 30]. The unipolar pulse occurs where the voltage is negative with a shut off time, or bipolar where the voltage changes between positive and negative and possibly with a shut off time as well [27, 30]. During Pulsed DC sputtering, the positive bias electrons can move to the surface from the plasma and neutralize any charge build up generated during the negative portion of the cycle (effective

sputtering period). The possibility of a transition between negative and positive voltages applied to the target is the reason that Pulsed DC can sputter insulating materials as by balancing the charge flow in each part cycle no net current flow is required [24-27, 30].

Advantages of using pulsed DC power supplies for the reactive deposition of oxide films are well recognized, especially in the elimination of arcing and enhanced process stability. Cooke et al [29] and his co-workers used Pulsed DC to bias the substrates. They used Pulsed DC for biasing the substrates for surface cleaning (elimination of substrate arcing), and interface formation (ion clean insulating oxide films present in the substrate, improving adhesion). The coating of components has been investigated and optimized through adjustment to various parameters like: voltage, frequency and pulsed width [31]. A major conclusion reached by Cooke and co-workers [29] was that the usage of pulsed DC sputtering, which allowed a decrease in the substrate temperature and an increase in ion bombardment compared to regular DC supplies, could be achieved.

#### **1.4. Reactive Sputtering Deposition**

Reactive sputtering occurs when a reactive gas mixture is injected to the process chamber to react with a pure metal or alloy in order to deposit a compound film. The forming films occur after the sputtered material reacts with the gas species [3-8]. Reactive sputtering is a reliable way of depositing a wide range of films with variable film properties [24, 26]. The most common example is TiN and CrN/Cr coatings for wear resistance [32, 33]. Reactive sputtering is a complex process, it involves the sputtering process, the physics of the plasma discharge, the transport of the sputtered and gas species, the kinetics of film growth and chemical interactions between the target and film surfaces affect the properties of the film [4, 16, 34].

When using a high flow of gas reactive species it is possible to form an oxide compound on the target surface that cannot be removed by the sputtering

process, effectively contaminating it, therefore leading to the development of Pulsed DC techniques as we seen before in section 1.3.3.

The target poisoning will only stop when the flow of reactive gas is reduced to a flow where the sputtering of the target material occurs without reaction of the gas, producing a pure film. This is known as hysteresis effect [35]. This process depends of the total gas flow, and the pumping speed.

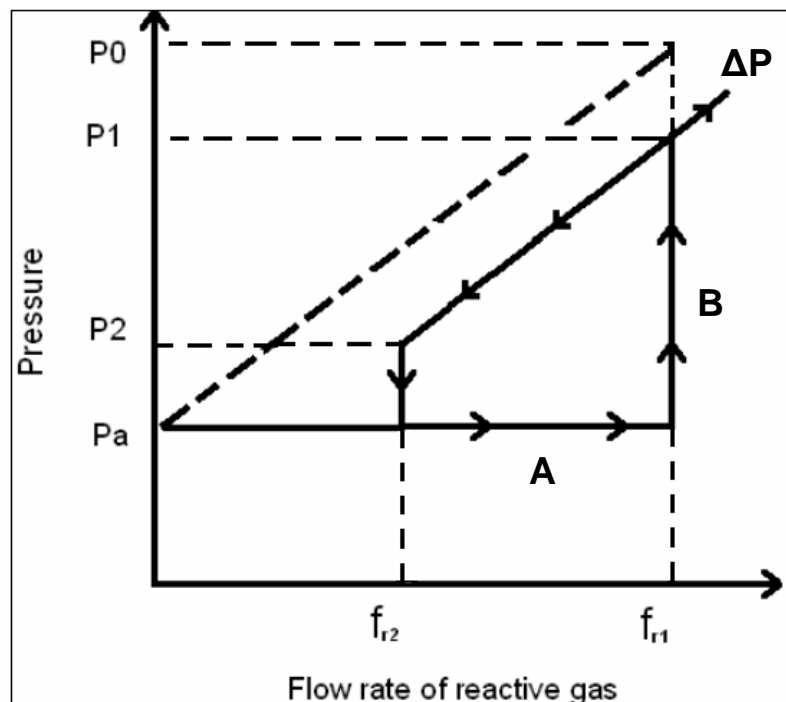


Figure 9 - Generic hysteresis curve for system pressure,  $P$ , as a function of reactive gas flow rate,  $f$  [35].

In Figure 9 is shown the hysteresis cycle for Al deposition with  $O_2$  as the reactant gas. In order to achieve a hysteresis cycle a constant flow of reactive gas,  $f$ , and chamber pressure,  $P$ , must be achieved [35]. In Figure 9 the dashed line shows a linear increase as the gas flow is increased. Stage A can be considered as a zone in which the sputtered metal is doped with reactive gas. There is a small variation in the total pressure as the reactive gas flow  $f_r$  is varied. In stage B a constant volume of reactive gas is consumed independent of the gas flow, so the formation of a compound film is the ideal, although being lower than  $\Delta P$ , the total pressure without any sputtering occurs [4, 11, 18, 35].

### 1.4.1. Sputtering Target

Targets are the source of material during sputter deposition processes. Targets are available in a wide range of materials such as metals, alloys and polymers. They can be found in a wide range of purities and sizes depending on the type of vacuum chamber and magnetron. The most used shapes are: flat rectangles, squares, circles and many more as shown in Figure 10 [36].



Figure 10- Sputtering Targets [36].

### 1.4.2. Ion Bombardment

Since the 1970's ion bombardment has been used as assistance tool used in thin film technology. Ion bombardment was first developed to act as in-situ surface cleaning, increasing in the surface coverage and adhesion. After this well established use it started being regarded an effective tool to control film properties like [4, 5, 7, 16-19, 22, 26]:

- Stress
- Stoichiometry
- Microstructure
- Hardness
- Density

- Pinhole density
- Adhesion

This property control is achieved as the substrate surface and growing film are placed under bombardment by a flux of energetic particles [4, 7, 16, 19]. This is a wide concept because it does not specify the source of the depositing film material and the source of bombarding [4, 19]. This particle bombardment induces sputtering/re-deposition effects on film morphology/microstructure and annealing effects on the film structure due to the heating caused by the incoming particles [17, 18]. The technique was later shown to enhance chemical reactions in the reactive deposition of compound thin films [26].

#### **1.4.3. Gas Incorporation**

When a thin film is being deposited, there are energetic gas particles present during film formation. These gaseous particles can be incorporated into the film depending on the process conditions: particle energy, substrate temperature [4, 7, 37].

These particles are incorporated in the film due to concurrent bombardment. This incorporation can have severe effects in the growing film. The gas particles can precipitate and form voids interfering with the overall performance of the film [4, 7, 37].

### **1.5. Thin Film Growth**

Independent of the PVD method, there are several film properties (e.g. hardness, Young's modulus, adhesion) that are very important in coating technology. These properties and parameters have an important influence on the properties of the coating produced. There are mainly four aspects of the deposition process that affect film growth, properties and performance [3-9, 12, 16-19, 22, 38-40]:

- Substrate condition – roughness, composition, contaminants, flaws caused by surface preparation, chemical stability of the surface,
- Deposition process – depositing flux, process temperature, deposition rate, gas contamination, ion bombardment;
- Film growth – surface mobility, interface formation, defects creation, ion bombardment, inert gas entrapment, deposition environment,

Surface preparation can consist of polishing to a required surface finish and cleaning of the substrate. The surface preparation is an important factor to assure film reproducibility and quality, and should be the first step in the design of thin films. It is also necessary to assure that the preparation does not change the surface in any undesirable or uncontrolled manner [3, 17, 22].

PVD techniques can provide environments with a reduced contamination level and gaseous particle fluxes that can be carefully controlled and monitored [4, 7, 9, 12, 16-19, 22]. The plasma state provides ions that are accelerated towards the target permitting particle bombardment to the growing film allowing modification of the film properties [6] as we seen before in section 1.1.

During film formation/growth stages an important controlling parameter is the surface mobility. The surface mobility of an atom depends of it's energy, the chemical bonding, and the surface temperature [8]. This surface mobility can change due to both the process chemistry and/or crystallography.

### **1.5.1. Thin film growth modes**

Three distinct modes of film growth may be considered [16-19, 41, 42]:

- 1) Layer by layer growth or Frank-Van der Merwe, two-dimensional (2-D) layer-by-layer(Figure 11 – top); Growth occurs when the binding energy between film atoms is equal or less than that between the film atoms and the substrate;

2) Three-dimensional (3-D) island, or Volmer-Weber growth (Figure 11 – middle), where small clusters are nucleated directly on the substrate surface.

3) Island growth mode and layer-plus-island growth mode, that is also called Stransky-Krastanov (Figure 11 – bottom); each named after the investigators associated with their initial description.

In the first mode of film growth the interaction between the substrate and the layer atoms is stronger than between neighbouring atoms [16-19]. Each new layer starts to grow, only when the last one is completed. Otherwise, the interaction between neighbouring atoms is stronger than the overlayer-substrate interaction. The particles will form aggregates over the surface that grow in size and eventually coalesce during film growth. This is known as island growth mode [16-19] as visible in Figure 12.

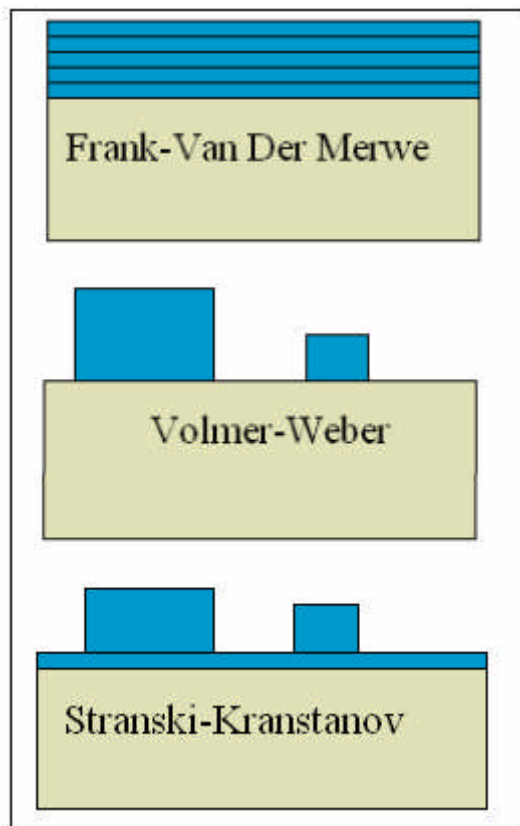


Figure 11 - Three modes of thin film growth processes [14].

The layer-plus-island growth mode is an intermediate case where the film starts to grow layer by layer in a first stage and only afterwards begins the formation of island agglomerates due to a change in surface energy and chemistry [16-19]. During island growth mode, each material island is a single crystal or it contains just a few crystals usually with some crystallographic orientation [3, 14, 16-19].

If the surface atoms have high mobility, there is greater probability of finding low energy positions consistent with crystal growth. With the rise of temperature crystal growth is promoted, because of the surface mobility is increased [16-19]. The same effect can be achieved by reducing the deposition rate, which gives more time for the adsorbed species to find an energetic favourable lattice position. Epitaxial growth was also found to be promoted by electron or ion bombardment and the associated increased energy of deposited atoms [16-19].

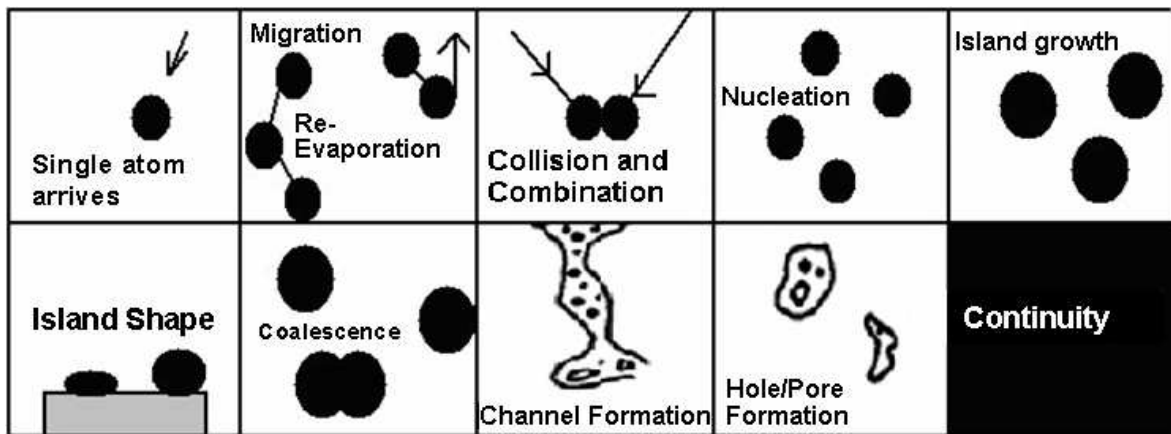


Figure 12 – Film Growth [43]

### 1.5.1.1 Structure zone models

Mochvan and Demchishin [7-9, 16-19] studied the effect of the substrate temperature on coating growth during both evaporation and sputtering deposition. They divided the different structures in 3 zones (relatively to  $T_s/T_m$ , where  $T_s$  is the substrate temperature and  $T_m$  is the coating material melting point measured in degrees Kelvin as we can see in Figure 13 [19].

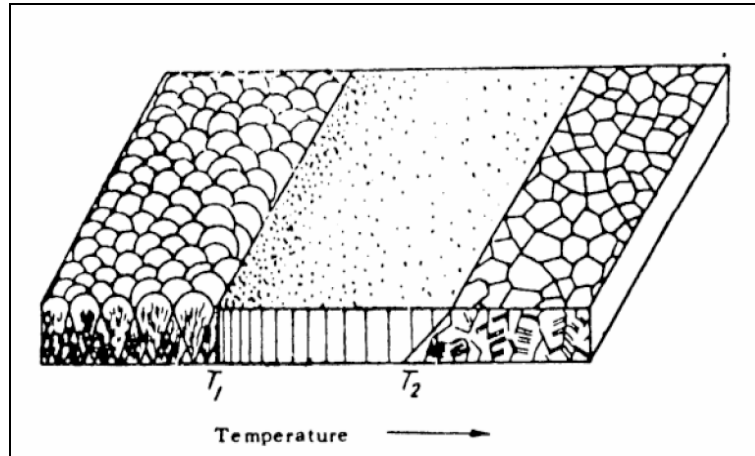


Figure 13 – Mochvan and Demchishin Model [19] .

Zone 1 ( $T_s/T_m < 0.3$ ): the film is composed of crystallites and surface is characterized by domed shapes. These domes can increase in width with deposition temperature and the internal structure of the crystals is not defined and presents high dislocation density. This zone is characterized by low adatom mobility [19] .

Zone 2 ( $0.3 < T_s/T_m < 0.45$ ): the films are composed of columnar grains with a smooth surface. The columnar structure is separated by dense crystalline boundaries. The boundaries have a high dislocation density. The grain width increases with the temperature ratios [19].

Zone 3 ( $T_s/T_m > 0.45$ ): is composed of similar size columnar grains, and presenting a bright surface. If there is stress accumulated during deposition recrystallisation may occur to form an equiaxed grain structures [19].

Thornton [3-5, 7-9, 16-19] extended these studies and studied the coating structure dependence on temperature and pressure during the sputtering process. He showed that during the time of deposition, the argon pressure influences the coating morphology. In a low argon pressure zone, a new zone (Zone T), was identified located between zone 1 and 2, the structure of this new zone consists of densely packed fibrous grains as we can see in Figure 14. Films formed in this zone are subjected to energetic reflected atoms or ion

bombardment during growth giving the “Zone T” structure (Figure 14). This zone exhibits high compressive internal stress [3, 9, 16-19] and has been described as the limiting form of the zone 1 at zero  $T_s/T_m$  on smooth substrates. The structure consists of a dense matrix of not well defined fibrous deposits with non-voided boundaries. The structure presents a high dislocation density [7-9, 16-19].

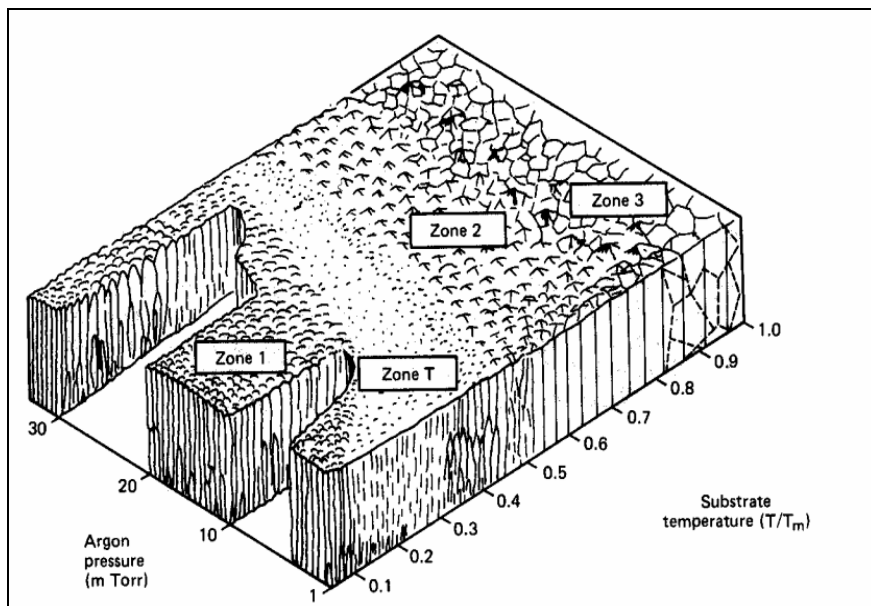


Figure 14 – Thornton’s Model [19].

Metals deposited in the transition zone present high hardness, high strength but with low ductility. The packed structure in zone 1 has the same hardness as in zone T but with poorer strength. Ceramics at low  $T_s/T_m$  (in zone 1) have low hardness. The dislocation density and the hardness of metals decrease rapidly with increase in  $T_s/T_m$  until zone 2 develops. In zone 2 and 3, the size of the columnar grains increases with  $T_s/T_m$  and the hardness and strength of metal films decrease. Metals deposited in the low  $T_s/T_m$  range of zone 2 can show low strength and low ductility [3, 8, 16-20].

### 1.5.1.2 Growth Defects

Missing atoms (vacancies) or atoms clusters, and lattice misalignments such as dislocations, Figure 15, are known as lattice defects [16-18].

During film growth, vacancies are formed by the depositing atoms not filling all of the lattice positions. These vacancies can agglomerate into voids in the crystal structure [16-18]. Lattice defects in the films can be reduced by increased substrate heating during deposition or ion bombardment during deposition [16-18].

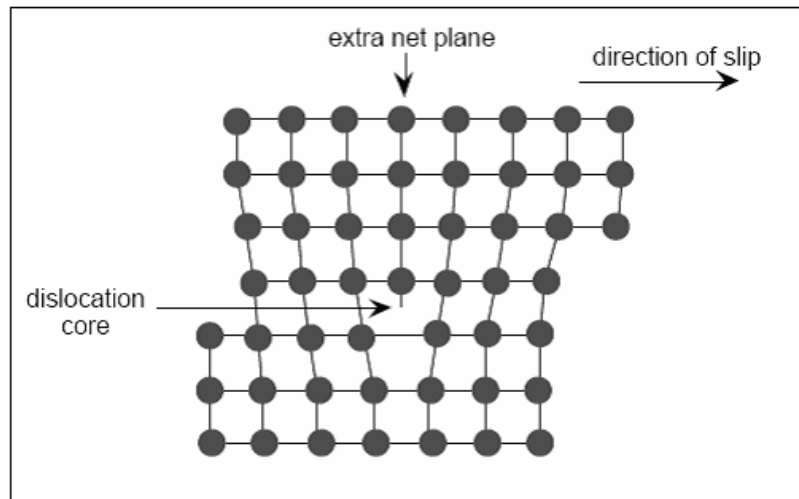


Figure 15 - Dislocation in a crystal lattice [37].

Lattice defects in the film may affect the electrical conductivity in metallic films and lifetime in semiconductor materials [20]. Generally high defect concentrations result in poor electro-migration properties. Lattice defects have been shown to be important to the properties of the high transition temperature superconductor films [20]. In depositing a film with ion bombardment, the defect concentration is a function of the energy of the bombardment. The number of lattice defects initially decreases with bombarding energy [16-18, 20].

### 1.5.1.3 Void Formation

During a PVD processes it is normal for the resultant film to have defects in the lattice structure. Voids are visible in Figure 16 and can decrease film density because they are pores inside the film and are not in contact with a free surface. In some extreme cases these pores can be caused by gaseous species trapped inside these internal cavities [37] as we saw in section 1.4.3.

These cavities can assume a spherical shape to minimize their surface area and therefore surface energy. These defects can be concentrated along grain boundaries, around precipitated phases, and/or at the interface between the film and the substrate these being preferential nucleation sites[4, 17, 18, 20].

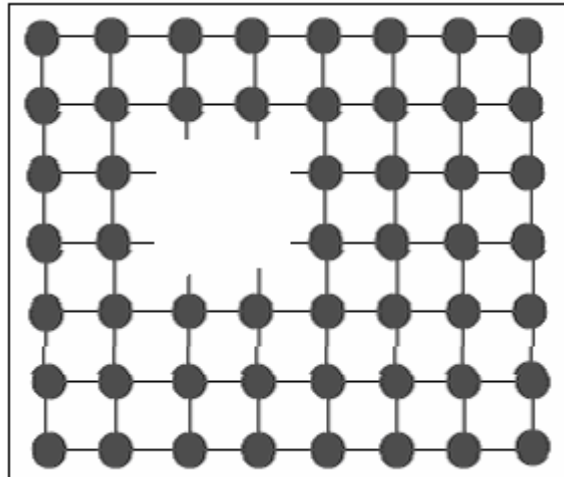


**Figure 16 - Void in crystal structure [37]**

When a film is exposed to a heat treatment the defects can migrate to free surfaces and agglomerate into larger voids. In multilayer film structures, the porosity in the film layers are trapped and can collapse into voids. If the deposited film has a high residual stress the stress can be relieved with time by the formation of voids even at room temperature. If the film is encapsulated, then the voids will precipitate along grain boundaries and at interfaces [4, 17, 18, 20].

#### **1.5.1.4 Flaking**

During or after deposition when a small area of the substrate suffers local loss of adhesion (pinhole flaking) caused by geometrical shadowing, these are called pinholes, which are uncovered areas of the surface [17]. Particles poorly bonded to the surface can change the surface morphology. The pinholes in the film are not visible until the nodule is disturbed and lands on the substrates surface. The pinhole flaking can be a source of contamination both for the chamber and the samples placed in the chamber, which can result in nodules in

the film [17]. Nodules can be usually created during multilayer deposition. They are caused by small particles (“seeds”) which arrive in the film surface, causing a deformation in the film, sometimes until the surface [17], as visible in Figure 17.

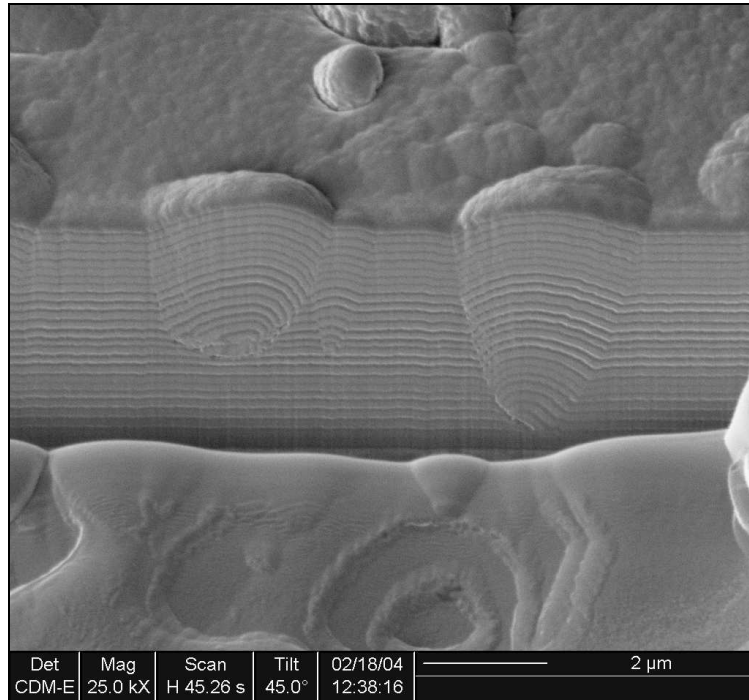


**Figure 17 – Nodules in a Multilayer coating.**

#### **1.5.1.5 Columnar Growth**

The morphology of a depositing film is determined by its surface mobility and the substrate surface roughness [3-5]. When the surface is rough, the peaks receive the adatom flux from all directions and, if the surface mobility is low, the peaks grow faster than the valleys due to geometrical shadowing [3-5].

Some films exhibit a unique growth morphology that is similar to needles aligned and piled together. This is known as columnar morphology, as visible in Figure 18 [44]. This growth morphology develops due to geometrical effects and is found whether the material is crystalline or amorphous [3, 16, 17, 44, 45].

A columnar morphology will be formed on a smooth substrate surface as long as the roughness increases with the growing film due to the growth on preferential crystal planes. In a rough substrate, the surface features (peaks

and valleys) cause variation in the angle of incidence and in this case less dense than on a smooth substrate [4, 17, 42]

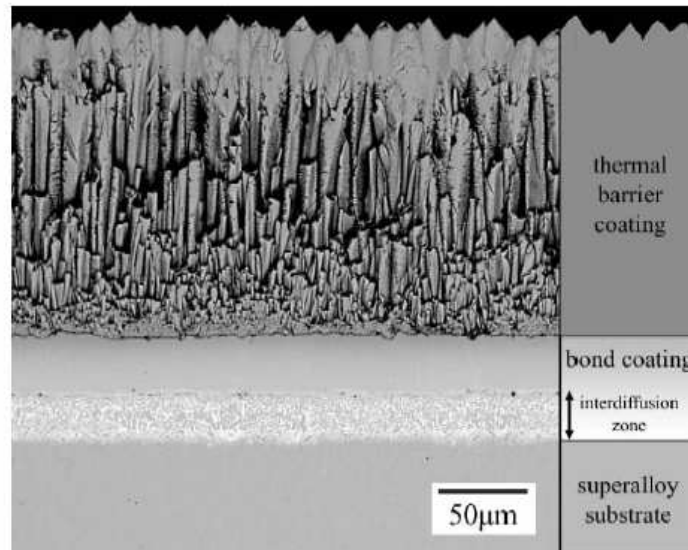


**Figure 18 – Thermal Barrier Coating cross section with visible columnar growth [44].**

#### **1.5.1.6 Amorphous Film Growth**

Amorphous materials are those that have no detectable crystal structure. Amorphous film materials can be formed by [3, 5, 8, 16, 18]:

- Deposition of a natural glassy material such as a glass composition;
- Deposition at low temperatures where the adatoms do not have enough mobility to rearrange and form a crystalline structure;
- Deposition of materials some of whose bonds are partially saturated by hydrogen – for example, a-C:H (amorphous hydrogenated carbon);
- Sputter deposition of complex metal alloys

## 2. Multilayer Concepts

Industrial and scientific interest in PVD coatings has been focused for many years on producing ultra-hard coatings, with hardness values ranging over 70GPa [46]. A distinction has to be made between coatings which exhibit intrinsic hardness like diamond (70-100 GPa), cubic boron nitride (50-70 GPa) and some compounds, like B-C-N [47], and extrinsic effects due to morphology and grain size of the thin films [46-49].

Multilayers can be considered a subclass of thin films where alternating layers of different materials are deposited. An example of a multilayer is shown in Figure 19. Two consecutive layers are described as a bilayer, and its thickness is described as the composition wavelength ( $\lambda$ ).

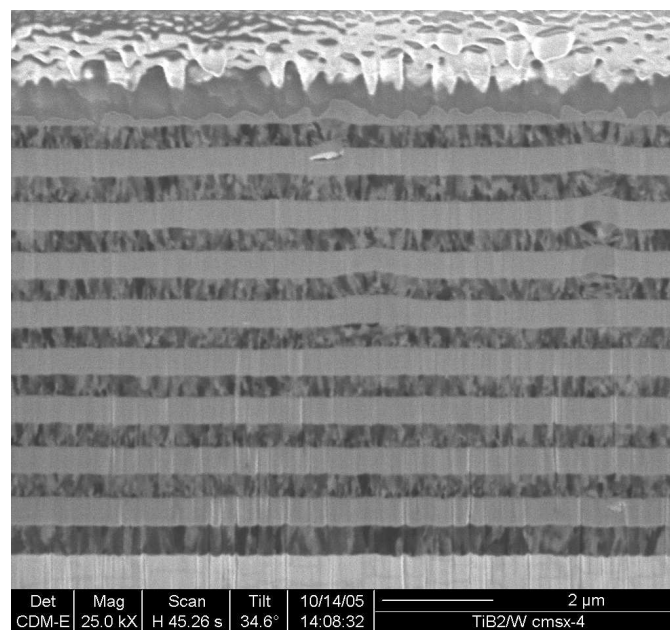


**Figure 19 – Cross-section of a TiB<sub>2</sub>/W Multilayer Coating**

Through the combination of different materials and an optimization of the microstructure, hardness values well beyond the constituent materials can be obtained [9]. The observed hardness enhancements are evident as the layer dimensions reduce and reach the nanometer region.

This has been shown by several researchers over the last decades, and hardness increases exceeding 100% have been reported [50-52]. The hardness enhancements are observed in a wide variety of material systems, e.g. metal/metal multilayers [9] metal/ceramic [9, 12], and ceramic/ceramic [9, 12, 53-55] systems. The common aspect in all of these studies is that hardness increases with a decrease in layer dimensions, and often this increase is followed by a decrease for a further reduction in wavelength [50, 56].

Veprek and co-workers [46-49, 57-59] describe materials which exhibit extrinsic hardness from their microstructure. These are the heterostructures known as the multi-layer superlattices [58]. These structures have an artificial arrangement of epitaxial layers; the layer thickness can be in the nanometer range, as long as the deposition method provides a controlled range of layer thicknesses. In multilayers hardening effects can occur, which are not predicted by conventional metallurgical theory. In 1970's Koehler [60] reported this work with the objective of producing a strong solid. Koehler [60] and Lehoczy [61, 62] while studying nanolayered heterostructures of binary metal systems (i.e. Al/Cu and Al/Ag) reported that the dislocations were unable to multiply or propagate from layer to layer [61]. This phenomena was explained based on strain coherency effects at layer interfaces, although other mechanisms have been reported, like the Hall-Petch effect [63, 64] where the hardness increase is a result of grain size reduction.

The Hall-Petch effect [63, 64] leads to an increase in grain boundary area and these grain boundaries subsequently act as dislocation obstacles. Depending on layer thickness they may show Orowan-like strengthening [65] where plastic deformation occurs by dislocation movement and bowing inside individual layers.

Helmerson [50, 52, 66] and co-workers have contributed considerably to the knowledge of the behaviour for superlattice coatings and have demonstrated the deposition of these coatings on the laboratory level.

Nanolayered superlattice coatings present great theoretical possibilities, the processing aspects of coating active engineering components with well-controlled epitaxial nanolayers can present practical problems, for example, meeting the coating requirements for high speed and dry cutting applications [67]. When these requirements are met there are considerable mechanical property improvements to have from these polycrystalline and even amorphous multi-layer coating structures, as demonstrated, for example, by Springer and co-workers [68, 69]. One of the first research groups to systematically study the multilayering concept for tribological coatings was led by Prof. Holleck, from the Institute of Materials Research in Karlsruhe. They used multilayers of different ceramic materials, such as  $\text{Si}_3\text{N}_4$ ,  $\text{SiC}$ ,  $\text{TiN}$ ,  $\text{TiC}$ ,  $\text{ZrN}$ , and  $\text{TiB}_2$ . These materials were selected on the basis of their dominant bonding mechanism: metallic, covalent, or ionic [70-73]. Holleck confirmed improvements in mechanical properties like: hardness, indentation toughness, adhesion and wear performance with optimised layer thicknesses and compositions [72, 73]. They have attributed these improvements to the crack deflection and stress relaxation mechanisms for the  $\text{TiC}/\text{TiB}_2$  system [74]. Several research groups [75-79] have since demonstrated that multilayer coatings in the nanometer and submicrometer layer-spacing range can potentially be extremely effective in improving wear in a range of metal cutting and sliding-contact applications.

Holmberg, Matthews and co-workers [80-82] have described how multilayer stacks with alternating high and low Young's modulus layers can provide improvements in situations where substrate deformation occurs. For coatings which are thick, hard and brittle, under bending conditions the internal stresses created in the coatings can be high. Under the same conditions, thin coatings can bend to the same radius and not have the same bending stress levels [81]. When alternating materials with high and low modulus [12], the harder materials can slide over each other and this prevents the build-up of high-bending stresses [12, 80]. The soft layers act as deformable zones permitting sliding in a way similar to bending paper sheets stacked together. Coatings with

discontinuous properties can combine high hardness with a capability to accommodate deformation and have been shown to perform well in a range of wear conditions, including erosion and abrasion (Ti/TiN, HfN/TiN, TiB<sub>2</sub>/W) [83, 84]. Metal carbide/DLC multi-layers are an effective solution in bearing and gear applications, where substrate deformation has to be accommodated by the coating system [15].

When bending hard/soft multilayer coatings the layer interaction does not depend on a discrete interface between the layers. It could be argued that a graded interface is to be preferred, as the possibility of delamination or interlayer separation can occur in sharp layer systems under deformation conditions [85]. This is true for systems using layers with very different chemical compositions. The advantages in multilayering materials with high modulus and low modulus have been demonstrated in erosion and impact tests [83, 84, 86, 87]. Such publications have confirmed that a multilayer stack provides an advantage in transition of mechanical properties from the substrate to the surface.

### **2.1.1. Multilayer Advantages**

Multilayer films are advantageous when compared to alloying and monolayer films for many applications [9, 12, 70-73]. The main advantages of multilayer coatings are summarized below [9, 12, 70-73]:

- Increase compatibility between film and substrate.
- The ability to produce films with low or no chemical reactivity.
- Increase hardness of the coating.
- Increase adhesion between film and substrate.
- Overcome any lack of toughness of the coating.
- Act as a diffusion barrier.
- Interrupt layer growth.

- Multilayer coating materials with different shear modulus allow the composite strength to be greater than predicted by rules of mixtures.
- Multilayers with optimum interface strength should enable an optimum hardness/toughness ratio, fatigue strength and adherence.
- Auxiliary effects – the layer material can influence the microstructure of the overall coating. Multilayer coating on drill bits present enhanced performance than most with monolayer coatings [73].

However the processing aspect multi-layers are much more demanding with respect to the manufacturing process control and material selection, and the challenges are outlined below [9, 12, 70]:

- The number of layers required can range from two to superlattices.
- Ensuring sufficient interface quality (adherence between layers).
- Auxiliary layer effect - interface compatibility/ stability.
- Avoiding interfacial reactions between layers that can decrease interfacial strength.
- High amount of favourable, low-energy interfaces, suitable for energy dissipation in the layer should be used where possible.
- Coherency of the phases forming the layer and the chemical bonding may be used to advantage.

### 3. Titanium Diboride

Materials can be classified as a function of their mechanical, chemical and physical properties. Properties like hardness, Young's modulus, transverse rupture strength, and other characteristics, like corrosion resistance, melting point, are essential to material selection.

There are several categories of hard materials: super-hard materials that can include diamond-like composites, cubic boron nitride (c-BN), and boron carbides, like tetra-boron carbide, boron carbide ( $B_4C$ , BC). These materials have high hardness, for example:  $B_4C$  has a hardness of 39.2GPa, over a range of temperatures between 200-1400 °C. The hardness of BC is between 29.4GPa to 68.6GPa depending on it's route of manufacture [9].

Such materials are used mainly in wear resistance applications. Pure carbides are not used for tool applications because they are too brittle. Titanium carbide (TiC), is a transition metal carbide that is at the low strength limit, but has high hardness. Tungsten carbide (WC) to the contrary, has high strength but lower hardness. Silicon carbide (SiC) is available in two allotropic forms; cubic and hexagonal, with hardness variations between 27.5GPa, and 44.1GPa. Alumina based ceramics are the most used and most thoroughly studied with hardnesses between 14GPa and 19GPa. Metal can be classified according to their composition; adding to the carbides are metals like Fe, Co, Ni, which are characterized by high strength and can form a first group of metals. Another group is formed by adding light metals, which are abundant and cheap (e.g. Al, Mg) [9, 12].

The borides have a good combination of thermal, mechanical, electrical and chemical properties [88]. Borides were identified more then 65 years ago. They belong in a group of interstitial alloys, and are a compound of a metal and boron with the ability to form a wide range of structures and compositions, TiB,  $TiB_2$ ,  $Ti_2B_5$ ,  $HfB_2$ ,  $ZrB_2$ ,  $VB_2$ ,  $NbB_2$ ,  $TaB_2$ ,  $CrB_2$ ,  $MoB_2$ , [9, 88]. One of the biggest

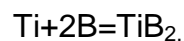
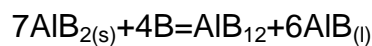
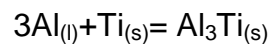
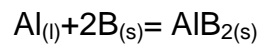
drawbacks is the fact that they are brittle. Another disadvantage is that the application of these materials may be inhibited by economic factors, particularly the cost of densifying a material with a high melting point. The boride, composition is controlled by the ratio of atomic sizes of the boron and metal atoms. This electrochemical factor is linked to the electronic transition, electron concentration and by the distribution of electrons around the boron atom.

Titanium diboride ( $\text{TiB}_2$ ) may be considered as a hard-metal which is classified in the first group, combining an expensive metal (Ti) and a light element (B), giving a unique set of fascinating characteristics, such as high hardness, high Young's modulus, good corrosion resistance and high melting point.

The formation of Titanium diboride results from the combination of  $\text{TiO}_2$  and  $\text{B}_2\text{O}_3$ , with methane gas as a reactant of the process.  $\text{TiB}_2$  can be produced by a variety of methods, sintering, hot pressing, hot isostatic pressing and microwave sintering. In the past few years some new techniques to form titanium diboride have been developed [9, 89-91]. Welman [91], formed titanium diboride from rutile (the most abundant of three naturally occurring forms of titanium dioxide) by room temperature ball milling. In this case he used a powder mixture of rutile, boron oxide and magnesium which were ball milled together. After milling for 10 to 15 hours titanium diboride was formed as shown by XRD analysis. The reaction also formed MgO and left no residual Mg. The MgO, which is an unwanted phase, was removed by leaching in acid, leaving a fine powder composed of aggregates of titanium diboride. The crystallite size of the products after annealing the milled powders was approximately 18nm for titanium diboride and 40nm for MgO. This technique has proved not to be commercially viable because of the time expense in milling, and also because the high-energy and inefficiency of the process.

Brinkman et al [90] studied the reaction mechanisms and phase formation sequence of the reactive sintering of Al- $\text{TiB}_2$  composites from elemental powders. The in-situ formation of reinforcements is easier in this reactive

sintering of a composite in an exothermic reaction between powders. One of the main advantages of reactive sintering by this process is the possibility of obtaining small-sized reinforcements over a wide range of volume fractions. In terms of reinforcement capabilities Al and its alloys are attractive due to their low melting points and wide liquid temperature range. Titanium diboride is suitable as an reinforcement phase for Al-based reactive sintered composites because of the high exothermic heat of formation and the thermodynamic stability of  $TiB_2$  in Al. In the reactive sintering of an Al-40vol% $TiB_2$  composites from elemental powders,  $AlB_2$  and  $Al_3Ti$  are identified as transient phases in the reactive process. The  $AlB_2$  is formed before the  $Al_3Ti$  phase. Brinkman et al [90] proved that if there was no unreacted Al left after the formation of those two compounds. The reaction did not take place until the decomposition of the  $AlB_2$  in to a more stable  $AlB_{12}$  phase and an Al liquid phase which had a small amount of B in the solution. That liquid phase enabled the reaction between Ti and the B in solution to form  $TiB_2$ . The reaction sequence can be written as [90]:



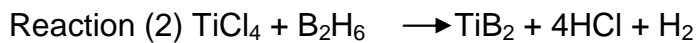
Lu et al [92] studied that the formation of  $TiB_2$  via a thermodynamic salt reaction. The study showed that the chemical reactions that occurred during the formation of  $TiB_2$  are similar to those that occur in the grain refinement of Al using an Al-Ti-B master alloy [92, 93]. The formation of  $TiB_2$  was found to be function of the reaction time. By using TEM analysis, the  $TiB_2$  particles were found to have a size between 0.5 and 1  $\mu m$ .

Gu et al [94] formed  $TiB_2$  in an autoclave using a benzene-thermal reaction of metallic sodium, with amorphous boron and titanium tetrachloride at 400 °C. The advantage of this technique was that the process temperature was much

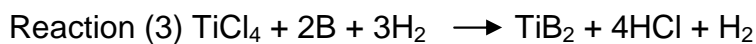
lower than other methods, such as direct reaction of titanium, its oxides or hydrides, with elemental boron which occurs over 1000°C. As a result, they were able to produce nanocrystalline TiB<sub>2</sub> of 15 to 40 nm with a hexagonal cell structure. Gu et al [94] demonstrated that solvothermal synthesis could be a method for preparing Titanium Diboride nanomaterials.

It is also possible to find some examples of how TiB<sub>2</sub> can be formed by CVD techniques, just by using different chemical compounds [95, 96]:

The reactions are illustrated in the following example regarding the formation of Titanium diboride using either boron trichloride or diborane as a boron source [95, 96]:



In the case of Reaction (2), it is possible that B<sub>2</sub>H<sub>6</sub> may already decomposed to boron and hydrogen and the equilibrium of the reaction might be closer to:



By using any of these techniques Titanium diboride is formed. The unit cell is visible in Figure 20 and the properties are described in Table 3 [9, 97-99] .

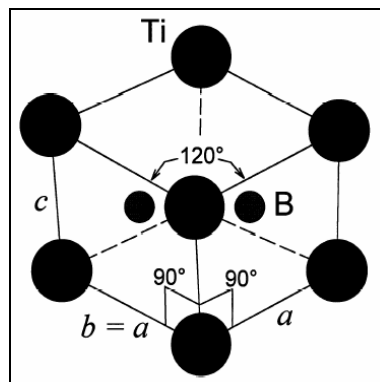
Property [unit]	20 °C	500 °C	1000 °C
Bulk Modulus [GPa]	240	234	228
Compressive Strength [GPa]	1.8		
Density <sup>a</sup> [g/cm <sup>3</sup> ]	4.5	4.449	4.389
Elastic Modulus [GPa]	565	550	534
Flexural Strength [MPa]	400	429	459
Fracture Toughness [MPa m <sup>1/2</sup> ]	6.2		
Friction Coefficient <sup>b</sup>	0.9	0.9	0.6
Hardness <sup>c</sup> [GPa]	25	11	4.6
Lattice Parameter <sup>d</sup> a [Å]	3.029	3.039	3.052
Lattice Parameter <sup>d</sup> c [Å]	3.229	3.244	3.262
Poisson's Ratio	0.108	0.108	0.108
Shear Modulus [GPa]	255	248	241
Sound Velocity, longitudinal [km/s]	11.4	11.3	11.2
Sound Velocity, shear [km/s]	7.53	7.47	7.40
Specific Heat [J/kg·K]	617	1073	1186
Thermal Conductivity [W/m·K]	96	81	78.1
Thermal Diffusivity [cm <sup>2</sup> /s]	0.30	0.17	0.149
Thermal Expansion <sup>e</sup> , a axis [10 <sup>-6</sup> K <sup>-1</sup> ]	6.4	7.0	7.7
Thermal Expansion <sup>e</sup> , c axis [10 <sup>-6</sup> K <sup>-1</sup> ]	9.2	9.8	10.4
Thermal Expansion <sup>f</sup> , average [10 <sup>-6</sup> K <sup>-1</sup> ]	7.4	7.9	8.6
Wear Coefficient <sup>b</sup> [10 <sup>-3</sup> ]	1.7		
Melting point [°C]	2850		
Structure	HCP		

Table 3 - Titanium diboride properties [9, 12, 97-99]

Caption:

- a) Single crystal density;
- b) Density = 4.32 g/cm<sup>3</sup>, grain size = 2 μm,  $v_{slide}/P_{load} = 0.2 \text{ m s}^{-1} \text{ MPa}^{-1}$ ;
- c) Vickers indentation, load = 5 N;
- d) Single crystal, hexagonal unit cell;
- e) Single crystal, for cumulative expansion from 293 K (20°C);
- f)  $CTE = (1/x_{293})(x - x_{293})/(T/K - 293)$ , x = a or c;

K.L. Tee et al [100] studied the in-situ TiB<sub>2</sub> reinforcement of aluminium composites. In their studies they have been successful in synthesising chemical reactions between Al, B and Ti. The incorporation of carbon in Al<sub>3</sub>Ti decreased because of the formation of TiC. Al<sub>3</sub>Ti is more stable in the presence of TiC, because TiC is more stable in the presence of carbon. In this way mechanical properties were improved, including Young's modulus and ductility. Ductility improved in terms of elongation of the composite as the incorporation of carbon increased. It gave a 26% improvement in comparison with the composite without carbon. This increasing in ductility can be explained by the decreasing amount of Al<sub>3</sub>Ti and the increase amount of TiC. The composition of Al-4.5%Cu-15% vol TiB<sub>2</sub>, incorporated with 3%C, was found to produce a tensile strength of 258MPa, and a yield strength of 203MPa [100].



**Figure 20 - The hexagonal unit cell of single crystal TiB<sub>2</sub>, space group in the following conditions: P6/mmm,  $a = b \neq c, \alpha = \beta = 90^\circ, \gamma = 120^\circ$ , 1 formula unit per cell, Ti At (0,0,0), B at (1/3,2/3,1/2) and (2/3,1/3,1/2) [98].**

A wide range of studies has been made concerning the use of TiB<sub>2</sub>. A few of these studies used different types of deposition processes to produce TiB<sub>2</sub> coatings. Pfohl et al [101] used PACVD (Plasma Assisted Chemical Vapour Deposition) to deposit coatings on substrates with complex shapes. The main application was wear protection in the diecasting of Al, extrusion or dry cutting. The coatings showed crystalline structures with grain size of 2nm. The hardness reached 33GPa and the critical load in a scratch test was 35N. Karner et al [96] developed a new type of reactor for the PACVD. This new type of reactor permits deposition on all surfaces of objects of complex geometry. The

films were deposited in different gas mixtures, Ar, H<sub>2</sub>, N<sub>2</sub>, TiCl<sub>4</sub> and BCl<sub>3</sub> as the plasmas used were both R.F. and pulsed direct current. The coatings presented hardness values up to 29.42GPa. The coatings also exhibited an amorphous fracture pattern when deposited by R.F. or a fibrous structured if deposited by direct current.

Riviere et al [102] deposited TiB<sub>2</sub> coatings of stoichiometric composition at room temperature using Dynamic Ion Mixing. The films were obtained by ion beam sputtering of a composite TiB<sub>2</sub>+B target in an argon atmosphere. The authors concluded by TEM and XPS analysis that the internal structure of the films corresponded to the hexagonal TiB<sub>2</sub> phase. The XPS analysis showed that a large amount of oxygen was present in the first layers, but after sputter cleaning TiB<sub>2</sub> material was found.

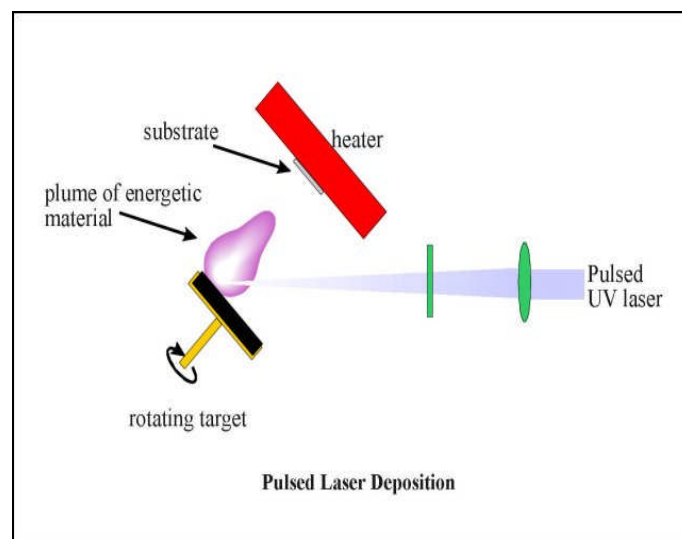


Figure 21 – Pulsed Laser Deposition Overview [103]

Argawal et al [104, 105] studied the deposition of TiB<sub>2</sub> ultra-hard ceramic by using a Nd:YAG laser on to AISI 1010 steel with fixed processing parameters. The coating was composite in nature. By analysing the coatings, they concluded that the coatings were hard and tough and TiB<sub>2</sub> possessed a high interfacial energy.

Zergioti et al [106], deposited refractory TiC and TiB<sub>2</sub> on different substrates, steel and silicon. The substrates were held at a range of temperatures, from 40°C-650°C. The films were grown by pulsed laser deposition, viewed schematically in Figure 21. TiC and TiB<sub>2</sub> films produced by this method had a fine morphology, with a grain size of 10nm-70nm at all substrate temperatures. The XRD analysis peaks presented some shifts, which were attributed to the presence of residual stresses in the films that decreased as the substrate temperature was increased [106].

### 3.1.1. Practical Applications for Titanium Diboride

Titanium diboride is being studied to perform as a high-temperature material. There are many industrial applications for TiB<sub>2</sub>, where enhanced mechanical properties are required like: erosion resistance, corrosion resistance, high temperature stability and electrical conductivity. These are some of the applications identified for titanium diboride [9, 101, 107-109]:

- Impact resistant armour, due to high Young's Modulus and good fracture toughness;
- Cutting tools;
- Crucibles;
- Wear parts;
- Mechanical seals;
- Electric devices;
- Thermoelectric material;
- Heat resistant ceramics with high electric conductivity;
- Diffusion barriers between ohmic metastable contacts and the semiconductor substrate Si or GaAs;
- Used as a reinforcement;
- Sliding electrical contacts;
- Applications in the Aerospace industry;
- Wear protection in the diecasting of Al;
- Surface coatings on first wall components ;

- Applications in the Magnetic recording industry.

Agarwal et al [104, 105], compared the tribological properties of TiB<sub>2</sub> deposited by two methods: the Pulsed Electrode Surfacing (PES) and Laser Surface Engineering (LSE). PES is characterized by high current and a short duration pulse via a discharge capacitance and a voltage circuit which results in melting the electrode and depositing the material on the substrate. LSE uses a pre-placed powder precursor which is melted along with a thin layer of the substrate to produce a laser melt zone of desired composition. They concluded that the wear resistance for LSE coated TiB<sub>2</sub> is better than the PES deposited TiB<sub>2</sub> coating. The friction coefficient values for the LSE method ( $\mu=0.6$ ) is lower than the PES method ( $\mu=0.7$ ). Wear occurs in the PES deposited coating by the brittle fracture and attrition type mechanisms. On the LSE adhesive-abrasive wear occurs by localized plastic deformation.

Berger et al [110] compared TiB<sub>2</sub> coatings in dry sliding against PVD titanium nitride (TiN), titanium aluminium carbonitride (TiAlCN) and titanium carbonitride (TiCN). The test used two cross elongated cylindrical with test specimens forced to slide axially against each other. The sliding was performed at a constant sliding speed and a gradually increasing normal load, while recording the friction. They performed the tests on coated cemented carbide cylinders sliding against cylinders of titanium alloy (Ti-6Al-4V), Al alloy (Al7075) and Inconel 718. The TiB<sub>2</sub> surface displayed superior friction and anti-sticking properties, when tested against the aluminium alloy. Against the Ti alloy and Inconel there was no significant difference. They concluded that in this case the friction coefficient is determined by the plastic properties of the counter material. When sliding against aluminium the TiB<sub>2</sub> coating gave a significantly lower friction value in the load range studied, except for the highest load (750N). Below 500N the friction coefficient was 0.3 against TiB<sub>2</sub>. All others coatings display friction coefficients around 0.4-0.5.

Data on the fretting wear behaviour of bulk  $\text{TiB}_2$  is limited. Praskah et al [111] studied the friction and wear behaviour in fretting wear tests. They studied the coatings after annealing in air for  $600^\circ\text{C}$  for 1 hour. The coatings showed a better wear resistance ( $2000 \mu\text{m}^3/\text{J}$ ) than a hard TiN coating ( $23000\mu\text{m}^3/\text{J}$ ) for tests performed in ambient air. The annealed  $\text{TiB}_2$  coatings showed a low wear resistance ( $14000\mu\text{m}^3/\text{J}$ ) due to cracking and oxidation. The main phase that they detected on the surface after annealing was  $\text{TiO}_2$  and  $\text{B}_2\text{O}_3$ . The higher wear rate of annealed  $\text{TiB}_2$  was attributed to the formation of  $\text{TiO}_2$  on the surface during annealing. The same reason was presented for the presence of cracks. One phenomenon that the authors could not explain was the formation of a low friction  $\text{B}_2\text{O}_3$  which is a type of glass.

The industrial application of  $\text{TiB}_2$  coatings is limited due to the high compressive stress present in the coatings. Berger et al studied  $\text{TiB}_2$  [107, 108, 110, 112], with the aim of reducing the high compressive stress present in the films. They decreased the amount of stress in the coatings by depositing them with magnetron sputtering using electrons to enhance the adatom mobility of the growing film. The authors changed the nature of the stress just by switching the polarity of the substrate bias from negative to positive. By changing the bias, the substrate bombardment by positive ions stops, instead the high electron current passing through the substrate causes energy to be released due to electron bombardment and leads to an increase in temperature from  $350^\circ\text{C}$  to  $500^\circ\text{C}$ . As a result the amount of stress is reduced. They compared the coatings produced using negative bias and using positive bias from which they concluded that the mechanical properties were not affected. The only difference was the amount of stress in the coatings.

Gilmore et al [113-115] have studied the application of  $\text{TiB}_2$  for low friction applications. The authors produced low friction coatings by combining a lubricant phase (C) and a hard wear-resistant phase ( $\text{TiB}_2$ ). They deposited the coatings in the form of a multilayer ( $\text{TiB}_2/\text{C}$ ) or as homogeneous ( $\text{TiB}_2\text{-C}$ ) films. The co-sputtered coatings had two phases: diamond like carbon (DLC) and a

hexagonal MoS<sub>2</sub>-type structure in which carbon is incorporated. The concentration of carbon (C) needed to produce a friction-reducing effect was high, as high as 50%. The high concentration of carbon leads to the preferential incorporation of carbon atoms in the TiB<sub>2</sub> lattice and results in the lubricating phase of DLC starting when the saturation is reached. In the multilayer coatings, the increase of the overall carbon content required to obtain a friction-reduction effect varies from 10-50%. This effect is caused by an increase in the relative proportion of carbon bonded with the TiB<sub>2</sub> in the interface regions. The same authors had also studied the incorporation of MoS<sub>2</sub> into the coating. The reduced friction effect was obtained even at low concentrations of MoS<sub>2</sub>. Low friction was obtained at temperatures up to 400°C for the TiB<sub>2</sub>-MoS<sub>2</sub> coatings. The TiB<sub>2</sub>-C coatings exhibited a sharp increase in the friction coefficient above 150°C. This is a typical behaviour for graphite containing coatings [114].

In order to overcome the brittleness of TiB<sub>2</sub> and to have a more wide industrial range of applications, several authors have been working with multilayering TiB<sub>2</sub>. Holleck et al [72, 73] fabricated multilayer coatings with titanium diboride (TiB<sub>2</sub>) and titanium carbide (TiC) prepared by magnetron sputtering coupled with ion bombardment during deposition. The authors have prepared multilayers composed of 10, 100, 250, 500 and 1000 individual layers with an overall thickness of 5µm. The multilayers produced were TiC/TiB<sub>2</sub>, TiN/TiB<sub>2</sub> and TiC/TiN. These coatings were produced using magnetron sputtering without biasing the substrates. They reported that the microhardness changed with the number of layers. For a specific number of layers 100-200 for a total thickness of 5µm, it was shown that the number of layers had a beneficial effect on the crack propagation resistance and hence improved the wear behaviour.

Lee et al [54] also have deposited multilayer coatings using titanium diboride and titanium carbide. The authors have deposited coatings using unbalanced magnetron sputtering with stationary and rotating substrates. The coatings produced with a rotating work table exhibited a high compressive stress (4-7GPa). The same stationary coatings presented a much lower value of

compressive stress ( $<2\text{GPa}$ ) and with a high hardness ( $60\text{GPa}$ ). The authors reported that the mobility of the surface species was improved and there was more time for surface diffusion with the substrate rotation. The films that were produced under these conditions had improved density and lower void concentration.

Wolf et al [116] deposited  $4\mu\text{m}$  and  $14\mu\text{m}$  thick polycrystalline multilayer coatings of titanium carbide and titanium diboride. The coatings were deposited using ion assisted, electron beam – physical vapour deposition. The hardness increased with the increasing number of layers. The adhesion of the coatings was tested using a scratch test. The adhesion was greater than  $50\text{N}$  for the  $4\mu\text{m}$  thick and less than  $30\text{N}$  for the  $14\mu\text{m}$  thick. The grain size, the compressive stress and the fracture toughness was found to decrease with the increasing number of layers.

Lim et al [54] prepared multilayer coatings of titanium nitride (TiN) and titanium diboride. The coating thickness was  $2\mu\text{m}$  on steel substrates. Using Plasma enhanced – CVD (PECVD) they prepared the coating by alternating depositions of TiN and  $\text{TiB}_2$ , using a gas mixture of  $\text{TiCl}_4$ ,  $\text{H}_2$ , Ar,  $\text{N}_2$  and  $\text{BCl}_3$ . The hardness of the coatings increased with the decreasing thickness of the layers of TiN and with the increased thickness of the layers of  $\text{TiB}_2$ . The hardness values had a linear relation with the titanium diboride volume fraction. The wear resistance increased with the thickness of TiN layers. They also reported that the multilayer coatings with periods  $<24\text{nm}$  showed better wear resistance than the monolayer coatings.

## 4. Diamond and DLC films

Recently great progress has been made in the deposition of diamond and diamond-like carbon (DLC) coatings for industrial applications. Natural diamond with its high hardness, low coefficient of friction, high thermal conductivity, good visible and infrared transparency, and chemical inertness has long provided a goal for the thin film deposition industry [117].

Two companies in the US have perfected techniques for creating cheap artificial diamonds, virtually indistinguishable from the real thing. The story of how they got there is fascinating - retired army generals purchasing cold war soviet technology, indirect death threats to scientists at conferences and best of all, a very real threat to the De Beers diamond cartel/monopoly [118].

The most important application for this technology is likely to be semi-conductors, biomedicine and wear resistant coatings. Kato et al [119], researchers at the Diamond Research Center (DRC) and the National Institute of Advanced Industrial Science and Technology (AIST), have succeeded in synthesizing n-type diamond semiconductors on (001) oriented diamond substrates through vapour deposition. They have successfully realized ultraviolet emission with a UV emitting device prepared on the basis of a p-n junction using the (001) n-type diamond semiconductor. This is a very significant achievement eliminating the restriction by the substrate orientation, which has been a blockage in the development of electronic devices derived from diamond semiconductors [119].

Diamond is characterized by high thermal conductivity, high breakdown voltage and very high mobility for electrons and positive holes; proving to be a promising requirement for the application as electron devices based on diamond materials [42, 120-122]. In the area of power devices and short-wavelength light emitting devices, good performance may be expected among these various types of semiconductors, and for this reason, a number of

research organizations are racing for the development of diamond semiconductor devices. Diamonds can handle far higher temperatures than silicon, implying increased chip speed resulting in chips so fast that silicon would just melt under the strain [121, 122].

Polycrystalline diamond films can be formed with a variety of methods of PVD and CVD, such as sputtering, ion beam deposition, PACVD, HFCVD just to name a few [120]. The deposition temperature needs to be higher than 600°C to allow atomic rearrangement [121, 122]. If the deposition temperature is lower, the atoms rearrangement does not occur and the film becomes amorphous.

Diamond presents a very specific crystal structure and chemical bonding. When a film possesses a bonding majority of  $sp^3$  bonds it is also known as Diamond-like carbon (DLC), which can also be called amorphous diamond [42, 45, 120-122].

The mechanical properties of DLC films are controlled by the amount of  $sp^2$  and  $sp^3$  bonding present in the film. Carbon is a versatile element because it can present different types of bonding. This variety in bonding structure is only possible due to three different bonding configurations as we can see in Figure 22 [123]. This bonding control can be done using reactive deposition with hydrocarbon gases such as  $CH_4$ ,  $C_2H_2$  [124-127]. The inclusion of hydrocarbon gases during deposition provides the hydrogen component which etches the  $sp^2$  (graphite) bonds [42, 45, 120, 124-127].

DLC films are being the subject of extensive research and are being used in many industrial applications such as abrasion resistant coatings, infrared optics and optical products, sensors, cutting tools, recording media and protection of polymers [124, 125, 127-131]

In nature, elemental carbon is usually found in one of its two allotropic forms, graphite and diamond. In the  $sp^1$  configuration the covalently bonded electrons

are in orbitals directed along the x-axis while the other two electrons are along y and z directions, forming much weaker bonds in these directions. In the diamond crystal structure carbon atoms are  $sp^3$  bonded and densely packed: the lattice is fcc (face-centered cubic) with strong bonds in a tetrahedral coordination. In amorphous DLC coating, the carbon atoms are arranged so that no long range order is present [123, 132]. In diamond, the carbon atom's four valence electrons are each assigned to a tetrahedral directed  $sp^3$  orbital, which makes a strong covalent bond with an adjacent atom. In graphite, three valence electrons enter trigonally directed  $sp^2$  orbitals and form covalent bonds [123, 132].

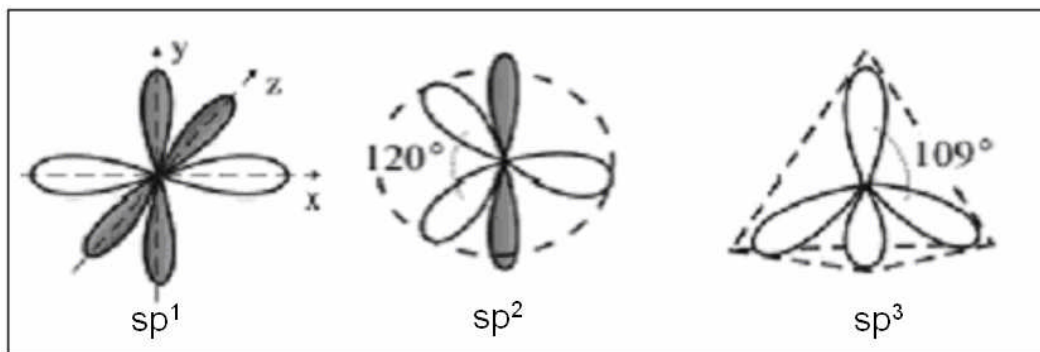


**Figure 22 – Three different bonding configurations of carbon [123].**

The fourth valence electrons form a 2D electron gas and the  $sp^2$  bonded planes interact via weak Van der Waals forces. The strong and equivalent covalent  $sp^3$  bonds in diamond explain its extreme physical properties. In graphite the weaker bonds between the covalently bonded planes explain its more brittle behavior and also its use as a solid lubricant because its covalently bonded planes are able to move with respect to each other as a result of the weaker interplane Van der Waals bonding. Differences between graphite, diamond, and DLC are reproduced in Table 4 [42, 45, 95, 120, 122, 123, 132]:

	<b>Graphite</b>	<b>Diamond</b>	<b>DLC</b>
<b>Composition</b>	Pure carbon	Essentially carbon (<1 at% hydrogen)	Up to 50 at. % hydrogen
<b>Microstructure</b>	Crystalline	Crystalline	Amorphous
<b>Atomic bonding stage</b>	sp <sup>2</sup> only	sp <sup>3</sup> only	sp <sup>1</sup> , sp <sup>2</sup> , sp <sup>3</sup> (variable ratio)
<b>Stability</b>	Stable	Stable	Metastable
<b>Raman spectrum</b>	Sharp peak at 1580 cm <sup>-1</sup>	Sharp peak at 1332 cm <sup>-1</sup>	Broad peaks at 1330 and 1550 cm <sup>-1</sup>
<b>Electrical conductivity</b>	Conductor	Insulator	Insulator
<b>Thermal conductivity</b>	Good	V. Good	Poor

**Table 4 – Comparison of Graphite, Diamond and DLC properties [42, 45, 95, 120, 122].**

#### **4.1.1. Deposition conditions**

The conversion between lower energy and density of graphite to higher energy and density of diamond occurs due to energetic particles involved in the manufacturing process, generated by a glow discharge or ion beam, which promotes and controls the bonding changes from sp<sup>2</sup> to sp<sup>3</sup>. When depositing DLC films in a hydrogen containing atmosphere (a-C:H), the ion bombardment and the hydrogen presence are influential factors to promote the sp<sup>3</sup> bonds within the film [132, 133].

Graphite and diamond have well defined crystal structures and mechanical properties. The variations in mechanical properties between DLC and diamond are expected depending on the manufacturing route. This variation is a sign of versatility due to the mechanical properties control. This control allows the mechanical properties to be manipulated to fit a particular application. Diamond DLC and properties are similar but may differ as can be seen in Table 5 [42, 45, 95, 120, 122, 127].

As a result of the high compressive stress the DLC coatings have a tendency to delaminate and separate from the substrate when a few microns thick. These high stress levels are influenced by the presence of hydrogen in the films and

when using steel substrates due to the Fe-C interdiffusion [134, 135]. The adhesion of DLC to most substrates is good if suitable cleaning by ion bombardment is undertaken prior to deposition. Adhesion to carbide formers like Ti, Cr, W, Mo, Ta and iron alloys is sometimes good [120], but depends on the compressive stresses generated in the film and across the interface.

	<b>CVD Diamond</b>	<b>DLC</b>
<b>Density, g/cm<sup>3</sup></b>	3.40 ± 0.1	1.8 - 2.8
<b>Thickness range, μm</b>	1 - 1000	0.1 - 5
<b>Internal stress</b>	Tensile	Compressive 1.3 – 1.6GPa
<b>Thermal conductivity, W/m<sup>°K</sup></b>	>1300	400 - 1000
<b>Bandgap, eV</b>	5.48	0.8 - 3
<b>Index of refraction, @10 μm</b>	2.34 – 2.42	1.8 – 2.4
<b>Electrical resistivity, Ω cm</b>	10 <sup>12</sup> – 10 <sup>16</sup>	10 <sup>5</sup> - 10 <sup>15</sup>
<b>Vickers hardness, kg/mm<sup>2</sup></b>	5000 – 10000	2000 - 9000
<b>Friction coefficient</b>	0.05 – 0.15	0.01 – 0.3

**Table 5 – Properties of DLC and CVD Diamond Coatings [42, 45, 95, 120, 122, 127].**

In order to avoid or minimize the stressing of the films hydrogen free films have been produced by several authors. Wang et al [136] developed Ti-doped and hydrogen-free DLC films (a-C:Ti) which were synthesized by unbalanced magnetron sputtering using graphite targets. The high residual stress of the DLC films was dissipated through a compound interface consisting of a series of Ti, TiN, TiC<sub>x</sub>N<sub>y</sub> graded interlayers. The substrates were cleaned by ion bombardment before deposition and pre-heated. Directly on to the substrate a Ti/TiN layer was deposited and the transition from TiC<sub>x</sub>N<sub>y</sub> to DLC was done by reducing first the nitrogen flow and the Ti deposition was reduced and co-deposited with the start of the DLC film. Adhesion strength of 70N was achieved with this graded layer configuration. These a-C:Ti films had low surface roughness and high adhesion strength. Another relevant aspect of this work was the improvement in residual stress control.

Several authors [15, 133, 136-139] have proposed the addition of a transition metal within the matrix of DLC films, which can lead to some improvement of their mechanical properties. The insertion of Me (Metal) atoms in the DLC matrix helps reduce its high intrinsic stress. Multilayered structures, composition graded or the deposition of a buffer layer constitute alternative solutions to the poor adhesion in DLC films. Corbella and co-workers have studied [137, 138, 140] the addition of W to the DLC matrix. They prepared the films using pulsed DC reactive magnetron sputtering in an argon-diluted methane environment. This gas variation in the methane dilution led to the deposition of Metal-DLC films (Me-DLC), with either metal-rich or carbon rich films. Metal carbide particles were embedded within the film. These Me-DLC films were homogeneous, although they lost their uniformity when grown under high methane flow conditions. The films deposited with 25% dilution on a thin metal-carbon interlayer were continuous and uniform. The W-DLC films were the least stressed films comparing with the other metal films examined (Mo-, Ti-, Nb-). The stress reduction was caused by the columnar structures generated by the W component in the multilayer. The route to minimal stress, coming from the Me-DLC, film is accompanied by a loss of hardness. The minimum hardness appears to be associated with a change in structure from a columnar to more granular morphology [137, 138, 140].

Another metal that has been used successfully as a bond layer for DLC films is Chromium, by deposition of a Cr intermediate layer using magnetron sputtering with substrate bias. Intermixing at the Cr-steel interface was further achieved by ion bombardment, thus improving the adhesion. Chen et al [141, 142] chose Cr as a bond layer because the thermal expansion coefficient is closer to Fe (The dominant elements in steel are Fe, Cr and C). The melting point of Cr is lower than TiN or TiC which is used in other bond layers, suggesting that Cr exhibits better toughness and acceptable strength. The matching of thermal expansion coefficients between Cr and steel substrates reduces thermal stress and improves the adhesion of Cr on steel. The ability to form Cr-Fe alloys is a further positive aspect in order to improve adhesion. The intermixed Cr-steel

interface can be further enhanced by the deposition of a Cr interlayer at high temperature and at high bias applied to the substrate. Chen et al [141] found that the optimum thickness of the Cr layer in order to achieve good adhesion was 300nm [141]. The Cr layer was deposited with bias applied to the substrate. When it exceeded 700V, the DLC film had the highest adhesion. For high bias a greater inter-mixing at the Cr-substrate interface occurred, improving the adhesion [141].

Ryeol Lee et al [15] showed that chemical compatibility between carbon and the intermediate layer element and microstructure control of the intermediate layer are important factors to improve adhesion. Columnar grains were found to induce a rough surface, which enhanced mechanical interlocking. When a W-C mixed layer was deposited, an excess fraction of hydrocarbon gas can result in a mechanically weak carbon layer due to target poisoning [15].

Yang et al [139, 143] reported that the tribological properties of Cr/Carbon films are characteristic of the deposited carbon and not dependant on the Cr, but are dependant on the thickness of this bonding layer. The C/Cr multilayer produced had a microstructure consisting of amorphous graphite and possessed a low friction coefficient giving a low wear rate, with little dependence on the loads up to 140N during pin-on-disk tests, corresponding to a counter pressure of 3.4GPa. The pure carbon coatings were harder than the Cr containing coatings, and had similar friction coefficients and wear rate at lower loads; the difference related to the behaviour at high loads [139, 143].

It is difficult to obtain metastable structures, such as DLC, by magnetron sputtering without the use of the substrate bias, because of the low ion energy and neutral particle density in the plasma, hence the use of substrate bias as reported by several authors.

Capote et al [124, 125] studied the effects of the dilution of precursor methane atmosphere by noble gases on the mechanical properties and the

microstructure of hydrogenated amorphous carbon films. Amorphous hydrogenated carbon films are obtained by plasma decomposition of a hydrocarbon-containing precursor atmosphere. In a-C:H films deposited by methane plasma decomposition, the structure is composed of  $sp^2$  clusters (graphite like) interconnected by  $sp^3$  hybridized carbon atoms (diamond like). The authors [124, 125] reported that the precursor atmosphere, when diluted by different noble gases, did not induce any substantial modification in the microstructure or in the mechanical properties of the films. The authors [124, 125] further reported that the films produced by rf-PECVD are dependant on the self-bias voltage attained as this has a strong effect on microstructure and mechanical properties of the films [124, 125].

Ahmad et al [144] reported that the usage of ion bombardment applied to the substrate during deposition, results in the occurrence of structural changes due to a substrate effect, revealing the key role the substrate plays on film microstructure. The substrate structure was shown to be significant for PECVD growth and a similar effect may be appropriate in the situation described by the authors. Elastic collisions between ions and substrate atoms are responsible for atom displacements and energy transfer. Inelastic collision energy is rapidly converted to thermal and is not available for nonequilibrium processes (such as  $sp^3$  bond creation), although it may lower the effective activation energies for surface adsorption/diffusion. These authors [144] reported that applying a substrate negative bias voltage had a strong influence on the formation of chemical bonds in a-C films. The bias voltage affects the carbon ion bombardment energy, the degree of argon ion bombardment and the substrate temperature. Substrate temperature, in turn, will affect the adsorption/reflection of ion and atom species. Thus, the use of higher temperatures during deposition can lead to an increase in  $sp^2$  content. At low bias voltages, a low substrate temperature can be maintained. When using higher bias, etching of carbon films occurs leading to a reduction in growth rate [144].

From the foregoing it can be seen that the stepwise graded layer concept solves the problem of high compressive stresses in diamond-like carbon (DLC) films by generating a graded constitution through stepwise increasing the bias voltage, during sputter deposition. As mentioned before, in sputter deposition a strong ion bombardment of the growing carbon film is used to provide a strong densification of the depositing amorphous carbon material [42, 124, 125, 144, 145]. This is necessary to increase the fraction of diamond-like  $sp^3$  bonds. The high compressive stresses that can be developed in the DLC films may limit either their maximum thickness or their maximum  $sp^3$  bond fraction. While ion bombardment provides a high density and high hardness, the modification of the interface regions between the substrate and the graded layers ensures good adhesion [42, 145]. Ziebert et al [145] deposited DLC films with a maximum thickness of 10  $\mu\text{m}$  and a maximum hardness of 5300Hv. The deposition started with a bias voltage of 0V to initiate a high adhesion of the growing film. Then the bias was increased to -150V and finally to -300V to produce a hard film surface. The authors reported that the hardness values of the individual graded layers are independent of the thickness ratio of the graded layers, while expansion of the interface regions showed a strong influence on this ratio and on the applied load [145].

Zhang et al [146, 147] also proposed the use of substrate bias-graded deposition during the deposition of DLC. The bias voltage was applied to the substrate in a graded manner, gradually increasing as the deposition progressed and coating thickness increased, creating in this way a graded  $sp^3/sp^2$  bonding throughout the thickness of the coating. The result was a coating of high adhesion with graded hardness, the lowest value at the coating-substrate interface, increasing as the coating thickens, with the highest hardness at the coating surface. The films produced with such graded bias resulted in a smooth and crack free surface. The Raman spectra of the coatings produced indicated that an increase in bias voltage results in a decrease in  $I_D/I_G$  ratio. The  $I_D/I_G$  ratio is not a direct measurement of  $sp^2$  or  $sp^3$  bonds; however the  $I_D/I_G$  ratio is proportional to the  $sp^2/sp^3$  ratio. The degree of plasticity was

also measured, reported as the ratio of the plastic displacement over the total displacement in a nanoindentation test and the authors showed that the degree of plasticity decreased from 59.3% to 47.3% as the bias increased. The increased bias grading had a practical effect on the variation of the  $sp^3/sp^2$  bonding and it reduced the residual stress. The  $sp^3$  percentage was found to be the lowest at the interface between the coating and substrate (due to low energetic ion bombardment) and gradually increased to a maximum at the surface of the coating (due to high energetic ion bombardment). This improves the bonding adhesion of the coating on the substrate surface and at the same time provides high hardness at the coating surface [146].

## 5. Nanoindentation

Indentation tests were first performed by Brinell in the 20<sup>th</sup> century. He used spherical and smooth ball bearings as indenters to measure the plastic properties of materials. The need to characterise, understand and optimise the properties of thin films for particular applications has become greater since then. In the past three decades, a great deal of effort has been directed towards the development of techniques for characterizing the mechanical properties of thin films and small volumes of material. Load and depth sensing indentation, commonly referred to as nanoindentation, is a way by which this has been achieved [12, 148, 149].

When performing a hardness test, all hardness measurement should indicate which load was applied. When using a medium load range, test reproducibility is achieved but depends on the load used to do the test. To account for the dependence of the hardness value on the load used on the test, several models have been proposed [150-152] for both bulk materials and coated samples. The material's properties can be accessed by nanoindentation but the results depend on the indenter tip geometry used for the test. Conventional hardness tests (Vickers, Rockwell, Knoop) are used to measure the hardness of different materials.

Considering the width and depth of the indents of the measurement type, the hardness measurement cannot be conclusive on thin films. For a thin film analysis, a very small load has to be applied, because of the effect caused by the interaction between the indenter, the coating and with the substrate [12].

Conventional hardness tests involve an optical imaging of the indent. This causes a limitation on the scale on the length of the indentation. In general, sharp, geometrically-similar indenters such as the Berkovich triangular pyramid are useful when the objective is to probe properties at the smallest possible scale. The Berkovich tip is frequently chosen over the Vickers for hardness

measurements because the highest point can be more readily shaped to meet at a point rather than the expected line that occurs with the Vickers four-sided geometry. In addition, it has no major defects and is easier to calibrate. Therefore, the force/area relationship can be reliably calculated at very low loads [17, 22]. The nanoindenter was developed in order to measure the force and displacement as indentation take place. This instrument provides a continuous record of load and displacement as an indenter is pushed into the surface. This method has proved to be useful in thin films because the typical load range is approximately 0.1-100 mN, and displacements are small, 0.2 nm displacements can be measured [9, 153, 154].

The advantages and disadvantages of analysing thin films by the method of nanoindentation are [9]:

**Advantages:**

- Nanoindentation can be performed on a thin film;
- Film properties can be determined at variable displacements so that properties can be determined as function of the changing substrate effect;
- A wide range of properties can be measured without removing the film from the substrate;
- The size of contact impression can be small compared to the film thickness in order to avoid the substrate effect;
- No special sample preparation is necessary.

**Disadvantages**

- The mechanical properties measured by indentation do not eliminate the substrate effect caused by the substrate;
- An imaging method needs to be included with a nanoindenter;
- Long calibration time;
- Long wait, to allow a total thermal stabilization.

The properties measured with the Berkovich indenter are the hardness and the elastic reduced modulus. When the specimen temperature can be controlled, it is also possible to determine parameters characteristic of thermally-activated plastic flow, such as the activation energy and stress exponent for creep. With cornered indenter tips (i.e. Vickers, Knoop), it is possible to make indentations in brittle materials at a load high enough to produce radial cracks extending from the edges of the contact. This method allows measurement of the fracture toughness and the state of surface stresses at the sub-micron scale in small volumes of material. However, in some cases the Vickers indenter is not suitable for assessing the fracture toughness. As Veprěk [155] has shown for superhard nanocomposites, due of their high elasticity and high toughness, only circular cracks within the crater but no radial ones are formed, even when the indentation depth is larger than the coating thickness.

## **5.1. Theoretical Indentation Models**

As the nanoindentation test progresses, the indenter is pushed at a predetermined load against the substrate. This results in elastic and plastic deformation. As a result, an impression is left with the shape of the indenter. As the indenter is taken out, the elastic portion of the displacement is recovered. In order to determine the hardness and elastic properties of a material using load and depth sensing indentation techniques, several methods have been developed since the mathematical foundations started being presented in the 19<sup>th</sup> century until today [156-170]. Nanoindentation presents a significant advantage to conventional hardness tests, as it is not necessary to use an optical microscope to measure the area of impression. The contact area and the mechanical properties are determined from the data of one complete cycle of loading and unloading. The unloading data is treated assuming that the displacement recovered is mostly elastic. Then, the hardness and Young's modulus can be determined by solving the elastic contact problem [161, 166, 170].

Tabor et al [161] performed experiments in with load and displacement sensing indentations using conical indenters. The authors reported that the shape of the impression was still conical during unloading. After Tabor's findings [161] the elastic modulus and the size of the contact impression could be derived from the shape of the unloading curve and the total amount of recovered displacement. Another key progress was the definition of reduced modulus ( $E_r$ ), a composite Young's modulus, which takes into account the effects of non-rigid indenters on the load-displacement behavior, using [161, 170]:

$$\frac{1}{E_r} = \frac{1-\nu^2}{E} + \frac{1-\nu_i^2}{E_i}$$

$$S = \frac{dP}{dh} = \frac{2}{\sqrt{\pi}} E_r \beta \sqrt{A}$$

where  $E$  and  $\nu$  are the Young's modulus and Poisson's ratio for the specimen.

$E_i$  and  $\nu_i$  are the corresponding quantities of the indenter.

$P$  - Applied load.

$h$  - Indentation depth.

$A$  - Projected area of the elastic contact measured from the indentation hardness impression.

$\beta$  - Dimensional parameter of the indenter.

$S$  - The stiffness of the contact between the indenter and the specimen, i.e. the slope of the upper portion of the unloading data.

In the late 1980's Nix et al [166, 167] presented a methodology to determine hardness and reduced modulus using the load-displacement curve. The authors [166, 167] reported that the indentation contact area is similar to a flat cylindrical punch and remains constant during initial unloading [166, 167].

Nix and co-workers [166, 167] extrapolated the initial part of the unloading curve to zero loads and determine the extrapolated depth, in order to evaluate the

contact area. Then, using the indenter shape function, the contact area can be calculated. Knowing the indenter contact area, the hardness,  $H$ , which is equivalent to the average pressure under the indenter, is calculated from [166, 167]:

$$H = \frac{P_{\max}}{A}$$

where,  $P_{\max}$  - The maximum load.

$A$  – Projected area of the elastic contact

At the present time, there is an agreement in the scientific community that the unloading curve typically deviates from a straight line, especially for hard ceramic materials such as Ti-based coatings [165].

When analyzing thin coatings, the slope of the unloading curve and the consequent projected area of the elastic contact decreases continuously during unloading due to elastic recovery within the indentation.

Oliver and Pharr [162] have developed a methodology that accounts for the elastic recovery expanding the findings of Loubet [171] and Doerner and Nix [166, 167]. This methodology [162] is applied to any type of indenter as long as the indenter could be described geometrically as a body of revolution. The unloading curve can be expressed by a power law due to the unloading curve if often non-linear in the initial stage, is shown schematically in Figure 23 [167] and described by the following equation [167, 172, 173]:

$$P = \alpha(h - h_f)^m$$

where:  $h$  – The elastic displacement of the indenter

$h_f$  - The final displacement after complete unloading

$\alpha$ , and  $m$  are constants

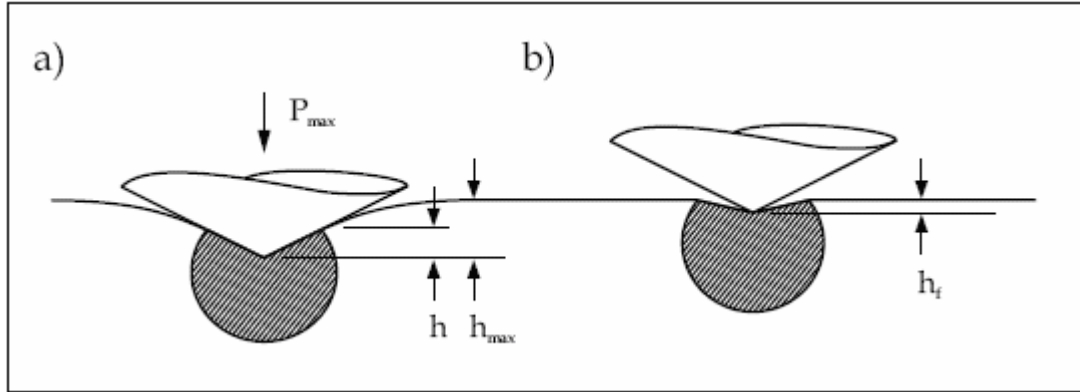


**Figure 23 – Illustration of elastic and plastic deformation during nanoindentation: a) indentation at maximum load; b) unloading indenter with a smaller contact area. The darker zone shows plastic deformation [167].**

A drawback of the analysis proposed by Oliver and Pharr [162] is that the suggested power law relationship does not take into account any residual plasticity present in an elastic/plastic material.

The unloading stiffness is calculated by differentiating the load-displacement relation at the maximum depth of indentation,  $h = h_{\max}$ , leading to [172, 173]:

$$S = \frac{dP}{dh}(h = h_{\max}) = m\alpha(h_{\max} - h_f)^{m-1}$$

The contact depth  $h_c$ , is estimated from the load-displacement data through the equation [173]:

$$h_c = h_{\max} - \varepsilon \frac{P_{\max}}{S}$$

The previous equation depends on the indenter geometry, being  $\varepsilon=0.72$  for a conical indenter,  $\varepsilon =0.75$  for the Berkovich tip and  $\varepsilon =1$  for a flat punch. Figure 24 [172] represents the cross section of an indentation and a schematic load-displacement curve, where the parameters used in the analysis are identified.

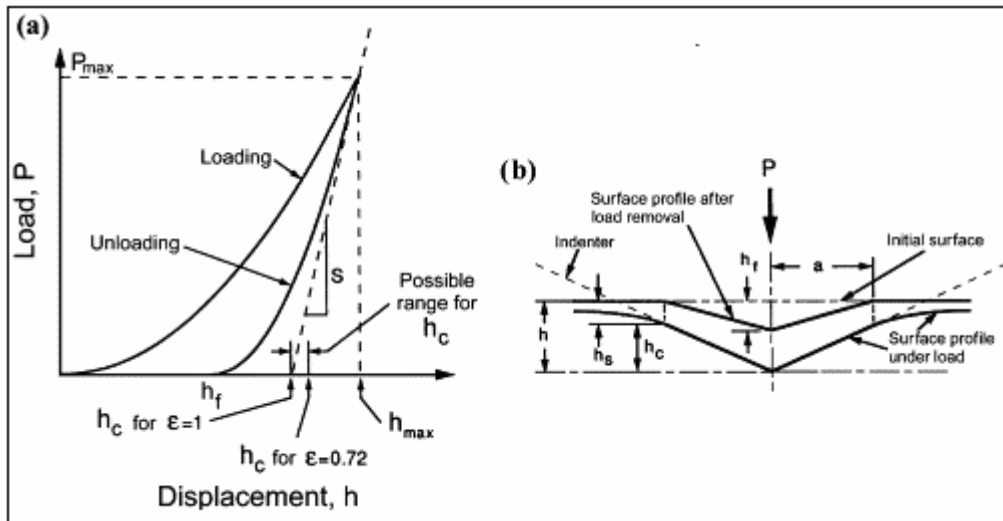


**Figure 24 - Representation of a cross-section of an indentation : (a) A typical load–displacement curve and (b) the deformation pattern of an elastic–plastic sample during and after indentation [172].**

The Oliver and Pharr [162-164] method is based on an elastic analysis and takes into account for sink-in only. The accuracy of this method depends on the correct estimation of the contact area, which depends on the amount of pile-up. When the remnant depth is higher than 0.7, the accuracy of the method relies on the work-hardening characteristic of the material. If the material does not work harder, the method underestimates the contact areas by as much as 60% [162-164]. However, the contact areas for materials with a large amount of work hardening are predicted very well by this method.

When using a Berkovich indenter, visible in Figure 42 and Figure 43, the shape function is complex due to tip rounding caused by its use. The contact area is calculated for different indentation depths in a material with well-known elastic properties (usually fused quartz or silica). The contact depth values are fitted to a polynomial function and the new values of the machine compliance are then calculated by using the obtained area function and the procedure is repeated until the curves convergence. Then, the contact area can be determined from the load-displacement data, and the hardness and reduced modulus are calculated from previous equations.

Testing certain materials using this methodology can lead to significant errors of the mechanical properties. The underestimation of the contact area and the occurrence of pile-up in the vicinity of the indentation can result in measurement errors. The underestimate of the contact area occurs because of the purely elastic contact solution and may not work well for elastic/plastic indentation.

In the last decades with the improvement of the hardware and software, the mechanical properties can be measured using this method with accuracies around 10% [162].

Ding et al [174] studied multilayer hard coatings. They showed that the load-penetration depths are necessary in order to have a more thorough understanding of the coating system. The interfacial failure and the critical load of interfacial failure of the coatings were showed. They also found that a step occurs in the force-displacement curves at the onset of coating fracture and a straight line segment occurs in the load-penetration depth squared curves.

In nanoindentation, measurement errors related to the direct measurement of the indentation diagonals are eliminated, as the data is obtained directly from the data measured by a computer. In the nanoindentation technique Veprek et al [59] showed a possible source of errors:

1. Indentation size effects (indenter tip blunting, non-representative small volume of the material to be tested upon nanoindentation and a too small stress under the indenter which does not reach the yield stress of that material if a too low load is used);
2. The composite effect of the system of super-hard coating on a softer substrate;
3. High compressive or tensile stress in the coatings, drifts and/or stiffness of the indenter.

They concentrated on the load–depth sensing automated indentometers which introduce further sources of possible errors of the measurements on super-hard ( $H_v \geq 40$  GPa) coatings, such as severe elastic deformation of the diamond indenter which falsifies the measured indentation depth obtained from the extrapolation of the unloading curve.

Chudoba et al [175], found that the creep depends on the material and normally diminishes to very low values within seconds. It influences the maximum depth and the upper part of the unloading curve. It can incorporate measurement errors of more than 20%. They showed that creep during nanoindentation can be reproducibly determined if the temperature drift during the measurement is corrected. The amount of creep for a distinct time, divided by the maximum depth (relative creep), is approximately constant for homogeneous materials and does not depend on the maximum depth or maximum load. The creep behaviour of a layer is influenced by the substrate, when the ratio of the plastic depth to film thickness reaches approximately one-tenth.

Herrmann et al [176] studied the key calibration problem at nanoindentation measurements—the determination of the indenter tip geometry. To reduce this error, they used SFM (scanning force microscope) techniques. When the area function of the indenter is known, an iterative procedure, by high load indentation in tungsten is able to yield reliable and reproducible values of frame compliance. Using a combined iterative approach based on the Oliver and Pharr method [162-164, 177], using tungsten and fused silica as reference materials, the area function obtained agreed well with that obtained by SFM. In both cases, this technique detected the aberrant tip geometry of a Berkovich indenter. As a consequence, the value of frame compliance obtained in the latter method also corresponds to that obtained by using the SFM area function directly.

The substrate roughness is also a factor of great importance in nanoindentation. Cekada et al [178], proved that the indentation is strongly dependant upon

sample preparation. In Figure 25 [148] illustrates three potential nanoindentation cases:

1. on an ideal polished horizontal surface;
2. a rough valley;
3. on a rough peak;

The resulting contact areas in each of the three cases are different in shape, leading to different consequent penetration depths under the same penetration load. An indentation on a rough valley results in a contact area that requires a lower penetration depth in comparison to the penetration on a polished horizontal surface. On the other hand, an indentation on a rough peak, for the same contact area, results in an indentation depth increase in comparison to the indentation on an ideal plane horizontal surface. Under such circumstances, when indenting on rough specimens, indentation depth scatter may occur as a consequence of the surface topography.

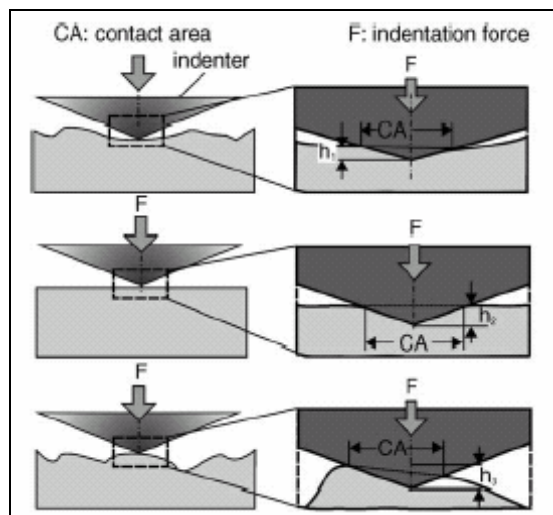


Figure 25 – Effect of the substrate roughness in nanoindentation [148].

Saha et al [179, 180] examined the effects of the substrate on the determination of mechanical properties of thin films by nanoindentation. By studying soft films on hard substrates and hard films on soft substrates they were able to assess

the effects of elastic and plastic inhomogeneity, as well as material pile-up, on the nanoindentation response.

The effect of the substrate hardness on the film was negligible in the case of soft films on hard substrates because the plastic deformation was contained within the film and the substrate yielded plastically only when the indenter penetrated the substrate.

## **5.2. Analysing the Coatings**

Depending of the properties for the materials used in a coating and in the substrate, the nanoindentation technique in this case differs from the “normal” indentation and depends on the strength of the coating compared to the substrate.

### **5.2.1. Soft coating**

In the case of a substrate coated with a soft material, during the indentation, as the indenter goes deep, the coating is pushed aside by the indenter. Xu et al [181] shown that the indentation process can be divided into two stages, according to the critical penetration depth for every soft coating. For penetration depth smaller than the critical depth, the soft coating behaves the same as the bulk material. For penetration depths larger than the critical depth, the influence of the substrate is triggered and deviation from the dislocation model occurs.

The dislocation model was developed by Nix et al [182] based on mechanism-based strain gradient (MSG) theory [183]. According to MSG theory, the deformation resistance depends on the densities of both statistically stored dislocations and the geometrically necessary dislocations introduced by indentation.

The deformation behaviour of the coating would be expected to be different from bulk material and certain deviation from the prediction of the Nix et al [183] dislocation model would be expected.

1. The dislocations would accumulate at the interface of the coating and the substrate. This dislocation accumulation would increase the hardening of the coating and the stress at the interface of the coating and substrate, which would trigger a larger influence of the substrate.
2. Pile-up of the indented surface would increase with the increasing penetration depth because of the truncation effect of the hard substrate and a significant underestimate of the contact area would thus be introduced.

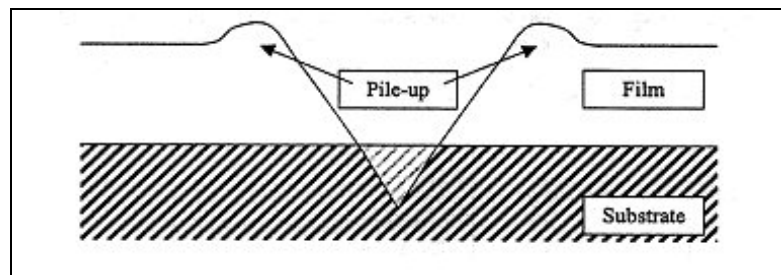


Figure 26 - Indentation of a soft coating [12].

Saha et al [179] studied the pile-up on the indentation properties of soft films on hard substrates. They observed that the pile-up occurs only along the flat faces of the indenter, and only along the sides of the triangle and not at the corners. They assumed that the piled-up material forms an arc around the edge of the indentation as we can see in Figure 26.

As we can see in Figure 27, the substrate curve is displaced to the right by an amount close to the coating thickness ( $t$ ).

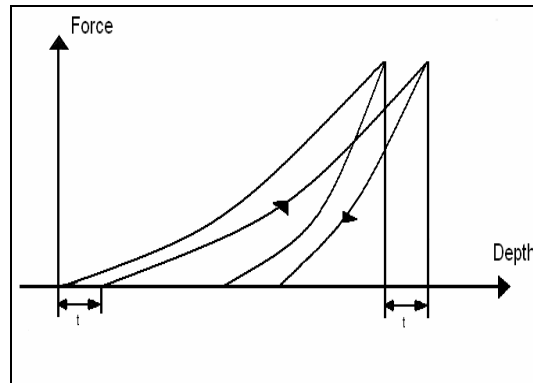


Figure 27 - Coating yields before the substrate[154].

### 5.2.2. Hard Coating

In case of a substrate being softer than the coating, during indentation the coating bends and flexes to accommodate the substrate deformation.

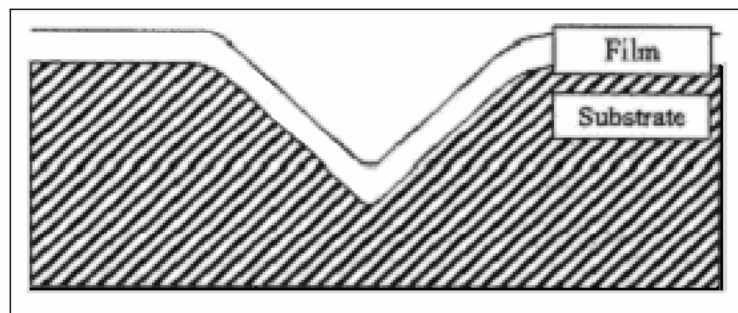
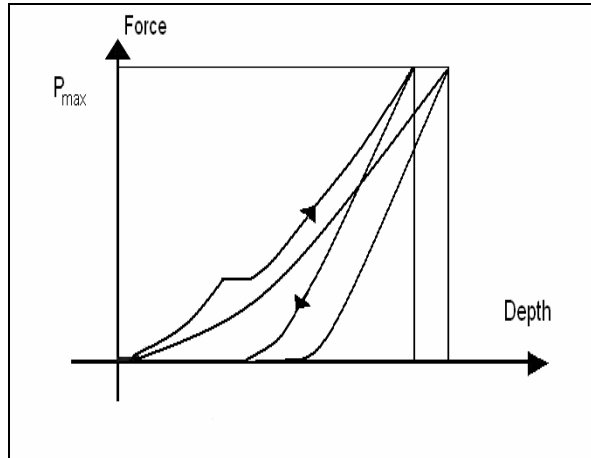


Figure 28 - Indentation of a hard coating, coating only deflects due to the indentation [12].

In this case, the coating fractured in some parts and the load displacement curve will show displacement by steps or “pop-in”, represented in Figure 29 by the horizontal line. Ohmura et al [184, 185] performed nanoindentation tests in hard substrates, sapphire, coated with aluminium, platinum and gold. The plastic deformation of films was constrained by the hard substrate in penetration depth range deeper than  $1/5$  of film thickness, using a Berkovitch indenter. The pop-in phenomenon was often found in aluminium films, caused by the natural oxide layer of the film surface.



**Figure 29 - The substrate yields before the coating and we get local fracture [154].**

New indentation techniques have been researched to access more properties of thin films. Interfacial adhesion is becoming a critical material property for improving the reliability of multilayer thin film structures used in microelectronics. Sanchez et al [186] have been working on Cross-section nanoindentation (CSN) for measuring the fracture toughness of thin film interfaces.

Interfacial fracture is achieved by nanoindentation in the structure cross-section. A model based on the elastic plate theory has been developed to calculate numerically the interfacial critical energy release rate for ceramic systems from CSN test results. The model inputs are the thin film elastic properties, thin film thickness, interfacial crack area and maximum thin film deflection during the test.

### **5.2.3. $H^3/E^2$**

Nanoindentation is a well established technique to measure mechanical properties in thin film. In the last few years the coating industry has focusing on the production of nanostructured films. This accurate control has permitted the control of mechanical properties such as hardness and reduced modulus. By being able to control these essential mechanical properties, the production of hard coatings with excellent wear behaviour is possible. As was discussed in

section 1.1 PVD processes allows very accurate control of deposition parameters and conditions, enabling researchers and industry to develop new coatings with optimized properties. For many years it was thought that hardness was one of the main properties to evaluate the wear resistance of a thin film [187, 188]. In most hard materials the Young's modulus is also high. The elastic strain to failure can be described as a ratio between hardness and Young's modulus ( $H/E$ ), a high value of which is an indicator of a long elastic strain to failure. Also the resistance to plastic deformation ( $H^3/E^2$ ) is an important parameter to consider when manufacturing coatings, testing and then predicting their wear resistance. An increase in  $H^3/E^2$  can indicate an improvement in the elastic recovery of the coating [189].

Mayrhofer et al [190] studied the influence of deposition conditions on the mechanical properties of hard coatings, with the objective of comparing the different single- and dual-phase coatings. They established a correlation between the coating structure and the mechanical properties of the thin films. This correlation is a first step to the development of coatings with a high hardness and a high  $H^3/E^2$  ratio (resistance to plastic deformation).

Several researchers [173, 188-190] have reported that low Young's modulus and high hardness can be favourable in industrial applications such as the magnetic recording industry. These researchers have used nano-indentation to measure the hardness and the Young's modulus of the coatings. These studies show that  $H/E$  or the  $H^3/E^2$  describes well the coating properties in terms of wear resistance.

## 6. Scratch Test – Introduction

In the last decades the thin films have had a widespread use in several industry sectors like electronic, optical, biomedical and aerospace. Thin films can show resistance to abrasion; good erosion, corrosion, wear and high temperature oxidation properties; reduced friction, electrical resistance or thermal conductivity, good self-lubrication, and dielectric properties. When applying a thin film to a particular application one of the most important aspects is the adhesion between the coating and the substrate.

Adhesion can be defined as the state in which two surfaces are held together by interfacial forces. These forces can be Van der Waals forces, electrostatic forces or chemical bonds across the coating-substrate interface [191-194].

When testing a coating, if the break occurs at the interface then the failure is adhesive, otherwise if some coating still is attached to the substrate then is cohesive failure as observed in Figure 30 [195].

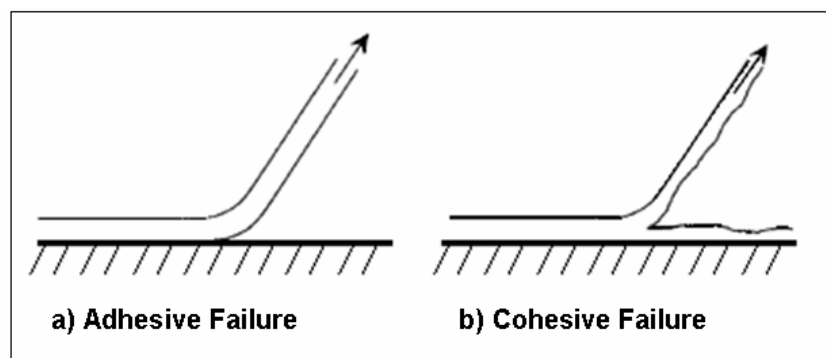


Figure 30 – a) Adhesive vs. b) Cohesive failure [195]

### 6.1. Scratch testing

With the widespread use of thin films in the 1980's it was crucial to develop a reliable method of measuring the adhesion of coatings to the substrate [196].

The scratch test set-up is a simple concept. It is a diamond indenter (usually a Vickers or a Rockwell C) which is placed in contact with the film and then it's loaded to a user defined value. Then the indenter is dragged across the surface

(as visible in Figure 31 [197] at a certain load (can be continuous load or increasing load) with a user defined speed, with a well defined length until some failure pattern occurs [198]. The test causes elastic and plastic deformation on the film until damage is monitored by the apparatus and visible in the coating surface. The critical load ( $L_c$ ) quantifies the adhesive strength between the coating and the substrate. The first sign of failure is referred as lower  $L_c$  while upper critical load corresponds to a region where the coating is completely removed along the scratch track.

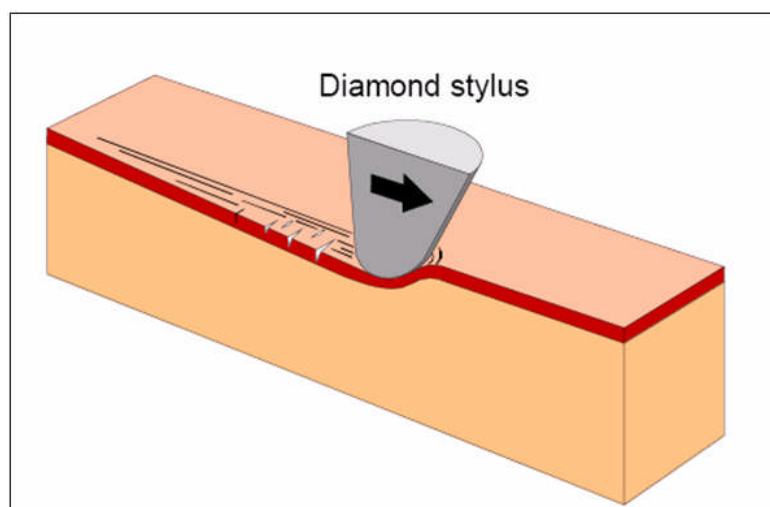


**Figure 31 - Schematic illustration of the scratch tester stylus drawn along the coated sample [197].**

Once critical load has been exceeded, the coating fails according to a pattern which is conditioned by the nature of the coating and substrate, the coating thickness, internal stress [191-194, 196, 198-200], as we will see in section 6.1.2.

### **6.1.1. Testing modes**

When performing adhesion testing three modes of testing are currently employed depending on the apparatus available, the apparatus available is visible in Figure 32. In the progressive loading scratch test mode, the load on the indenter increases linearly as the indenter moves across the test surface. In the constant load scratch test, the normal load is set by the user (usually a

value between 2N and 60N) and several scratches are carried out under a pre-defined loads at different locations on the sample until failure occurs as visible in Figure 33 [197].

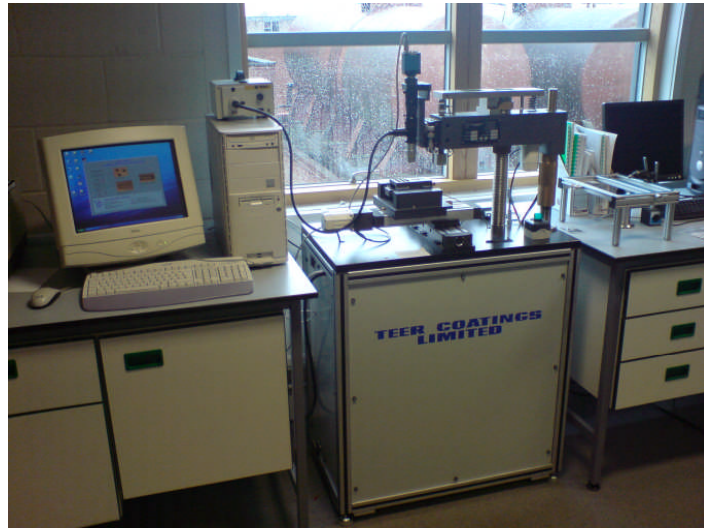


Figure 32 - Schematic of a scratch tester.

The most realistic test on a material or coating is to test it in service. If the piece or the machine are produced in quantity, it will be possible perform these tests in the machine or in the work piece, but it takes time and it is expensive.

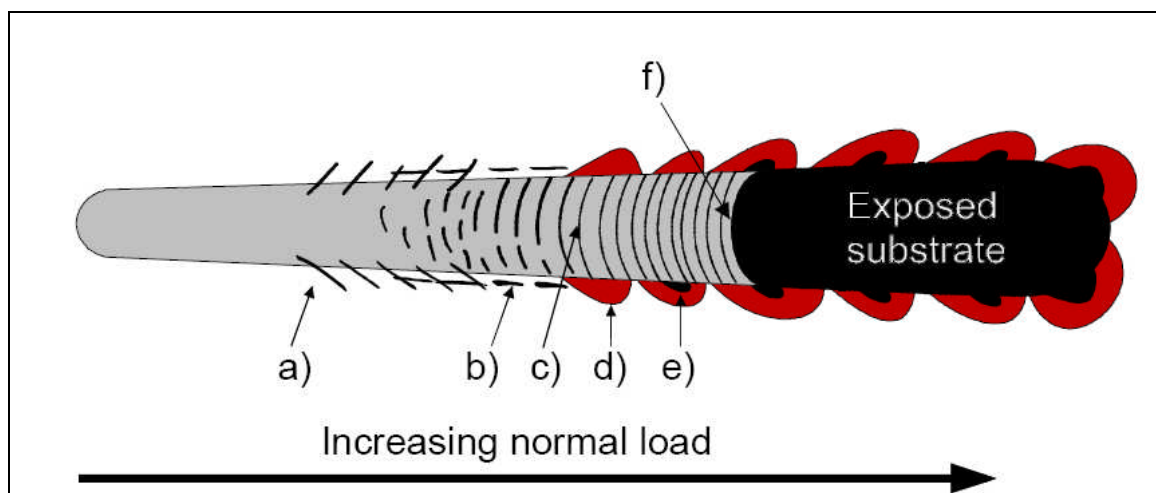


Figure 33 - The surface cracks generated in a scratch test track can be classified as a) angular cracks, b) parallel cracks, c) transverse semi-circular cracks, d) coating chipping, e) coating spalling, and f) coating removal [197]

The most important objective in a scratch test is to access the critical load and the failure mode in order to quantify and qualify the adhesion.

### **6.1.2. Failure Modes in Scratch Test**

In scratch test there are two main groups of possible failure patterns. There is brittle failure and ductile failure. Brittle failure is associated with the hard ceramic materials while ductile failure occurs in samples coated on ductile substrates. In the case of ductile failure, the area of film detached by the indenter is small and confined within the track. With brittle failures, the damaged area extended to the vicinity of the scratch track [201, 202].

The critical loads for ductile failure are higher when compared with the brittle failure. For ductile substrates interfacial failure can occur due to compressive stress if the interfacial adhesion is poor, but if the adhesion is good, failure usually occurs in the coating. For brittle substrates interface decohesion is observed if the adhesion is poor [201, 202].

A number of failure modes have been observed in the case where the substrate is brittle. The main brittle failure modes are show below in Figure 34. Large area spallation (Figure 34 a)) is a common failure mode if the adhesion is poor or if the residual stress level in the coating is high. In this case, as the indenter contacts the coating surface, cracks are formed at the coating/substrate interface which can propagate at considerable distance on either side of the track. These crack's may nucleate at an interfacial flaw/void or be created from through-thickness cracking [201, 202].

When coating spallation occurs the coating is detached to minimize the amount of elastic energy stored by the large compressive stresses created directly in front of the moving indenter. This reveals poor adhesion and leads to semicircular cracks which propagate outward from the centre line of the track, Figure 34(b). This failure mode leads to chipping at the track side (for brittle substrates) if the interfacial crack propagates outside scratch track before the

diamond stylus passes over it. Once the stylus has reached the spalled region, it will either press the coating back into contact with the substrate or cause a chip to be removed. This type of failure leaves signs of damage in the track as well as chipping along the edges. As the coating thickness increases, this type of failure becomes more likely [201, 202].

In addition to the chipping in the track, chipping may be observed but is not related to any delamination initiated ahead of the indenter. This is the result of the differential elastic recovery of the coating and the substrate, Figure 34(c). Such recovery tracks can often be found along the scratch scar with compressive spalling cracks on a prearranged crack segment [201, 202].

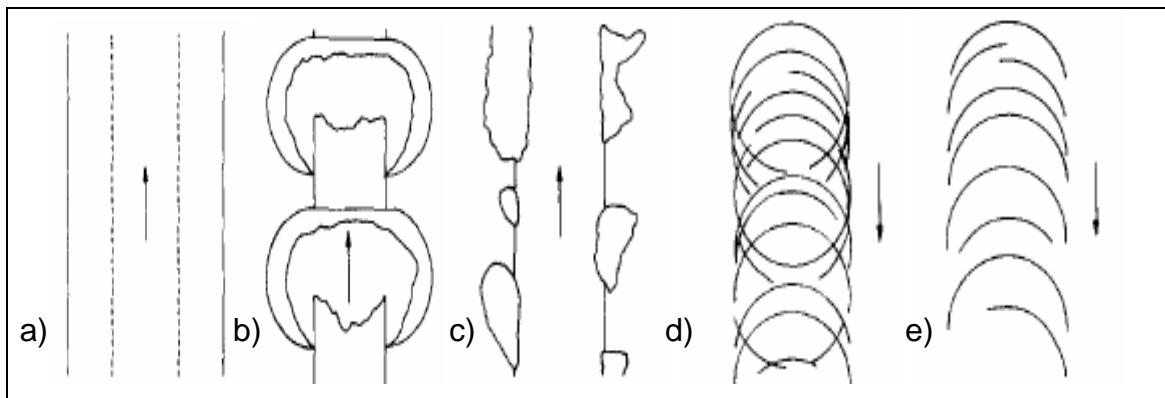


**Figure 34 – Brittle failure modes in scratch testing: a) gross spallation, b) spallation ahead the indenter, c) recovery spallation, d) Hertzian cracking, e) tensile cracking [201, 202].**

As the level of residual stresses in the coating increases, the compressive spallation failures become more visible. Both types of failure depend on coating/substrate adhesion and can be used to determine the critical load. They will both lead to different values since the recovery cracking occurs at lower applied loads. The occurrence of elastic recovery spallation can be enhanced by increasing the difference in elastic modulus between the coating and the stylus [201, 202].

Figure 34(d) shows a failure mode typical of very brittle substrates. The tensile radial stresses at the edge of the diamond contact generate a ring crack which

propagates from the surface through the coating into the substrate (Hertzian cracking). As the stylus moves, several of these rings are formed which interact and create a network along the edge of the crack. Considerable chipping occurs where such cracks overlap. These Hertzian cracks may provide the through-thickness cracking that initiates the elastic recovery cracking. This may also originate from the cracks which form at the rear of the diamond contact in response to the tensile stresses generated during sliding, Figure 34(e). If no scratch crack is formed, this looks identical to the Hertzian cracking. Once a crack channel is formed, the shape of the contact between the indenter and coating changes and the load is then mostly supported on the front half of the indenter. This will lead to cracks that run perpendicular to the sliding direction with less curvature than in the Hertzian case [201, 202].

Since brittle failure modes tend to occur for hard substrates, very little plastic deformation of the substrate occurs during the test. The failure modes associated with the bending of the coating into the scratch track are only observed at relatively high loads [201, 202].

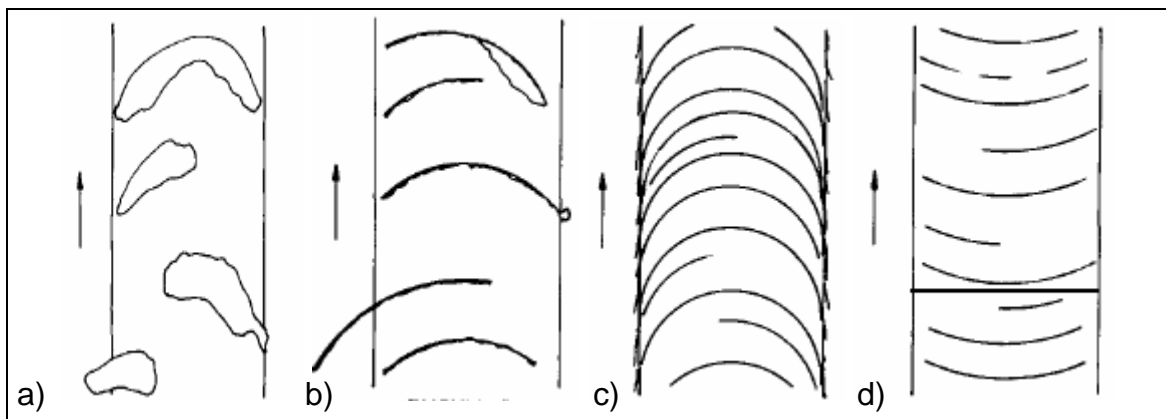


**Figure 35 – Ductile failure modes during scratch testing: a) spallation, b) buckling, c) conformal cracking, d) tensile cracking [201, 202].**

The ductile failures are usually characterized by smaller crack areas, chipped or spalled regions and a larger number of failure events. Typical failure mode schematics are shown in Figure 35. The spallation and buckling failure modes, Figure 35(a) and (b), are similar to the spallation mode for brittle failure except that the magnitude of failure is smaller and is generally confined within the

scratch track for very thin coatings. Both of these failure modes occur ahead of the moving indenter with spallation being promoted by the pile-up of soft substrate material ahead of the moving indenter. In general, spallation occurs where the adhesion is poor or for thicker coatings where the driving forces to reduce stored elastic energy is larger. Elastic recovery spallation initiated behind the stylus is not usually observed for ductile failure [201, 202].

Two other common modes of ductile failure are conformal cracking and tensile cracking. Considerable groove formation is observed for ductile materials since the load on the diamond indenter is transferred to the front half of the indenter once sliding starts, effectively doubling the contact stress.

Since there is virtually no load on the back of the indenter, Hertzian cracks will not be found in this region. Two factors then contribute to the stress ahead of the indenter [201, 202]:

- (1) The pile-up of materials ahead and to the sides of the indenter causes bending of the coating, placing its surface in tension;
- (2) The friction between coating and stylus causes the maximum radial tensile stress to occur at the sides of the indenter.

This is supported by a tensile stress at the rear of the contact where the indenter separates from the deformed material. The tangential friction adds compressive stresses ahead of the indenter which may lead to spallation and buckling failures. Tensile cracking will thus occur initially at the sides of the indenter and this is marked by cracks at the track edge parallel to the scratch direction. Partial ring cracks can occur ahead of the indenter which it then passes over and pushes into the track. The coating can become cracked ahead of the stylus as it is bent into the scratch track. This leads to through-thickness cracking or conformal cracking, Figure 35(c). Cracking also occurs at the rear of the contact due to the tensile stress generated on sliding as observed for brittle materials, Figure 35(d) [201, 202].

### 6.1.3. Acoustic emissions

Acoustic emissions (AE) are used to detect the first signs of damage [203]. When the critical load,  $L_c$ , is reached as a result of formation and propagation of cracks, the AE curve presents a shape of a wave burst as we can see in Figure 36 [203]. These cracks can originate in intrinsic defects within the coatings, created during deposition, as described in section 1.5, where the internal stress is higher than the fracture stress of the coating [200, 203]. The damage caused by the moving stylus is related with the amount of AE released by the coating as visible in Figure 36 [201, 202].

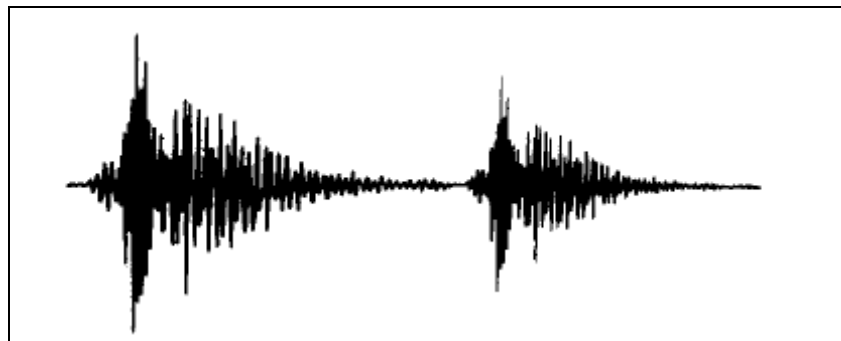


Figure 36 – AE signal curves during scratch testing [200].

Large amount of AE monitored during a scratch test is a clear indication that failure has occurred in the coating, from which a critical load value can be estimated [200-203]. When testing a brittle coating, the AE curve usually presents a wide interval, due to the cracking of the film.

The AE emissions during the scratch test of a ductile failure present usually a much narrow interval [201, 202]. Therefore in this case the other parameters recorded during the test (friction force and first derivative of friction force) must be considered to assist in a accurate determination of the critical load [201, 202].

#### **6.1.4. Good practice guide to identifying critical loads**

When assessing the adhesion in thin film there are critical steps to be considered to evaluate the critical loads. The data monitored in the test are important, like the friction force, acoustic emissions, and the resulting scratch scar is also very important.

The friction force is a critical parameter on the determination of the critical load. One of the simplest ways of observing the critical load is the change in slope of the friction curve. During a test the initial stages the curve behaves almost linearly if you are performing an increasing load test. As the critical load is reached there is a visible change in slope, almost comparable to an exponential curve. As the friction curve is derived and plotted, if during the test there wasn't any visible change in slope the 1<sup>st</sup> derivative should be a strong indicator of when the critical load occurred.

The acoustic emission (AE) is also an important factor to take into account. When the critical load is reached during a test, the AE should present a burst like it was discussed in section 6.1.3. In some cases there are no noticeable bursts in the AE so in this case it should be considered the increase or decrease in the values, and their range. If a wide range of AE is monitored by the sensor it can also be a sign that the critical load was reached.

The inspection of the scratch scar is also very important not only to access the critical load point, but also to access the failure mode before the critical load was reached; it provides essential information about the coating nature and has a strong impact in coating design.

To summarize, all of the data of the scratch test should be analysed together and no parameter should be disregarded on critical load assessment.

## 6.2. Summary of Literature

As reviewed in the previous section 3, TiB<sub>2</sub> is a desirable material for use in many applications in industry. The main drawbacks are the brittle nature that TiB<sub>2</sub> possesses and its internal stress. All of these are conditioning factors for the application of TiB<sub>2</sub> coatings.

Several authors have developed multilayer coatings in order to achieve hard, highly adherent coatings.

Vales Silva [9] produced TiB<sub>2</sub> multilayered coatings with several materials, Al, NiCr, Mo and Ti, with a range of layer thicknesses and using different deposition conditions. In the case of the multilayer with Al, N<sub>2</sub> was also incorporated but this had a severe effect in distortion on the Al material lattice causing an increase in hardness and a decrease in Young's modulus. No tribological testing was carried out with this range of multilayer coatings.

Silva Cruz [12] progressed with these types of multilayer coatings and produced TiB<sub>2</sub> multilayers with Al, and Ti with a new coating design. The composition wavelength was constant and the same as that used by Vales Silva [9] ( $\lambda=200\text{nm}$ ). However, the ceramic content was varied from 75% ceramic to 95%; the same range of ceramic percentages will be used in this thesis. Silva Cruz [12] reported that the hardness values for the high ceramic content (95%) were  $\approx 20\text{GPa}$  for TiB<sub>2</sub>/Al multilayer and these were far greater than the ones achieved by Vales Silva [9]  $\approx 8\text{GPa}$  for a 75% ceramic content.

The high hardness reported by Silva Cruz [12] is explained by the Al content in the film. This low content (5%) allowed TiB<sub>2</sub> layers to be in contact during deformation because the Al at a 5nm thickness presented island growth and a mobile Al layer during deformation. For the TiB<sub>2</sub>/Ti multi-layers this effect was no longer visible due to the influence the Ti layer had on the TiB<sub>2</sub> layer. There was a continuity of columnar growth throughout the multilayer, and all the damage has to be sustained by the individual columns.

In the last years the coating industry has focused research in developing coatings that combine high hardness, high adhesion and low friction. These coatings are to be used in the advance tool technology and allow lubricant-free machining.

Gilmore et al [113-115] initiated the development of  $TiB_2$  coatings co-sputtered with a solid lubricant, namely  $MoS_2$  and C. The samples were placed in a vacuum chamber and the composition was controlled by the distance from the plasma confocal point. Both depositions were made in a non-reactive atmosphere. They observed that the friction coefficient above  $150^\circ C$  had a sharp peak. This is typical behaviour of graphite like coatings, as we have seen in section 4, The deposition of carbon in an Ar atmosphere produced graphite like films with low hardness due to the fact that the hardness in DLC films is directly linked with the  $sp^3$  content. The authors reported [113-115] that the C was incorporated into the  $TiB_2$  matrix forming a two-phase material. The friction was only reduced with a C content of above 66%. In the case of co-sputtering the deposition conditions are crucial to determine the film composition which directly influences the properties. The authors also produced a series of multi-layers in which the conditions were not varied. Their main observation was that C bonds well with  $TiB_2$  to form  $Ti(B,C)_2$  and the graphite film is only formed when this phase is saturated which has a direct effect on the friction coefficient

In this thesis multi-layers of  $TiB_2$  and different types of carbon were produced using PVD techniques, on a range of substrates, ranging from tool steel, as used in the tooling industry (section 8.2) and Al alloy, as used in the motorsport industry (section 8.4 and 8.5). The sputtering techniques used were RF, DC, and Pulsed-DC, which were revised previously in section 1.3.

In section 8.1 the deposition of  $TiB_2$  using the different sputtering techniques was studied and the tribological effects on film performance determined.

In section 8.2 TiB<sub>2</sub> was multilayered with carbon in a non-reactive atmosphere with the layer thickness and composition wavelength as defined by Silva Cruz [12] and the tribological performance evaluated.

In section 8.3 the carbon was manufactured in an Ar + 7.5% CH<sub>4</sub> atmosphere to promote sp<sup>3</sup> bonding in the film, with a constant composition wavelength ( $\lambda = 200\text{nm}$ ) but with the DLC content varied from 25% to 75%.

In sections 8.4 and 8.5 the TiB<sub>2</sub> was coated onto an Al alloy used in the motorsport industry. There has seen an increase in the use of light weight components which require coatings with high hardness, good adherence and with low friction coefficients. In these sections the TiB<sub>2</sub> was deposited in a non reactive atmosphere while DLC was deposited in Ar + 7.5% CH<sub>4</sub> atmosphere. The multi-layers were formed by alternating the plasma between the two cathodes, the gas switched off and the chamber purged to avoid gas contamination between the layers.

## 7. Experimental Work

The goal of this section is to describe the experimental procedure which has been followed to develop, produce and characterise the multilayer coatings systems.

### 7.1. The Sputtering System

The Sputtering system used in for section 8.1, 8.2 and section 8.3 consists of a pumping station, a vacuum chamber, three planar magnetron targets DC power sources and RF generator, with a bi-RF switch and two matching networks.

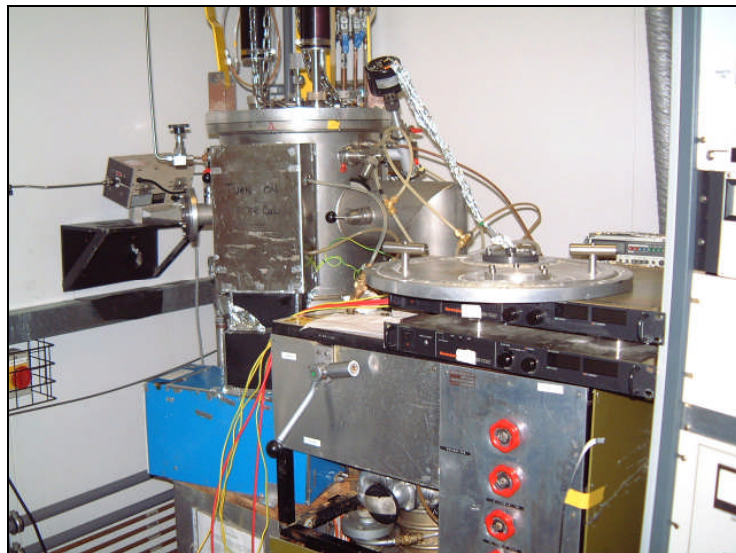


**Figure 37 – Overview of the Sputtering system.**

The vacuum chamber is made of stainless steel, with a double wall, with a water cooling system to prevent it of overheating, a pumping station, two gas inlet ports, and a substrate rotating table, as we can see in Figure 38. The system is equipped with three circular magnetron cathodes placed on top of the chamber, Figure 38. Attached to the magnetrons there is water-cooling system to avoid cracking of the target at different temperatures. The cathodes are connected to matching network units, and to a RF generator working at 13.56 MHz, as previously described in section 1.3.2. A voltage probe is also connected to the output of the matching network to monitor the potential of each

of the targets. During deposition the process conditions (target power, substrate bias, chamber pressure, plasma and matching) conditions can be changed to vary coating system conditions to the deposition rate and conditions.

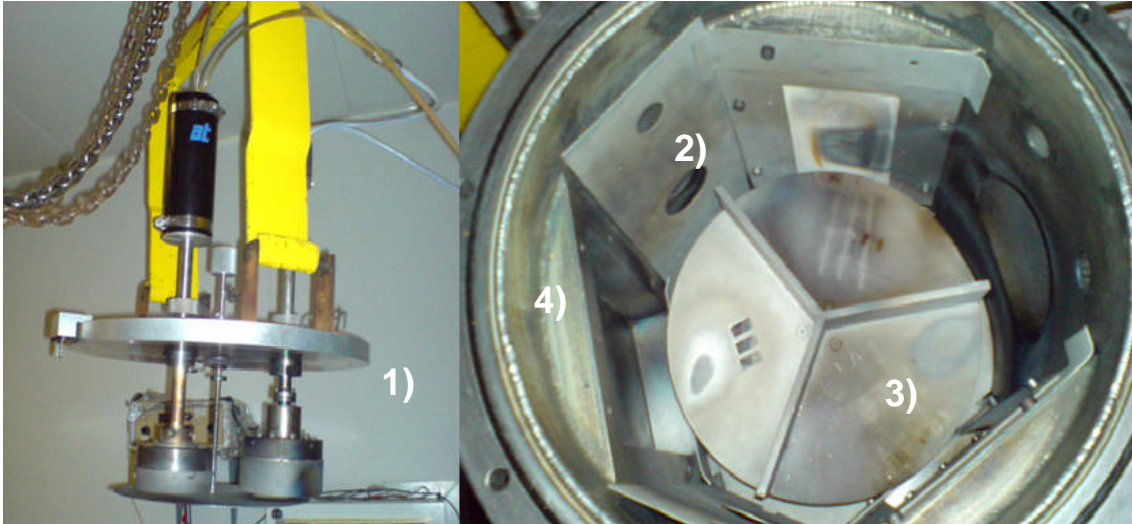


**Figure 38 – Overview of the Sputtering chamber.**

**Key:**

- 1 – Magnetron Electrodes
- 2 – Shields
- 3– Substrate holder
- 4 – Chamber wall

In section 8.1 the system was pumped to a base vacuum of  $1 \times 10^{-6}$  Torr. The power densities ranged from 4.5 to 6.8 W/cm<sup>2</sup>, and Argon (Ar) was used as the sputtering gas at a pressure of 10mTorr. Bias was applied to the substrate work-table promoting ion bombardment of the tool steel substrates prior to deposition. Film deposition was initiated by deposition at a low power of 50 W for the first ten minutes of deposition, and then at the desired power with the bias turned off for 2.5 hours. For RF magnetron sputtering, a Coaxial Cables 600 W (MAX) RF power supply was employed, while for the DC magnetron sputtering, a MKS Instruments RPG-50 was used. This could be used in either pulsed or continuous DC mode.

In section 8.2 Multilayers of TiB<sub>2</sub>/C were fabricated using conventional DC magnetron sputtering as described in section 1.3.1. The carbon and TiB<sub>2</sub> sputtering targets were 7 cm in diameter with a purity of 99.99%. The power density on the TiB<sub>2</sub> target was approximately 8.1 W/cm<sup>2</sup>, and on the carbon target it was approximately 11 W/cm<sup>2</sup>. Ar was used as the process gas and was maintained constant at a pressure of 10 mTorr and an Ar flow of 27 sccm. During fabrication, the substrate worktable was biased to -200 V. Biasing is known to promote ion bombardment and thus improve film adhesion and it is also suggested that ion bombardment may increase the formation of sp<sup>3</sup> hybridised carbon [204].

In section 8.3 the sputtering system employed is as described above. Power to the targets was supplied by an ENI RPG50 pulsed-dc supply, pulsing at a frequency of 150 kHz and a pulse duty factor of 2016 ns. Power densities of 4 and 5 W/cm<sup>2</sup> were utilised for the carbon and TiB<sub>2</sub> targets, respectively, and all sputtering took place in an Ar + 7.5% CH<sub>4</sub> atmosphere.

After insertion of the Ti substrate into the vacuum chamber, a nitrogen plasma with the TiB<sub>2</sub> target was initiated for 5 min, providing a thin Ti–B–N interfacial layer, allowing a strong chemical bond to form with the coating layer of TiB<sub>2</sub>. The nitrogen gas was then switched off and the reactive gas of Ar + 7.5% CH<sub>4</sub> admitted into the chamber, to a pressure of 10 mTorr, for the duration of the experiment.

For section 8.4 and section 8.5 a Leybold L560 box coater, equipped with multi-target sputtering cathodes was used, as shown in Figure 39 and Figure 40.

In Section 8.4, power to the targets was supplied by an ENI RPG-50 pulsed-DC supply, at a frequency of 150 kHz and a pulse duty factor of 2016ns. Power densities of 6.5 W/cm<sup>2</sup> were used to sputter the TiB<sub>2</sub> target.



**Figure 39 – Leybold Box coater L560**

Section 8.5 used Argon (Ar) + 7.5% Methane (CH<sub>4</sub>) gas mix that was ionized by a pulsed-DC voltage plasma to magnetron sputter the DLC. The TiB<sub>2</sub> was deposited using pure Ar and also ionized by a pulsed-DC plasma. Pulsed-DC plasma deposition is a versatile technique that allows the deposition of dielectrics in reactive atmospheres with high deposition rates and low target contamination [27], as we seen in section 1.3.3.

This section studies the sequential deposition of a hard ceramic phase, TiB<sub>2</sub> and a hard lubricating phase of DLC to form a multilayer structured coating deposited onto a commercial powder metallurgy, Al alloy (Al 2618). Depositing alternating layers of different materials is a method now adopted by many researchers as a route to limit the stress build up in coatings [87] and to limit crack propagation in ceramic films [205].

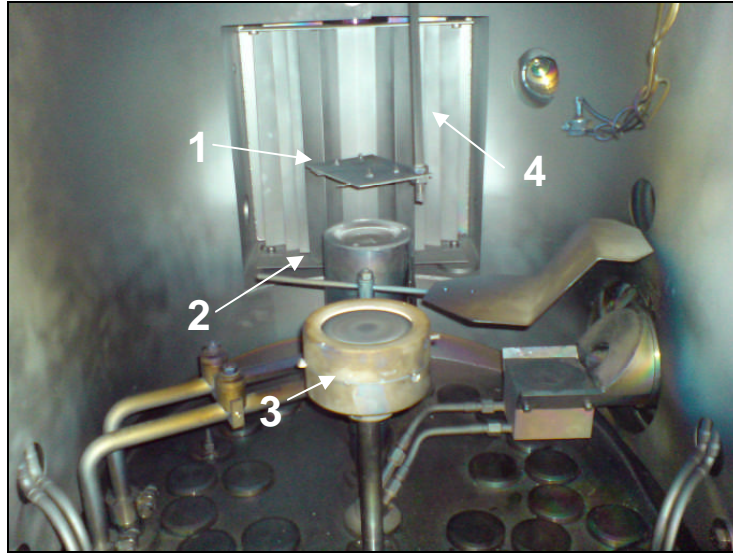


**Figure 40 – 3” Magnetrons details**

**Key:**

- 1 – Substrate holder
- 2 & 3 – Magnetrons (TiB<sub>2</sub> and Carbon)
- 4 – Pumping station

Power to the targets was supplied by an ENI RPG-50 pulsed-DC supply, at a frequency of 150 kHz and a pulse duty factor of 2016ns. Power densities of 6.7 W/cm<sup>2</sup> were used to sputter both the carbon and TiB<sub>2</sub> targets.

## **7.2. Process conditions**

### **7.2.1. Set-up the of conditions for Multilayer Coatings**

Multilayers are formed by alternating layers of two different materials, in a periodic manner. The characteristic micro-structural scale is the composition wavelength ( $\lambda$ ) which consists of the sum of two layers of the different materials.

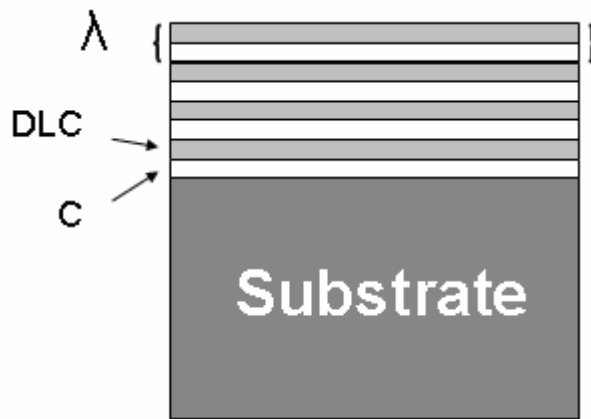


Figure 41 – Parameters for Multilayer Coating

The two varying parameters for multilayer coatings are the composition wavelength ( $\lambda$ ) and the volume fraction of ceramic ( $V_c$ ) and the volume of DLC ( $V_{DLC}$ ). They are given by the equations:

$$\lambda = t_c + t_{DLC}$$

$$V_c = \frac{t_c}{(t_{DLC} + t_c)}$$

**Key:**

$\lambda$  - Combined thickness

$V_{DLC}$  – Volume fraction of DLC

$t_c$  - Ceramic Thickness

$t_{DLC}$  – DLC Thickness

In sections 8.2 and 8.5, the coatings were performed for a constant value of composition wavelength (sum of two layers [ $\lambda$ ] =200nm) and for 4 different values of ceramic fraction, 75%, 85%, 90%, 95%. The thickness of individual DLC layers varied between 10nm and 50nm. The thickness of the ceramic layers varied between 150nm and 190nm. The thickness variations of the ceramic and the DLC layers are described in Table 6.

$\lambda(nm)$	$V_c$ (%)	$t_c$ (nm)	$T_{DLC}$ (nm)	$t_f$ ( $\mu m$ )	Total n° of Layers
200	75	150	50	5	50
	85	170	30		
	90	180	20		
	95	190	10		

Table 6 – Thickness variations of the ceramic and metal layers

Key:

$\lambda$  - Composition Wavelength (sum of one layer of ceramic and one layer of metal)

$V_c$  - Volume of Ceramic

$t_c$  - Thickness of the Ceramic layer

$t_{DLC}$  - Thickness of the DLC layer

In section 8.3, the principle of varying the volume fraction of carbon with the volume fraction of ceramic, namely TiB<sub>2</sub>, follows on from section 8.2. Thus a carbon/ TiB<sub>2</sub> multilayer stack has been fabricated by varying the thickness of the layers, keeping constant the bilayer thickness of carbon/ TiB<sub>2</sub> to a planned thickness of 200nm. In this way, a stack of 10 bi-layers of carbon/TiB<sub>2</sub> have been fabricated to a total film thickness of 2 $\mu$ m.

$\lambda(nm)$	$V_c$ (%)	$t_c$ (nm)	$T_{Carbon}$ (nm)	$t_f$ ( $\mu m$ )	Total n° of Layers
200	75	150	50	2	20
	50	100	100		
	25	50	150		

Table 7 - The experiments conducted in this part of the study. T represents the thickness of the individual layers. The percentage content of carbon was varied by modifying the thickness of the individual layers. The bi-layer was kept constant, aimed at 200nm. A multilayer coating of a stack of 10 layers was formed with a planned total film thickness of 2 $\mu$ m.

In practice, the thickness was  $2.75\mu\text{m}$  suggesting each bi-layer to be  $275\text{nm}$ . The nominal film structures investigated in this part of the study are summarised in Table 7.

### 7.2.2. Nanoindentation

The hardness and reduced modulus of the various coatings produced were measured using a Nanotest 550 (Micromaterials Limited, UK) equipped with a Berkovitch indenter, further details can be found in section 5. The tip used as an indenter was a Berkovitch diamond tip as shown in Figure 42.

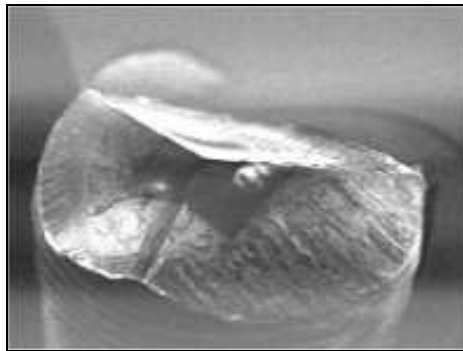


Figure 42 – Berkovitch Diamond Tip [12]

The total included angle on this tip is  $142.3$  degrees, with a half angle of  $65.35$  degrees. This makes it a very flat tip. This tip geometry has been used as the standard for nanoindentation. This tip is used primarily for bulk materials and thin films greater than  $100\text{nm}$  thick. The average radius of curvature for a Berkovitch tip is typically between  $100\text{nm}$  and  $200\text{nm}$ .

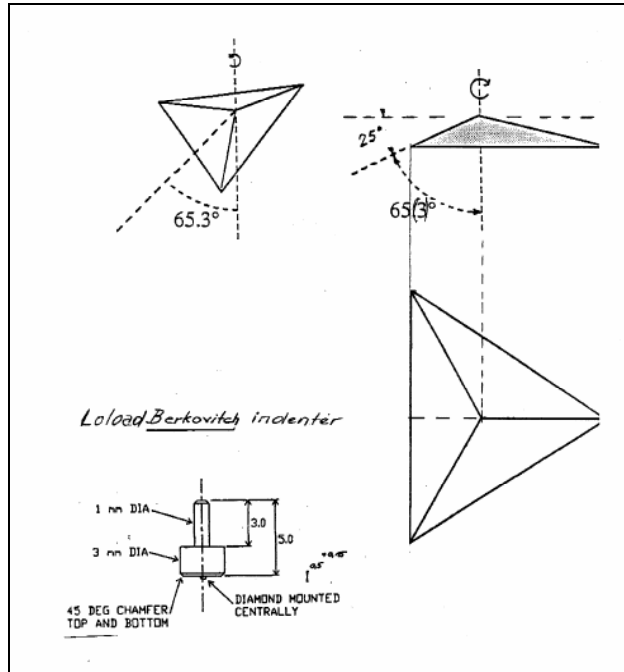


Figure 43 – Drawing of the basic geometry of a Berkovich diamond tip[12]

The nanotest pendulum can operate at low loads from 10  $\mu\text{N}$  up to 500mN and at high loads from 0.1N up to 20N.

The nanotest operates by using an increasing load applied to the indenter, which is compressed in to the sample. When it reaches a pre-determined value the load is reduced and the penetration depth decreases because of the materials elastic recovery.

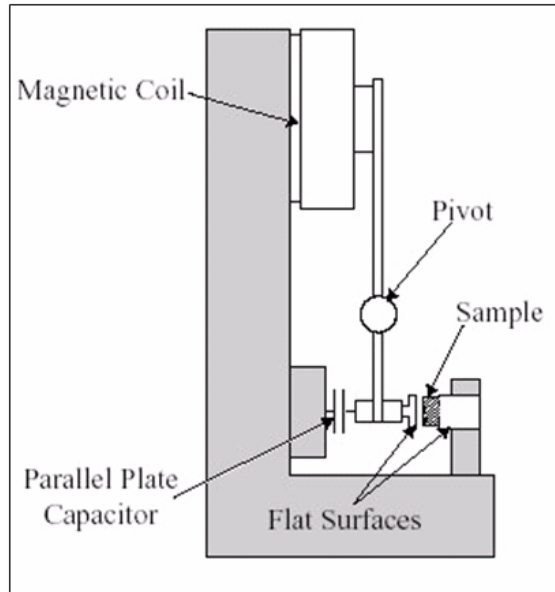


Figure 44 – Nanotest pendulum[12]

The values of Depth vs Load are constantly recorded, as shown in Figure 45, as well as other data, which includes maximum depth, maximum load, plastic depth, hardness and reduced modulus.

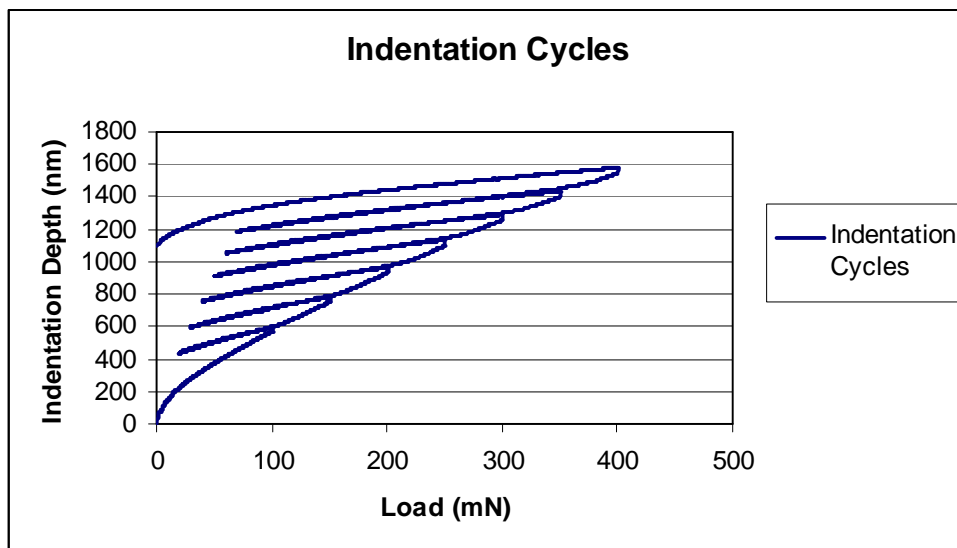


Figure 45– Nanoindentation Loading and Unloading Curves[12]

In section 8.1 the loads ranging from 0 to 6mN were applied to a maximum depth of 200nm. An increasing load procedure was employed with 8 loading steps, using a loading rate of 2mN/s and a dwell time of 15s at the highest load. Elastic contributions were determined from the unloading portion of the load-

displacement curves and provided values of the reduced modulus. The reduced modulus takes into account the deformation of the indenter as well as the film, as was discussed in section 5.1.

For section 8.2, 5 indents were made per sample with load ranging from 50 to 400mN to a maximum depth of 1800nm. The increasing load procedure had 8 steps with a loading rate of 2mN/s and a dwell time of 15s on the highest load. The mathematical model used was the Olivier and Pharr method [162] as reviewed earlier in section 5.1.

In section 8.3 five indents were made per sample with loads ranging from 100 to 400mN to a maximum depth of 3 $\mu$ m.

In section 8.5 5 indents were made per sample with loads ranging from 20mN to 100mN to a maximum penetration depth, using the same loading rate and dwell time as mentioned above.

### **7.2.3. Tribological testing**

Tribological testing was conducted using a ST-3001 Tribo Tester (Teer Coatings Ltd, UK). For adhesion testing, a diamond Rockwell C was employed. For sections 8.1, 8.2 and 8.3 the scratch testing conducted used an increasing load from 10 to 60N. For section 8.4 and 8.5 the scratches were produced with continuous loads of 2N, 5N, 7N, 10N, 15N, and 20N, at a constant speed of 10mm/min due to the soft nature of the substrate.

The Tribo Tester system permits operation in either a uni-directional or bi-directional mode. The friction testing was carried out using a fixed WC-Co 5 mm diameter ball slid against a coated test piece with a range of load and displacements. In section 8.1 tests were also performed at 10N load. In section 8.2 two different loads were chosen 10N and 20N loads with 100 cycles. In section 8.3 loads of 10N were used. For the bulk coatings 50 cycles were used

and for the multilayers 20 cycles were used. In section 8.4 the load used was 20N over 100 cycles, and in section 8.5, 50 cycles with a constant load of 10N.

## 7.3. Substrates

### 7.3.1. Tool Steel

Carbon steels can be designated by unique AISI (American Iron and Steel Institute) four-digit numbers. The first two digits indicate the grades of the steel, while the last two digits give the nominal carbon content of the alloy in hundredths of a percent.

Substrate Material	Steel (AISI 1095)
Length (mm)	30
Width (mm)	20
Thickness (mm)	0.635
Chemical Analysis (%)	C 0.9-1.05 Mn 0.3-0.5 P 0.04 max Cr 0.1-0.3 S 0.05 max Si 0.15-0.35
Tensile Modulus (GPa)	206.9
Tensile Strength (N.mm <sup>2</sup> )	1900
Thermal Expansion Coefficient 10-6K <sup>-1</sup>	12.1
Density (Kg/m <sup>3</sup> )	7861.4
Specific Heat (J/Kg K)	447.6
Melting Point (Deg C)	1515.5
Poisson's Ratio	0.3

**Table 8 – Properties of the substrate AISI 1095**

The substrates were made of Steel AISI 1095. This is a plain carbon steel with a maximum manganese percentage of 1.0%, as we can see in Table 8. This grade of steel is characterized by high carbon content, 0.95%. The main properties are described in Table 8.

The steel samples were prepared for coating by using various polishing/grinding papers. The polishing papers used were: SiC 120 grit, SiC 240 grit, SiC 1200 grit, D-Plane 6µm Diamond and for finishing Colloidal Silica polish. The samples were then cleaned in a re-flux column for 30 minutes with IPA as the cleaning agent.

### **7.3.2. Powder processed Al Alloys substrates**

Isostatic pressing was used for compressing powdered materials into shaped pre-forms or general products. There are two main types of isostatic presses; cold isostatic presses (CIP) that function at room temperature and hot isostatic presses (HIP) that function at elevated temperatures. Typical HIP applications include processing high performance ceramics, ferrites and cemented carbides, net-shape forming of nickel-base superalloy and titanium powders, compacting of high-speed tool steel, diffusion bonding of similar and dissimilar materials, and eliminating voids in aerospace castings. Cold pressed metals or ceramic powder compacts may require additional processing, such as sintering, to provide a finished part.

The manufacturing process of this Al alloy used fine grain sizes, with particles sizes ranging from 5 - 45µm. The powder was then canned in an Al can and evacuated in heat and vacuum to prevent contaminations. Then, the cans are CIPed to a max pressure of 200 bar, with 5 cycles. Afterwards the cans are HIPed at approximately 500 °C at 1000 bar during 45 to 90 minutes followed by a very slow cool. To finalize the process the Al is solution treated at 525 °C and then quenched in a polymer solution and aged at temperatures between 150 - 180°C between 8 and 16 hours.

The substrates were supplied by TR Engineering Ltd, UK, manufactured from Al powder with a commercial composition of Al 2618 (Aluminium: Balance, Iron 1.33%; Silicon 0.11 %; Copper 2.67 %; Magnesium 1.3 %; Nickel 1.22 %; Ti 0.07%). The powder pressed Al alloys were prepared for coating using successive grinding steps. The grinding/polishing papers used were: SiC 120 grit, SiC 220, SiC 1200 grit and SiC 2500 grit, to a surface roughness better than 0.2µm. After grinding they were cleaned following the procedures described in section 7.3.1.

## 7.4. Focused Ion Beam

Focused ion beam (FIB) has proved an indispensable tool in the arsenal of analytical techniques. FIB is similar to scanning electron microscopes (SEM) in that a beam of charged particles is generated, raster scanned (scanning pattern of parallel lines that form the display of an image projected on a cathode-ray tube of a television set or display screen), and used for submicron imaging. The system uses ions, which have a larger mass than electrons; FIB systems can also produce a protective layer prior to milling. It can be used to localise and removed certain undesired materials by adding reactive gas chemistries and changing the operating procedures. Ion-induced deposition techniques are also available and with the addition of gas chemistries both conductive and insulating films can be deposited [12, 206-208].

The ion beam is generated from a metal ion source. Positively charged gallium ions accelerated at 20-50KeV are focused to a submicron beam diameter with electrostatic lenses. The background pressure in the turbo-pumped sample chamber is about  $3 \times 10^{-7}$  Torr and rises to about  $2 \times 10^{-5}$  Torr with the introduction of gas chemistries [3, 206-208].

The interaction of the ion beam with the surface of the sample results in ejection of atoms from the surface and the production of secondary electrons and ions. The gallium (Ga+) primary ion beam hits the sample surface and sputters a small amount of material, which leaves the surface as either secondary ions or neutral atoms. The primary beam also produces secondary electrons [3, 12, 206-208].

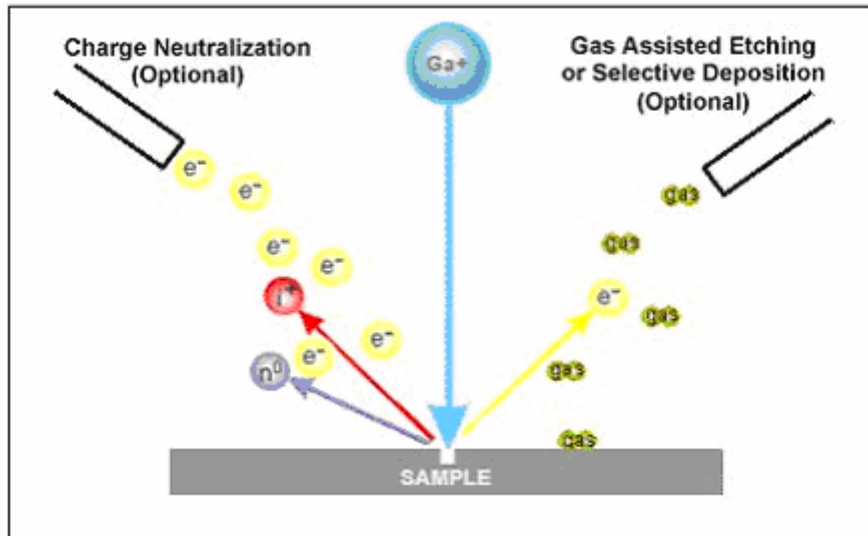


Figure 46 - FIB system detail [206]

The ion beam is scanned over the surface of the sample in a previously defined pattern. At low primary beam currents, very little material is sputtered; modern FIB systems, can achieve 5 nm imaging resolution. At higher currents, a great deal of material can be removed by sputtering, allowing precision milling of the sample down to a sub micron scale.

If the sample is non-conductive, a low energy electron flood gun can be used to provide charge neutralisation. In this manner, by imaging with positive secondary ions using the positive primary ion beam, even highly insulating samples may be imaged and milled without a conducting surface coating, as would be required in a SEM.



**Figure 47 - FEI 200XP FIB Microscope.**

FIB can be employed to make precision modifications to a variety of samples. These modifications can be as simple as a single hole or as complex as a three-dimensional cross-sectioning of a circuit. One of the primary advantages of the FIB is the capability of localize a certain area and the ability to modify it.

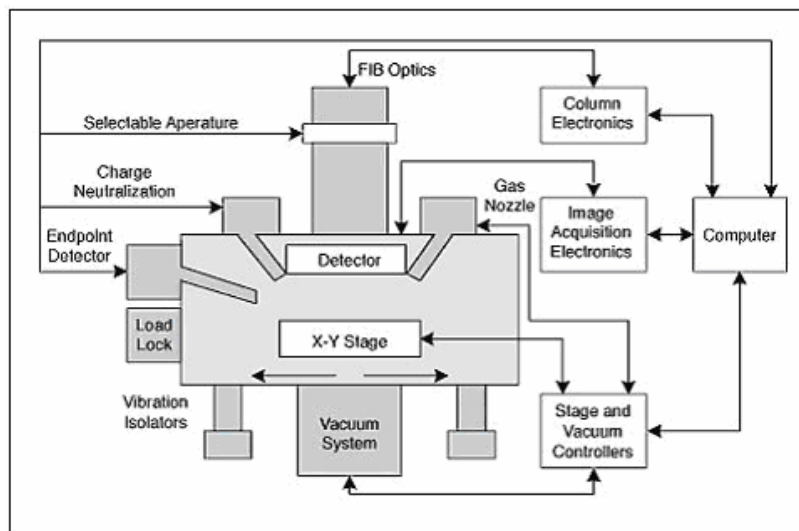


**Figure 48 - FIB system Overview [12]**

As we seen before FIB can drill holes and cut metal lines. It can also deposit metal and insulators to protect the surface. These capabilities allow the FIB to

be used for failure analysis and test structures as well as the repair of nearly-functional parts [12, 206, 208, 209].

#### 7.4.1. Applications:

When higher currents are selected the FIB can be considered as an atomic milling machine, which performs stress-free precision sectioning and machining with a high accuracy as we can see in Figure 49 and Figure 50.

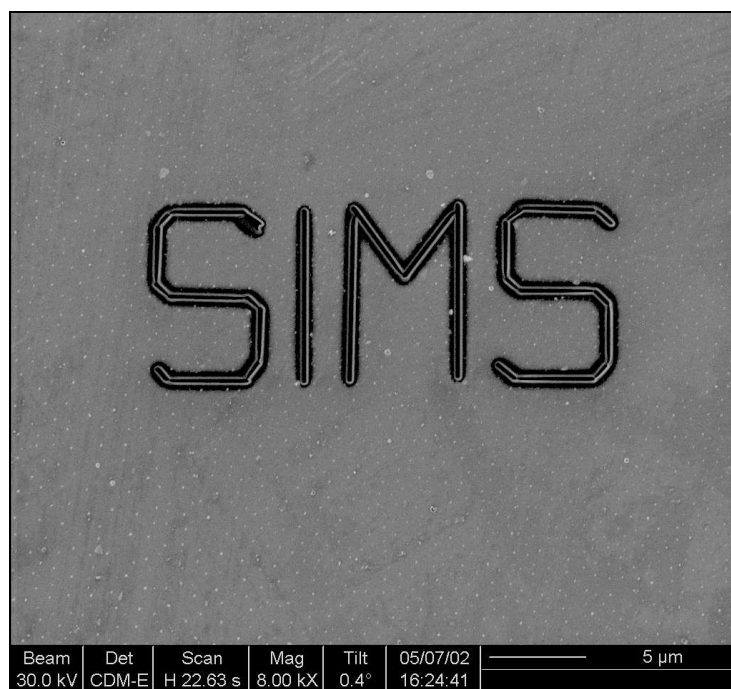
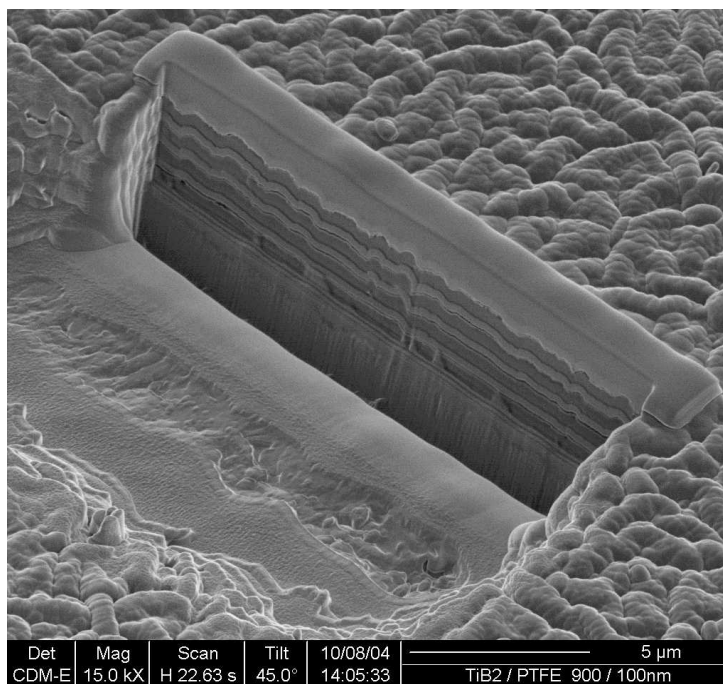
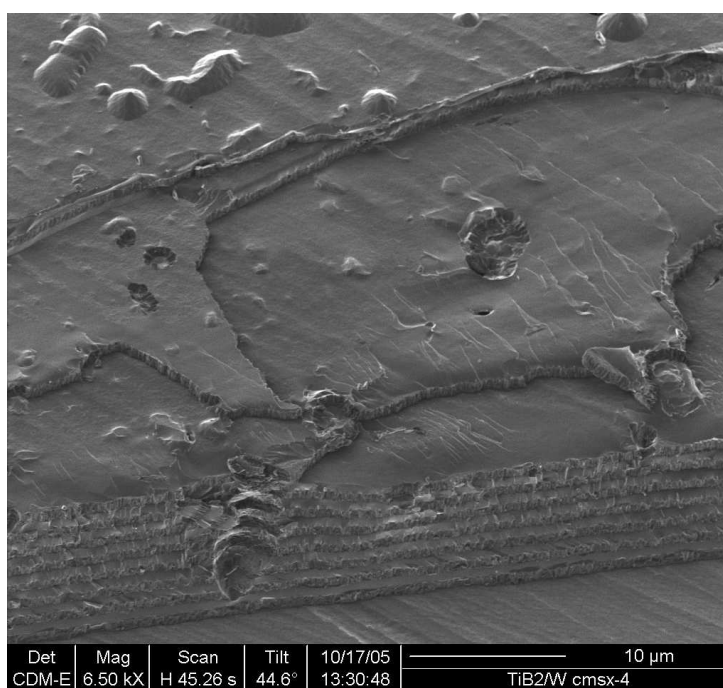


Figure 49 - FIB Image of milling capabilities



**Figure 50 –FIB Micrograph of TiB<sub>2</sub> Multilayer with a Pt protective layer**

At lower beam currents, FIB imaging resolution begins to rival the more familiar scanning electron microscope (SEM) in terms of imaging topography, however the FIB's imaging modes, offer many advantages over SEM. As can be seen from Figure 51.



**Figure 51 – Delaminated TiB<sub>2</sub>/W multilayer**

FIB can show intense grain orientation contrast, Figure 52. As a result grain morphology can be readily imaged without resorting to chemical etching. Grain boundary contrast can also be enhanced through careful selection of imaging parameters.

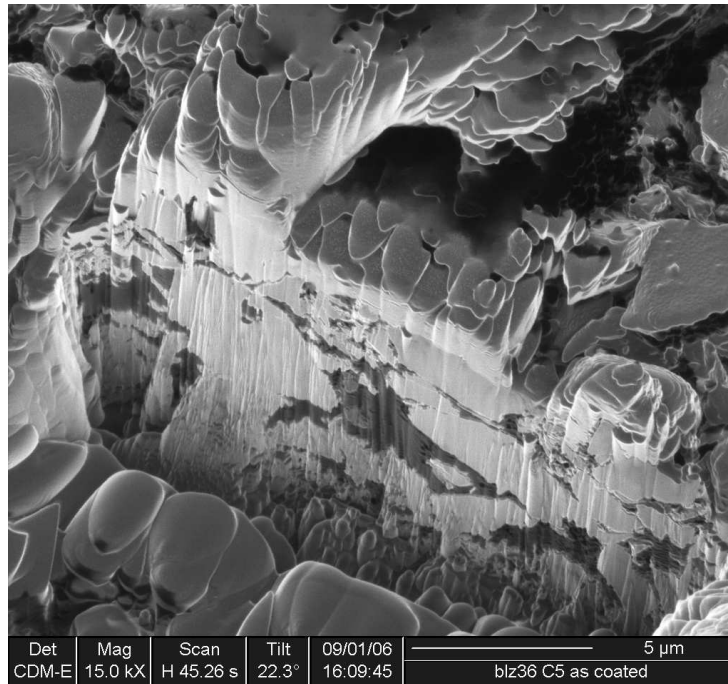


**Figure 52 - Grain contrast by FIB techniques**

## **7.5. Raman Spectroscopy**

Raman spectroscopy is a method of chemical analysis that enables real-time reaction monitoring and characterization of compounds in a non-destructive manner[210-212].

The spectrum is more sensitive to the lengths, strengths, and arrangement of bonds in a material than to the chemical composition of the material. The Raman spectra of crystals also respond to details of defects and disorder than to trace impurities and related chemical imperfections [210, 211].

The basic components for Raman spectroscopy, Figure 53, include a light source (normally a laser), collection optics to gather the Raman-scattered light, and a detection system.

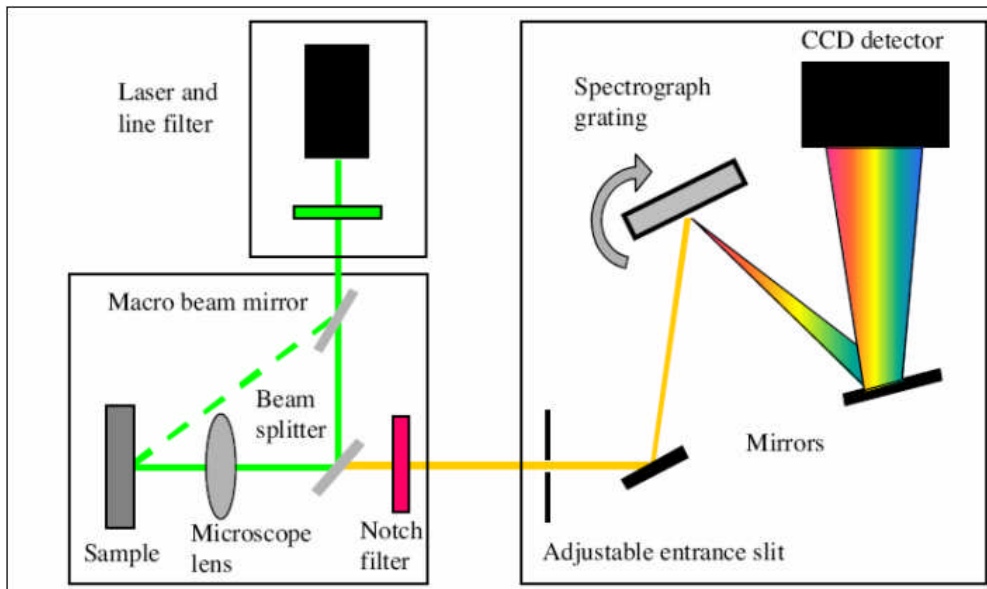


**Figure 53 - Basic hardware components for Raman spectroscopy**

### 7.5.1. Applications of Raman spectroscopy

Raman spectroscopy has been used for the characterization of CVD and PVD - grown diamond films, proving the formation of diamond and characterizing the presence of graphite and various amorphous carbons [132, 145, 213-215]. Due to its non destructive nature it can be finely focused and used in a backscattering geometry.

Raman has proved a useful tool for characterizing thin films and layers such as silicon, germanium and gallium arsenide. The Raman spectra can give information about the crystal nature of the film and the presence of impure or contaminant layers[210, 211]. When analysing a thin film the depth of penetration of the laser depends on the transparency of the sample material and the wavelength of the laser radiation used. If a film or coating is transparent, the film/substrate interface and any other material deposited there is also accessible and may provide a detectable Raman signal. The absolute

sensitivity of the Raman technique is such that a film thickness of at least 0.1  $\mu\text{m}$  is required to provide a workable signal [132, 145, 210, 213-215]. Raman spectroscopy is used in section 8 to characterise the DLC produced.

## **8. Results and Discussion**

### **8.1. Tribological characteristics of pulsed-DC, DC-sputtered and RF- sputtered titanium diboride (TiB<sub>2</sub>) thin film coatings**

#### **8.1.1. Introduction**

This section discusses the attributes of titanium diboride (TiB<sub>2</sub>) fabricated by physical vapour deposition (PVD) sputtering. Three methods of PVD sputtering were employed, namely; RF magnetron sputtering, DC magnetron sputtering and pulsed-DC magnetron sputtering. The aim of this section is then to investigate the properties of the fabricated TiB<sub>2</sub> in terms of its hardness and wear-resistant properties, relate this to the film microstructure and processing parameters that have been used.

Previous studies have investigated the fundamental properties of TiB<sub>2</sub> as a coating; however those studies have been limited to studying either TiB<sub>2</sub> fabricated by DC [216, 217] or RF magnetron sputtering [97]. It has been well documented that the microstructure, mechanical and tribological properties of TiB<sub>2</sub> are affected by processing parameters such as power and substrate bias voltage [107]. Furthermore, the impact of high-energy ions on a substrate will affect both film stress, and will result in re-sputtering of deposited atoms [218] .

As we seen in previous section 1.3.3 Pulsed-DC techniques have, in recent years, been an area of detailed research as they have enabled high-rate stable deposition conditions to be achieved, even under reactive conditions, allowing oxide and other ceramic [219] depositions to be undertaken. In this technique, the DC output from the power supply is pulsed at a frequency range set by the user which typically ranges from 50-350 kHz. Pulsing prevents charge build-up on the insulating parts of the surface of a target and the resulting arcing that would otherwise occur is greatly reduced. During the off phase, electrons from

the plasma are drawn towards the cathode, giving rise for a very short duration (100 ns) pulse of high electron current. The main uses of pulsed-DC sputtering techniques therefore have been associated with reactive sputtering, whereby the pulsing of the cathode limits target poisoning and enables films to be sputtered with a controlled stoichiometry. The published knowledge on metallic and ceramic films directly deposited by pulsed-DC magnetron sputtering, rather than reactively, is limited and thus is of interest to investigate and study the properties of such films, in the content of this thesis.

## 8.1.2. Results and discussion

### 8.1.2.1 Nanoindentation

Figure 54 illustrates typical load-displacement curves for all the films investigated in this study. The  $\text{TiB}_2$  deposited by RF sputtering at 200 W shows the most compliant behaviour, with a penetration depth of 175 nm for a load of 5 mN. The sample deposited with 300W had a load-displacement curve with a similar loading/unloading curve with a maximum depth of around 130nm.

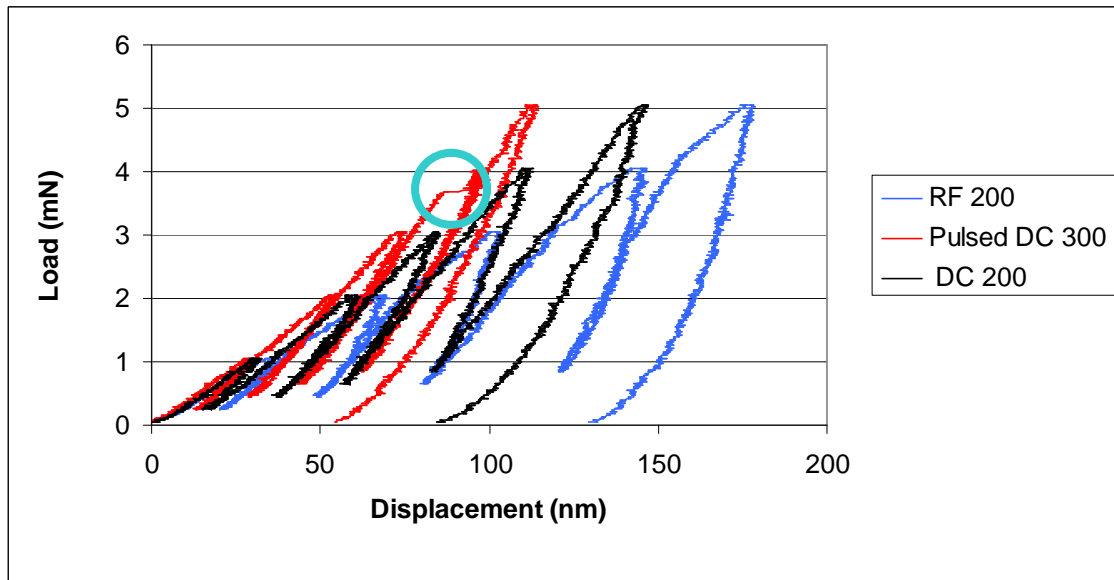


Figure 54: The Load-Displacement curves for the  $\text{TiB}_2$  films fabricated in this section, highlighted by a blue circle is a sign of creep occurring in the coating.

The films fabricated by pulsed-DC are almost fully elastic in their nano-indentation response, recovering from penetration depths of 110nm.

The curve for the Pulsed-DC 300 is shown in the Figure and highlighted in blue circle is a sign of creep occurring. The Pulsed-DC 200W coating had an equal curve, but with no creep occurring during the test. For the TiB<sub>2</sub> film deposited by DC sputtering at 200 W, the maximum penetration depth reached at a load of 5 mN is 140 nm a value close to a RF-deposited film at 200 W. The sample deposited with DC 300W had a curve very similar to the RF deposited films, with values between the RF curves and DC 200 W curves.

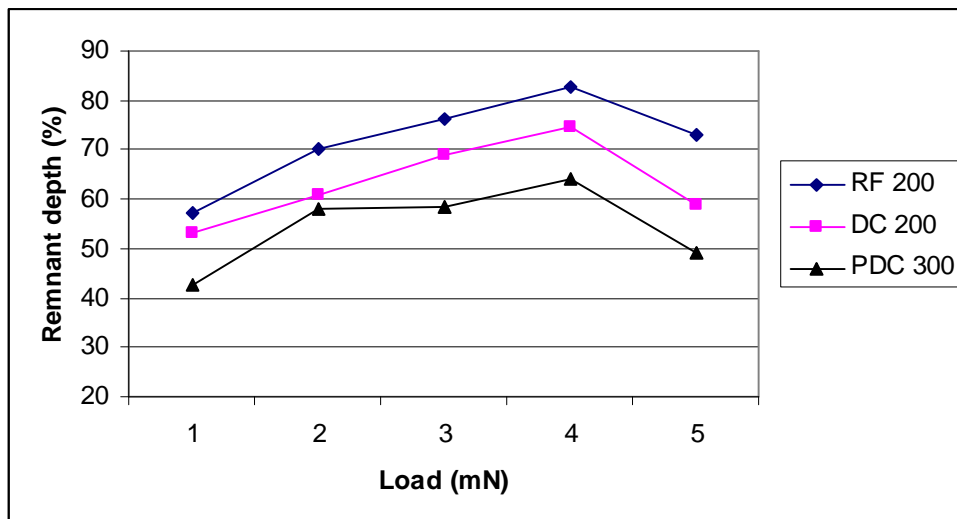


Figure 55 – Remnant depth for the of the coatings manufactured for this section

In Figure 55 the remnant depth is plotted. The remnant depth is the ratio between the depth after unloading and the depth at peak load. From observation of the Figure it is possible to see that the Pulsed DC is the coating which possesses the lower ratio. This is an indicator of a very high plasticity, which is confirmed by the hardness values and tribological testing.

Berger et al [107] has investigated the microstructure of TiB<sub>2</sub> coatings deposited by DC sputtering. From their results they concluded that the TiB<sub>2</sub> deposited at a negative bias is crystalline with dense grain boundaries. Similar studies, investigating the deposition of Al<sub>2</sub>O<sub>3</sub> by pulsed-DC sputtering, have concluded

that the films are denser compared to  $\text{Al}_2\text{O}_3$  deposited by conventional RF and DC sputtering techniques [10]. Thus, a lower density for the DC magnetron sputtered films could account for and explain the relatively large indentation depths ( $>150$  nm) and thus film compliance that have been observed for the  $\text{TiB}_2$  DC sputtered films in this study.



**Figure 56 – FIB cross section of the RF 300w sample, highlighted in red are pores visible in the section of the film.**

In Figure 56 one can see that the microstructure is dense and there are no major defects in the coating. Highlighted in red there is a void in the coating. This is a normal occurrence in PVD coatings as discussed in section 1.5.1.

In Figure 57 the sample produced using DC deposition shows a considerable level of delamination at the interface level, as it is possible to see highlighted in white. This feature is present in a considerable area of the  $25\ \mu\text{m} \times 25\ \mu\text{m}$  trench manufactured by the FIB, as visible in Figure 57. On the right there is an area in which the delamination no longer is visible but, this delamination is an indicator that the interface is weak as it will be discussed in 8.1.3.

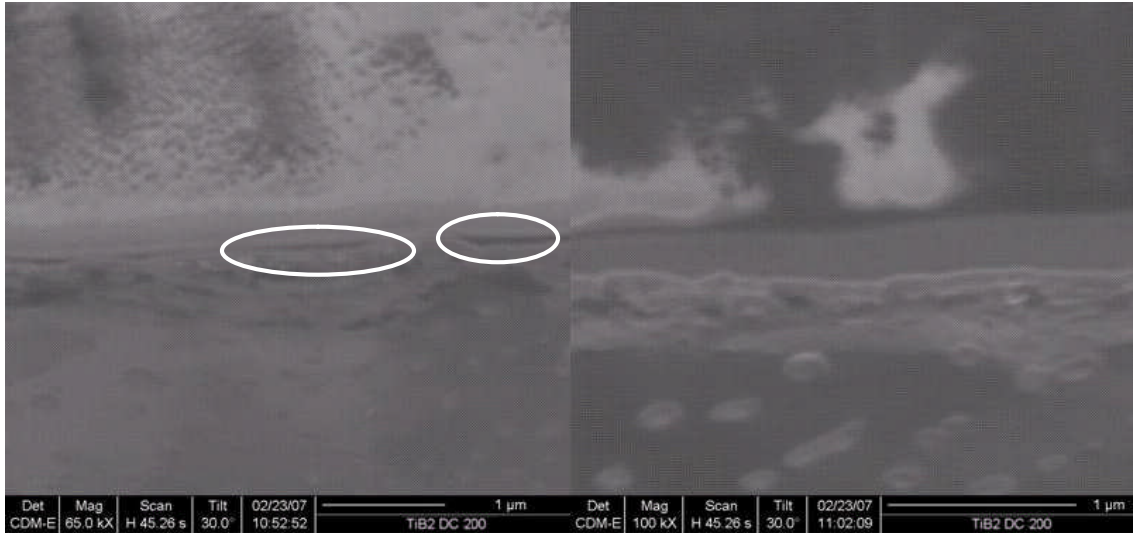


**Figure 57 – FIB section of the DC 200W samples, in the picture on the left there are signs of detachment at the interface, highlighted in a white circle.**

Figure 58 shows a FIB section of the sample produced using Pulsed DC 300W. The coating is dense without the presence of any defects. Highlighted in blue there is an area which is similar to a pore but this is thought to be due to substrate preparation as seen in section 7.3.2. When the magnification is higher (Figure on the right) it is possible to see that there is no sign of defects at the interface level.

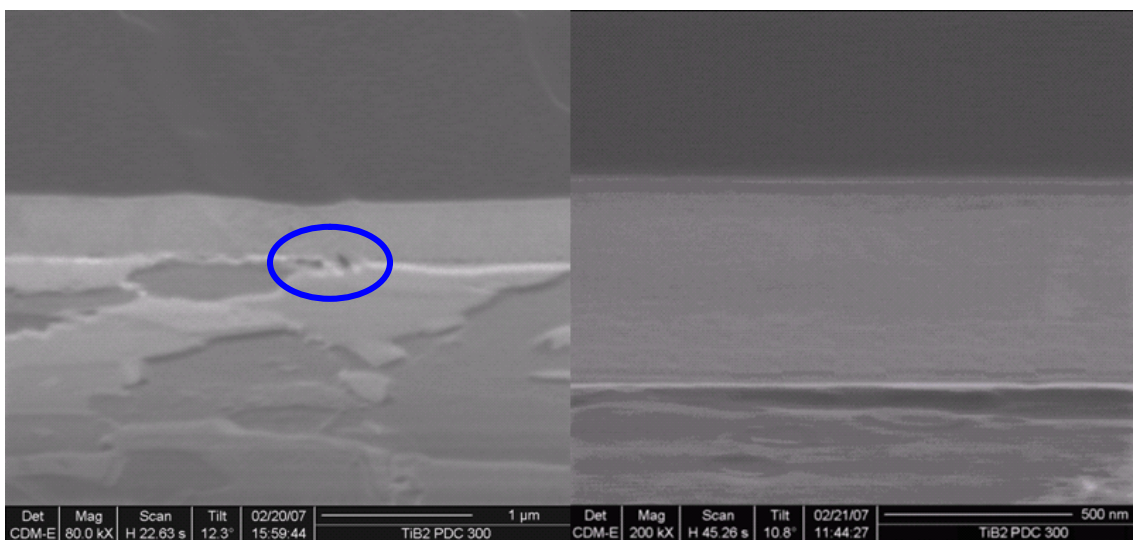


**Figure 58 – FIB cross section of the samples manufactured with Pulsed-DC at 300W, highlighted in blue are defects at the interface level.**

The hardness and reduced modulus results, Figure 59 and Figure 60, for the films show a scattering of data, however, the hardness is seen to decrease classically as a function of depth, with pulsed-DC the hardest and RF and DC magnetron sputtered the softest.

From the graph, it can be determined that the pulsed-DC films deposited at 300 W produced films with hardness values up to 21 GPa. The softest films (DC 300W) have a hardnesses of 12 GPa.

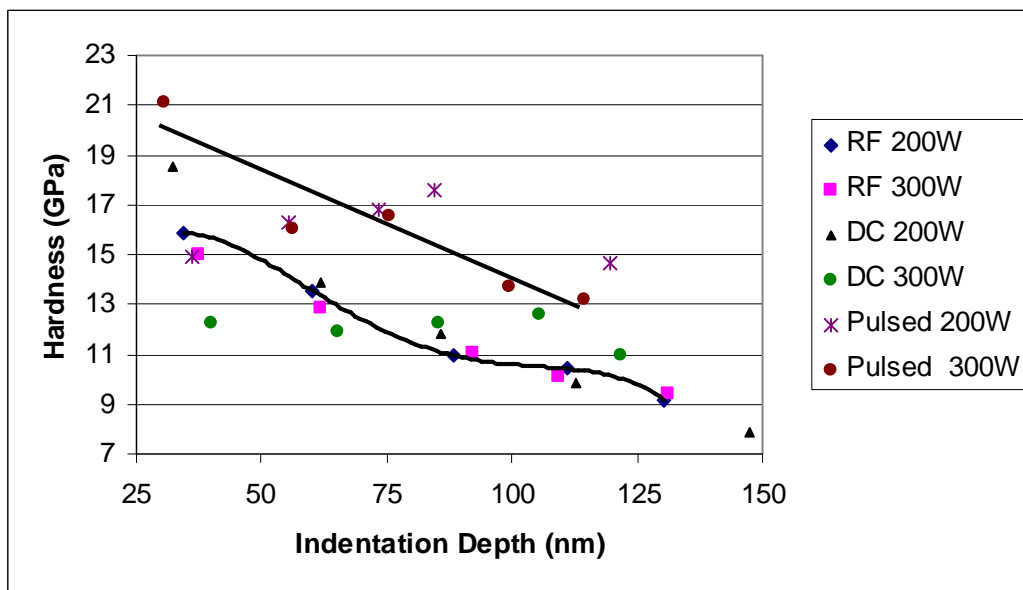


Figure 59 - The variation in hardness as a function of indentation depth into the film. Two lines are included showing the trend of the data.

Veprek et al. [220], tested materials which exhibited superhardness ( $\geq 40$  GPa), diamond, cubic boron nitride,  $C_3N_4$  and other carbonitrides. They used an automated load–depth sensing indentometer with a load range from 5 to 1000 mN. The authors observed an increase in hardness as a function of depth and suggested that this is due to enhanced ion bombardment during sputtering.

Such behaviour is not observed in the current study; however, the increased hardness seen by Veprek et al., [220] was further attributed to the nano-composite structure of their coatings compared to this study where mono-layered coatings were studied.

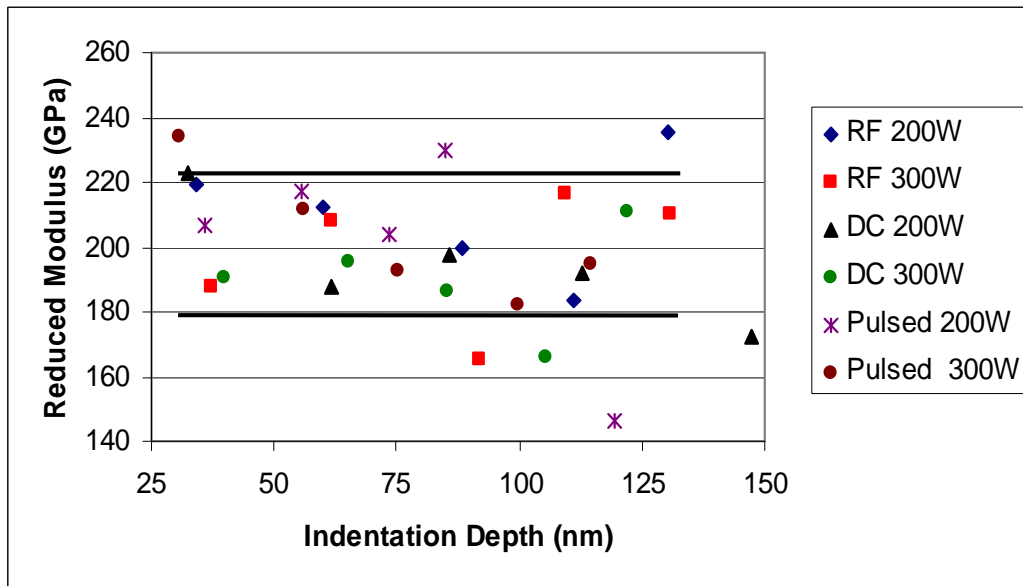


Figure 60 - The variation of the reduced modulus as a function of indentation depth into the film. The lines drawn at around 220 GPa and 180 GPa are an aid to the eye, highlighting the fact that the films have an average reduced modulus of 200 GPa, which varies by 10%, regardless of the deposition technique used to deposit the TiB<sub>2</sub>.

The measured reduced modulus and hardness values allow one to calculate the ratio of  $H^3/E^2$ , which provides information on a material's resistance to plastic deformation. A high resistance to deformation leads to a higher  $H^3/E^2$  ratio.

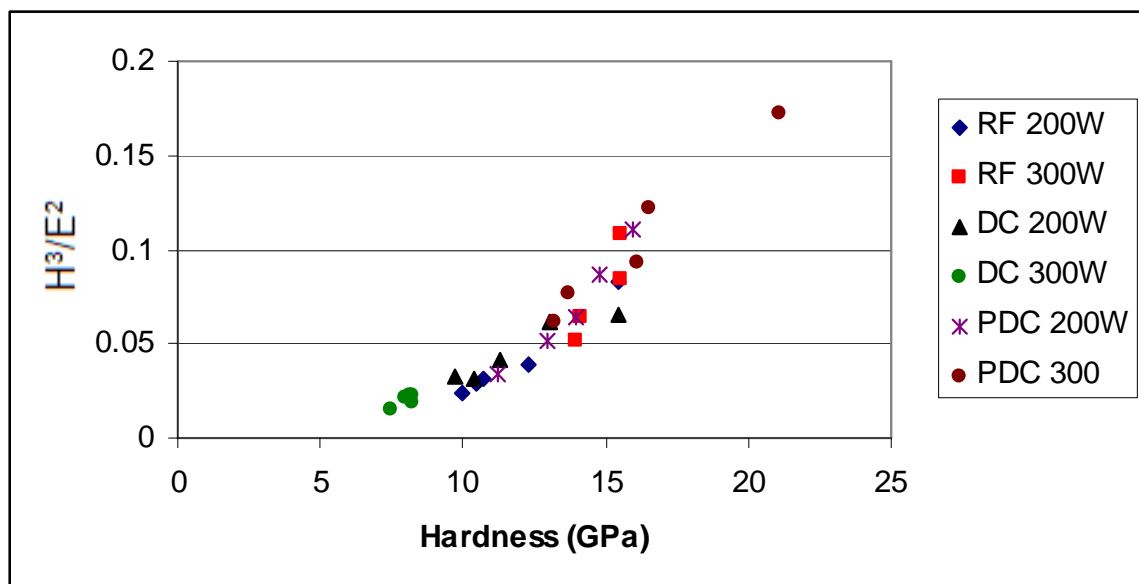


Figure 61 - Variation of  $H^3/E^2$  versus hardness for all the TiB<sub>2</sub> films fabricated in this study. From the data, the pulsed-DC films prove to have the desirable properties of high hardness, allowing a given load to be distributed over a wider area.

Figure 61, a plot of  $H^3/E^2$  against hardness is presented for the  $TiB_2$  films. The  $H^3/E^2$  ratio increases as a function of the hardness, as expected. From the data, the  $TiB_2$  fabricated by pulsed-DC produces both the hardest films and the most resilient against plastic indentation, making it desirable in terms of allowing a given load to be distributed over a wider area.

### 8.1.2.2 AFM results

The values for mean surface roughness (Ra) vary according to deposition condition. We can demonstrate that  $TiB_2$  fabricated by RF magnetron sputtering produces a film roughness far superior to that produced by either DC magnetron or pulsed-DC magnetron sputtering. As the sputtering power is increased from 200 W to 300 W, the ion impact energies at the surface of the substrate increase, which has been shown using Monte Carlo simulations [221], to affect surface morphologies of a growing film.

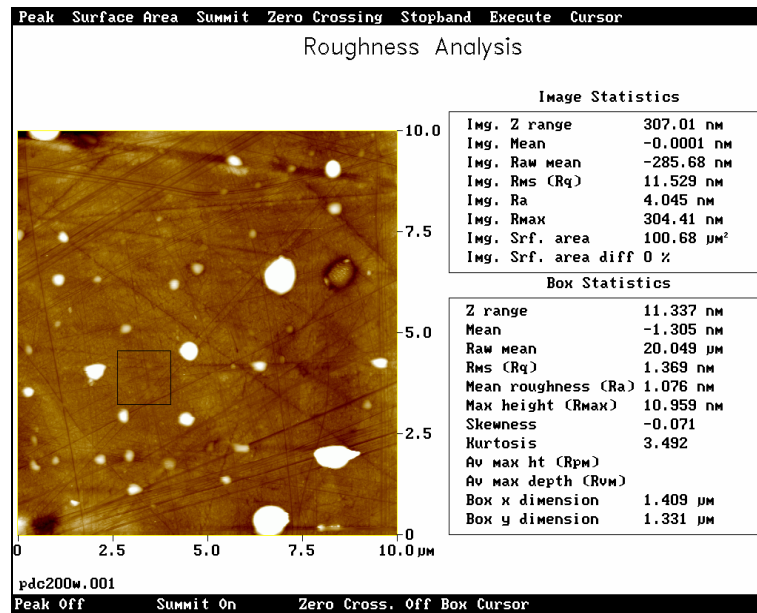


Figure 62 – AFM topography of Pulsed DC sample 200W.

Also we note that the roughness of the pulsed-DC magnetron sputtered film fabricated at 200 W is approximately 4 nm, Figure 62, this being similar in value to that of the roughness of the film fabricated at 300 W using RF magnetron

sputtering, Figure 63. The white spots are off-scale points on the AFM in the Z direction on the sample.

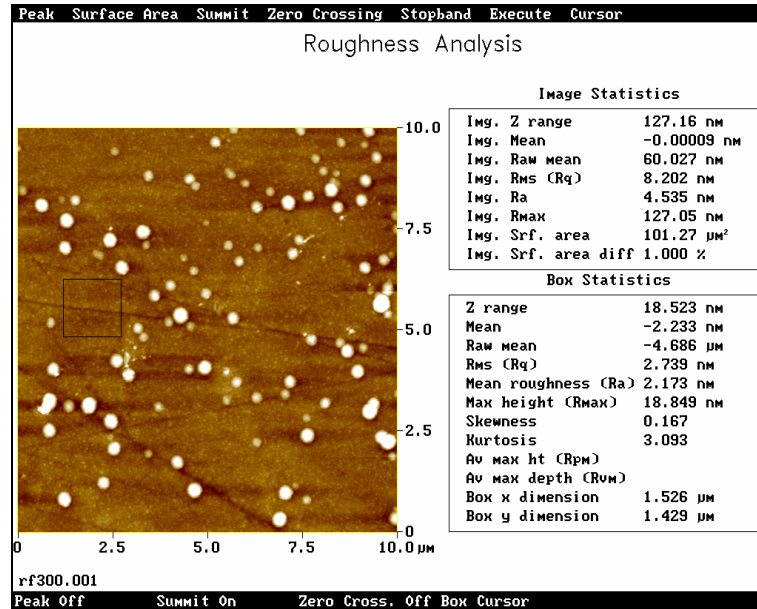


Figure 63 – AFM topography of RF sample 300W.

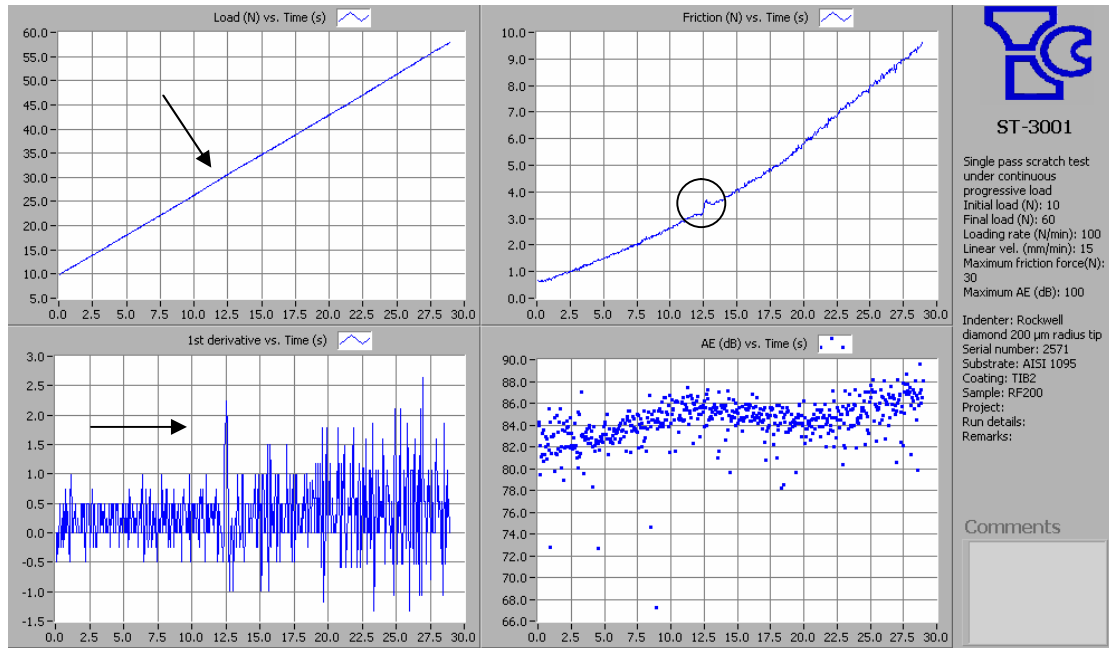
This suggests that ions generated by pulsed-DC (200 W), have similar energies at lower power to those RF generated ions at higher power (300 W). This is due to the fact that in RF the target is not coupled directly to the source, while in Pulsed-DC there is a very fast transition between the positive and negative part of the cycle and the supply is connected directly to the target.

### 8.1.3. Tribological testing of TiB<sub>2</sub>

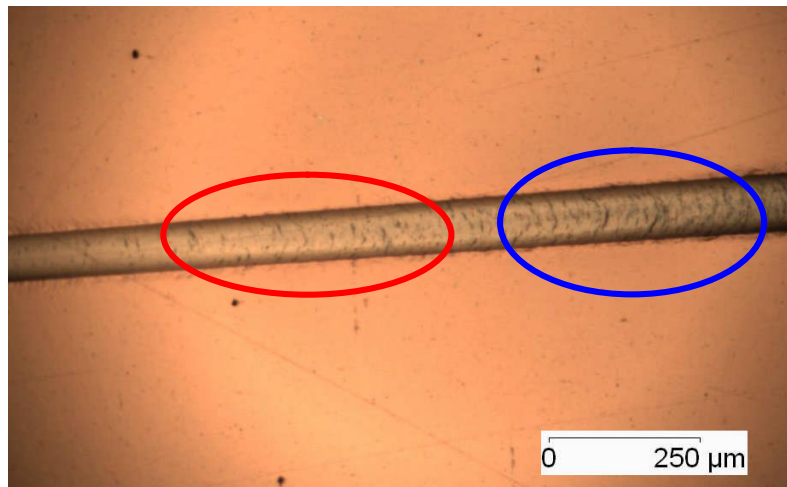
#### 8.1.3.1 Scratch Testing

The adhesion testing for the RF sputtered films showed very similar results presenting critical loads of around 30N, Figure 64 and Figure 66.

In Figure 64, the first derivative of friction has a larger peak at around 12.5s revealing that failure has initiated. The noise in this curve increases, thereafter in Figure 64; the revealing points are marked with black arrows or circles, revealing the peak in the friction and in the first derivative.



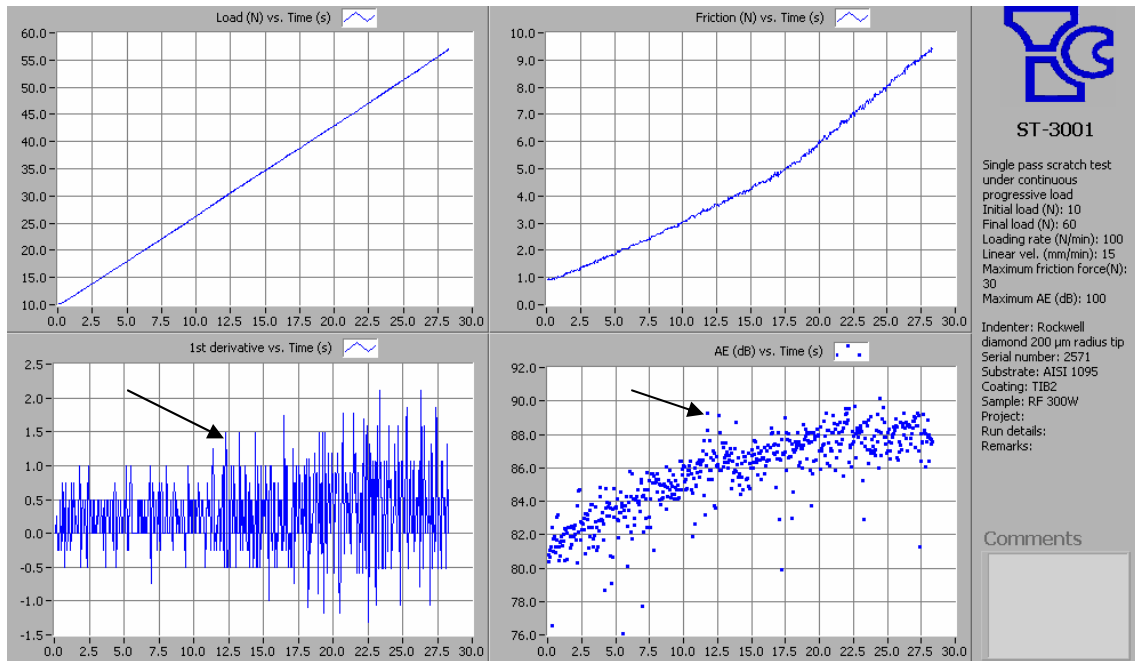
**Figure 64 – RF 200W, single pass scratch test with increasing load from 10N to 60N, in the chart are highlighted the points of critical load.**



**Figure 65 – RF 200W scratch testing with increasing load showing a mix failure mode between buckling (red circle) tensile cracking (blue circle)**

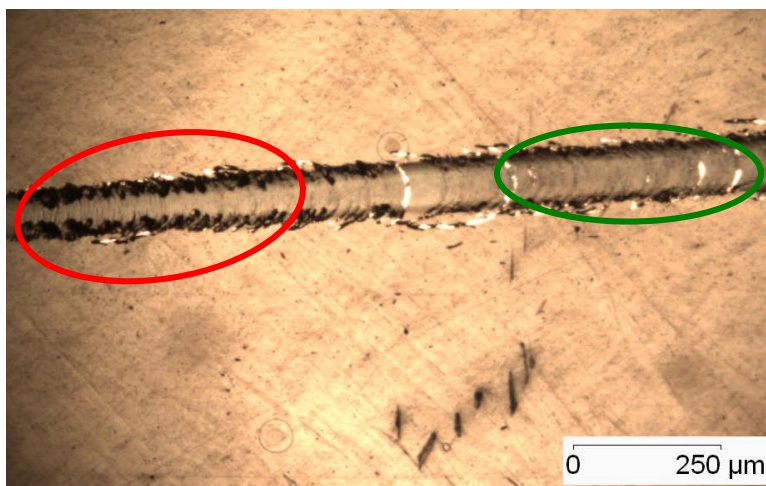
From Figure 65 it is possible to see that the failure mode present in the RF 200W is a mix between buckling and tensile cracking. As we have seen in section 6, the magnitude of the failure is smaller than the size of the scratch, being confined to the scratch scar, but revealing that pile up of the substrate materials occurs, ahead of the moving indenter.

From Figure 66, it's more difficult to access the critical load; there is no obvious inflection point in the friction curve and it's only by observing the AE response that it is possible to estimate the failure point. Failure is indicated by an increase in acoustic emissions, it's estimated that failure begins at 30N after 12.3 s into the scratch test.



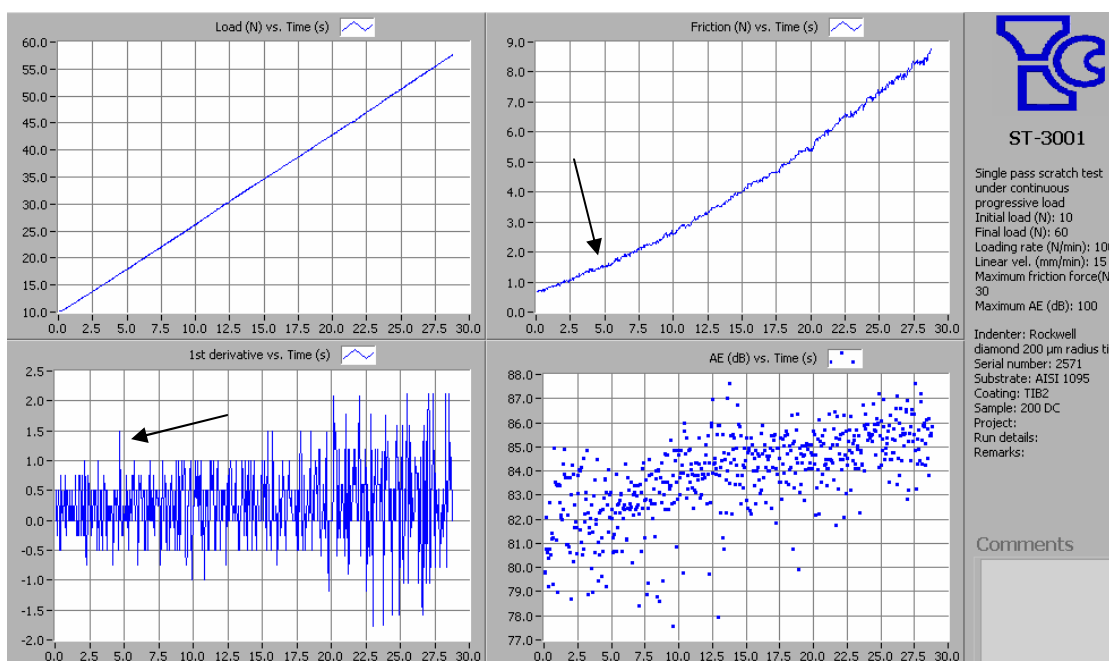
**Figure 66 - RF 300W, single pass scratch test with increasing load from 10N to 60N, in the chart are highlighted the failure points.**

From Figure 67 it is possible to see recovery spallation mixed with tensile cracking. This occurs as a result of the diamond stylus causing any interfacial crack to propagate to the outside of the scratch.



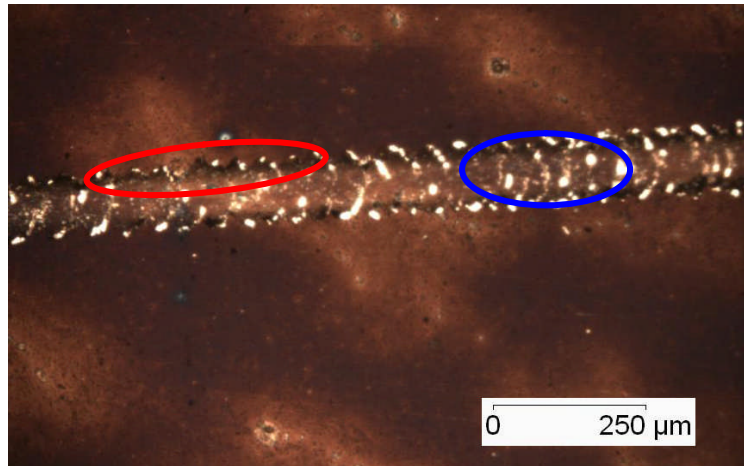
**Figure 67 - RF 300W scratch testing with increasing load showing recovery spallation (red circle) mixed with tensile cracking (green circle)**

Figure 68 shows the adhesion testing for the DC200W coating. In the figure it is possible to see that the first derivative of friction shows continual bursts of activity in, starting at about 4,8s. This indicates that the adhesion is poor and that the first failure occurs at around 17N. The AE emission in this case reveals a brittle failure (continual acoustic emissions) because the amount of scatter in the experimental AE results.



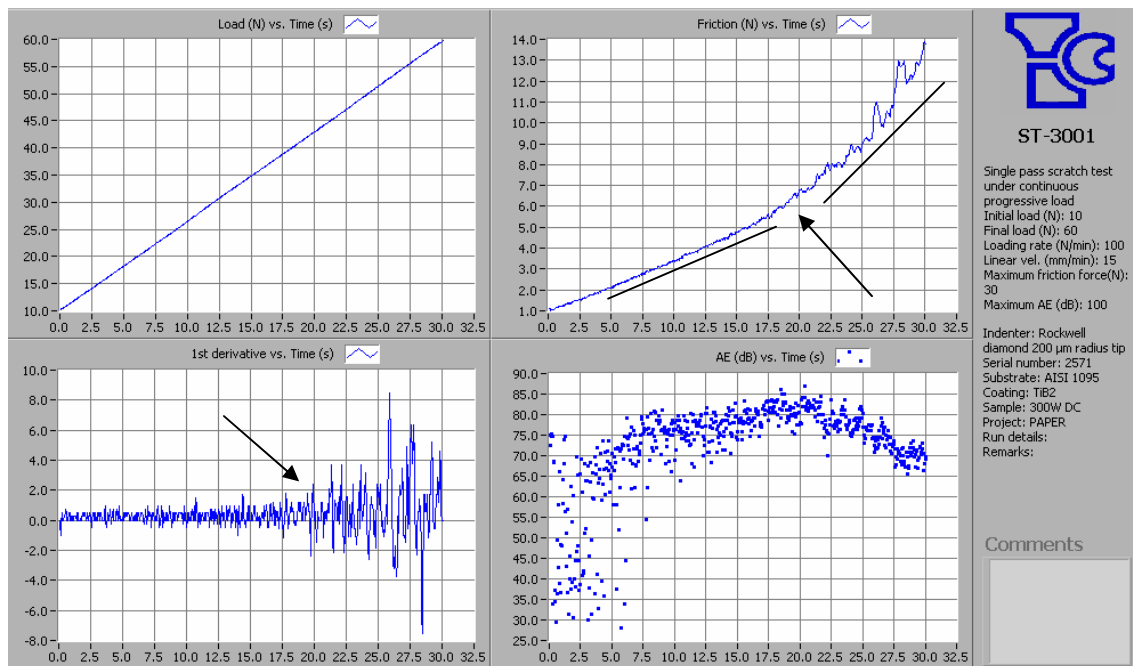
**Figure 68 - DC 200W, single pass scratch test with increasing load from 10N to 60N**

For this sample, Figure 69, the failure mode is a mix between recovery spallation and tensile cracking and is due to the difference in elastic recovery of the coating and substrate. Such recovery tracks are found along the scratch scar with signs of spallation (red circle) and tensile cracking (blue circle).



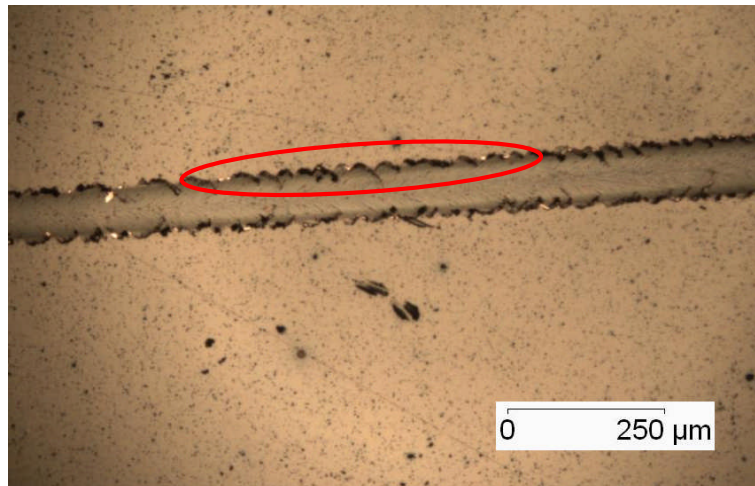
**Figure 69 - DC 200W scratch testing with increasing load with signs of recovery spallation (red circle) and tensile cracking (blue circle)**

Figure 70 shows the adhesion testing for the DC300W coating. From the friction force the change in slope of the curve, and the clear variation in the derivative of the friction curve, reveals that the critical load is around 42N.



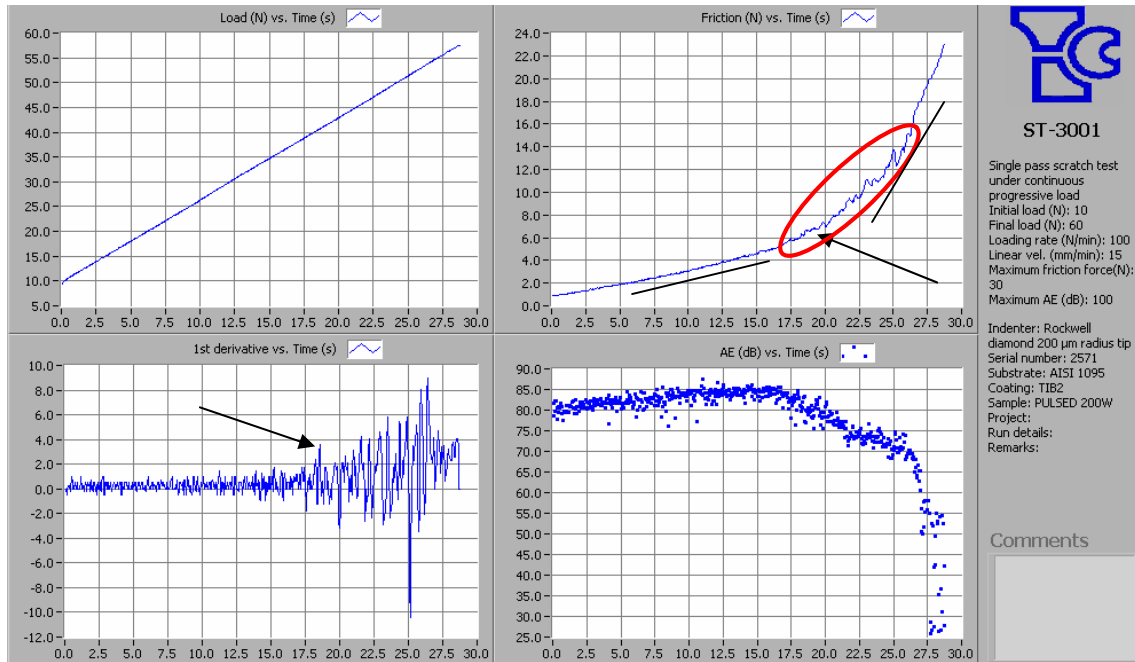
**Figure 70 - DC 300W, single pass scratch test with increasing load from 10N to 60N, the change in slope from the friction curve shows the critical load,  $\approx$  42N**

For this coating, Figure 71 the failure observed is recovery spallation, chipping can be observed along the scratch scar, which is not related to any delamination initiated ahead of the indenter.



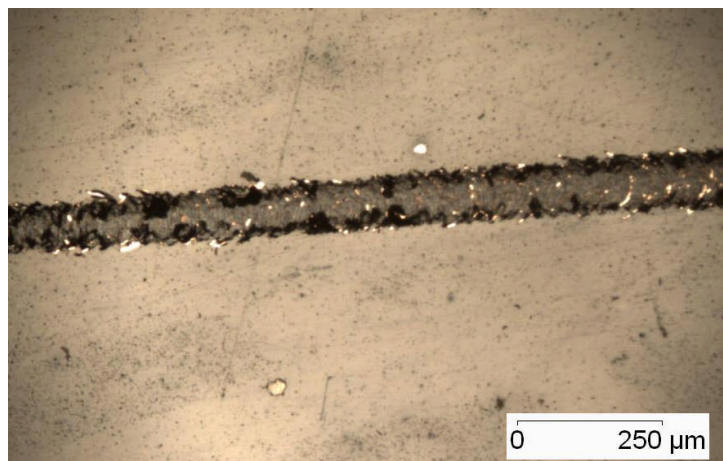
**Figure 71 - DC 300W scratch testing with increasing load, with signs of recovery spallation without any delamination**

Figure 72 shows the adhesion testing for the Pulsed-DC 200W coating. Again a change in slope of the friction curve is observed, this change in slope shows that a critical load is reached, around 41N (the onset of increased variability in the first derivative curve). Also note that the AE emission drops severely when the coating becomes detached from the substrate as is highlighted in the Figure 72.



**Figure 72 – Pulsed-DC 200W, single pass scratch test with increasing load from 10N to 60N, in the charts are highlighted the points relevant to the critical load  $\approx 41\text{N}$ .**

Figure 73, a micrograph of the failure track for the Pulsed-DC 200W coating, is similar to that seen for the DC 200W, Figure 69. The failure mode is a mix between recovery spallation and tensile cracking. Also, to note is the cracking visible inside the scratch scar. This occurs more frequently than for the one produced by DC sputtering, Figure 69.



**Figure 73 – Pulsed-DC 200W scratch testing with increasing load, with signs of recovery spallation and tensile cracking**

Figure 74 shows the adhesion testing for the Pulsed-DC 300W coating. In the figure it is possible to see that the first derivative of friction has an increasing

burst during the test. This indicates the coating can take some damage, but without failing catastrophically. This failure occurs at around 35N. The AE emission in this case reveals a brittle failure because the amount of scatter in the Figure 74.

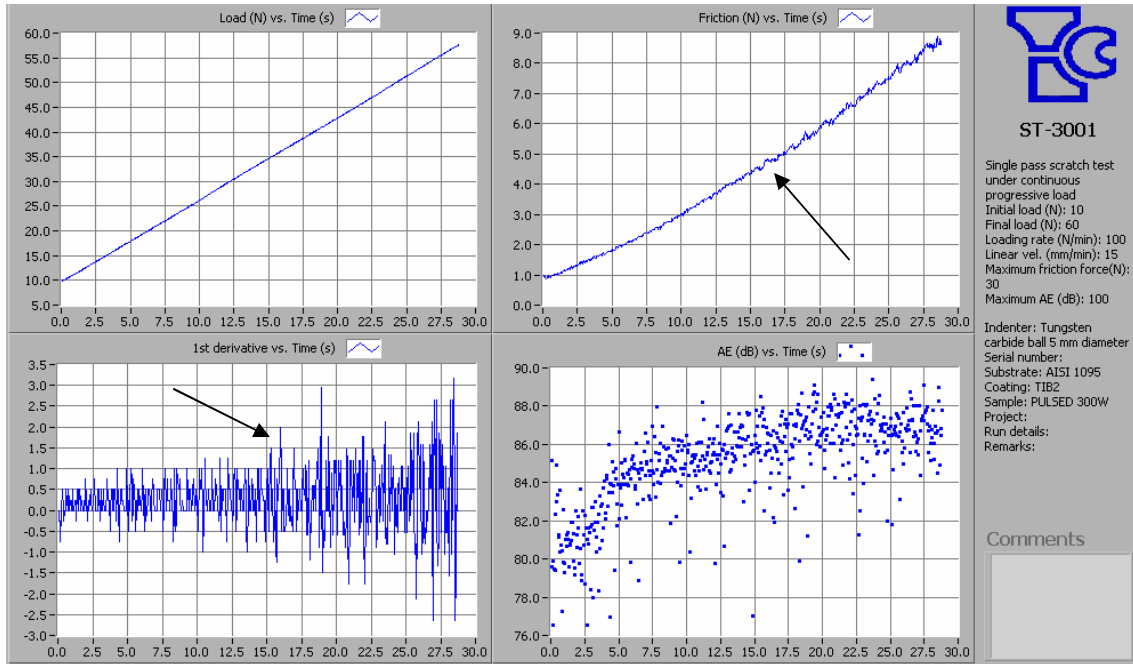


**Figure 74 – Pulsed-DC- 300W, single pass scratch test with increasing load from 10N to 60N, in the chart are visible the first failure points.**

From the micrograph of this scratch, Figure 75, it is possible to see the transition between recovery spallation, and gross spallation which is a very common result if residual stress in the coating is high [201, 202]. This occurs due to cracks which are formed at the coating interface and can propagate to the both side of the scratch scar. These cracks can be initiated at a defect in the coating and propagate thereafter.

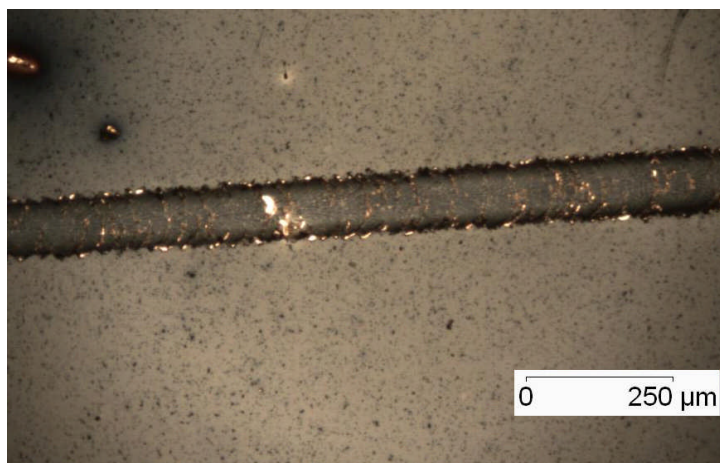


Figure 75 – Pulsed-DC 300W scratch testing with increasing load, with signs of recovery spallation and gross spallation

### 8.1.3.2 Wear testing

From the wear experiments, the friction coefficient vs. number of cycles showed a steady increase with increasing number of cycles. The region of the curve where the friction coefficient reaches a steady state value, allows a determination of the coefficient of friction for a WC ball rubbing against the coating during the test. The values obtained in this section are summarised in Table 9.

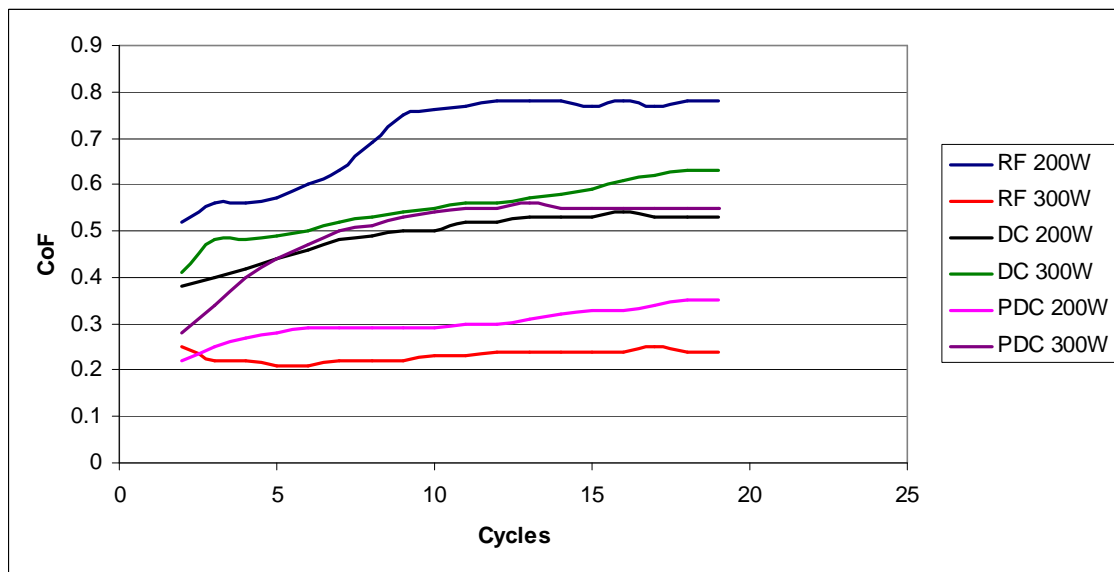
Coating	Hardness (GPa)	$H^3/E^2$ (average)	Critical Load (N)	CoF (average)	Wear Scar Volume (mm <sup>3</sup> )	Ra (nm)
RF 200W	16	0.04	30 ± 1	0.70	0.089072	2.1
RF 300W	15	0.07	30 ± 2	0.23	0.028047	4.5
DC 200W	18.5	0.04	17 ± 2	0.49	0.007627	2.6
DC 300W	12.6	0.02	42 ± 1	0.54	0.019781	5.1
PDC 200W	15	0.06	41 ± 1	0.30	0.001329	4.0
PDC 300W	21	0.1	35 ± 1.5	0.51	0.004636	6.7

Table 9 - Calculated and measured values of the properties of the TiB<sub>2</sub> films fabricated and tested in this section

The RF sputtered film at 300W produced the lowest CoF value of 0.23, as seen in Table 9. The RF sputtered film at 200W presents the higher value of CoF, 0.70, and an associated high wear volume, as visible in Figure 76 and Figure

77, respectively. Both conditions present a similar hardness value, 16N, 15N respectively. The critical loads were very similar with a value of 30N.

The average CoF value for the DC-magnetron sputtered films is calculated to be 0.49 for the 200W condition and 0.54 for the 300 W conditions. Although presenting higher values of hardness for the coating 200W, 18.5GPa, as the process power increases to 300W, the hardness decreases, 12.6GPa, but the adhesion is significantly improved, as measured by a critical load of 42N.



**Figure 76 - Bidirectional Wear testing of 18 cycles at 10N load**

The pulse-DC magnetron sputtered film deposited at 200 W produced a CoF value of 0.3, which increased to 0.51 as the power increased to 300 W, both of the coatings (200W and 300W) showed good adhesion presenting values of 41N and 35N, respectively. A trend emerges between CoF and  $H^3/E^2$ ; where the films are able to deform without fracture a lower CoF is observed, namely pulse DC-deposited films, and those that deform easily, namely RF 200W-deposited films, have a high value of CoF. This is due to the elasto-plastic deformation that the coatings are able to sustain, during deformation, both during nanoindentation and wear testing.

To determine the material loss due to abrasive wear, the wear volume of the scar was calculated using the length of the scratch scar, the width of the scar and the depth of the scar caused by the WC ball.

The calculated values are also summarised in Table 9. In Figure 77, a graphical representation of the data clearly shows that the RF deposited films have the biggest material volume removal. The DC has an intermediate value of material removed, increasing with the power.

Pulsed-DC magnetron sputtered films had the smallest wear scar volume presenting values very similar as possible to view by Table 9 and Figure 77.

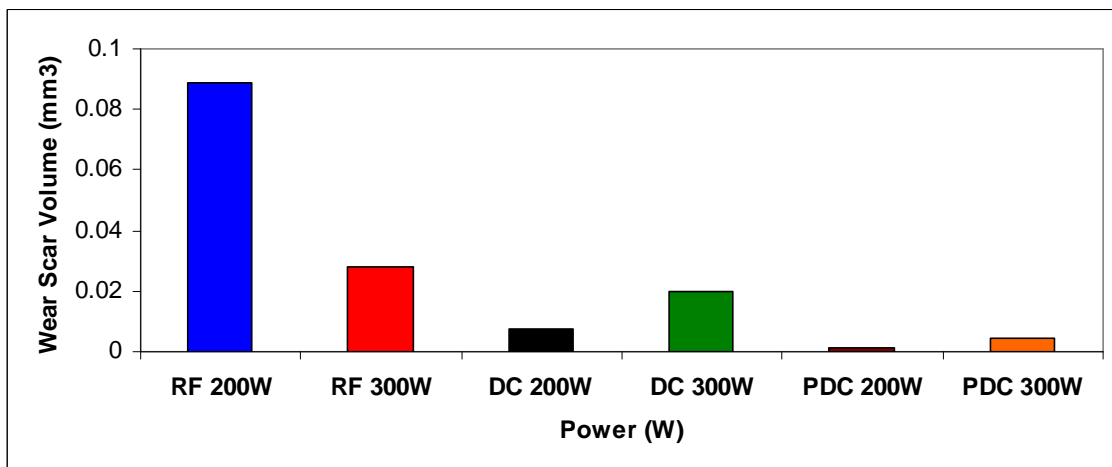


**Figure 77 - The wear volume of the DC, RF and pulsed-DC magnetron films fabricated. From the two different powers investigated, the DC and RF magnetron sputtered  $TiB_2$  films show similar behaviour (except for the 300W RF sputtered), however the pulsed-DC magnetron films have significantly less material loss in overall.**

This result further emphasises the superior qualities and properties of the pulse-DC deposited thin films of  $TiB_2$  when compared with RF or DC-deposited  $TiB_2$ .

From the wear tests, the wear tracks allows several observations to be made, and to categorise according to their behaviour. Figure 78, Figure 79 and Figure 80, show the wear track morphologies of the three different types of coatings, along with remarks made about their behaviour. Figure 78 shows a narrow and shallow track with sharp edges. There is no apparent film cracking or delamination along the track, this is the pulsed-DC film deposited at 200W.

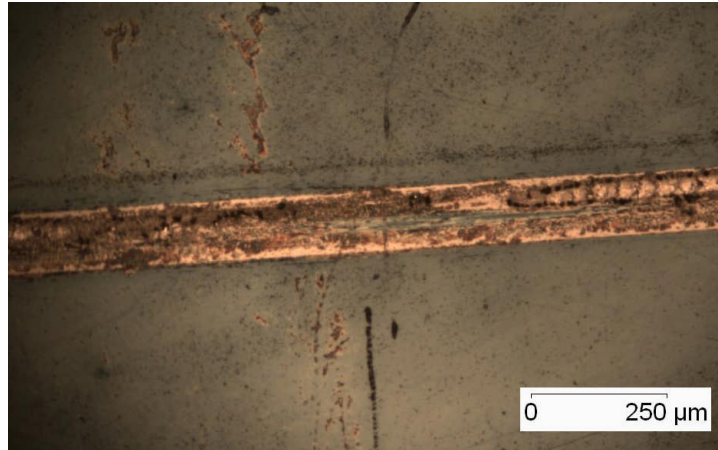


**Figure 78 – Bidirectional wear test on Pulsed DC 200W, good wear behaviour: thin shallow tracks with no film delamination**

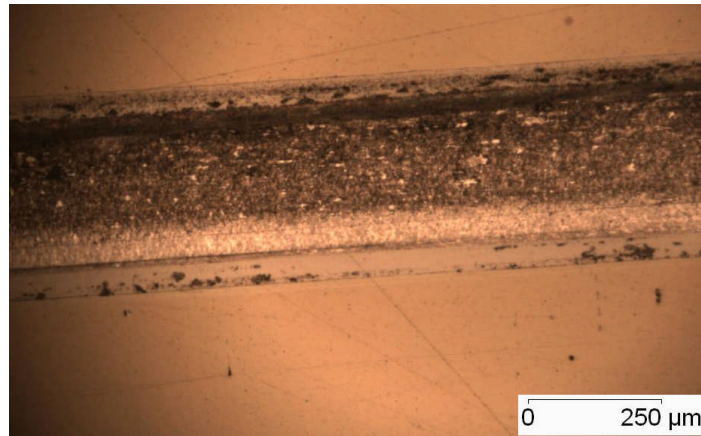
These films, deposited by pulse-DC magnetron sputtering, are also characterised by a small wear scar volume,  $\approx 4.6 \times 10^{-3} - 1.3 \times 10^{-3} \text{ mm}^3$  and a large  $H^3/E^2$  value, 0.12 - 0.175, indicating their good resistance to plastic deformation.

Figure 79, films deposited by DC magnetron sputtering, shows moderate wear behaviour and clear evidence of film cracking along the length of the wear track. The wear track is again narrow; however the wear scar volume is greater than in Figure 78, for the pulsed-DC deposited film.



**Figure 79 - Bidirectional wear test on DC 300W, moderate wear behaviour: thin shallow tracks with no film delamination, however there is evidence of film cracking along the length of the wear track.**

The RF sputtered samples, Figure 80 showed the poorest wear behaviour with a clearly wider wear track. The wear track shows a smeared appearance to the coating, and local coating suggesting poor adhesion. The films in this group are also characterised by a high CoF values and a high wear scar volume.



**Figure 80 - Bidirectional wear test on RF 200W, poor wear behaviour, characterized a large wear track with evidences of delamination at the edge of the wear track**

A summary of the results reveals that the wear behaviour can be separated into three groups; good wear behaviour, moderate wear behaviour and poor wear behaviour. Some correlation can be made with regards to coating performance values obtained from the CoF and wear scar volume. The largest influence on these performance indicator is that this study has observed, has been the deposition method used, namely DC, RF and pulse-DC magnetron sputtering, in producing the  $\text{TiB}_2$  coatings.

#### **8.1.4. Conclusions**

$\text{TiB}_2$  films have been fabricated using RF, DC and pulsed-DC magnetron sputtering. The coatings have been evaluated using nanoindentation, AFM and tribological testing consisting of wear and scratch testing.

From the nanoindentation results, we conclude the following:

- The hardest films are those produced by pulsed-DC magnetron sputtering at 300 W. The softest films are those produced by DC magnetron sputtering, also at 300 W.
- From the results of the reduced modulus, we conclude that the stiffness of the TiB<sub>2</sub> is 200 GPa ± 10%, regardless of the method used to deposit the TiB<sub>2</sub> film.
- The H<sup>3</sup>/E<sup>2</sup> data, calculated from these measured values show that the films produced by pulsed-DC magnetron sputtering have the best damage resilience, allowing a given load to be distributed over the widest area with much of this loading ability recovered elastically.
- From the AFM studies, we can conclude that RF-deposited films produce the smoothest films, while those deposited by pulsed-DC are the roughest with a Ra of 4 nm at 200 W deposition powers.

From the adhesion testing we can conclude:

- The adhesion achieved for all coatings in general is good, the critical loads are around 30 - 42N, with only one coating adhesion value below this range that is the DC200W, which showed first damage at a force of 17N.
- The failure mode reveals that these coatings are brittle, presenting mixed modes between spallation and tensile cracking, the pulsed-DC coatings are the most resilient.

Wear studies have identified and characterised the coatings into three classes:

- (a) Good wear behaviour is attributed to those deposited by pulse-DC magnetron sputtering. Films deposited by this method can be identified as having low wear scar volumes and a large value of H<sup>3</sup>/E<sup>2</sup>. The wear track formed was narrow and shallow with no evidence of coating delamination.
- (b) Moderate wear behaviour was found to be associated with films deposited by continuous DC magnetron sputtering. Films deposited by this method showed film through thickness cracking along the

length of the wear track. CoF values of 0.3 to 0.4 were measured with a medium wear scar volume.

- (c) The group that showed the poorest wear behaviour with evidence of film delamination at the edge of the wear tracks, were those produced by RF magnetron sputtering. The size of the wear track formed was significantly wider than that formed of either the Pulsed-DC or DC deposited films. These RF sputtered coatings, showing poor behaviour, can be identified as having large CoF values, large wear scar volumes, intermediate hardness's and low  $H^3/E^2$  values, consistent with the extensive plastic deformation to the substrate under the wear track.

## 8.2. TiB<sub>2</sub>/C Multilayer Films

### 8.2.1. Introduction

As we discussed in section 2, multi-layers coatings are formed by the deposition of alternating layers of two or more materials. The thickness of each individual layer can vary from a few nanometers thick to several microns.

Accurate thickness control has been used by several authors as a method to limit crack propagations in ceramic coatings [9, 109], the interface between the layers acts to stop or deflect the crack.

In this section amorphous carbon in its graphitic phase, with sp<sup>2</sup> bonding and sp<sup>3</sup> bonding, has been employed to act as an interfacial material to prevent crack propagation in the ceramic (TiB<sub>2</sub>) part of the coating. Tee et al [100] have used carbon in Al reinforced TiB<sub>2</sub> ceramic composite to improve the mechanical properties and tensile strength of this matrix. Gilmore et al [113-115] studied the effect of carbon films on TiB<sub>2</sub> ceramic coatings to be used in cutting tool applications.

In this section a multilayer stack has been produced containing 50 layers of TiB<sub>2</sub>/C, 25 layers of TiB<sub>2</sub> and carbon, respectively. The coatings had a total thickness of 5 μm and the volume fraction of TiB<sub>2</sub> has been varied from 50% to 95%. In section 3, the possible deposition techniques of TiB<sub>2</sub>-based coatings were reviewed. In this section the sputtering technique used was DC magnetron sputtering for the manufacture of TiB<sub>2</sub> and carbon layers. As reviewed in section 6.2. TiB<sub>2</sub> films manufactured using PVD show potential to be applied in tribological applications because of the low deposition temperatures involved. The effect of TiB<sub>2</sub> ceramic volume fraction on coating properties was characterized using nano-indentation to quantify the hardness and reduced modulus. FIB milling was used to characterize the multi-layer coatings structure. The carbon content and bonding was characterized by Raman spectroscopy. Tribological testing was conducted to evaluate the critical load and friction coefficient.

## 8.2.2. Results and discussion

### 8.2.2.1 Carbon characterisation – Raman

Raman spectroscopy was conducted to provide information about the quality of the  $sp^2$  bonds of the amorphous carbon films, and literature [222] has reported a highly orientated pyrolytic graphite (HOPG), which has a peak at  $1580\text{ cm}^{-1}$ . This peak refers to the graphite (G) and has a full width half maximum (FWHM) of  $16.3\text{ cm}^{-1}$ . It originates from the  $E_{2g}$  symmetry graphite chains and clusters. The amorphous carbon also has an additional peak referred as D peak, around  $1355\text{ cm}^{-1}$ , which originates from the  $A_{1g}$  mode of the crystal [223]. Natural diamond possesses peak at  $1332\text{ cm}^{-1}$  with an FWHM of  $2.6\text{ cm}^{-1}$  [223].

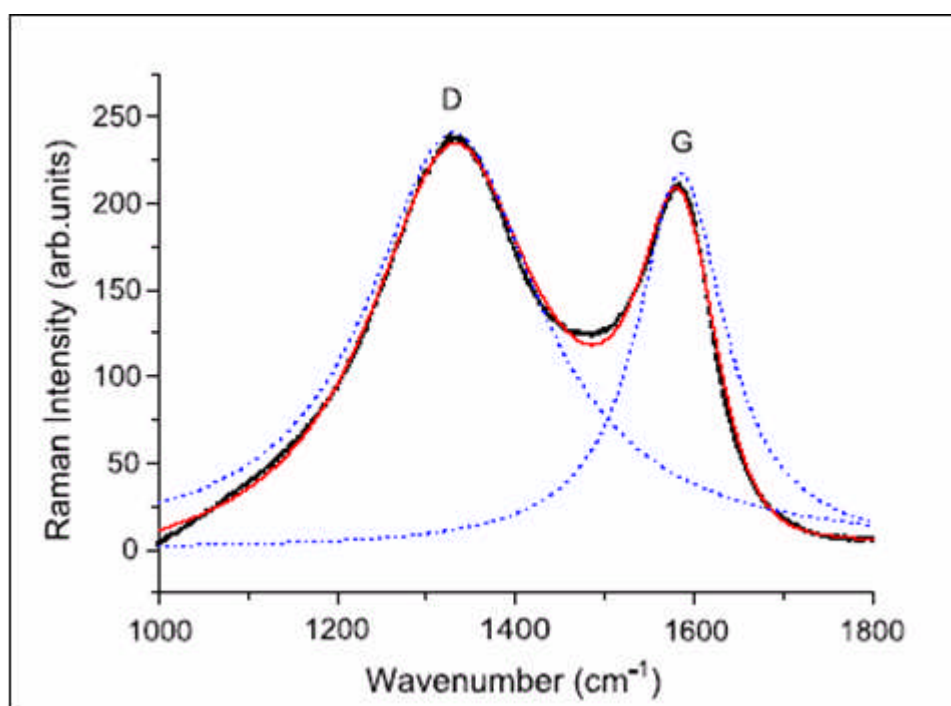


Figure 81 - Raman spectra from a carbon film fabricated as part of this study.

The Raman spectroscopy conducted on the graphitic films show two peaks, the internal area is calculated from a Lorentzian fit, and describes the ratio between the  $sp^2$  and  $sp^3$  bonding in the films. Figure 81 presents the Raman spectra of

carbon films fabricated as part of this study, illustrating the D and G Raman peaks.

Robertson [224] proposed that amorphous DLC films are mainly composed of  $sp^3$  bonding, but as the graphite contents increases the  $sp^2$  bonding also increases. Also, the ratio of the D and G peaks ( $I_D/I_G$ ) is an important parameter in the characterization of DLC films. By calculating the area of the plotted curves, the  $I_D/I_G$  ratio can be calculated providing essential information about the type of film deposited. A low  $I_D/I_G$  ratio is related to graphite-like layers, while a high ratio leads to DLC behaviour [224]. The carbon films fabricated for this section presented a ratio of 1.08 which indicated that the  $sp^3$  bonding content is below 50%.

In this study Figure 81 shows the Raman spectra of the films manufactured for this study. The films show a D peak around  $1330\text{ cm}^{-1}$  and a G peak at  $1590\text{ cm}^{-1}$ . When calculating the  $I_D/I_G$  ratio, two additional peaks at  $1170$  and  $1500\text{ cm}^{-1}$  have to be used in order to prevent errors in calculations.

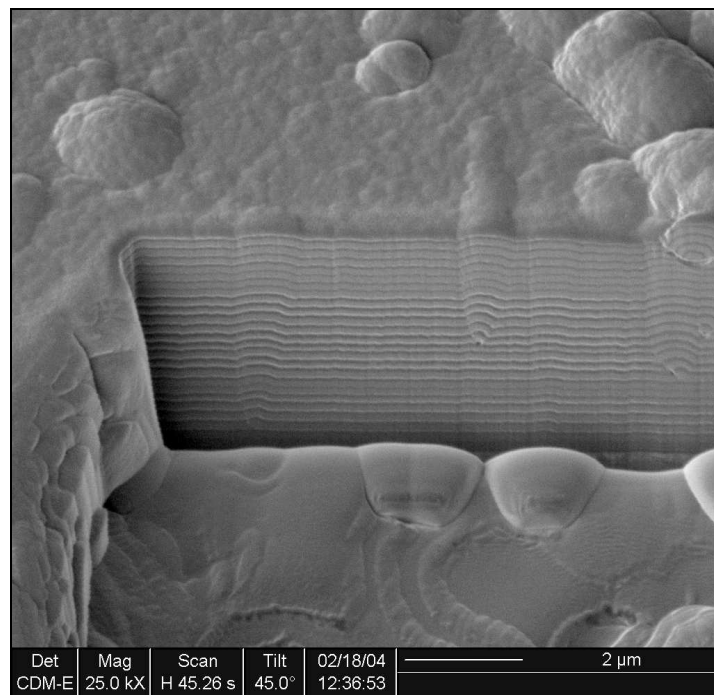


**Figure 82 – FIB micrograph TiB<sub>2</sub>/C multilayer stack**

These results agree with literature, Silva et al [135] and Ferrari [215] observed that two simple two-symmetric-line fits are not always in agreement to the experimental data, they have agreed that multi-peaks fits are found to provide a much better fit to the data. The same authors, Silva and Ferrari [135, 214] have also found Raman peaks in the range of 1100–1220  $\text{cm}^{-1}$  which are connected with hexagonal diamond [135, 214], while the peak present at around 1500  $\text{cm}^{-1}$  is connected to the stretching of carbon atoms in single rings [127].

In Figure 82 it is possible to observe a FIB micrograph of a multilayer stack, with some defects in the film caused by the coater configuration. These defects have started part way through film growth, probably associated with nano-metre size particles deposited from chamber walls during film growth.

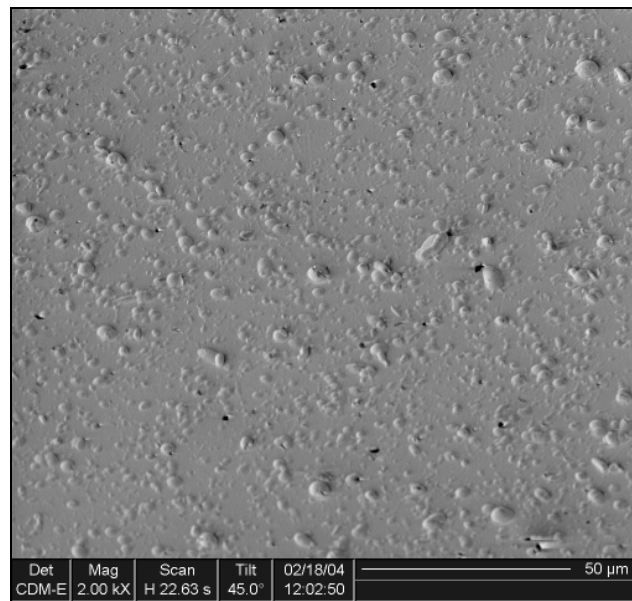


**Figure 83 – Surface topography of TiB<sub>2</sub>/C**

In Figure 83 the surface topography shows defects that occurred during deposition. These defects are caused by the high internal stress during the carbon layer deposition which has adhesive loss and becomes detached from the surface and the chamber walls due to the vertical assembly of the magnetrons (sputtering down). In this case the particle is not removed but can fall onto the substrate surface. These particles cause the growth defects in the multilayered film as we can see in Figure 82 and Figure 84.

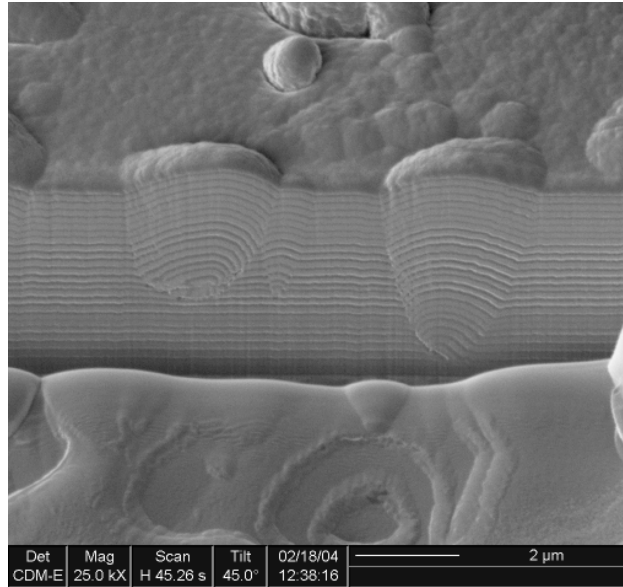
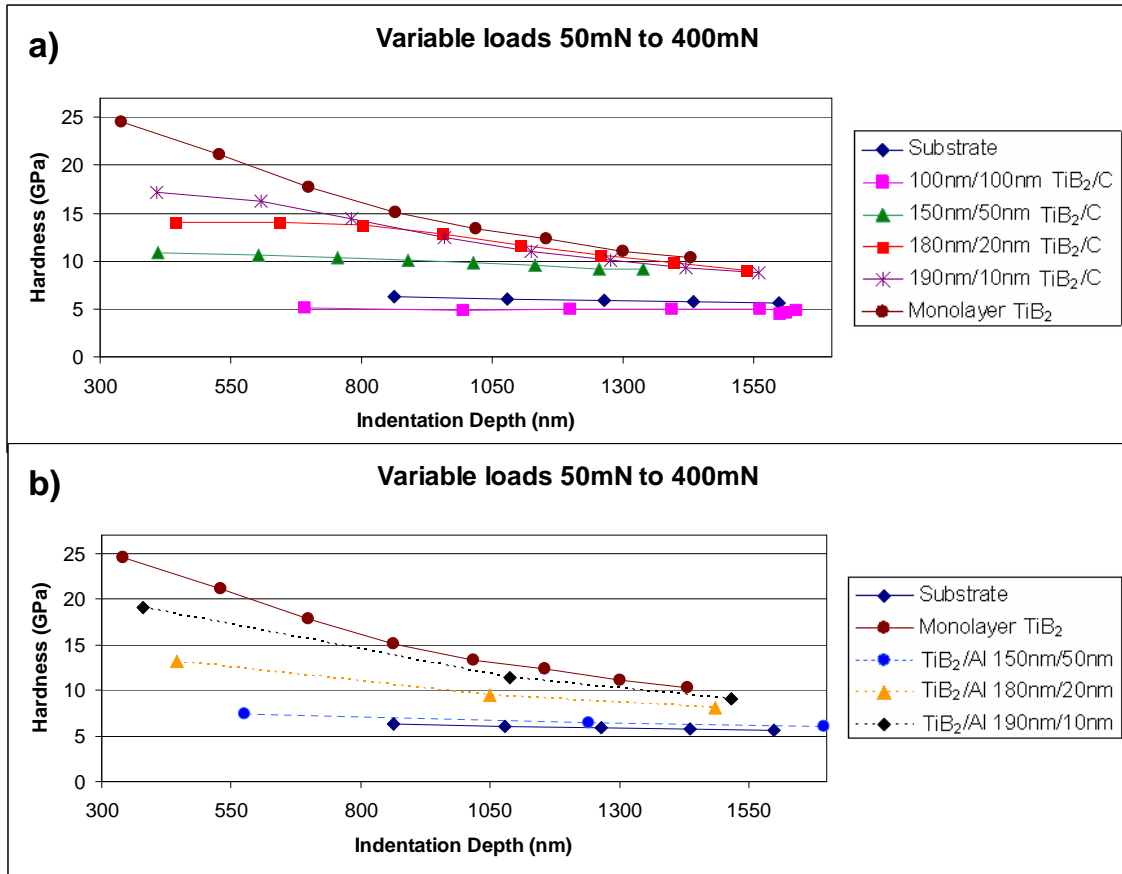


Figure 84 - FIB micrograph TiB<sub>2</sub>/C multilayer stack showing some carrot like defects

### 8.2.2.2 Nanoindentation

The nano-indentation performed was used to assess the hardness and reduced modulus. The loads used ranged from 50 to 400mN and are function of indent depth for all film compositions; the data is shown in Figure 85 and Figure 86, respectively.

For this section, the hardness values range from 5GPa in the 50% containing sample (100/100 nm) to 17GPa for the coating containing 95% ceramic (190/10 nm). The increase in layer thickness of the ceramic, from 50% to 95% has an effect of improving the hardness of the TiB<sub>2</sub>/C multilayers. During nanoindentation the TiB<sub>2</sub>/C layers become deformed and the hardness values result from the penetration into the layers. A pure TiB<sub>2</sub> monolayer showed a value hardness of 24 GPa.



**Figure 85 – The variation of the hardness as a function of indentation depth, a) TiB<sub>2</sub>/C multilayers, b) TiB<sub>2</sub>/Al multilayers.**

As the indentation test progresses the hardness and reduced modulus values for all the ceramic compositions converge to a single value, which are the mechanical properties of the AISI 1095 substrate. In Figure 85 b) and Figure 86 b) the data is compared to the studies from Silva Cruz [12] who fabricated a multilayer of TiB<sub>2</sub>/Al with a periodicity similar to this study and whose work was discussed in section 6.2. Equally, for similar layer periodicities, especially at high volume fractions of TiB<sub>2</sub> the hardness of TiB<sub>2</sub>/C and TiB<sub>2</sub>/Al are similar (compare the data for 190nm/10nm TiB<sub>2</sub>/C and 190nm/10nm TiB<sub>2</sub>/Al). At the other end of the spectrum, the 150nm/50nm multilayers, the TiB<sub>2</sub>/C films offer a 50% improvement in hardness over TiB<sub>2</sub>/Al reported by Silva Cruz [12].

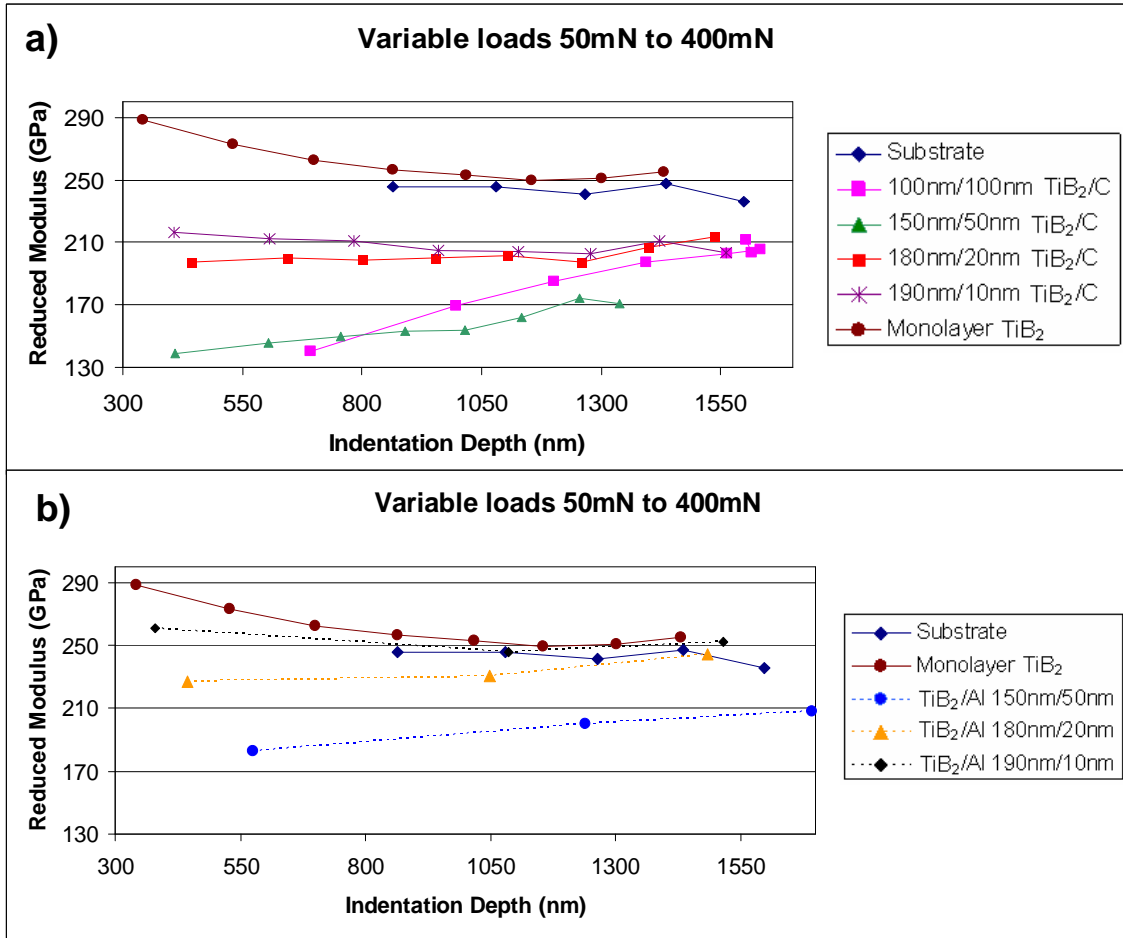


**Figure 86 - The variation in Reduced Modulus as a function of indent depth, a) TiB<sub>2</sub>/C multilayers, b)TiB<sub>2</sub>/Al multilayers..**

For the reduced modulus, the values of the TiB<sub>2</sub>/C films are always lower than the equivalent TiB<sub>2</sub>/Al multilayer. In Figure 86 the 50% ceramic volume fraction, the reduced modulus increases from 130 to 210GPa as the indentation depth also increases. For the high ceramic content 95% ceramic the reduced modulus has a constant value of around 210GPa. This is consistent with the 95% TiB<sub>2</sub> 5%C multilayer being a mix of TiB<sub>2</sub> and Ti(B,C)<sub>2</sub> both of which would be expected to have similar reduced modulus.

In Figure 87 the variation of the hardness values with the fraction volume of carbon is shown. The hardness values decrease as the fraction of carbon is increasing. Gilmore et al [113-115] have reported similar observations where the mechanical properties of a similar multilayer stack decreased from 40GPa for a 100nm layer thickness to 20 GPa for a 10nm TiB<sub>2</sub> layer thickness.

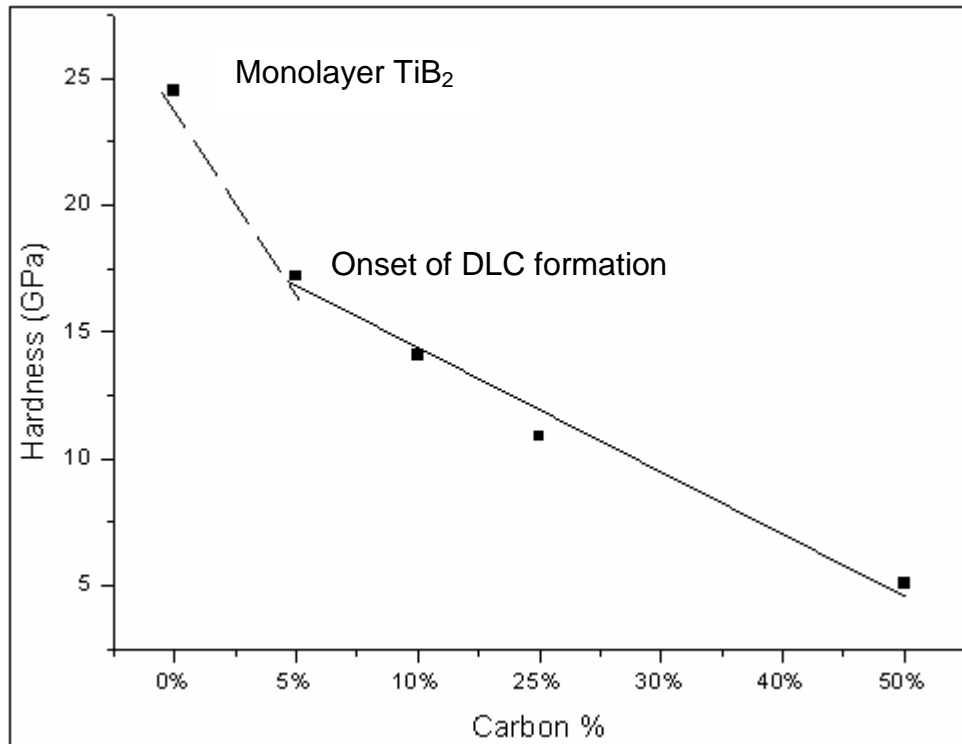


**Figure 87 - The variation of hardness with % of carbon in coating.**

Holleck et al [72] reports that several factors are responsible for these hardness variations; the number of interfaces, the total coating thickness and substrate directly influence the mechanical properties of the multilayer coatings.

Gilmore [113-115] reported that the carbon layers bonds with the  $TiB_2$  layer and form  $Ti(B,C)_2$ , and only after the saturation of the  $Ti(B,C)_2$  occurs, the DLC starts forming. Due to the saturation the  $TiB_2$  hard phase is reduced and the soft lubricating phase is promoted. Gilmore et al [113-115] reported a friction coefficient of around 0.2.

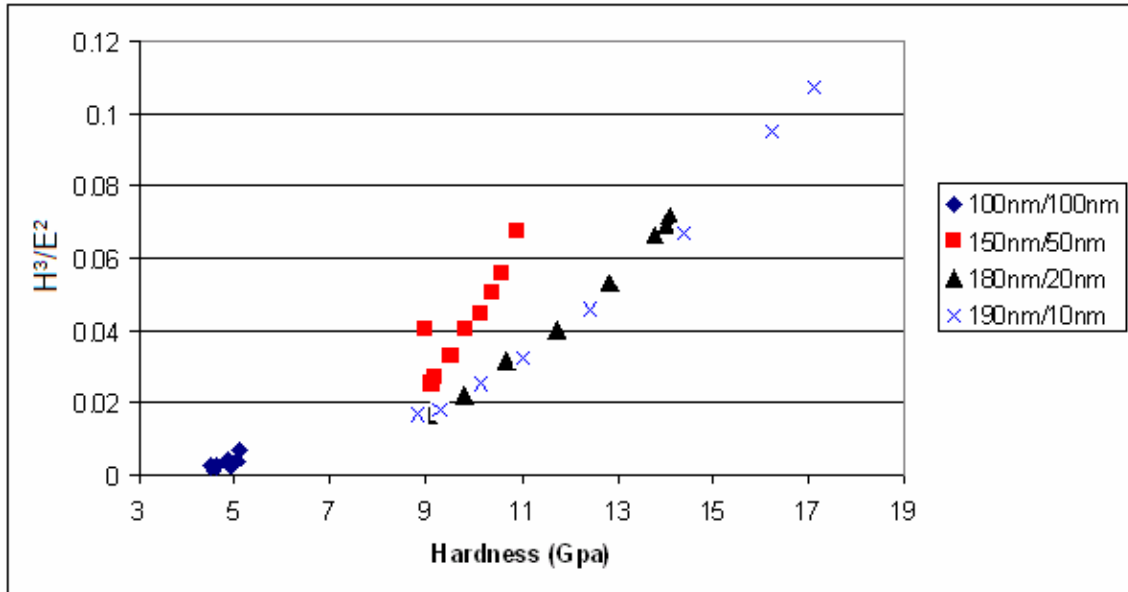
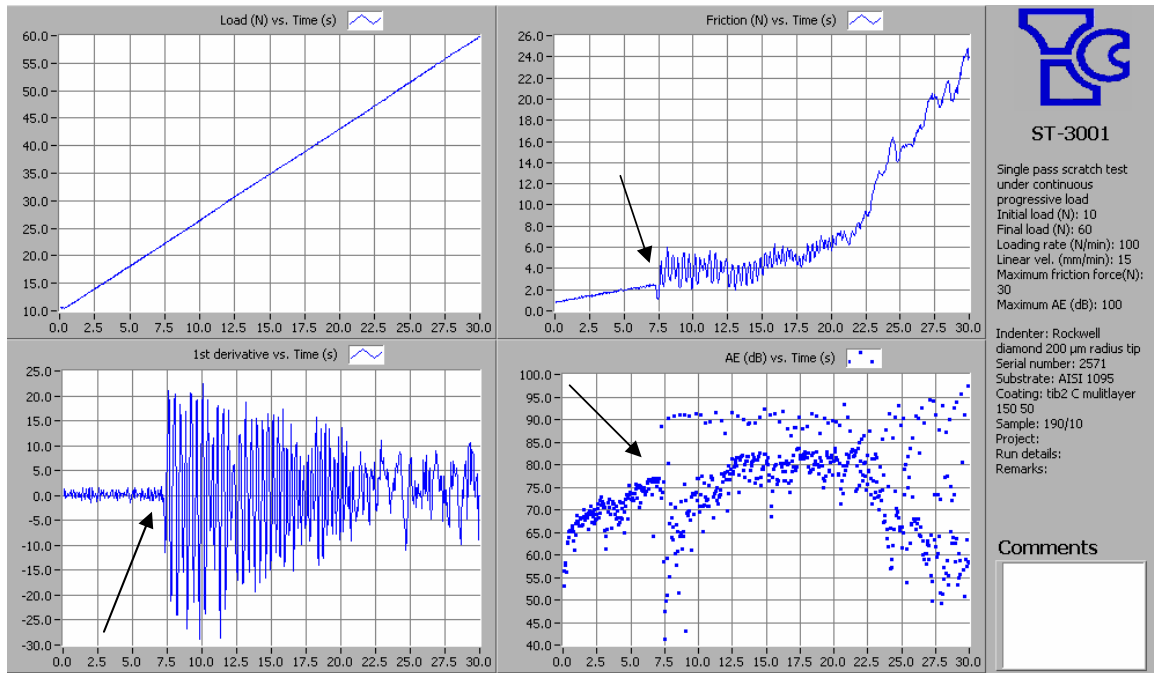


Figure 88 – Variation of  $H^3/E^2$  versus hardness for all the  $TiB_2/C$

In Figure 88 the plot  $H^3/E^2$  versus hardness shows a trend - as the ceramic volume fraction is increased there is an increased spread of the data. A higher  $H^3/E^2$  ratio reveals a higher resistance to deformation. The  $H^3/E^2$  ratio is connected to the yield strength of the material. When the  $H^3/E^2$  ratio increases, this is expected to lead to an improvement of the elastic recovery of the coating, which clearly is also related to the toughness of the multilayer coating. On this basis the most resilient  $TiB_2/C$  coatings are the 190nm/10nm coating and 180nm/20nm coating.

### 8.2.2.3 Adhesion testing

In Figure 89 it is possible to assess the adhesion performance of the coating containing 75%  $TiB_2$ . From the figure it is visible that a critical loss of adhesion occurs at  $\approx 22.5N$ . The 1<sup>st</sup> derivative of friction and the AE emissions have clear peaks, an indication that the critical load was reached.



**Figure 89 – Single pass scratch test with increasing load from 10N to 60N for the 75% TiB<sub>2</sub> content, in the chart black arrows highlight the critical load point**

In Figure 90 and Figure 91 which show micrographs of the scratch to this coating, is possible to see clear spallation ahead of the indenter. As we have seen before in section 6.1.2 the chipping is associated with the moving indenter.

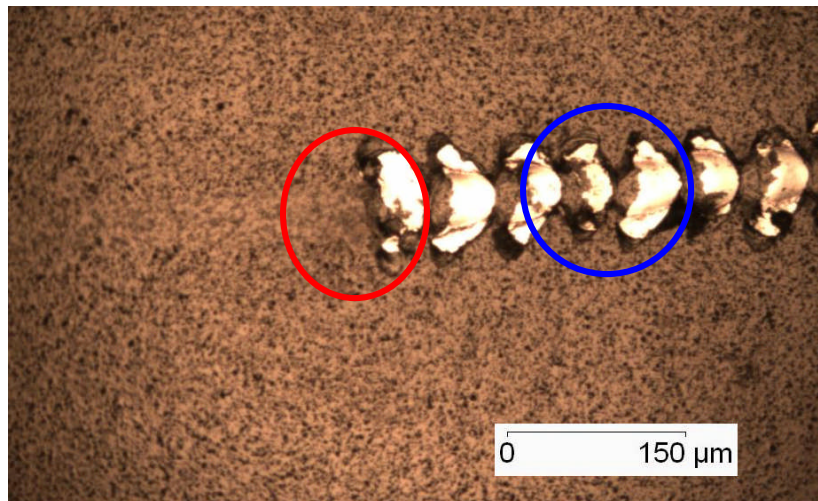


**Figure 90 – Spallation ahead of the indenter highlighted with a red circle the critical load and in blue circle the spallation for 75% TiB<sub>2</sub> content**

The crack propagates to the outside of the scratch scar before the stylus passes. After this, two things can happen: a chip is removed Figure 90 or the coating is pressed into the substrate surface.

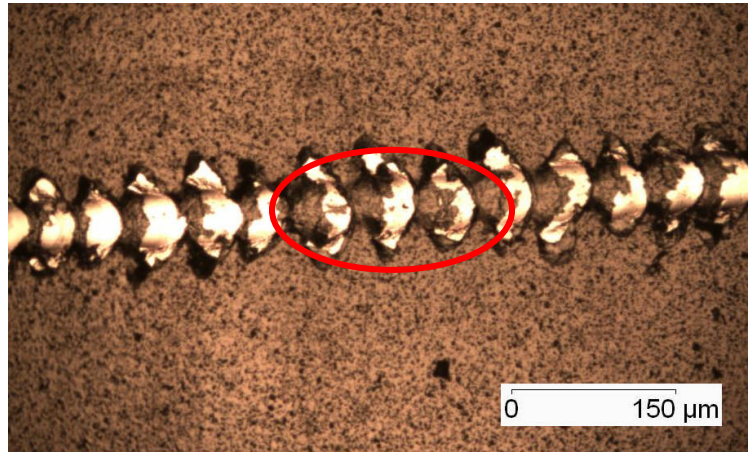


Figure 91 – Spallation ahead of the indenter with coating pressed to the indenter, highlighted in red.

A similar scratch on a 90% volume fraction  $TiB_2/C$  coating is shown in Figure 92. The black arrows highlight the critical point, where failure has occurred. The load required to remove the coating from the substrate was  $\approx 15N$ .

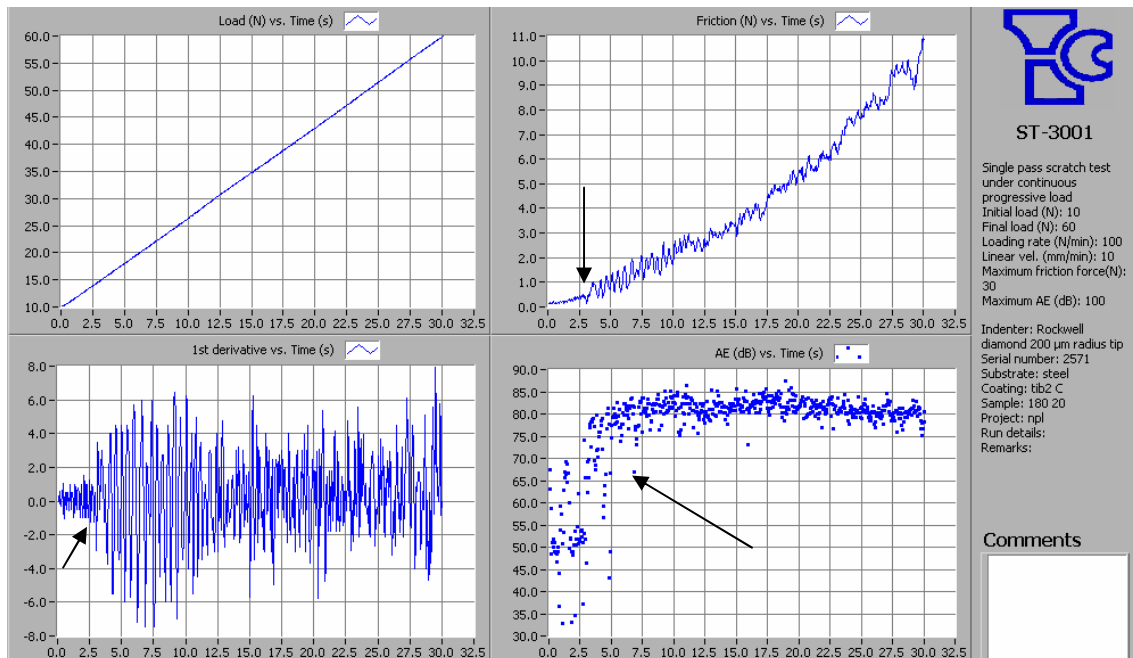
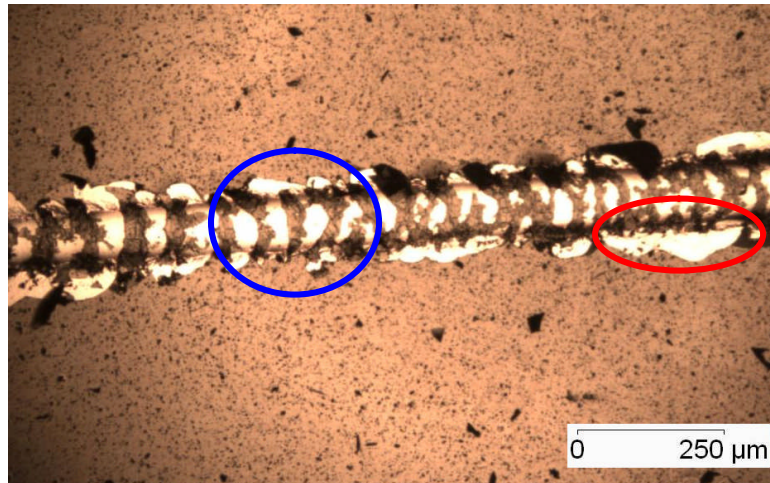


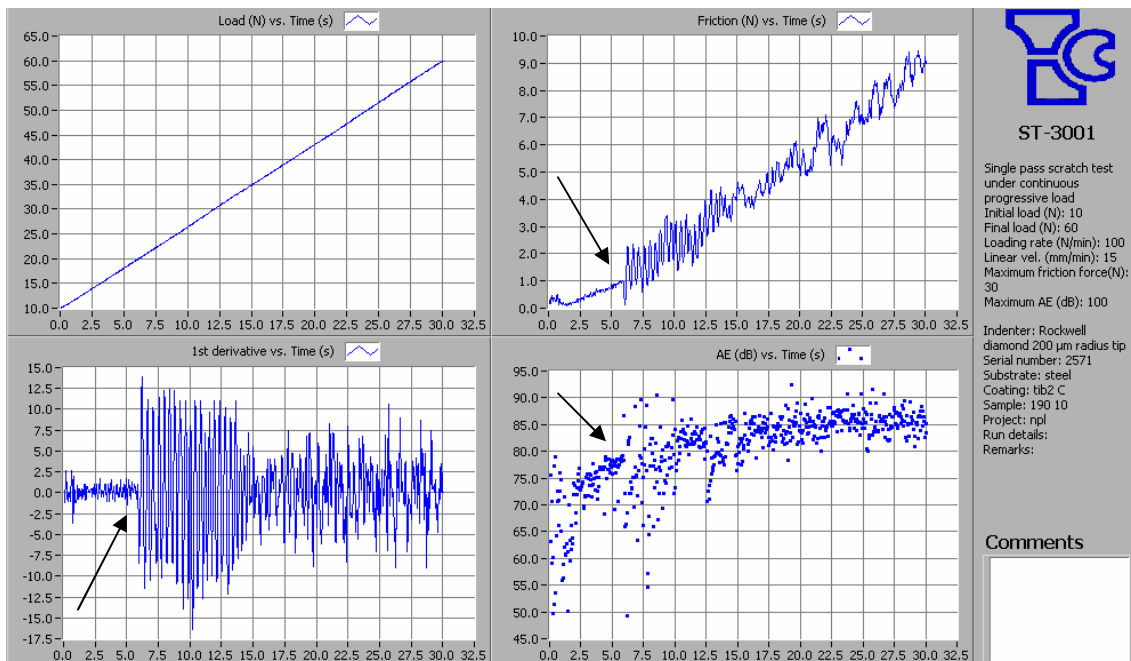
Figure 92 – Single pass scratch test with increasing load from 10N to 60N for the 90%  $TiB_2$  content, in the chart black arrows highlight the critical load point

As can be seen in Figure 93 this results in a mix between two failure modes. Highlighted in blue is the spallation, similar to that has been seen in Figure 89. In red it is possible to see recovery spallation, which is related to the chipping inside the scratch scar.



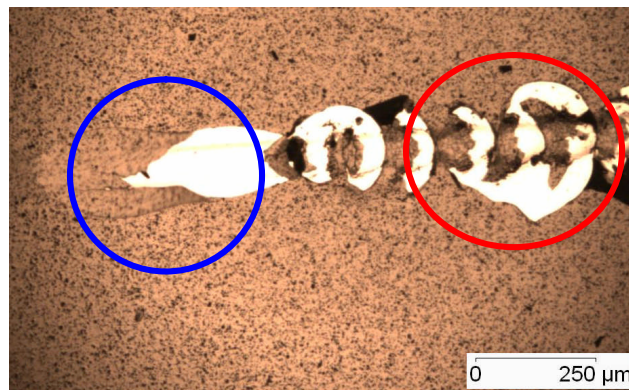
**Figure 93 – Spallation ahead of the indenter with coating pressed to the indenter, highlighted in blue, and recovery spallation marked in red.**

In Figure 94 it is possible to see the adhesion test for the 95% carbon containing sample. From the friction curve, and its derivative it is clear that the critical load was reached at approximately 20N.



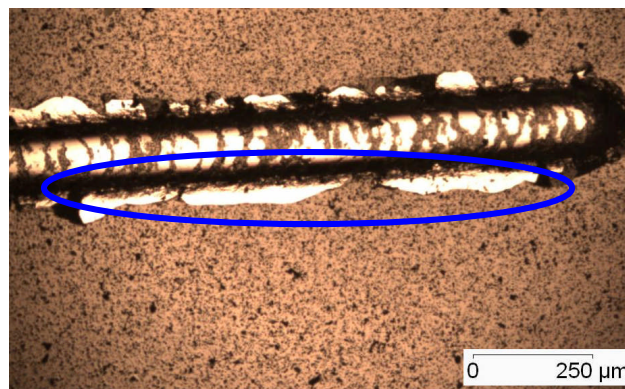
**Figure 94 – Single pass scratch test with increasing load from 10N to 60N for the 95% TiB<sub>2</sub> content, in the chart black arrows highlight the critical load point.**

Figure 95 and Figure 96 show the evidence for spallation and recovery spallation at a 95% volume fraction TiB<sub>2</sub>. This situation occurs due to the high level of residual stress present in the coatings. These types of spallation depend strongly on the degree of coating/substrate adhesion.



**Figure 95 – Critical failure point marked in blue, and recovery spallation marked in red.**

Also, the extrinsic recovery spallation may be caused by the difference in elastic recovery of the coating and substrate. In all the cases, recovery tracks were found with spalling cracks.



**Figure 96 – Recovery spallation marked in blue**

#### **8.2.2.4 Wear testing**

From the bidirectional wear test, the change in friction coefficient (CoF) can be plotted against the number of cycles (Figure 97 and Figure 99). The wear tests

were conducted at two different loads, 10N and 20N. The values obtained in this section are summarised in Table 10.

Coating	Hardness (GPa)	H <sup>3</sup> /E <sup>2</sup> (average)	Critical Load (N)	CoF (average)		Wear Scar Volume (mm <sup>3</sup> )	
				10N	20N	10N	20N
50% TiB <sub>2</sub>	5.1	3.45E <sup>-3</sup>	-----	-----	-----	-----	----
75% TiB <sub>2</sub>	10.9	4.2E <sup>-2</sup>	22.5 ± 1	0.141	0.133	6.3E <sup>-4</sup>	5.7E <sup>-4</sup>
90% TiB <sub>2</sub>	14	4.6E <sup>-2</sup>	15 ± 1	0.16	0.36	5.8E <sup>-4</sup>	1.0E <sup>-2</sup>
95% TiB <sub>2</sub>	17.1	5.0E <sup>-2</sup>	20 ± 1	0.22	0.5	1.2E <sup>-2</sup>	0.19

**Table 10 - Calculated and measured values of the properties of the TiB<sub>2</sub>/C multilayered films fabricated in this section**

In Figure 97 the data reveals two different parts to the wear test. The first part is the beginning of the test until 40-45 cycles where it is possible to observe a run-in period, suggesting polishing wear. From 50 cycles onwards the CoF stabilizes to a constant value, giving the actual friction coefficient.

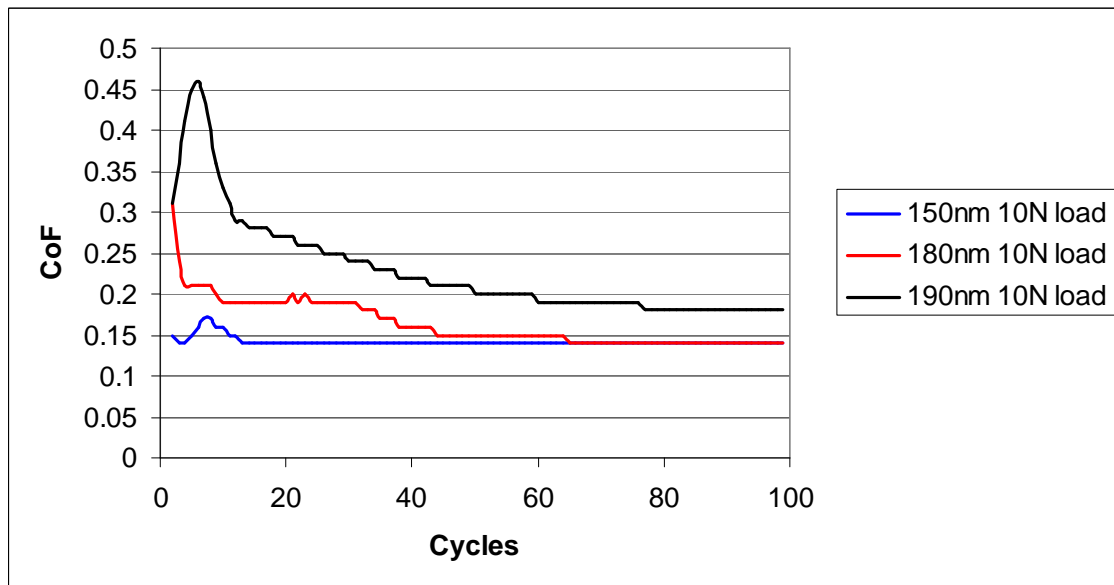


**Figure 97- Bidirectional Wear test at 10N load of the TiB<sub>2</sub>/C multilayers**

In Figure 98 it is possible to observe the wear scar left by the WC ball. It is clear that the scar is quite small in size Figure 98 – a) 46µm; b) 148 µm. there is no sign of the film being damaged, even when the load is increased to 20N

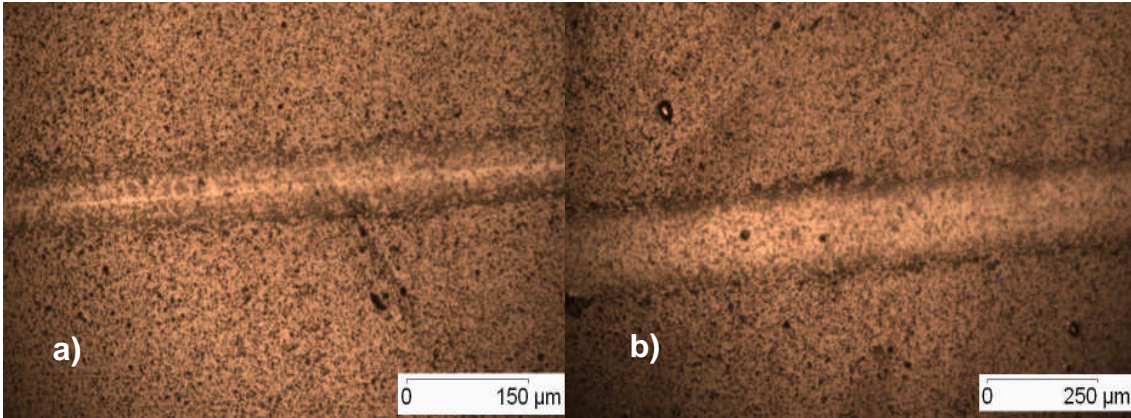


**Figure 98- Wear Scar of the bidirectional wear test, a) 10N load b) 20N load of 75%TiB<sub>2</sub>**

In Figure 99 the plots shows the wear test performed at 20N load. The increase in load reveals that there is a run in period until around 50 cycles and then the friction coefficient stabilizes, revealing that from the beginning of the test, the asperities of the coating are compressed to the surface of the coating, acting as a lubricant. For 90% TiB<sub>2</sub> (180nm TiB<sub>2</sub>) and 95% TiB<sub>2</sub> (190nm TiB<sub>2</sub>) the coating stabilizes at a higher friction coefficient after 50 cycles typically 0.45 to 0.5. This would suggest mechanical damage to these high volume fraction TiB<sub>2</sub> films at higher indentation loads.

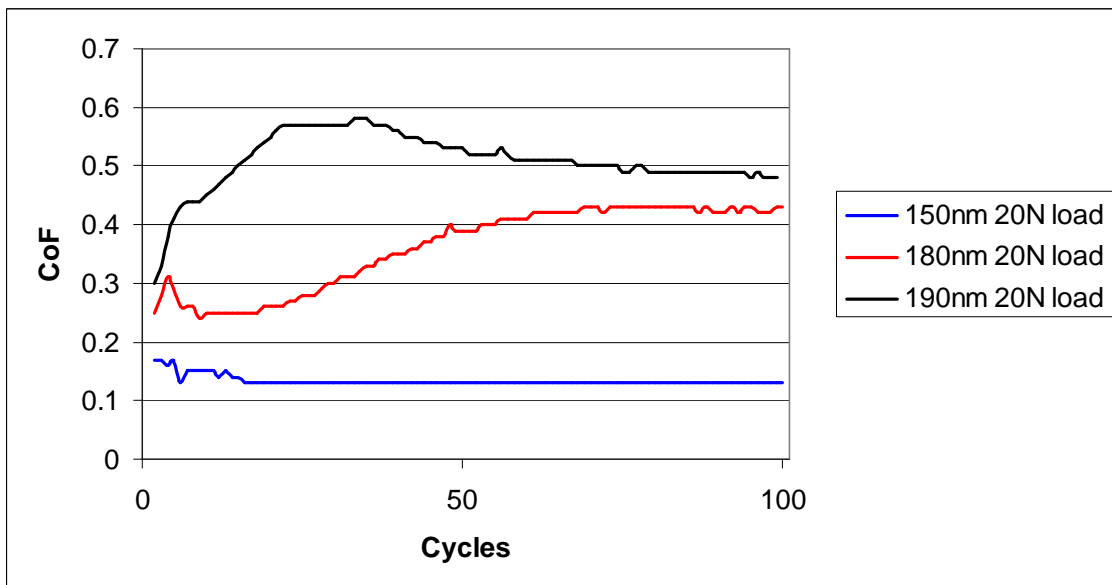


**Figure 99 - Bidirectional Wear test at 20N load of the TiB<sub>2</sub>/C multilayers**

In Figure 100 and Figure 101 it is possible to see the wear scar left by the moving ball at two different loads in samples with 90% and 95% TiB<sub>2</sub>. In Figure 100 a) and Figure 101 a) there is no sign of damage of the coating. The only conclusion that is possible to make is that the films possess sufficient lubricating properties, which can be seen by the low friction coefficient and low wear scar volume, see Figure 102.

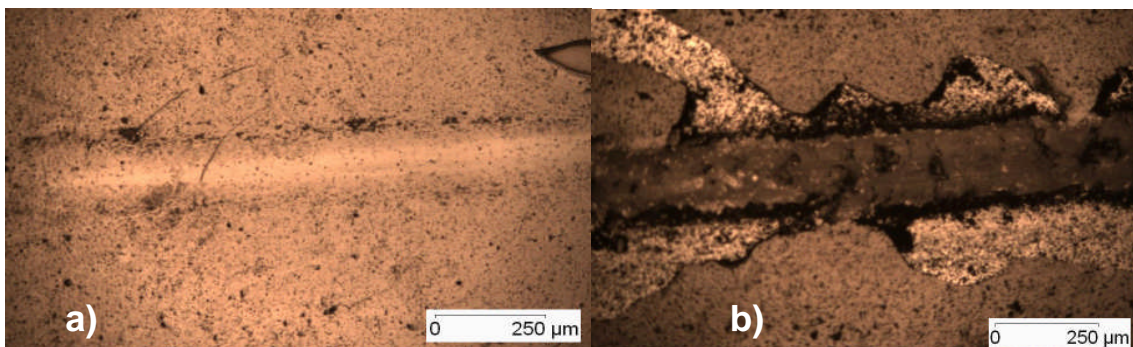


**Figure 100 – Wear Scar of the bidirectional wear test, a) 10N load b) 20N load of 90%TiB<sub>2</sub>**

In Figure 101 b) it is possible to see mechanical damage for the test performed at 20N load. In this case failure has occurred revealing signs of recovery spallation. This type of failure can also be seen in Figure 101 b). This failure mode is related to the amount of compressive stress in the film, which can be explained by increasing content of TiB<sub>2</sub> and the amount of stress that TiB<sub>2</sub> imposes when deposited.

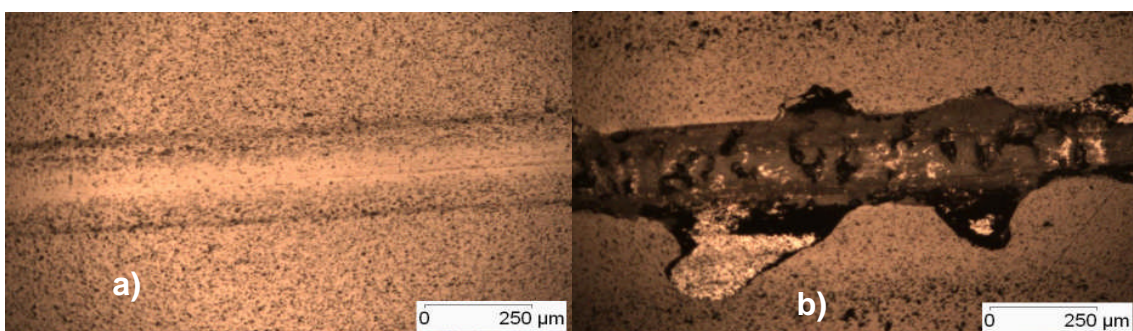


**Figure 101 – Wear Scar of the bidirectional wear test, a) 10N load b) 20N load of 95%TiB<sub>2</sub>**

Figure 102 plots the calculated wear scar volume, which indicated the amount of material removed during the test. It is clear that as the amount of  $TiB_2$  and the test load increases the amount of material removed also increases.

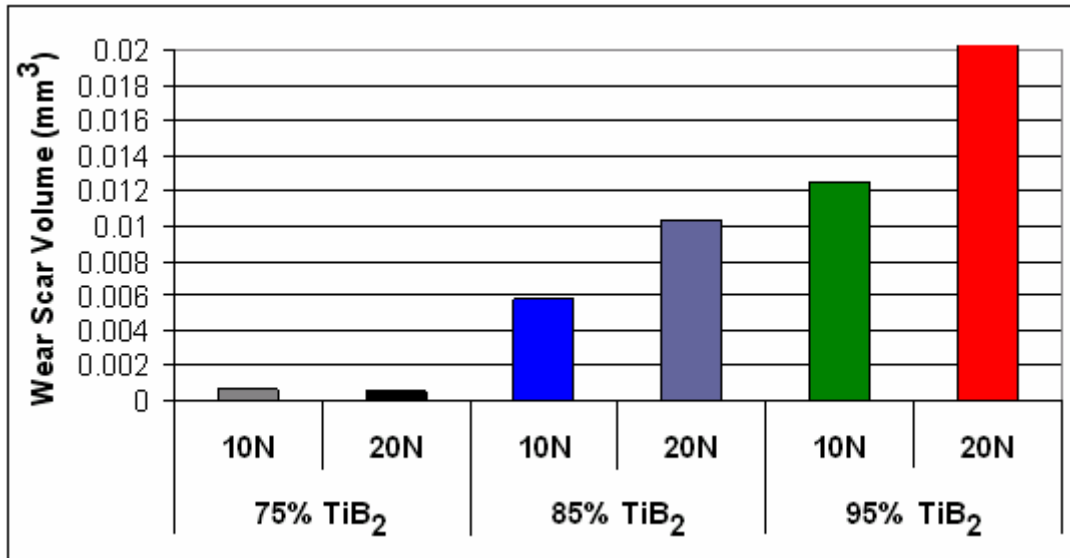


Figure 102 – Wear scar volume for two different loads during the bidirectional wear test

From this data is possible to see that there is an optimum amount of  $TiB_2$  and C which possesses good wear properties, typically 85%  $TiB_2$  at 10N loads, or 75%  $TiB_2$  at 20N loads.

### 8.2.3. Conclusions

- A range of  $TiB_2$  volume fractions ranging from 50% to 95% were fabricated. DC magnetron sputtering was used to deposit 50 layer stacks of  $TiB_2$  and C to a total coating thickness of 5 $\mu$ m.
- From nanoindentation analysis the harnesses presented variations from 5 GPa for the 50%  $TiB_2$  ceramic to 17GPa for the 95%  $TiB_2$  ceramic.
- From the scratch testing with increasing loads from 10N to 60N the adhesion values measured were between 15N for the 90% ceramic to 22.5N for the 75% ceramic.
- The friction coefficient was tested using two different loads, 10N and 20N. For 75% ceramic containing coating the recorded friction coefficient was 0.14 for the 10N load, which increased with the increasing ceramic

content from 75% to 95%. The testing performed at low loads presented no signs of spallation or delamination. The high load testing, 20N presented signs of coating spallation.

- The  $H^3/E^2$  reveals a trend, as the ceramic content increases the data the amount of spread also increases.
- When compared to the work done by Silva Cruz [12] the mechanical properties shows similar effects due to the  $TiB_2$  volume.
- The decrease in hardness is caused by the carbon layers, which is due to the graphitic layers not acting as load bearing but they act as a lubricant in the multilayer matrix.

## 8.3. (TiB<sub>2</sub>/DLC, CH<sub>4</sub>) Reactive atmosphere

### 8.3.1. Introduction

Surface engineered coatings are used to improve service life and overall machine reliability. TiB<sub>2</sub> based coatings have been regarded for many industrial applications as we have seen in section 3. These films present a drawback which prevents the use of TiB<sub>2</sub> coatings in mainstream industry, the brittle nature of bulk TiB<sub>2</sub>. Industrial development has brought the need of development of hard low-friction coatings. The design of coatings that offer the hardness values offered by TiB<sub>2</sub> (>40 GPa) with the low friction coefficients offered by carbon (0.01 – 0.5) are high desirable aspects in the development in the next generation of multilayered thin films.

As seen in section 4, DLC coatings have been considered for several industrial applications. By combining the soft - graphitic phase and hard - diamond like properties of carbon, which can be employed in several applications as we seen in section 4, ranging from cutting tools [129], magnetic recording hardware [130] and protection of polymers [131].

Gases containing hydrogen, such as CH<sub>4</sub> and C<sub>2</sub>H<sub>2</sub>, are used to etch the graphitic phase, sp<sup>2</sup> component, and promoting the sp<sup>3</sup> or diamond-like component, transforming graphite like films into DLC films. As a result, several authors like Wänstrand et al [225], Uglov et al [226] have studied the tribological properties of bulk DLC films, achieving low friction coefficients which can be improved by the addition of a ceramic (Gilmore et al [115]), or a metal (Podgornik et al [227]).

By developing multilayer coatings combining the hard TiB<sub>2</sub> phase with a lubricating phase of carbon, the brittle nature of bulk TiB<sub>2</sub> can be overcome.

This section, further investigates the tribological properties of multilayered coatings of DLC and TiB<sub>2</sub> which were sputtered in a reactive atmosphere of Ar + 7.5% CH<sub>4</sub> from a graphite and a TiB<sub>2</sub> target. The multilayers of TiB<sub>2</sub>/DLC were

fabricated with a variable layer thickness, keeping constant the bilayer thickness of carbon/TiB<sub>2</sub> to a planned thickness of 200nm. The ceramic fractions were varied from 25% to 75%. In this way, a stack of 10 bi-layers of carbon/TiB<sub>2</sub> have been fabricated to a total film thickness of 2µm.

The sputtering method used in this section was pulsed DC. As we have seen in section 1.3.3. Pulsed DC sputtering has been used in the by the coatings industry mainly in reactive processes. As seen in section 1.3.3, Pulsed DC presents several advantages when compared to conventional sputtering techniques (RF and DC sputtering), such as: high process stability, reduced target poisoning, denser films, high deposition rates [25], higher plasma densities and electron temperatures at the substrate surface [228] and providing higher ion fluxes to the growing film [229].

## **8.3.2. Results and Discussion**

### **8.3.2.1 Raman spectroscopy**

In previous section 8.2, carbon was sputtered from a graphite target, in a pure Ar atmosphere. In this section, carbon has been sputtered in a reactive atmosphere of Ar + 7.5% CH<sub>4</sub>. Teii and Jacobsohn [230, 231] have deposited carbon in reactive atmosphere using hydrocarbon gases in order to modify the film quality. Figure 103 shows the Raman spectroscopy conducted for the carbon and TiB<sub>2</sub> multilayers fabricated in this section of this study.

As seen in section 8.2, the DLC presented a D peak at 1340 cm<sup>-1</sup> originating from the A<sub>1g</sub> mode of the crystal, and a G peak at 1588 cm<sup>-1</sup> originating from the E<sub>2g</sub> symmetry graphite chain [214, 215]. The I<sub>D</sub>/I<sub>G</sub> ratio was calculated using a Lorentzian fit to the Raman spectrum which had an I<sub>D</sub>/I<sub>G</sub> ratio of approximately 1.25 indicating the presence of sp<sup>3</sup> hybridised bonding at above 50% level in the coating.

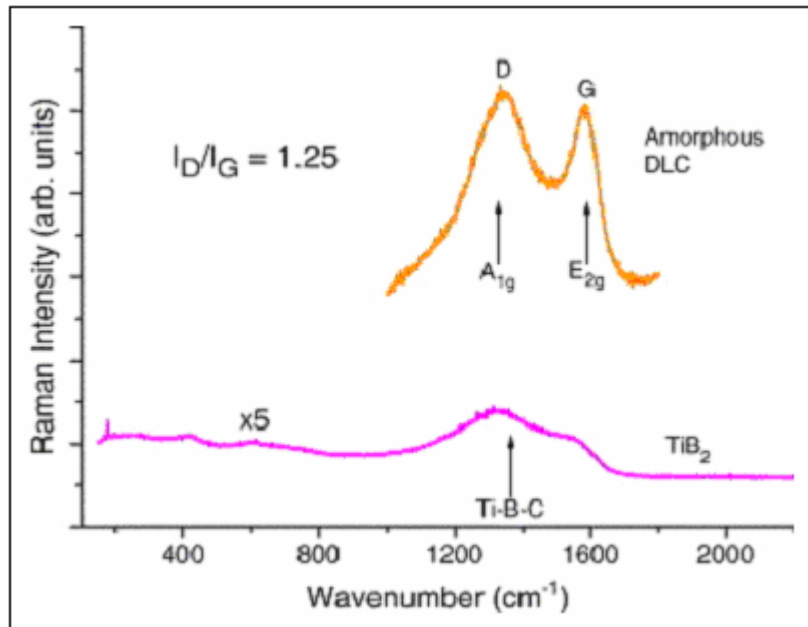


**Figure 103 - Plot showing the Raman spectra of carbon and TiB<sub>2</sub> sputtered in Ar + 7.5 % CH<sub>4</sub>. For carbon, we calculate an I<sub>D</sub>/I<sub>G</sub> ratio of 1.25, an indication of sp<sup>3</sup> bonding above 50 %. For the case of TiB<sub>2</sub>, a weaker Raman peak shows the presence of Ti-B-C, agreeing with the findings of Prakash et al,[232].**

The Raman data detected amorphous carbon, which indicated the formation of a DLC phase. Figure 103 also plots the Raman spectra in a range from 150 to 2000 cm<sup>-1</sup> of the TiB<sub>2</sub> sputtered in a reactive atmosphere of Ar + 7.5 % CH<sub>4</sub>, which forms a Ti-B-C phase.

Knotek et al [233] sputtered ion plated TiB<sub>2</sub> in reactive atmosphere of Ar mixed with high flow of CH<sub>4</sub>, ranging from (2x10<sup>-3</sup> – 2x10<sup>-5</sup> mbar). The authors reported that the TiB<sub>2</sub> phase formed a Ti-B-C phase. The coatings presented a constant Ti: B ratio (Ti:B ~2) with the inclusion of carbon atoms interstitially in the TiB<sub>2</sub> lattice.

Prakash [232] et al verified similar phenomenon when depositing Ti-B and Ti-B-C using by plasma immersion ion implantation. The Raman spectra of the Ti-B-C coatings deposited by Prakash [232] showed a shoulder peak at 1350 cm<sup>-1</sup> and peak at 1550 cm<sup>-1</sup> which agrees with the Ti-B-C phase produced in this section, visible in Figure 103. Prakash [232] concluded that the films deposited in a CH<sub>4</sub> atmosphere presented a hard Ti-B phase and lubricating DLC phases.

### 8.3.2.2 Nanoindentation

The number of layers was reduced to 20; therefore the coating total thickness was about 2  $\mu\text{m}$  as seen in section 7.2. The nanoindentation performed in the multilayer coatings is shown in Figure 104. Hardness values of 4.7 GPa were measured for the 75% carbon content. The coating containing 25% of carbon presented a hardness value of 3 GPa (extrapolated) while the 50% fraction of carbon presented a value of 2.2 GPa (extrapolated). These values indicate that the DLC has a direct influence on mechanical properties. By the observation of Figure 104, the coating with 75% carbon had behaviour closer to DLC than the 25% carbon fraction. The 50% carbon content showed a small hardness value, which indicates that the carbon layers have a mixed behaviour between graphite and DLC.

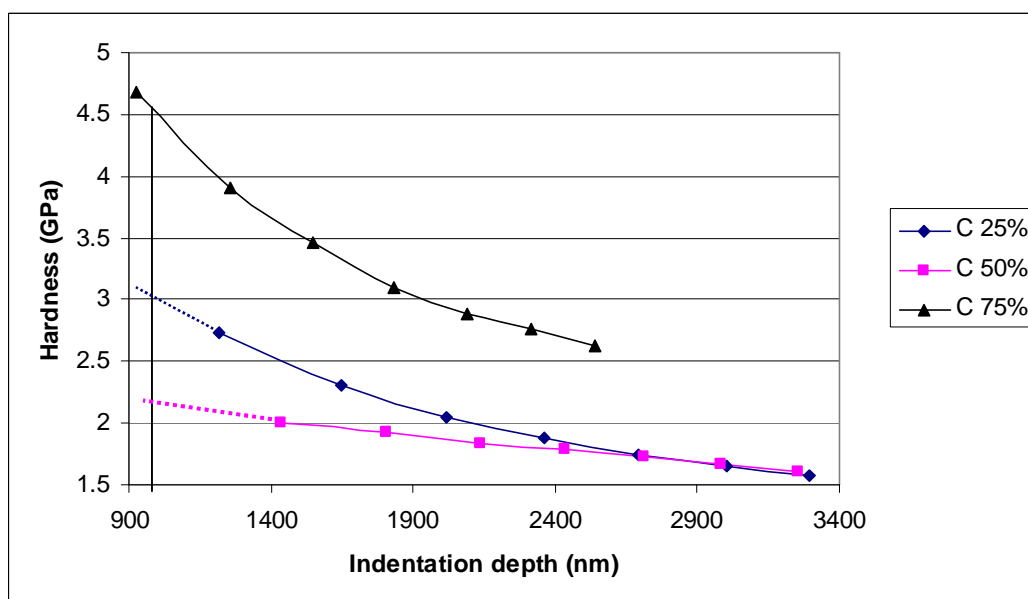


**Figure 104 - The Hardness of the multilayer films as a function of indentation depth. For high loads, the Hardness for the 75 % carbon-containing multilayer films is approximately 5 GPa, which decreases to 2.7 GPa for the 25% carbon-containing film at a 1200nm penetration depth.**

As the layers are deposited the interface between the ceramic and the next carbon layer has more  $\text{sp}^2$  due to the initial bonding between the Ti(B,C) and the carbon. As the layer builds up the carbon contains both  $\text{sp}^2$  and  $\text{sp}^3$ . The

reduced modulus values ranged from 40 to 60 GPa for the 50 % and 75 % carbon-containing films.

The DLC manufactured in this section has been evaluated using Raman spectroscopy. The  $sp^3/sp^2$  ( $I_D/I_G$ ) ratio calculated from the data was 1.25. This high ratio shows that the presence of  $sp^3$  ( $I_D$ ) bonds is above 50%, which allows the carbon layers to act as load-bearing. The deposition of the carbon in a 7.5 %  $CH_4$  atmosphere permits a good chemical adhesion between layers and the incorporation of  $sp^3$  bonds, which is related directly with the coating mechanical properties.

In section 8.2 the carbon and  $TiB_2$  layers were deposited in a pure Ar atmosphere which produced graphite like carbon layers with  $I_D/I_G$  ratio of 1.08 which indicated that the  $sp^3$  bonding content is below 50%.

For this section the hardness values are dependant on the carbon content, which lead to a decrease in hardness as the carbon content is increased. The carbon forms a lubricant phase after the  $Ti(B,C)$  phase becomes saturated at the interface. Carbon deposition in an inert atmosphere leads to graphite ( $sp^2$ ) like behaviour while the deposition in a reactive atmosphere with a hydrocarbon gas suppress the formation of  $sp^2$  bonds and promotes the formation of  $sp^3$  bonds.

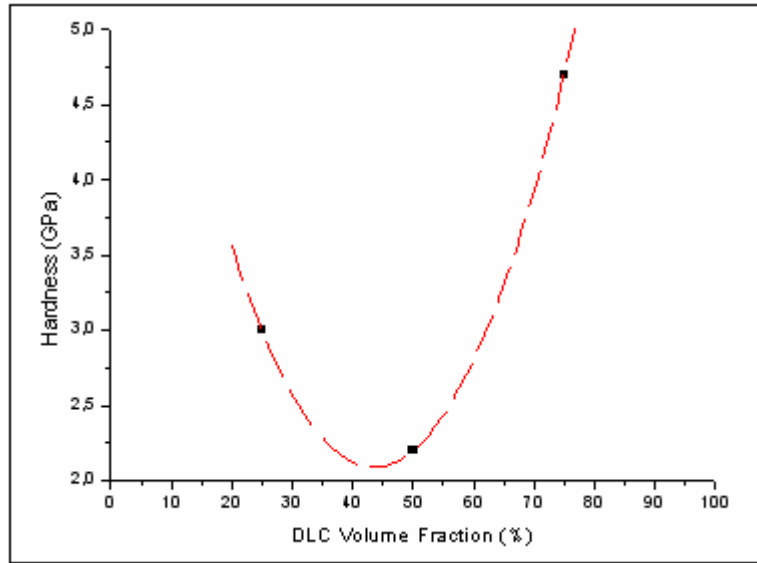


**Figure 105 – Hardness of the TiB<sub>2</sub>/DLC multilayer coatings vs the DLC volume fraction at approximately 1 $\mu$ m indentation depth**

In Figure 105 the lowest hardness at 1 $\mu$ m depth value (50% carbon) is when the equiatomic spacing is reached Figure 106 b). The other carbon contents (25% and 75%) are higher ~3GPa ~ 4.7GPa, respectively. This results from the predominant carbon bonding with the ceramic layer as it is deposited, which is shown schematically in Figure 106 a). As the carbon layer is deposited, it forms a reaction zone of Ti(B,C) with a constant thickness independent of the multilayer being deposited. Only after reaching the saturation point the carbon layer will have a DLC phase with the sp<sup>2</sup> + sp<sup>3</sup> amounts seen from the Raman spectroscopy, Figure 106 c).

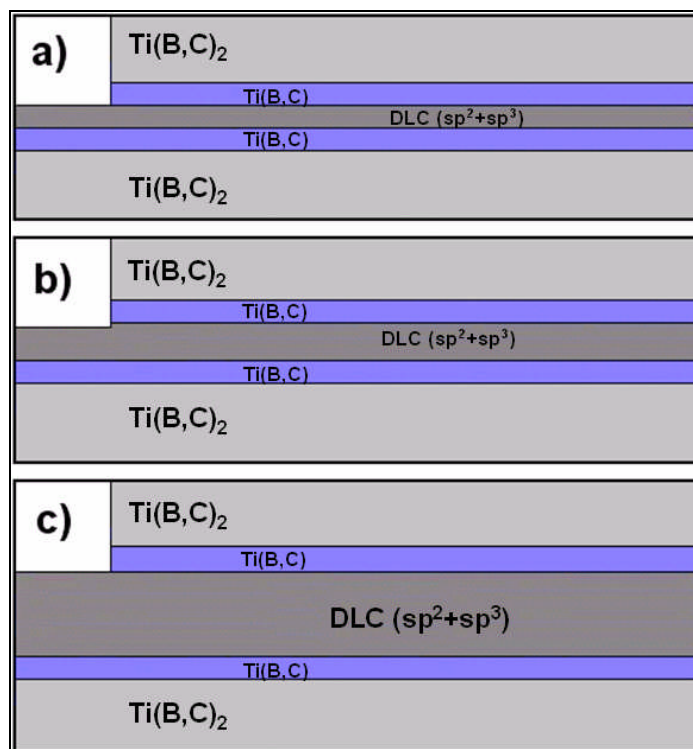


Figure 106 - Schematic of the interfacial zones a) 25%DLC b) 50%DLC c) 75% DLC.

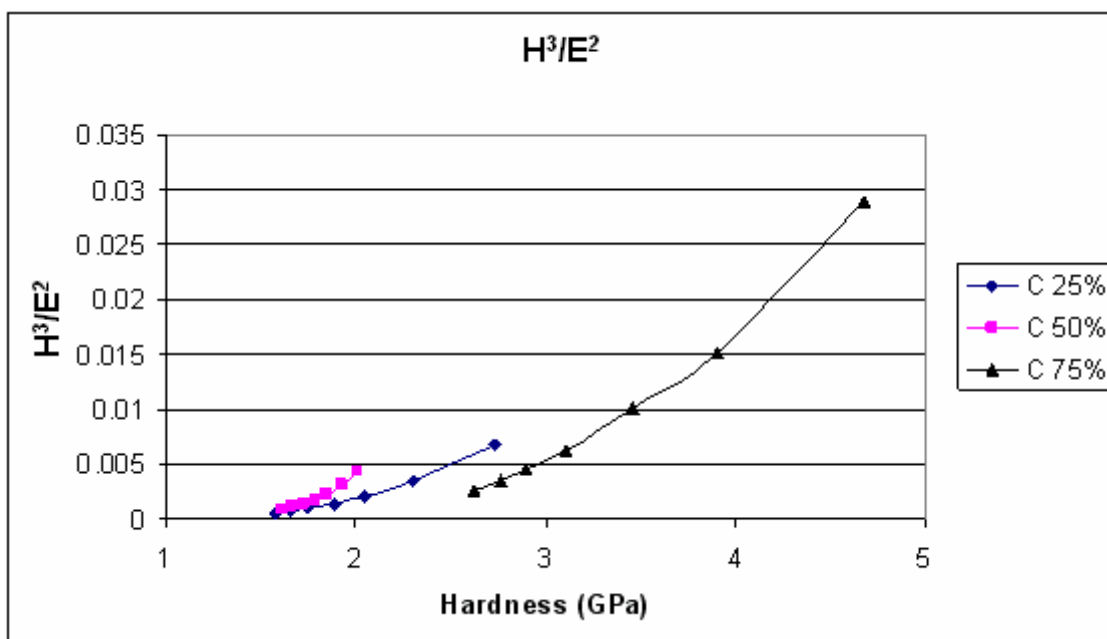


Figure 107 – Variation of  $H^3/E^2$  versus hardness for all the carbon multilayer films fabricated in this section.

In Figure 107 shows how the ratio  $H^3/E^2$  calculated from the hardness and reduced modulus values, changes with hardness for the multilayers manufactured in this section. From the figure a high volume fraction of  $sp^3$  (i.e.

75% C there is an increased spread in the  $H^3/E^2$  data, which indicates the carbon manufactured posses load bearing capacities.

### 8.3.2.3 Scratch testing

In Figure 108 it is possible to determine the adhesion of carbon sputtered in a reactive atmosphere of Ar +7.5%CH<sub>4</sub>. In the friction curve it is clear to see that the critical loads occurs about 28N with signs of Hertzian cracking. Over the next 10 seconds period the failure mode changes to spallation causing the removal of the coating from the substrate, highlighted in blue and red in the Figure 108.

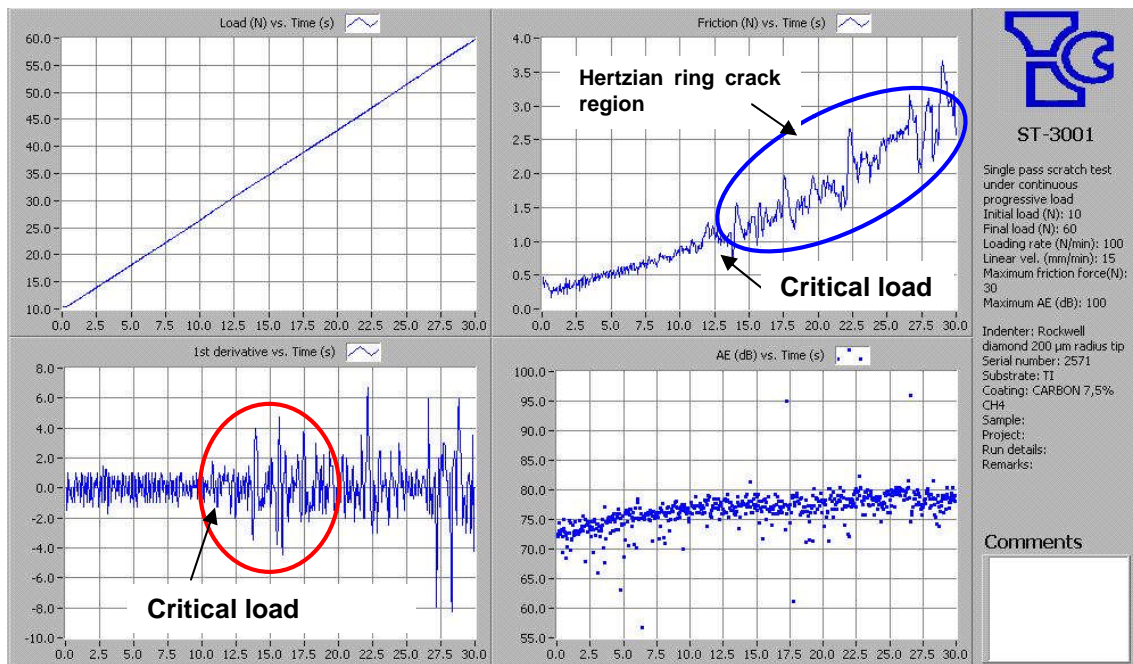


Figure 108 - Bulk Carbon adhesion testing on Ti sputtered in Ar 7.5% CH<sub>4</sub>

The failure mode visible in the case when the friction curve has several peaks is a mixture of failures, related to the nature of the substrate and the coating.



**Figure 109 – Sputtered carbon in reactive atmosphere, showing signs of Hertzian cracking**

In this case it is clear that one of the failure modes involved is Hertzian cracking, in which the stresses caused by the stylus generate a ring crack. These cracks propagate and create a network of cracks running from the surface of the coating to the substrate.

As the test continues loading, pressing the stylus into the coating/substrate, these crack networks connect when the ring cracks overlap and causes a chip to be removed.

In Figure 110 the results from a scratch test with increasing load are shown. The friction curve reveals a decreasing slope (highlighted in red) at first and then increasing towards the critical load.

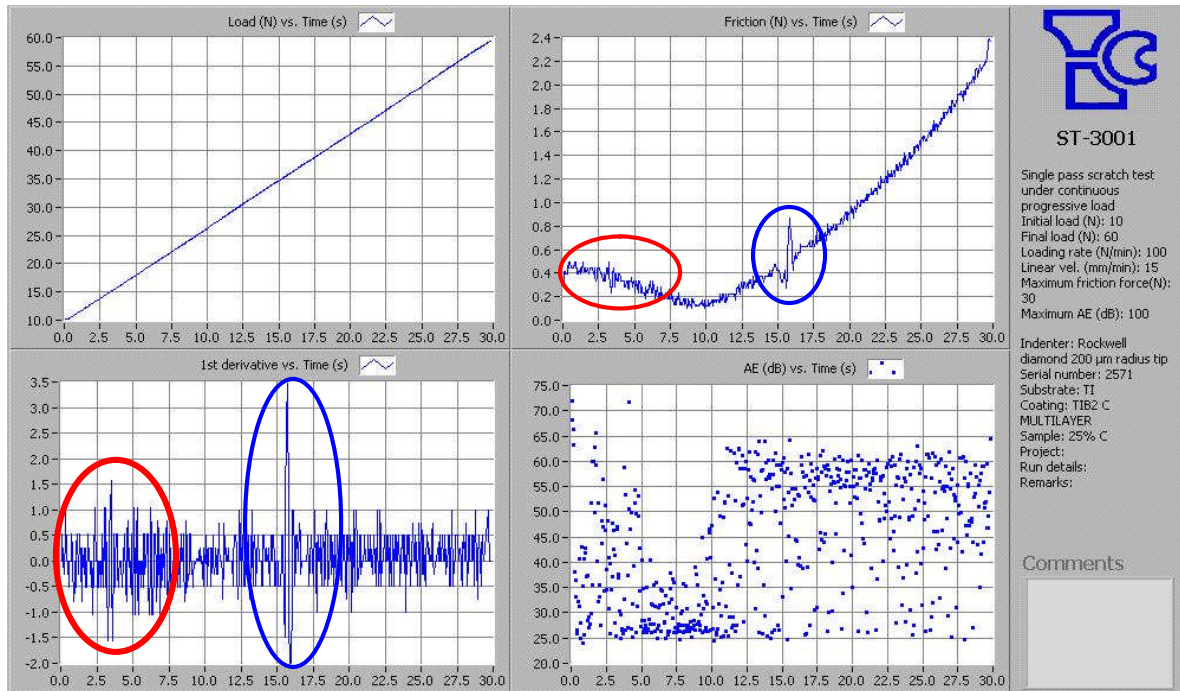


**Figure 110 – Single pass scratch test from 10N to 60N on 75%TiB<sub>2</sub>/25%C containing multilayer coating**

This variation in the friction curve is important. It indicates coating fracture as revealed by the 1<sup>st</sup> derivative of the friction curve, and also shown by the acoustic emission these coating fractures occur at ~16N.

In this case the plastic deformation is absorbed by the layered structure at a critical load and the coatings cracks in front of the indenter (Figure 110 at 16N). The release in strain energy can lead to spallation of the coating in front of the scratch track. If spallation does not occur, scratch debris can be compressed into the scratch scar surface by the action of the stylus.

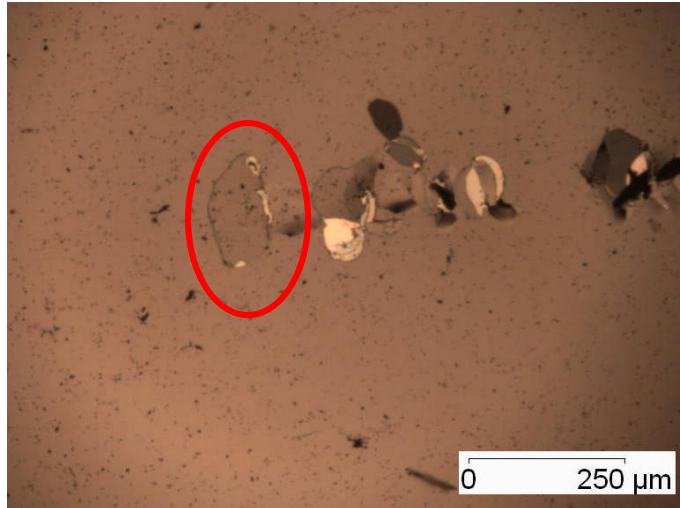


**Figure 111 –First failure point of 25%C containing multilayer coating marked in red in Figure 110**

As the test progresses and the loads are increasing, the amount of damage is increased. This causes the coating to further crack and eventually spalls. It is possible to see in Figure 111 and Figure 112 the onset of this spallation. In this case the critical load to onset of spalling is about 35N.

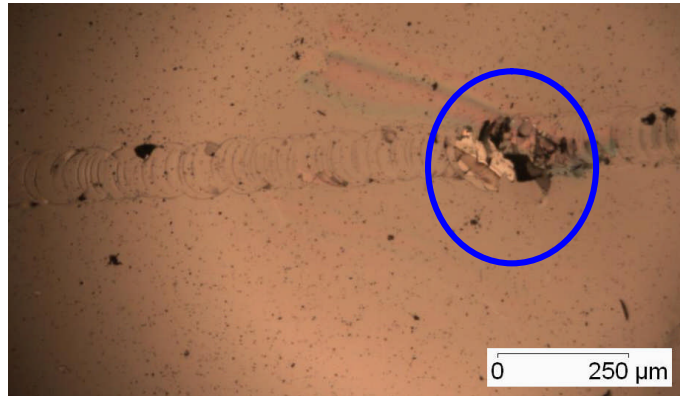


**Figure 112 – Critical load of 25%C containing multilayer coating marked in blue in Figure 110**

In Figure 113 the scratch test of the 50% volume fraction of DLC reveals poor adhesion. As soon the test begins the friction has a wide variation, and the derivative from the friction curve shows much scatter. This highlights early fracture which is further confirmed by the AE results.

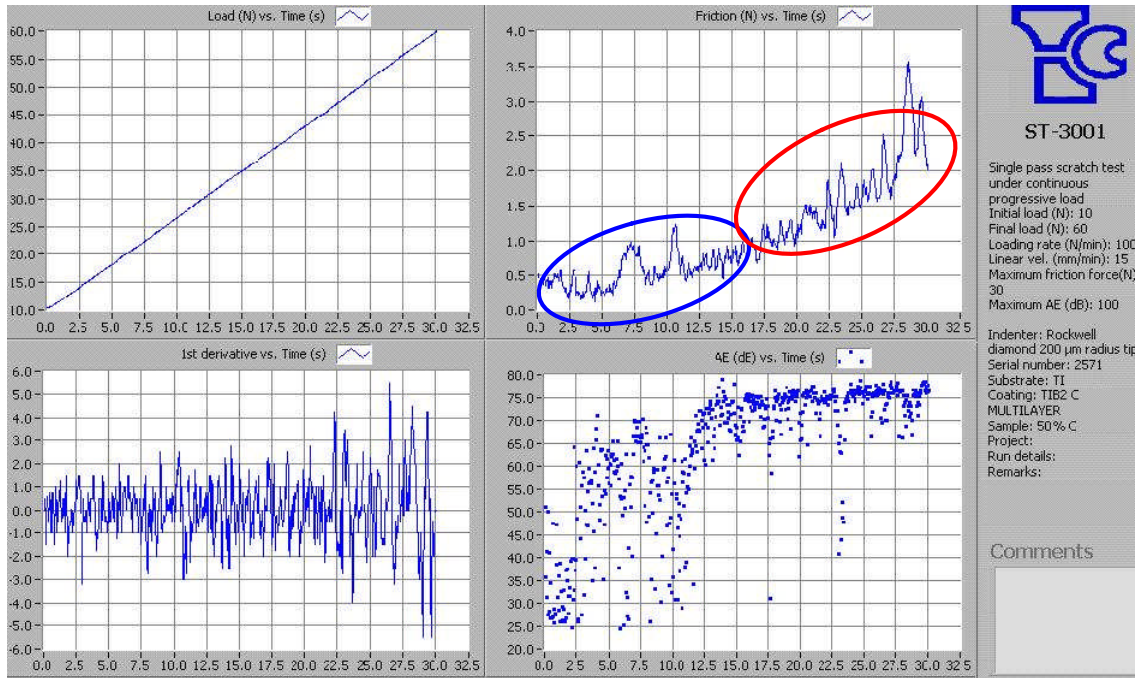


**Figure 113 – Increasing load scratch test with increasing load of the multilayer containing 50%Carbon, with clear signs of adhesion loss, showed in the friction curves and AE.**

In Figure 114 illustrates this coating failure for the increasing load scratch test of this multilayer coating containing 50% carbon. The figure on the left (highlighted in blue in Figure 113) shows the first delamination mechanisms are in operation. The figure on the right shows signs of severe adhesion loss, with a critical load of less than 15N (highlighted in red in Figure 113), with material being detached to the sides of the scratch scar.

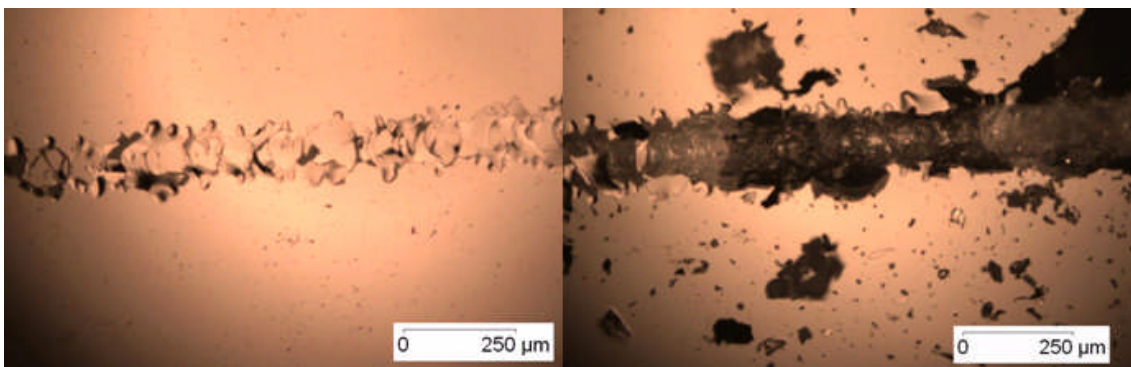


**Figure 114 – Optical micrograph of the multilayer containing 50% Carbon, detached from the substrate and chipping to the sides of the scratch scar.**

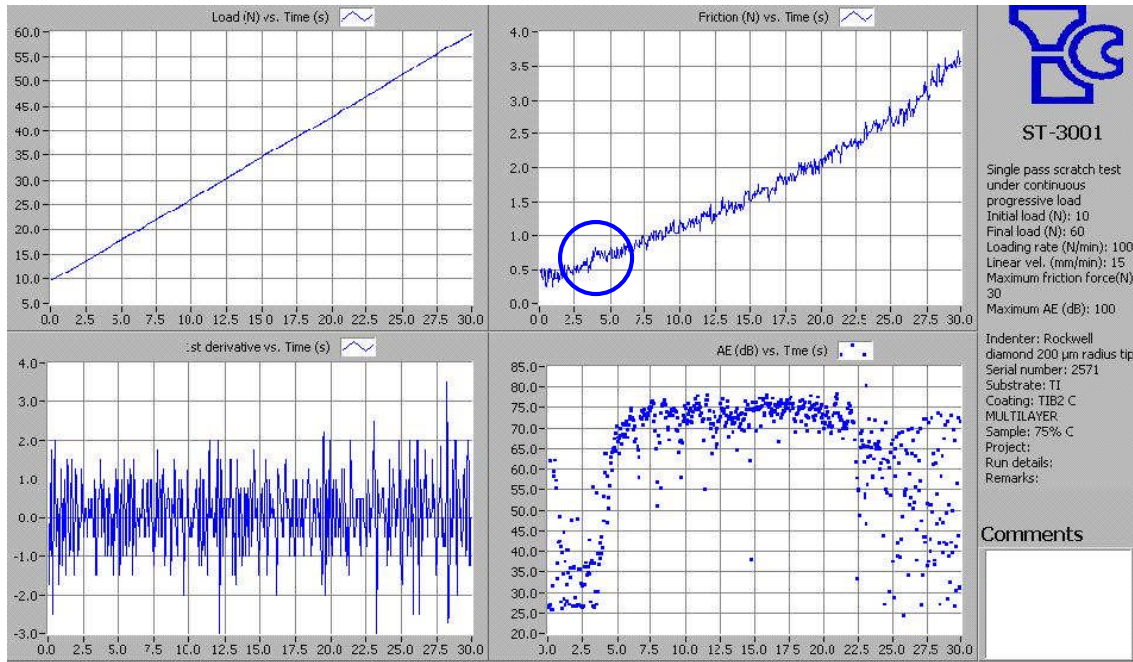


**Figure 115 –Scratch test with increasing load for the multilayer with 75% C**

In Figure 115, an increase load scratch test of the multilayered coating with 75% DLC, it is possible to see that the critical load is roughly about 15N as seen in the friction curve, and its derivative for a multilayer with 75% C.

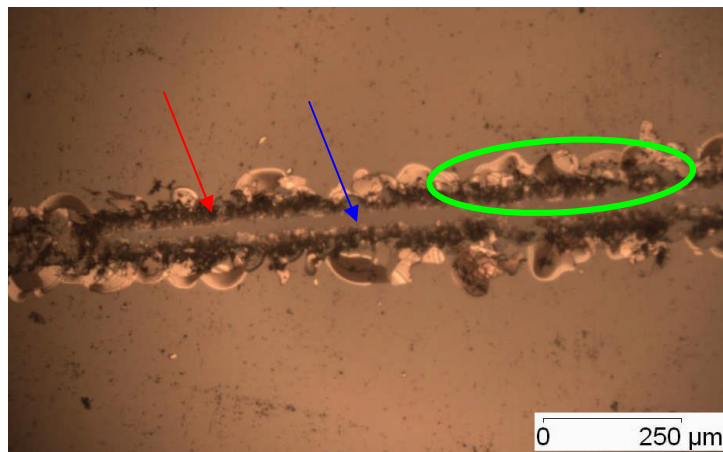


**Figure 116 – Scratch test scar with increasing load, from 10N to 60N for the 75% Carbon containing multilayer, where is clear to see that the adhesion is poor**

As a result of this loss of the adhesion the failure mode is very clear as can be seen in Figure 116. The red arrow indicates the edge of the scratch scar and a clear sign of recovery spallation. The blue arrow indicates the coating is being pushed into the surface by the indenter with enough stress generated in the

edge of the indenter that causes the coating to spall. The green circle indicates the recovery spallation to the surrounding area of the scratch scar.

### 8.3.2.4 Wear Testing

Measured coefficient of friction (CoF) for monolayer of carbon and TiB<sub>2</sub> coatings are shown in Figure 117. The test has consisted of 50 cycles and show average friction coefficients values of 0.22 and 0.19, respectively.

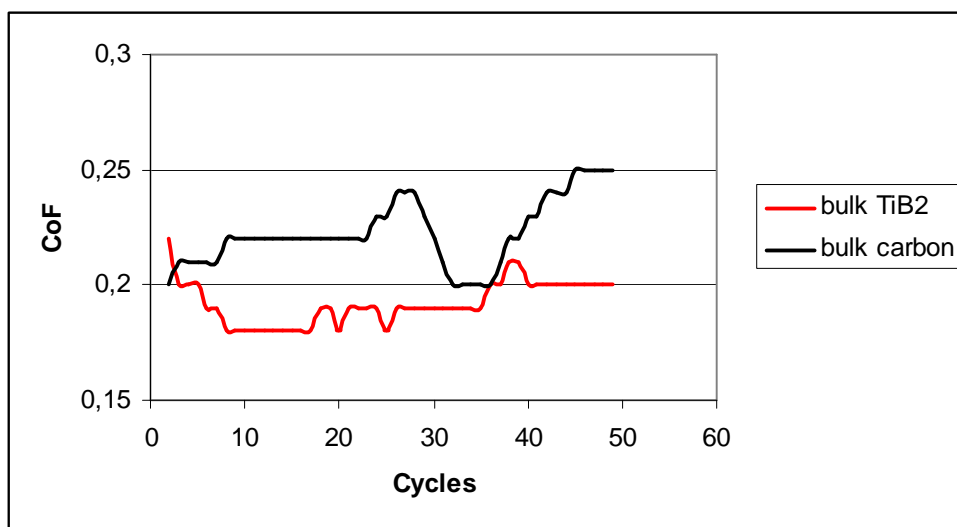
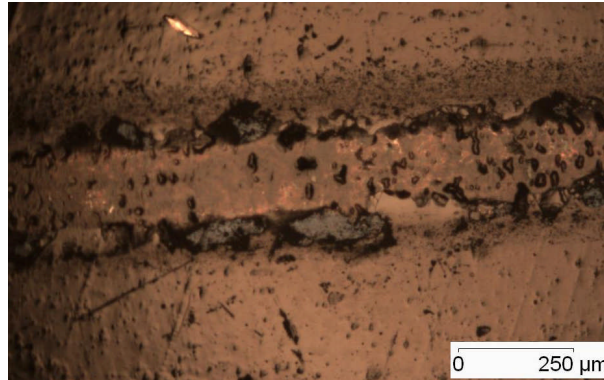


Figure 117 - The variation of the friction coefficient against the number of cycles. The bulk material of TiB<sub>2</sub> and carbon was tested over 50 cycles.

In Figure 118 the wear scar for a pure carbon film deposited with the conditions described in section 7.2 reveals signs of wear, without signs of coating detachment. The multilayered coatings have a friction coefficient below 0.3. This value suggests that the coatings have a graphitic behaviour.



**Figure 118 – Bulk Carbon sputtered in Ar + 7.5%CH<sub>4</sub> fabricated for this study**

In Figure 119 the TiB<sub>2</sub> coating shows signs of wear, the damage shown are not critical. Inside the red circle it is possible to observe an area with signs of delamination. Also, the most severe wear zone, inside the wear scar is related due to a change in loading direction within the test, because it is at this point the indenter stops, causing a high concentration of stress to be accumulated in that zone, causing a small part to spall possible due to a change in the CoF at a constant load.

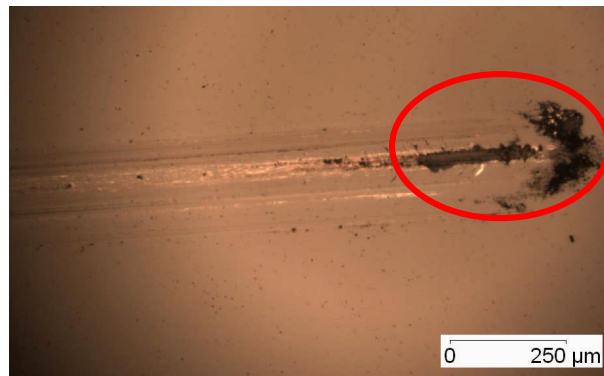


**Figure 119 – Bulk TiB<sub>2</sub> sputtered in a Ar + 7.5%CH<sub>4</sub> fabricated for this study. During the test the load is kept constant and the CoF may change causing an increase in the shear stress within the film, causing it to delaminate.**

This was reported by Meletis [234] which described that during un-lubricated contact a graphite layer was formed during the test. The friction coefficient for the coatings with 25% and 75% of carbon was 0.28 and 0.24, respectively after 20 cycles, visible in Figure 120. The coefficients of friction measured in this section are comparable to other studies such as Gilmore et al [113-115] which

measured values of 0.2 and Enke [235] which values were around 0,19 similar to the values measured in section 8.2.

This behaviour of the carbon layers deposited in this section shows that the layers have both a load bearing properties and a low friction coefficient, whose values are comparable to graphite based coatings as we have seen in section 8.2.

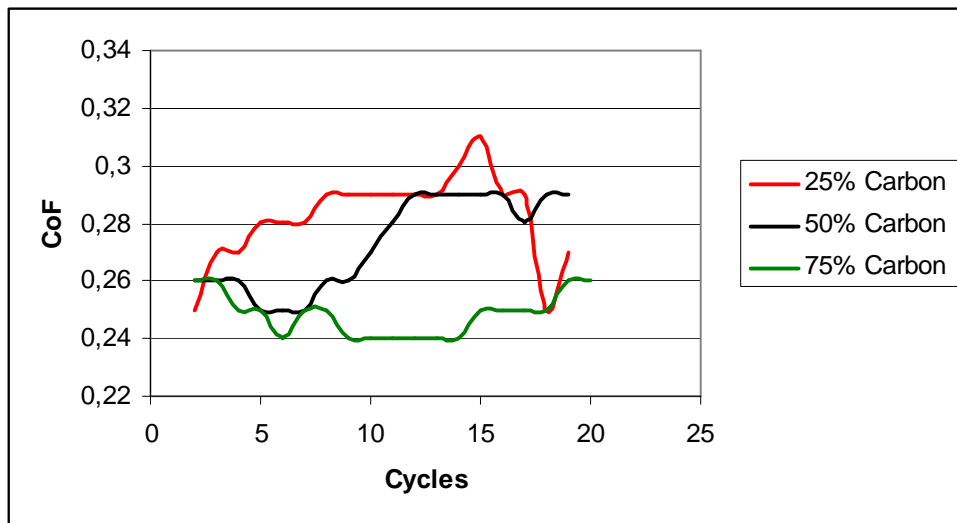


**Figure 120 - Multilayer films wear test over 20 cycles. All materials show an average friction coefficient less than 0.3.**

In Figure 121 some signs of loss of adhesion within the multilayer coating can be seen. Highlighted in blue is a region where the layers have resisted the amount of stress created by the movement of the WC ball, leaving signs of detached coating and adhered coating inside the scratch scar.

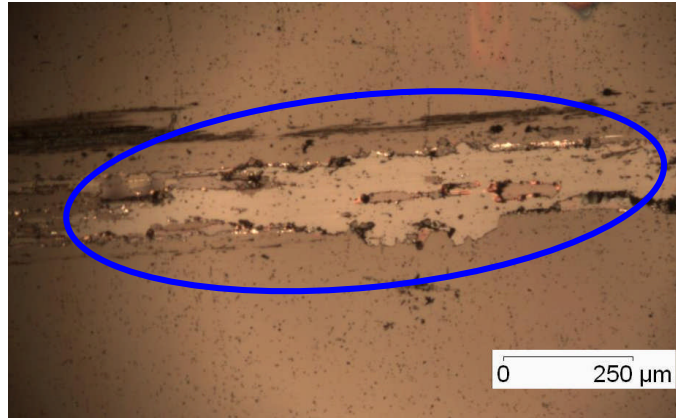


**Figure 121 – Multilayer coating containing 25%C highlighted in blue is a region with signs of coating removal.**

In Figure 122 there is some damage inside the wear scar. In the vicinity of the wear scar, highlighted in blue, there are signs of recovery spallation providing evidence sign of residual stress present in the coating.

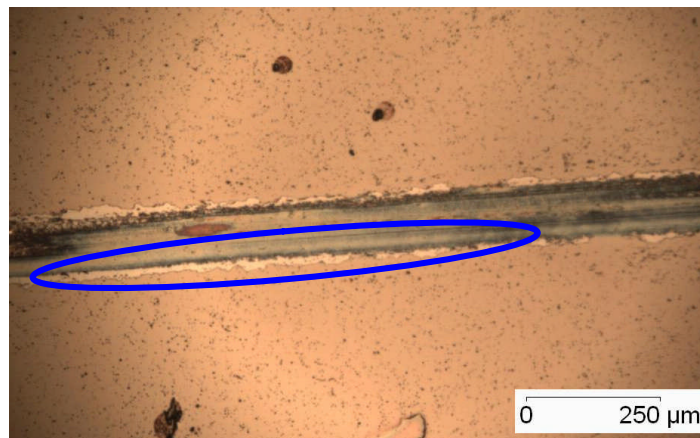


**Figure 122 – Multilayer containing 50% C, with a highlighted region of recovery spallation**

In Figure 123 it possible to see the wear scar left by the contacting indenter after 20 cycles. It is clear that the surface is worn, but the multilayer coating does not spall. This is a good indicator that the multilayer has a good load bearing ability and wear resistance. This good behaviour gave an average low friction coefficient, 0.24.

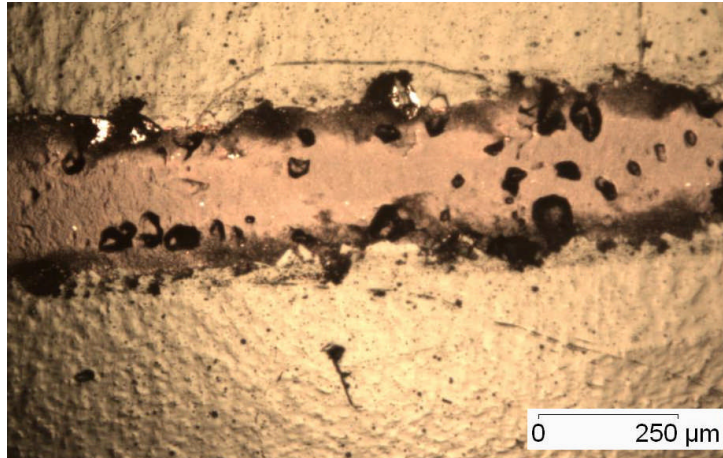


**Figure 123 – Optical micrograph of the wear scar surface of the multilayer containing 75%C**

In Figure 124 the wear scar volumes of the coatings produced for this section are presented. In the extremes of the Figure are plotted the wear scar volumes for TiB<sub>2</sub> and Carbon. These values are relatively low compared with the 75% carbon containing coating, which is several times higher than the other coatings produced. Although it has the lowest friction coefficient it presents the highest wear scar volume which indicates that the coating is capable of sustaining damage without spalling and provides a lubricant surface.

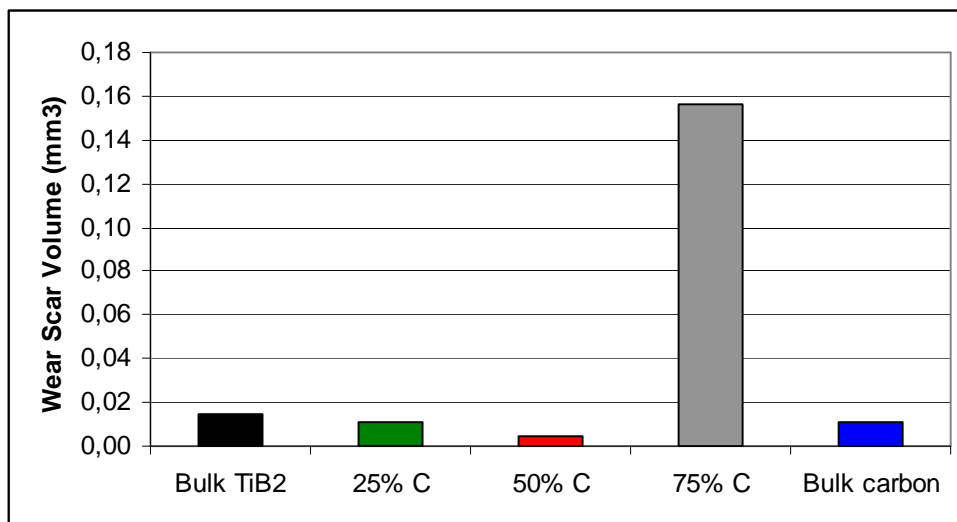


**Figure 124 – Wear scar volume for the bulk coatings of TiB<sub>2</sub> and Carbon compared against the multilayer coatings.**

The 50% carbon containing coating presented a low friction coefficient value (Figure 120) and the lowest adhesion value (15N) when compared with the other multilayers. This occurs possibly due to detachment within the layered structure. The graphite debris lubricates the surface causing the friction CoF to be low, even though the data from adhesion testing and hardness testing reveals a weak coating.

### 8.3.3. Conclusions

- The multilayer produced in this section contained 20 layers of  $\text{TiB}_2$  and carbon deposited in an Ar + 7.5 %  $\text{CH}_4$  atmosphere, using pulsed-DC. The ceramic percentage was varied from 25% until 75%. The coating total thickness was 2  $\mu\text{m}$ .
- Raman spectroscopy identified that the carbon produced was amorphous with  $I_D/I_G$  ratio of 1.25.
- The multilayer matrix was deposited in a reactive atmosphere with Ar + 7.5%  $\text{CH}_4$ , from which Ti-B-C was formed at the interface. This interface contained both a hard phase caused by the ceramic ( $\text{TiB}_2$ ) and a lubricating phase caused by the DLC.
- Nanoindentation studies presented hardness variations from 3 to 5 GPa for the 25% and 75% ceramic containing coating. It was found that the mechanical properties are influenced by the carbon content in the coating.
- The ratio  $H^3/E^2$  calculated from the hardness and reduced modulus from the multilayers shows that as the carbon content increases the scatter in the ratio also increases.
- The friction coefficient measured in this section was around 0.3 which is comparable to that in other studies on monolayer DLC films which presented values of around 0.2. This is an indicator that the DLC produced provides load-bearing properties, while maintaining a low friction coefficient similar to graphitic structure manufactured in section 8.2.

## **8.4. TiB<sub>2</sub> monoliths on powder processed Aluminium (Al) alloys**

### **8.4.1. Introduction**

So far in this study, these multilayer coatings have been deposited on tool steel (AISI 1095) substrates. However over recent years there has been a steady growth in the number of Al components used in the automotive industry as these alloys offer low reciprocating mass and high specific stiffness and can be used to provide increased power output in high performance vehicles or increased fuel economy for mass-market vehicles. With the widespread use of key aluminium alloy components, there remains a need to develop high quality, well adherent, hard lubricant coatings to protect these light alloy components.

This section focuses on the deposition of multilayer coatings of diamond like carbon and TiB<sub>2</sub> films on powder metallurgy derived aluminium alloys, primarily, designed for high strength and fatigue resistance. In this work, DLC films sputtered in a mixture of Ar and CH<sub>4</sub> favoured the formation of sp<sup>3</sup> bonding, where the H<sub>2</sub> component of the gas phase suppresses or preferentially etches the sp<sup>2</sup> component. The addition of a metal-based refractory ceramic, namely TiB<sub>2</sub>, into a multilayer stack further enhances the tribological properties of these DLC containing multilayer coatings.

#### **8.4.1.1 Wear testing**

All wear and adhesion testing was done using a Teer Coatings ST-3001 Tribo Tester as we seen in section 6.2. Wear testing was carried out using a fixed WC-Co 5 mm ball slid against a coated test piece. In this study, constant loads of 10 N and 20 N were applied over a total of 50 and 100 cycles, each cycle being a linear displacement of 3 mm at velocity of 150 mm/min.

For most sliding contact interfaces the extent of friction is controlled by a combination of physical, chemical and mechanical interactions at the micro-contact interface. Physically, the surface roughness is of major importance,

since rougher surface results in higher ploughing, and hence higher friction. Chemically, the amount of interactions between the rubbing surfaces may govern the extent of adhesive bonding across the interface. These chemical interactions of the coating also influence the friction.

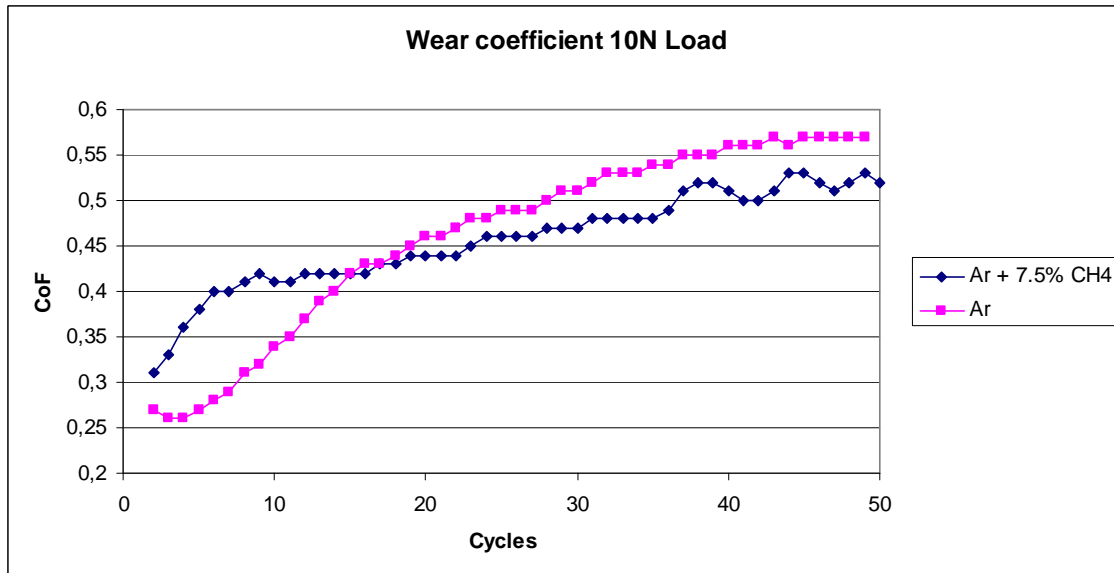


**Figure 125 – Showing the variation of the friction coefficient of the TiB<sub>2</sub> monolayers against the number of cycles with a 10N load influenced by the Ti-B-C phase.**

When interposed between two sliding surfaces, the film shears with relative ease, hence providing low friction when coated a hard substrate. For the case of using an Al Alloy with relative high load (i.e. 10 N, 20 N) from observing Figure 125 it is possible to observe that for the film produced in Argon there is a small run in period of 5-10 cycles with a steady increase in the coefficient of friction. For the Ar + 7.5 % CH<sub>4</sub> produced film the friction coefficient increases from the beginning and the curve has progressively increases throughout.

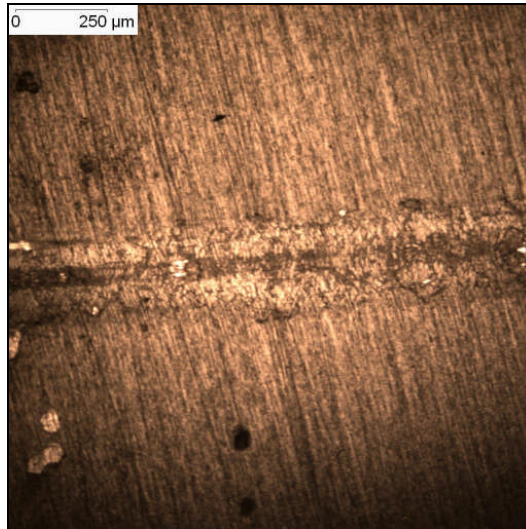


**Figure 126 – Micrograph of a wear scar with signs of visible Hertzian cracking**

As is showed Figure 126, the worn coating exhibits a very smooth surface topography with some signs of Hertzian cracking. The deformation of the substrate is significant due to the poor load-support capacity of the substrate and the film deflects in relation to the deformation of the substrate. The deformation of the substrate would, as a result, add either a ploughing or hysteresis effect to the measured friction. The repeated deflection of the film may cause fracture or fatigue cracks that damage the coating and/or the substrate; in this particular case the coating as shown by the conformal cracking present in the wear scar. An increase in the film thickness may lead to a reduction of the substrate deformation and hence the contact area between the film and sliding ball, providing a more stable friction coefficient.

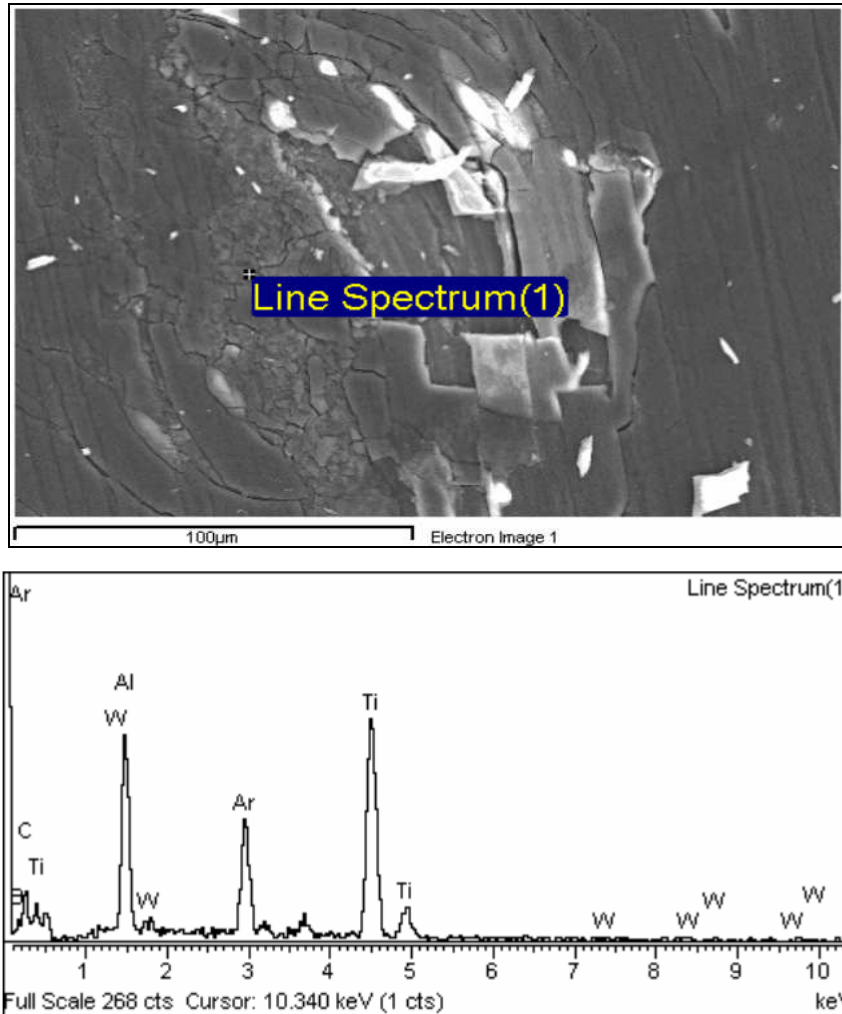


**Figure 127 – SEM micrograph and EDX spectra of wear scar in the  $TiB_2$  coating formed in an Ar + 7.5% $CH_4$  with presence of a W peak as a result of material transfer from the tribotest ball.**

Even though not directly observed in these wear test results, it is believed that the coating wear takes place in two steps; during the running-in period the surface asperities caused by the deposition technology are polished away leading to the initial increase in friction coefficient. Then, the wear of the surface at steady state occurs by smearing out of material from the coating, and transfer to the WC ball, which works as a counter surface. As we can see from the EDX spectra, Figure 127, material transfer has occurred, as evident by the presence of W inside the wear scar (the W comes from the WC ball of the tribotester).

The bidirectional wear tests showed that the films deposited using pure Argon have a low friction coefficient against a WC ball. The variation of friction

coefficient as a function of sliding distance is displayed in Figure 128 for a 20 N load. A running-in period of about 10-15 cycles with a higher coefficient of friction is identified. This high value gradually decreases with increasing cycles, achieving a relatively steady state at 100 cycles. While the TiB<sub>2</sub> films deposited in an Ar + 7.5 % CH<sub>4</sub> has a steadier initial friction coefficient, up to 20-30 cycles, which increase thereafter but with a high variability in the coefficient of friction due to the hard phase of Ti-B-C that can form which leads more Hertzian through thickness cracking in the wear scar visible by the variation of the friction coefficient.

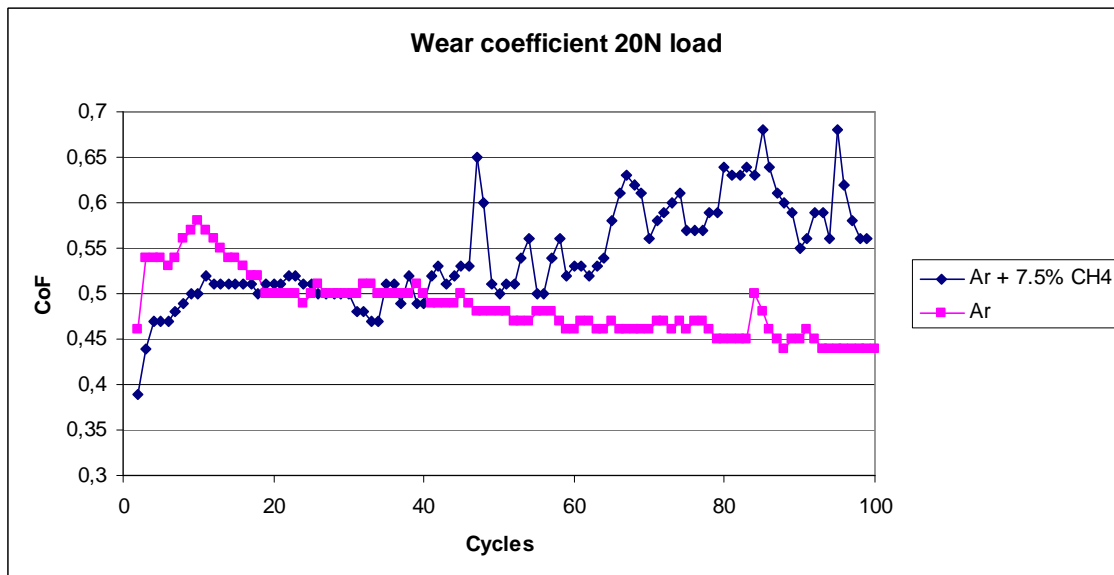


**Figure 128- Showing the variation of the friction coefficient against the number of cycles with a constant 20N load. The experiment in Ar + 7.5 % CH<sub>4</sub> has a clear phase of variability during the test as a result of the Ti-B-C phase present in these coatings.**

As long as this slippery transfer layer is maintained, a low friction coefficient and long wear life is obtained. The driving force for this smooth material transfer, instead of third body formation (wear debris), Figure 129, and sheared surface seems to be the lubricating effect of the film.

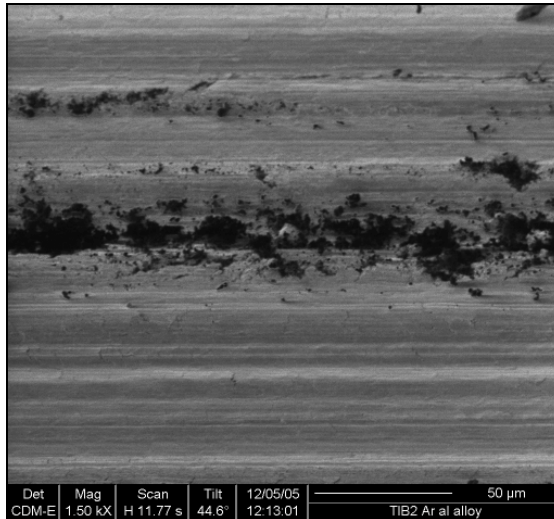


**Figure 129 – Wear scar at 20N load showing debris in the middle of the test scar. The debris is a powder mix between detached coating pieces, and transferred material from the WC ball**

Thus, the adhesive and cohesive properties of the coating control the wear rate. By observing the edge of the scar optically it is possible to differentiate a band differentiated by colour, following the whole length of the wear scar. This band can be interpreted as a gradient in thickness, increasing from the inner side to the outer side of the scar and indicates that material has been trapped there during the sliding motion.

#### **8.4.1.2 Adhesion Testing**

For adhesion testing, a diamond Rockwell C (0.2 mm tip radius) was employed. To assess the adhesion quality of the film a group of tests was performed on the samples. The samples were scratched with constant loads of 2N, 5N, 7N, 10N, 15N, and 20N. The software that controls the tribotester also monitors certain parameters associated with tribology. The friction coefficient, the load, the first derivative of the load, and the acoustic emission as a function of time are all plotted sequentially. This graphical output enables, at a glance, any changes in coatings performance over time.

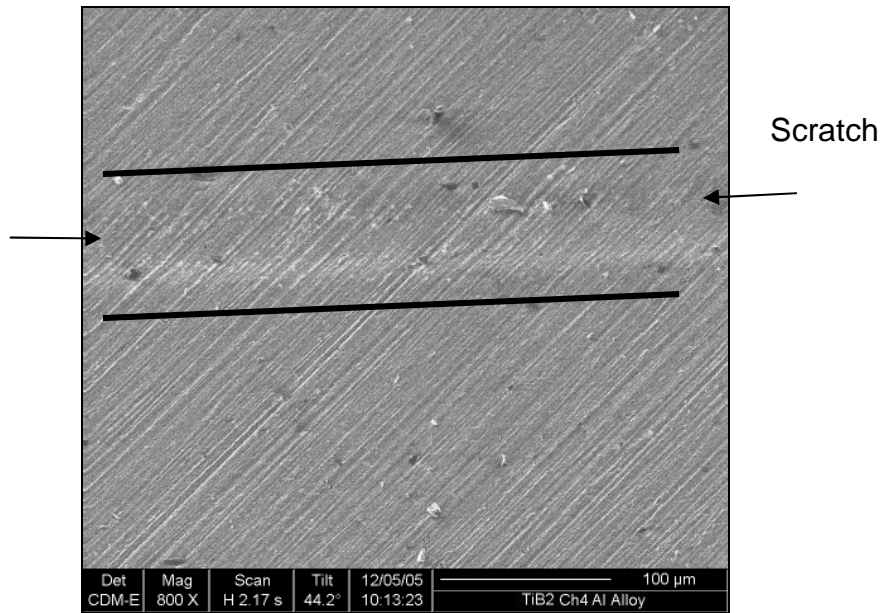


**Figure 130 – FIB micrograph of 2 N constant load scratch of TiB<sub>2</sub> sputtered in Ar + 7.5 % CH<sub>4</sub>, presenting signs of substrate deformation caused by Rockwell C diamond tip**

As we can see from Figure 130 - Figure 133 it is possible to observe that the substrate is highly deformed as described before in section 8.4.1.1. The first signs of coating cracking, at the high bending stress was at 5 N load for both coatings deposited in pure Ar and Ar + 7.5 % CH<sub>4</sub>.

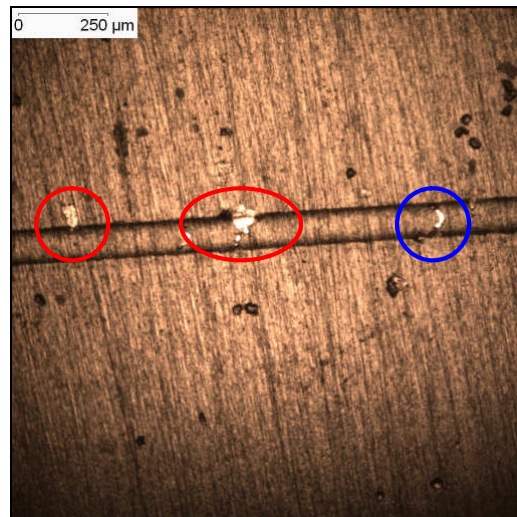


**Figure 131 – Optical micrograph of 5N constant load scratch of pure TiB<sub>2</sub> sputtered in pure Ar, with the initial sign of recovery spallation highlighted in red, in a blue circle there is a small sign of spallation**

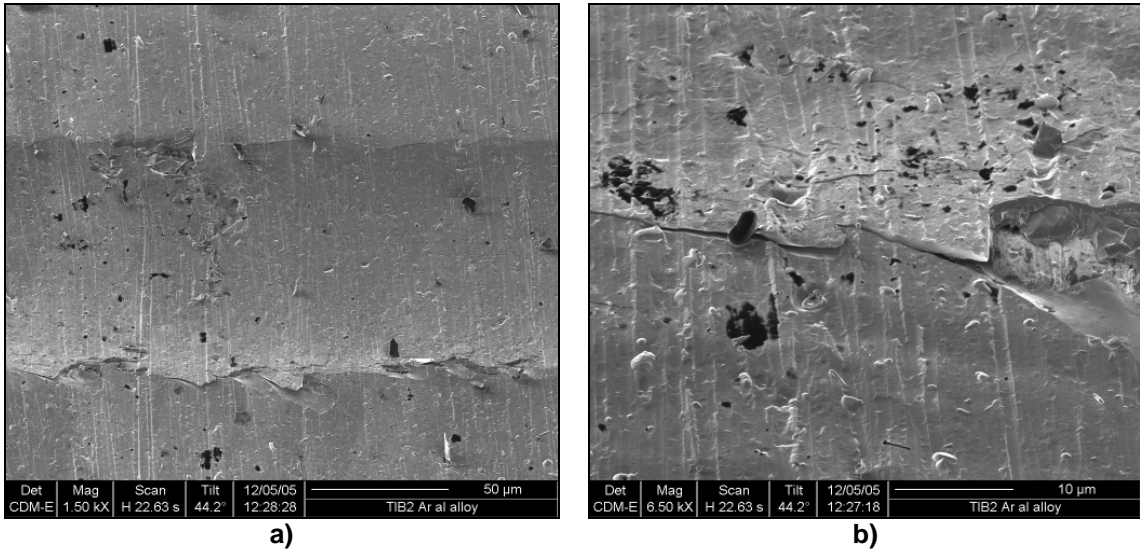


**Figure 132 – FIB micrographs of 5 N constant load scratch of  $TiB_2$  sputtered in pure Ar, presenting sign of cracking on the edge, and heavy substrate deformation caused by the diamond tip**

From observation of the edges of Figure 131-Figure 135, there is a clear sign of recovery spallation which is associated with the elastic recovery which occurs behind the stylus as it travels over the coated surface and depends on plastic deformation of the substrate which in this case suffers severe deformation. It also depends on through-thickness cracking in the coating. During the test after the stylus moves through that region and the surface is unloaded, the elastic deformation in the coating-substrate system is relaxed.

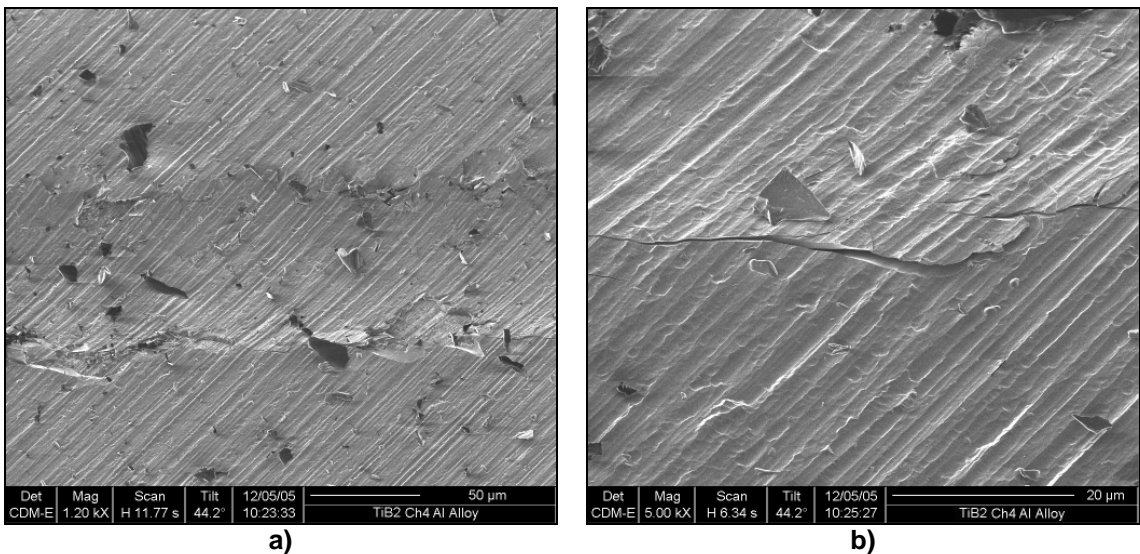


**Figure 133 – FIB micrographs of 5 N constant load scratch of  $TiB_2$  sputtered in Ar + 7.5 %  $CH_4$ , presenting cracks along the scratch scar**

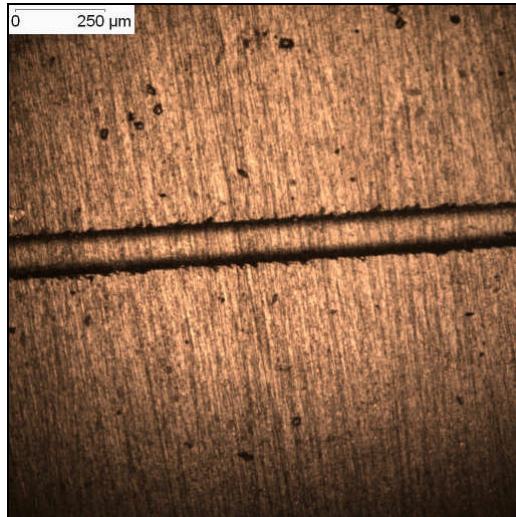


**Figure 134 - Optical micrograph of a 7 N constant load scratch presenting signs of recovery spallation**

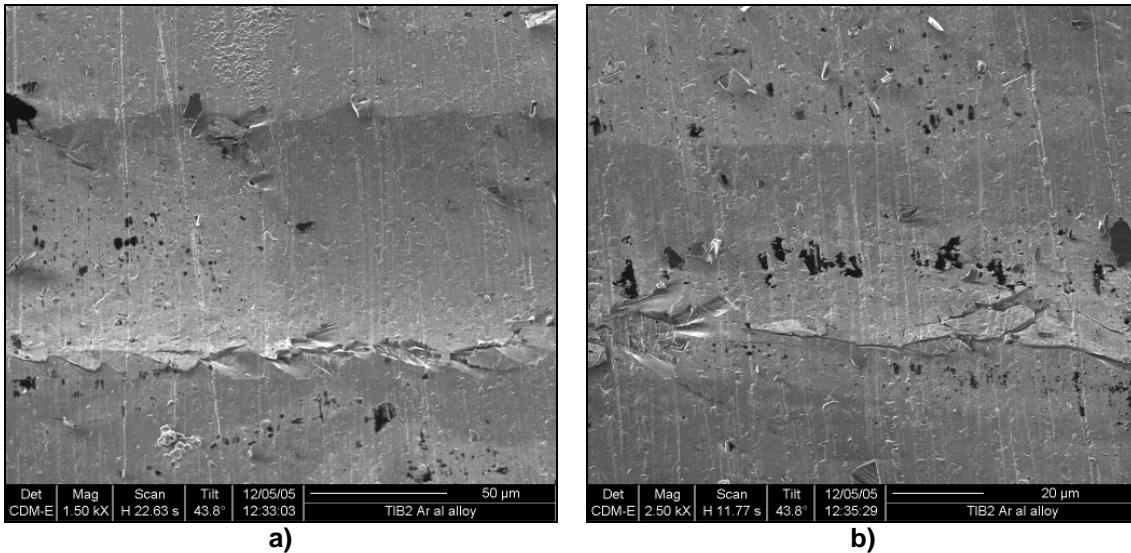


**Figure 135 - FIB micrographs of a 7N constant load scratch of TiB<sub>2</sub> sputtered in pure Ar, presenting damage on the edge of the scratch scar**

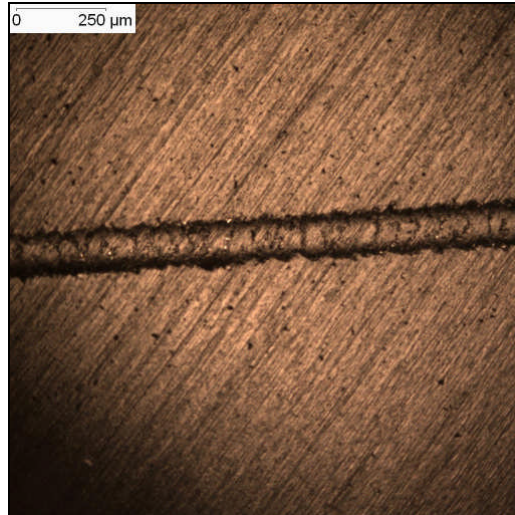


**Figure 136 – Optical micrograph of 7N constant load scratch of pure TiB<sub>2</sub> sputtered in Ar + 7.5 % CH<sub>4</sub>**

Due to plastic deformation in the substrate, which results in the visible deformation of the scratch region, the substrate is not completely relaxed as some elastic deformation and residual stress remains. This failure mode leads to chipping at the sides of the scratch scar, if the interfacial crack propagates to the outside of the scratch before the stylus passes over it.

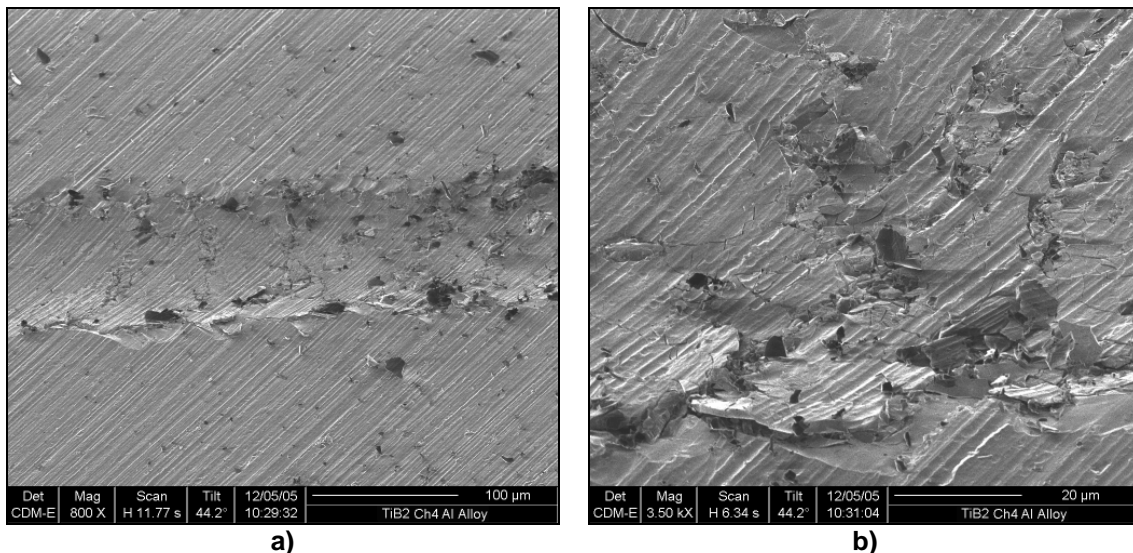


**Figure 137 - FIB micrographs of 7N constant load scratch of TiB<sub>2</sub> sputtered in Ar + 7.5 % CH<sub>4</sub>, presenting cracks along the scratch scar and signs of chipping inside the scar**

Once the stylus has reached the spalled region it will either press the coating back in to contact with the substrate or cause a chip to be removed, particularly if in the sample there is through-thickness cracking occurring. This chipping is due to the differential elastic recovery of the coating and substrate.

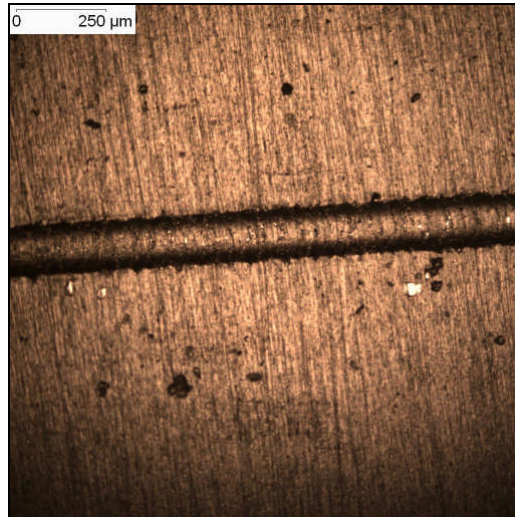


Figure 138 - Optical micrograph of 10N constant load scratch

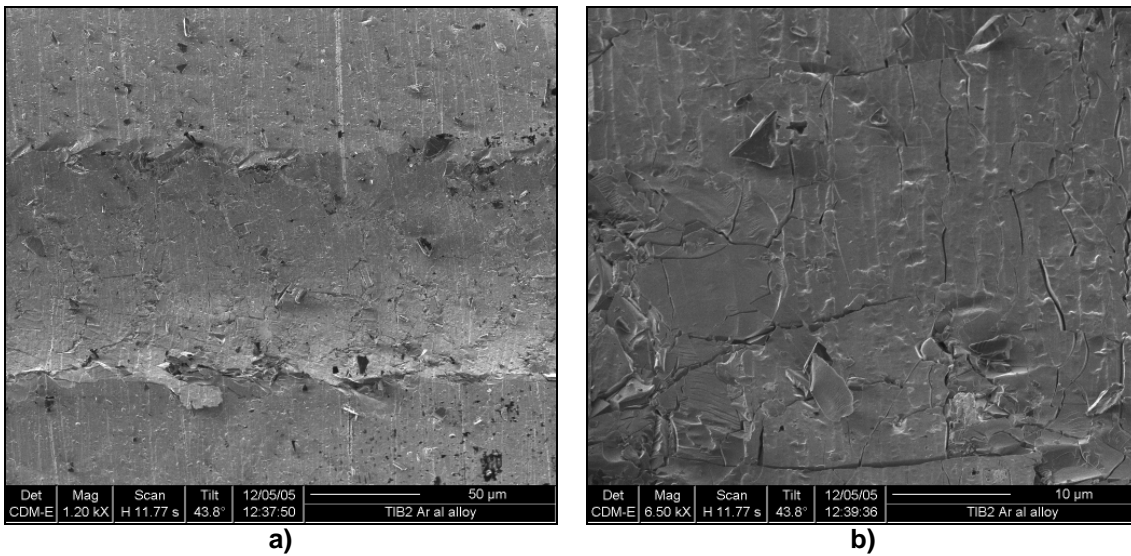
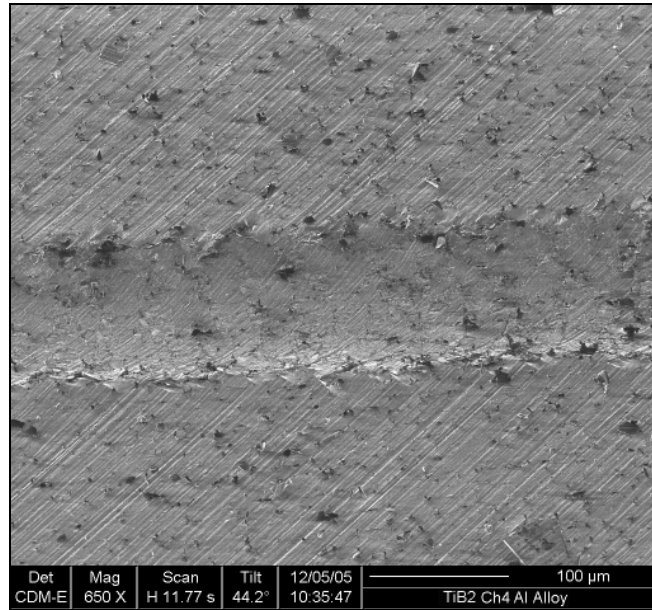
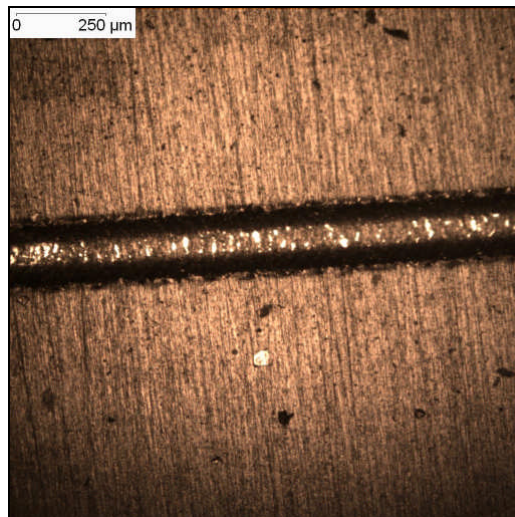


Figure 139 - FIB micrographs of 10N constant load scratch of  $\text{TiB}_2$  sputtered in pure Ar, showing signs of coating cracked inside the scratch scar



**Figure 140 - FIB micrograph of 10N constant load scratch of  $\text{TiB}_2$  sputtered in Ar 7.5% $\text{CH}_4$ , presenting cracks and debris along the scratch scar and the surface**

From Figure 138 to Figure 147, it is possible to see the transition between recovery spallation and gross spallation, present in Figure 142 - Figure 147. Gross spallation is a very common result if the adhesion is poor or residual stress in the coating is high.



**Figure 141 - Optical micrograph of 15 N constant load scratch presenting signs of cracking inside the scratch scar**

Also this failure mode starts to be seen at a load of 15N. As the diamond stylus contacts the coating at the start of the scratch, Figure 143-a), or at some point

along the scratch, Figure 142-a), cracks are formed at the coating-substrate interface which propagate until the edge of the deformed substrate of the scratch scar.

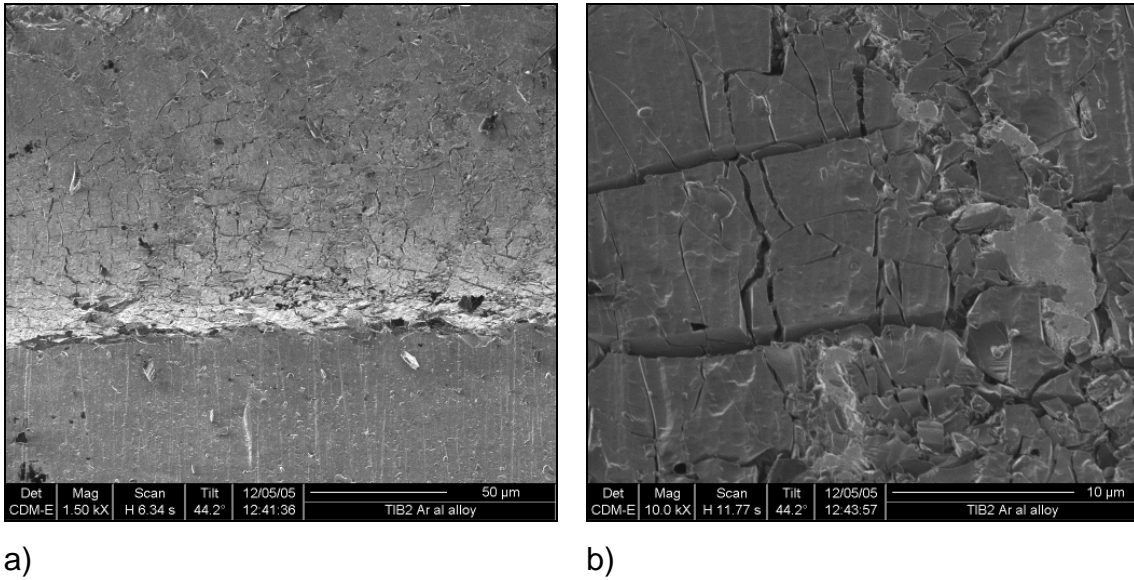


**Figure 142 - FIB micrographs of 15 N constant load scratch of TiB<sub>2</sub> sputtered in pure Ar, presenting sign of heavy damage and signs of coating compressed into the substrate**

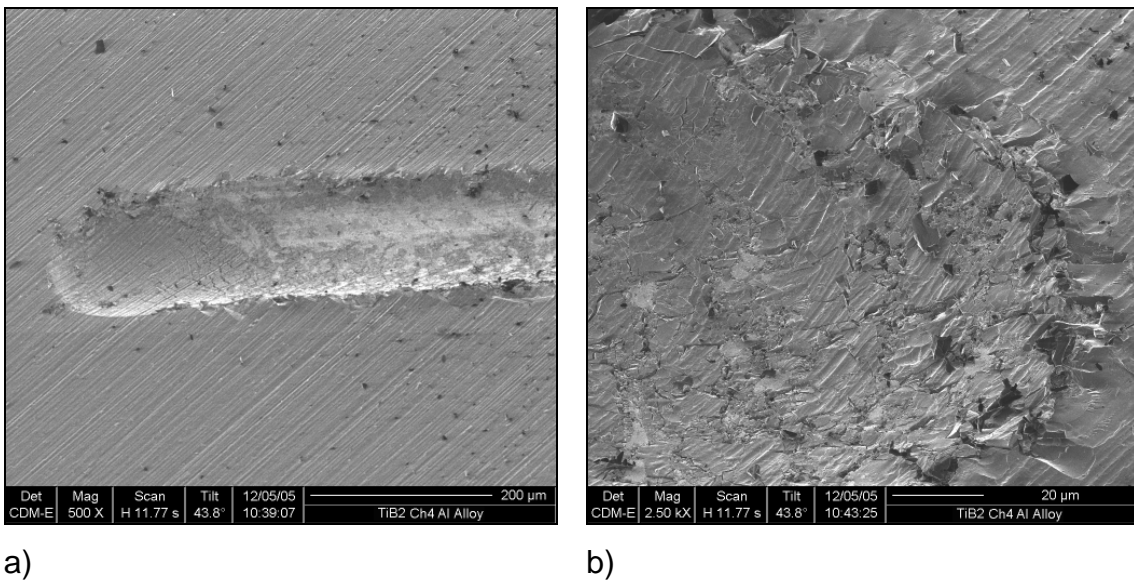


**Figure 143 - FIB micrograph of 15N constant load scratch of TiB<sub>2</sub> sputtered in Ar + 7.5 % CH<sub>4</sub>, presenting failure and debris along the scratch scar and the surface**

Figure 142-b) and Figure 143-b), show greater detail of the cracks that run along the scratch scar and the deformation by the diamond stylus caused at end of the test.

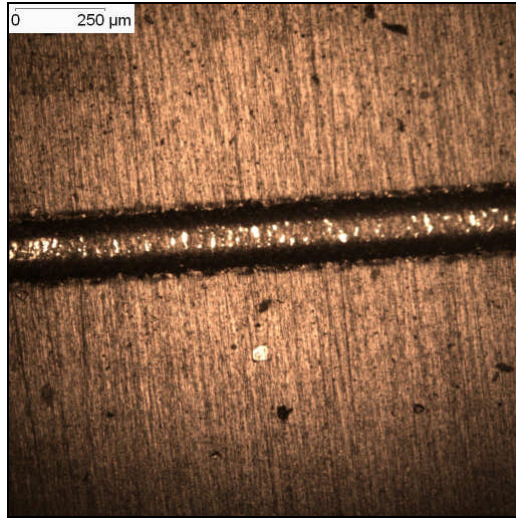
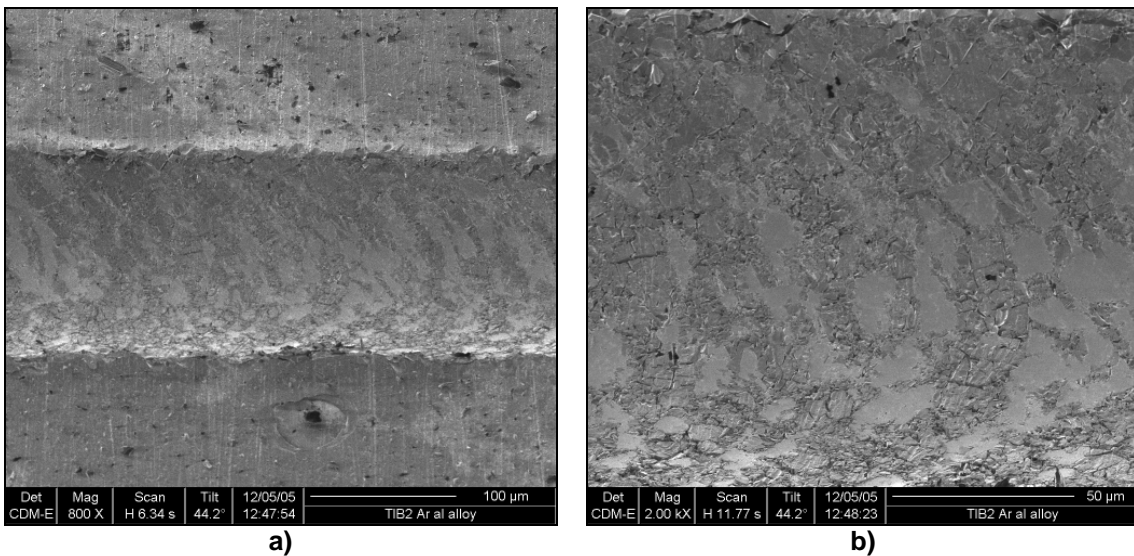
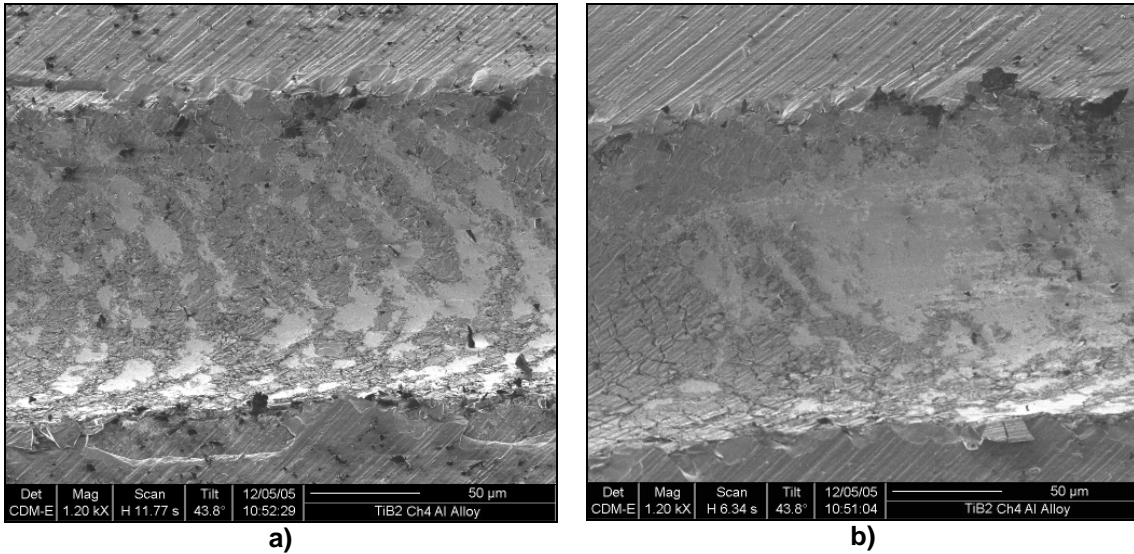


Figure 144 - Optical micrograph of 20 N constant load scratch



a) b)  
 Figure 145 - FIB micrographs of 20 N constant load scratch of TiB<sub>2</sub> sputtered in pure Ar, presenting signs of coating detachment

The cracks may be nucleated at an interfacial flaw or derive from through thickness cracking. Spallation occurs at high loads (>10N), in which the coating is detached to minimize the amount of elastic energy stored by the large compressive stress being created by the moving stylus.



**Figure 146 - FIB micrograph of 20N constant load scratch of  $TiB_2$  sputtered in Ar + 7.5 %  $CH_4$ , presenting failure and debris along the scratch scar and the surface**

This also implies poor adhesion, which in this case means that we are above a critical load for this coating. This leads to semi-circular cracks which propagate outwards to the side of the scratch scar.

As we can see in Figure 145 and Figure 146 the coating is cracked in a semicircular shape which propagates outwards from the centre line of the track, being the detached bits lodged along the surface in the vicinity of the scratch scar.

EDX analysis was carried out inside the scratch scar (with signs of recovery spallation at the darker spots in the scar).

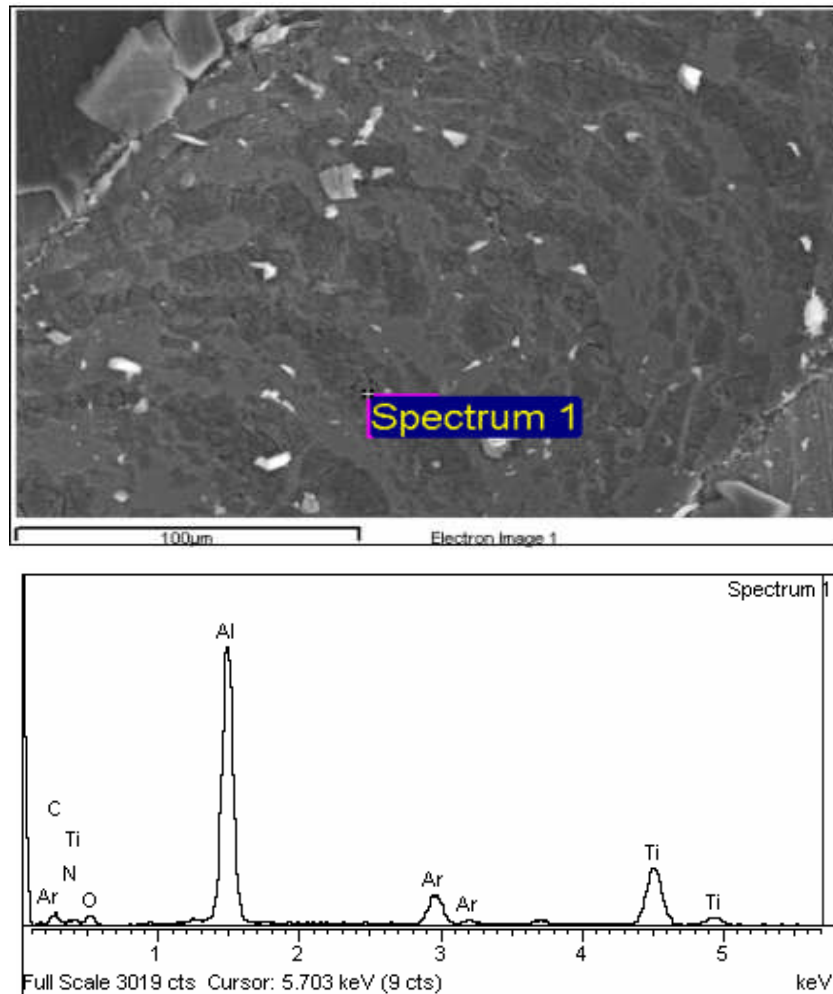


**Figure 147 – SEM micrograph and EDX spectra of the 20N constant load scratch scar in the  $TiB_2$  sputtered in a  $Ar + 7.5\% CH_4$**

There is still some coating left as we can see in Figure 147. The only difference is that regions where the coating has been removed are low in titanium and absent in boron evident by comparing the EDX spectra. From Figure 127 there is a boron spectra present, which is not present in Figure 147, equally the relative height of the aluminium peak, from the substrate has increased, This can be explained by the penetration depth of the electrons and sampling volume (pear volume) of the EDX detector and the fact that the coating is very thin in the area where spallation has occurred.

## 8.5. TiB<sub>2</sub>/DLC by Pulsed DC in Ar +7.5% CH<sub>4</sub>

### 8.5.1. Introduction

In the last decades, there has been a steady increase in the industrial use of diamond-like coatings for a wide variety of applications, like: cutting tools, wear resistant parts [236]. As was discussed in section 4, DLC coatings provide an array of desirable properties like high hardness, low friction, electrical insulation, smoothness, and good wear resistance [117, 138, 141, 142, 147, 236, 237]. As it was discussed in sections 8.2 and 8.3, Diamond-like carbon is a combination of sp<sup>2</sup> and sp<sup>3</sup> hybridized bonds. It can also be known as amorphous hydrogenated diamond-like carbon (a-C:H). The sp<sup>2</sup>/sp<sup>3</sup> ratio depend of adsorbed (i.e. chemically bonded and/or mixed) hydrogen atoms [117, 224]. As described in sections 4, 8.2 and 8.3, the performance of DLC based coatings depends on the different the bonding structure, the ratio between sp<sup>2</sup> and sp<sup>3</sup> [117]. This can lead to critical failure of the coating limiting the application range.

In previous sections, 8.2 and 8.3 it was demonstrated that the properties of diamond-like carbon coatings can be enhanced by the use of a ceramic, in this thesis TiB<sub>2</sub>, in a multilayer arrangement. In this section a set of 4 multilayer coatings was produced with a TiB<sub>2</sub> and DLC with volume fractions between 5% and 25% as discussed previously in section 7.2.1.

The deposition chamber used was a Leybold L560 box coater described in section 7.1. The ceramic component of the multilayers, TiB<sub>2</sub>, was deposited using pulsed DC in a pure Ar atmosphere, the deposition conditions were described in section 7.1. The DLC was deposited using a mixture of Ar + 7.5% CH<sub>4</sub> gas using a Pulsed DC generator to ionize the gas.

These coatings have been deposited on Al alloys substrate to improve the alloys hardness and wear resistance as it was described in section 7.3.2.

## 8.5.2. Results and discussion

### 8.5.2.1 Multilayer Hardness

The hardness and reduced modulus of the TiB<sub>2</sub>/DLC multilayers are showed in Figure 148 and Figure 149. In Figure 148 as the ceramic content is increased form 75% to 95% the hardness also increases from 21.7 GPa to 27.8 GPa. In this study the composition wavelength ( $\lambda$ ) was kept constant at 200nm. The thickness of the individual layers varied form 150nm to 190nm for the TiB<sub>2</sub> ceramic with DLC thicknesses decreasing from 50 nm to 10 nm.

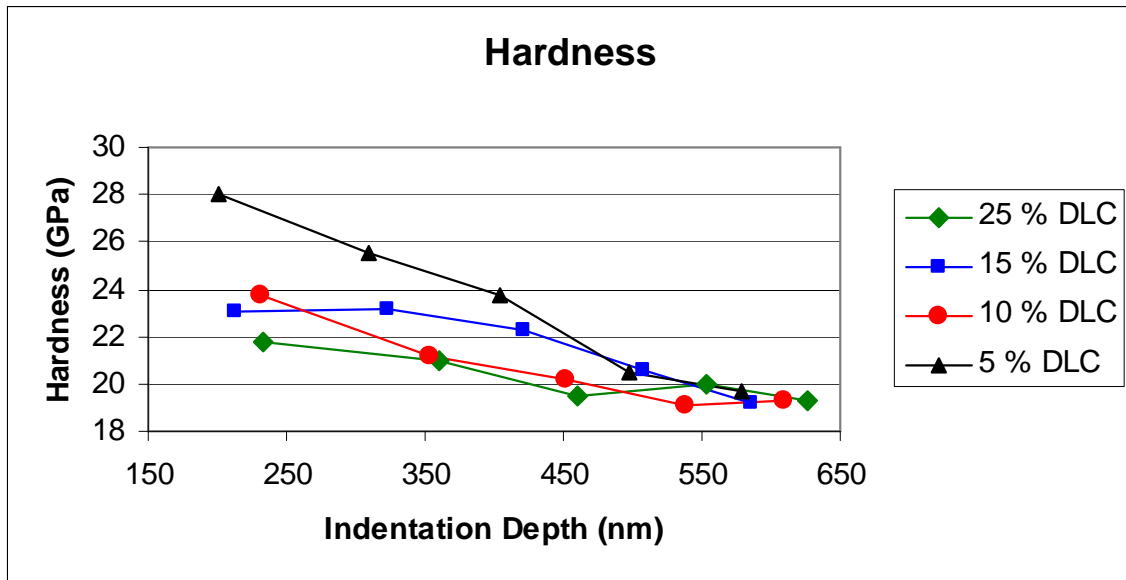


**Figure 148 - The hardness of the multilayer films as a function of indentation depth. The hardness for the 5 % DLC containing films is approximately 28 GPa, which decreases to 21 GPa for the 25 % DLC containing film.**

From the figure is possible to see a change in slope for coatings that containing 10% and 15% DLC. This change in slope indicates that there is possibly two different mechanisms occurring, one at low ceramic volume fractions and the second at high ceramic contents. These mechanisms suggest that the individual layer thickness is an important parameter and the properties depend less on the number of interfaces present in the coating.

In Figure 149 it is possible to see that the reduced modulus values are also influenced by the ceramic content, increasing from 204.6 GPa for 75 % TiB<sub>2</sub>, to

279 GPa for the 95 % TiB<sub>2</sub>. For comparison the reduced modulus of DLC is 162 GPa [238] and sputtered TiB<sub>2</sub> is 290 GPa. The variation in mechanical properties depends on the thickness of the individual layers, and also the number of interfaces present in the coating, which promotes hardening effects in the coating overall performance [239].

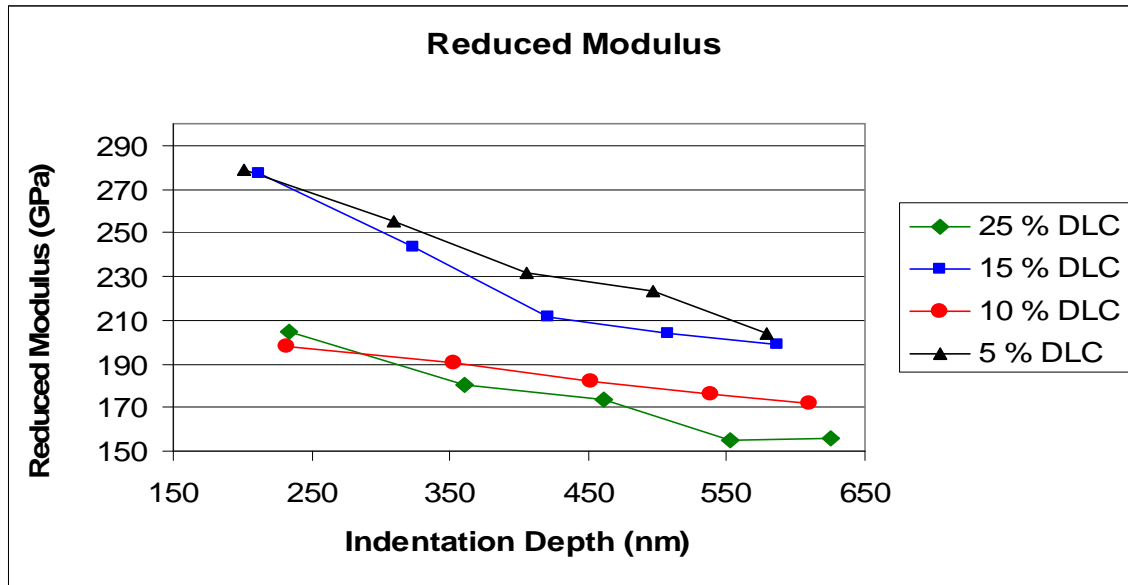


**Figure 149 - The reduced modulus of the multilayer films as a function of indentation depth. The reduced modulus for the 5 % DLC containing films is approximately 280GPa**

The hardening mechanisms, reviewed in section 2 are presented elsewhere [60, 63, 240]. The Koehler hardening [60] depends on the fact that the dislocations in the lattice are stopped by the number of interfaces present in a material, which can explain the difference in elastic reduced modulus. As discussed in section 5, elastic reduced modulus is a composite modulus which takes in account the film properties and the indenter properties to reduce the influence of the contact mechanics between the film and the indenter during a test, which can induce microplasticity.

Gouldstone et al [241] demonstrated that nanoindentation of a thin film is composed of purely elastic behaviour with occasional microplasticity. Microplasticity is the plasticity that exists in points of stress concentrations, where the rest of the material is in the elastic domain. As reviewed in section 5

nanindentation depends on several factors, such as: surface roughness, residual stress, film thickness, residual stress, type and shape of the indenter used. The Berkovitch tip, used in the nanoindentation testing throughout this thesis, can influence the indentation response due to the stress/strain field caused by the sharp indenter tip [242, 243]. This stress/strain field caused by the indenter is responsible for the nucleation and motion of dislocations under the indenter to which expands beneath the indenter with the neighbouring zone being in the plastic limit [241-243].

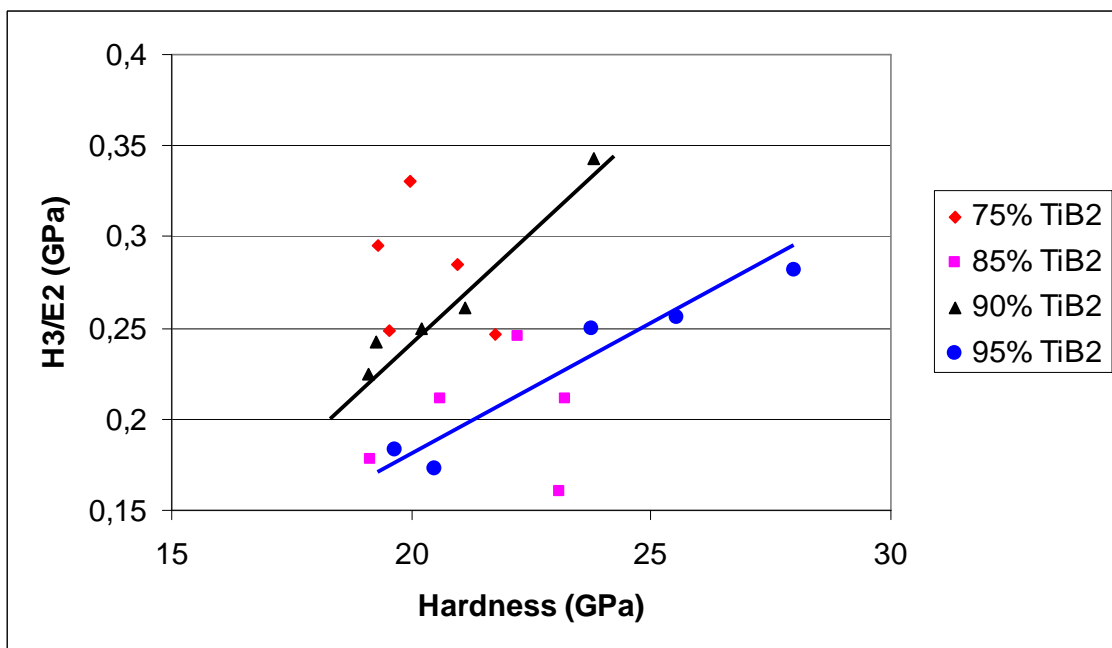
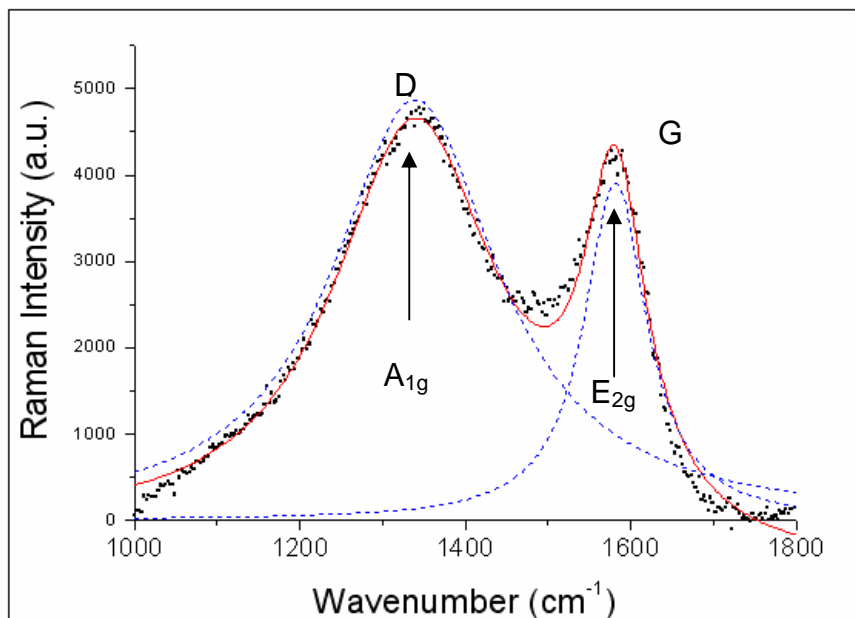


Figure 150 – The calculated  $H^3/E^2$  ratio for the multilayers fabricated in this section

In Figure 150 calculated  $H^3/E^2$  is plotted against hardness for these coatings, it shows that for the higher concentrations of ceramic, 90% ( $\blacktriangle$ ) and 95% ( $\bullet$ ) the ratio follows a trend. The lower ceramic content 75% ( $\blacklozenge$ ) and 85% ( $\blacksquare$ ) presents a similar behaviour which does not follow any trend. The absence of a trend in the low ceramic contents can be explained by the formation of a Ti(B,C) reaction zone with well defined thickness and will be explained in the section 8.6.

Several authors [124, 125, 230, 244, 245] have studied the deposition of diamond-like carbon in a reactive atmosphere with a hydrocarbon gas. The use of a hydrocarbon gas permits the optimization of the diamond-like properties. In this section the diamond-like carbon was manufactured in a reactive atmosphere of Ar + 7.5% CH<sub>4</sub>. The diamond-like carbon was characterized using the same method as described in section 8.2. The diamond-like carbon presented a D peak at 1340 cm<sup>-1</sup>, and a G peak at 1588 cm<sup>-1</sup>. The ratio of the I<sub>D</sub>/I<sub>G</sub> was calculated using a Lorentzian fit and presented a value of 1.25 which shows that the amount of sp<sup>3</sup> content of in the film is above the 50% level. This spectra is plotted in Figure 151.



**Figure 151– Plot showing the Raman spectra of carbon sputtered in Ar 7.5 %CH<sub>4</sub>. For carbon the I<sub>D</sub>/I<sub>G</sub> ratio was 1.25 and indication of sp<sup>3</sup> bonding above 50 %**

Figure 148 and Figure 149, shows the hardness and reduced modulus values, which indicate that the high sp<sup>3</sup> content in the films, allowing the film to act as load bearing. The uncoated substrate presented an average hardness value between 110 - 120 HV. This load bearing capability was also described by Prakash et al [232], who studied the effect of carbon in a TiB<sub>2</sub> matrix from which the authors concluded that the formation of an interfacial layer of Ti(B,C) gives an increase in load bearing capability, caused by interlayer chemical adhesion [232].

### 8.5.2.2 Scratch testing of a TiB<sub>2</sub>/DLC Multilayer coating

As discussed in section 6, failure modes observed in the scratch test can depend on many factors. These are most easily characterised in terms of the relative hardness of substrate and coating, modulus, thermal expansion coefficient, roughness, loading rate, scratch speed, tip radius and tip wear [191, 193, 246, 247]. For the case of a typical Rockwell 'C' diamond indenter (120° cone with 200 µm hemispherical tip), scratching soft coatings on a soft substrate, the test is dominated by plastic deformation and groove formation and little or no cracking is observed in the coating except at very high loads. For hard coatings on soft substrates deformation of the substrate is predominantly plastic whilst the coating may plastically deform or fracture as it is bent into the track created by plastic deformation of the substrate. Therefore the testing done in this section was a constant load scratch test using, 2 N, 5 N, 7N, 10N, 15N, 20N, because the high load ranges (increasing load from 10 N to 60 N) would significantly create large deformation causing the film to be detached from the substrate.

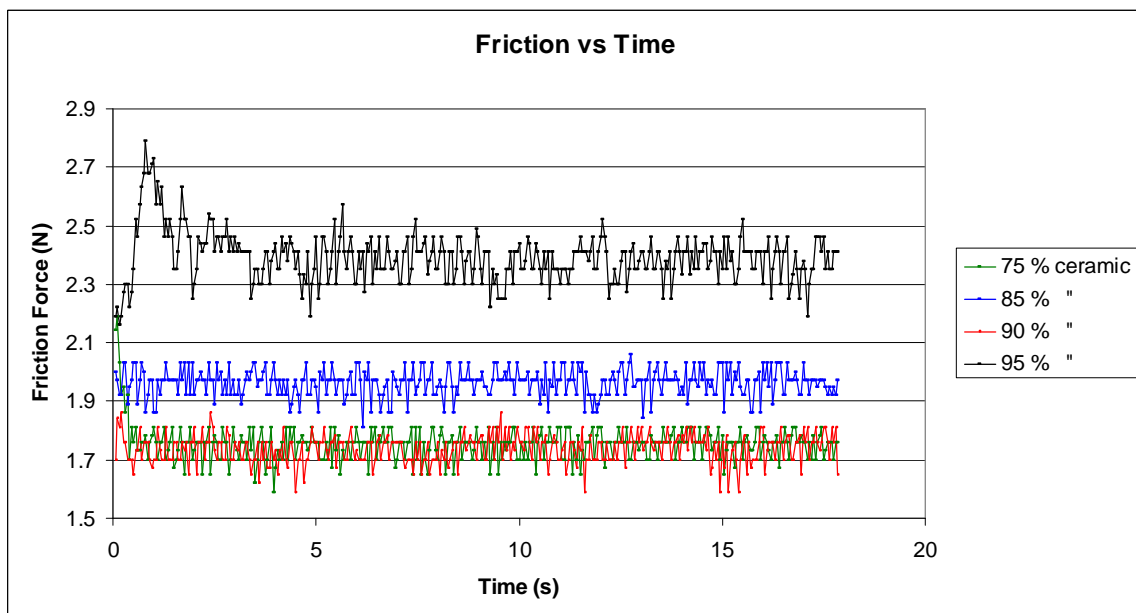


**Figure 152 – 2 N constant load scratch friction curve, where the 95 % ceramic shows failure occurring since the beginning of the test. The other ceramic percentages present similar behaviour but with no obvious early failure**

From observation of Figure 152, we can see that the behaviour of the low ceramic fractions is good when compared with the 95 % content film, which presents a higher friction force (2.3 - 2.5) leading to coating detachment, visible in Figure 153. At this low load for the 95% ceramic, there is a clear sign of failure as can see in Figure 153 and Figure 154. In Figure 153 one can see a FIB channel milled inside the scratch scar, in an area where some coating detachment has occurred.

For the 2N constant load scratch test on the 95% TiB<sub>2</sub> content on TiB<sub>2</sub>/DLC multilayer is observed that as the stylus is dragged across the surface, it detaches a part of the coating, leaving some coating inside the scratch scar as it is possible to see from Figure 154.

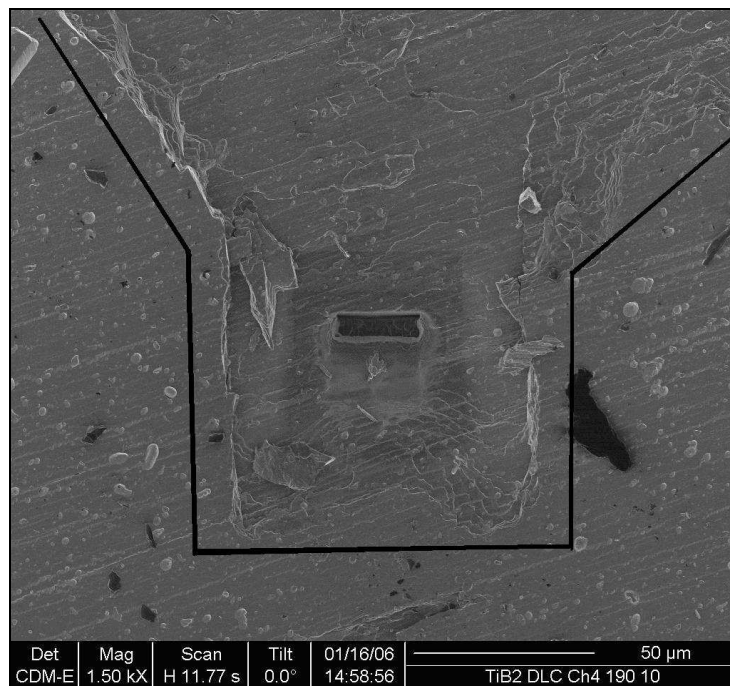


**Figure 153 – 2N constant load scratch test of 95% ceramic with a FIB milling inside the scratch scar, where some layers are removed**

Also it is possible to see signs of through-thickness cracking which is related to the high residual stress level formed after stylus passes over the track. These

through thickness cracks can lead to spallation. For the 95% TiB<sub>2</sub>/DLC coating each TiB<sub>2</sub> layer is 190nm thick and the DLC layer thickness is 10nm.

From a comparison of Figure 152 and Figure 155 one can see that the shapes of the curves are similar and the main difference being in the range of the friction force values in Figure 152 (1.7-2.7) and in Figure 155 (2.2-2.9).

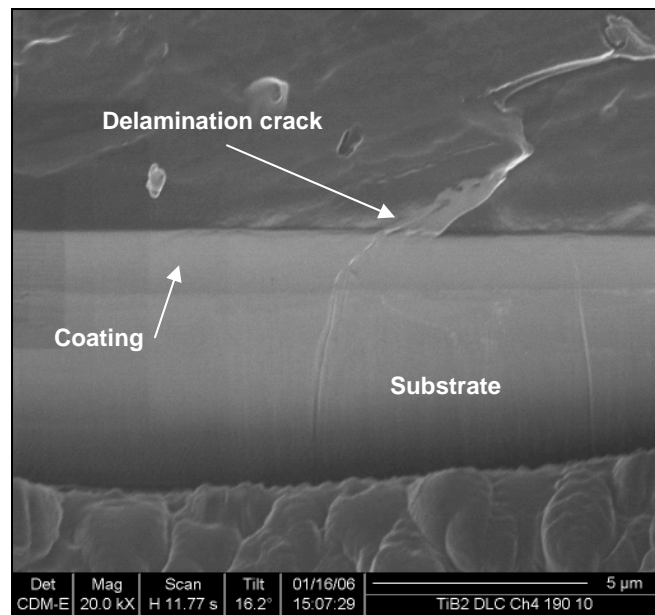


**Figure 154 – Multilayer cross-section of 2N constant load scratch where cracking runs through the thickness of the coating to the substrate**

This increase in friction force range is related to the different applied loading of the test (2N – 5N), the increase contact area between the indenter and the film and the response of the coating to the increased applied stress from the stylus.

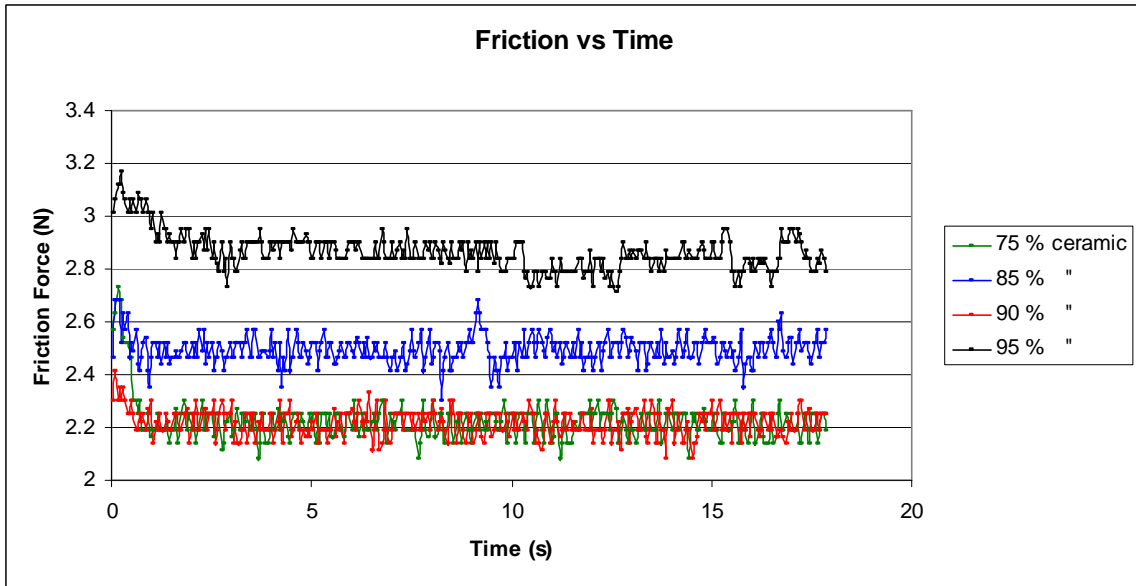


**Figure 155 – 5 N constant load scratch friction curve with failure occurring in the two top curves, 85 % and 95 % with a high coefficient of friction**

It can be noticed that some coating spallation/buckling occurs at 5N load as can be seen in Figure 156, and illustrates the response of the coating/substrate to the stresses generated in front of the moving indenter and in turn to the degree of through-thickness cracking.

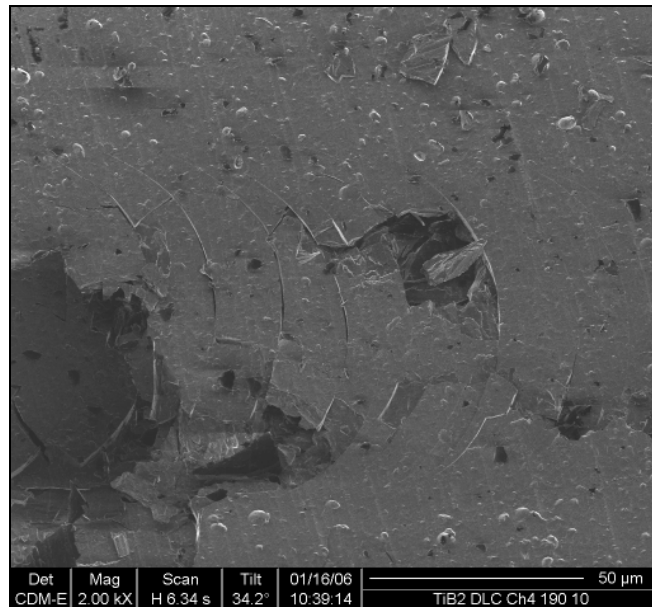


**Figure 156 – 5 N constant load scratch of 95 % ceramic in which the coating detaches in semicircular shape**

The AE signals during this scratch test at loads of 7N and 15N, Figure 157 and Figure 159, are a measure of the release of elastic energy from the film or from the interactions between the stylus, the coating and the substrate as a result of the friction forces, coating cohesion and adhesion.

In Figure 157 and Figure 159 there are some big variations in the AE response; those variations (highlighted in the Figures) can be interpreted as being energy released from the coating due to crack growth/propagation, small jumps are probably crack growth, while larger jumps are crack initiation and propagation.

The scale of the acoustic emission signal depends on the size of the crack produced since the energy in the AE signal scales with the energy released in the process [199].

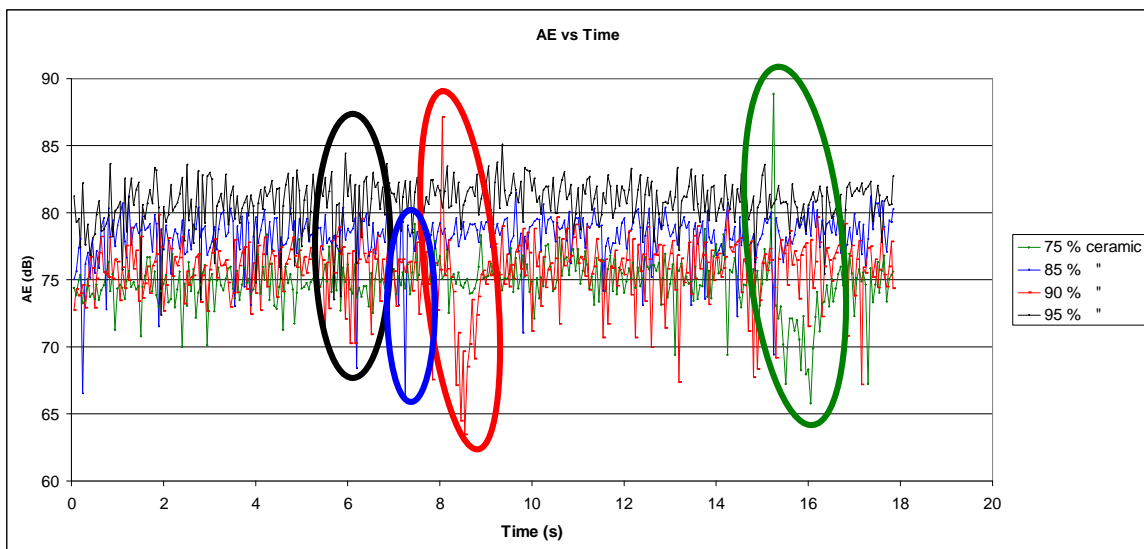


**Figure 157 – Acoustic emission 7 N constant load scratch where the variations of the curves are linked with the release of elastic energy from the film or from surface interactions such as friction and adhesion**

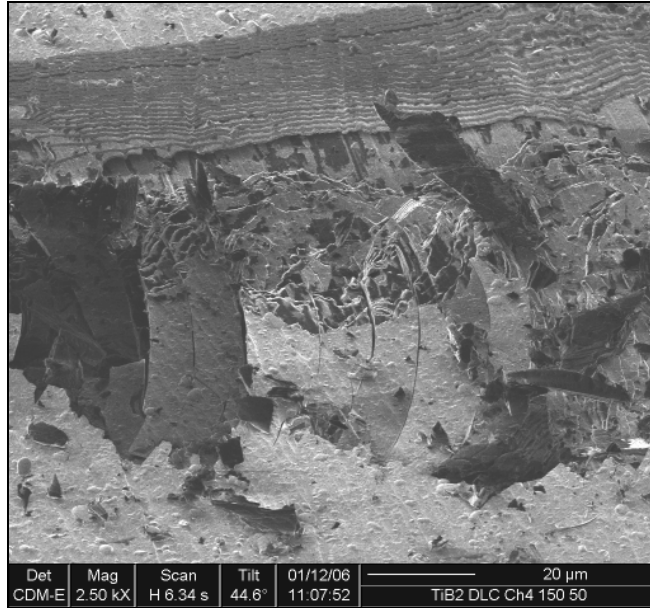


**Figure 158 – 7 N constant load scratch of 75 % ceramic in a failure region where its possible to see a region with removed coating (edge of the scar) and inside the scratch there is some coating left**

In Figure 158 for this coating, at 7N constant load scratch, the area of adhesive failure is large compared to the area of through-thickness cracks as described in previous section 8.4; a large variation in the acoustic signal is an indication of adhesive failure which is visible in Figure 157.

As described previously from the observation of Figure 157 the acoustic emission at 7N constant load scratch and observing the FIB micrographs, Figure 160 - Figure 162, clearly show adhesive failure occurring during the test.

From the AE at 15 N visible in Figure 159 and the observation of the FIB micrographs Figure 160 - Figure 162 we can see that spallation is observed and the coating is detached in relatively big pieces. This too minimizes the amount of elastic energy stored by the compressive stresses generated by the moving stylus as the test proceeds.

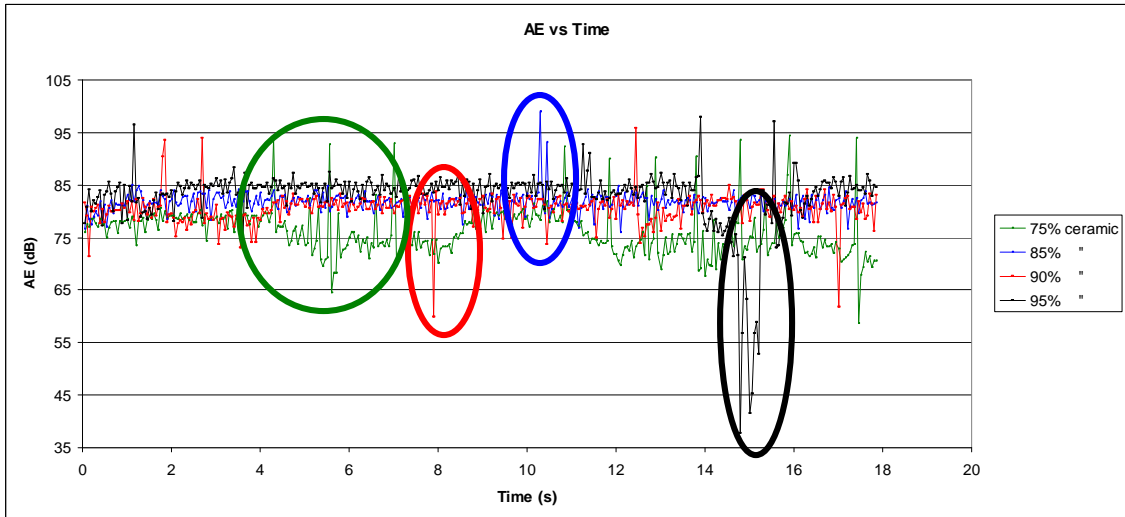


**Figure 159 –AE 15 N with failure occurring in all the coatings, to highlight the failure of the 95% ceramic**

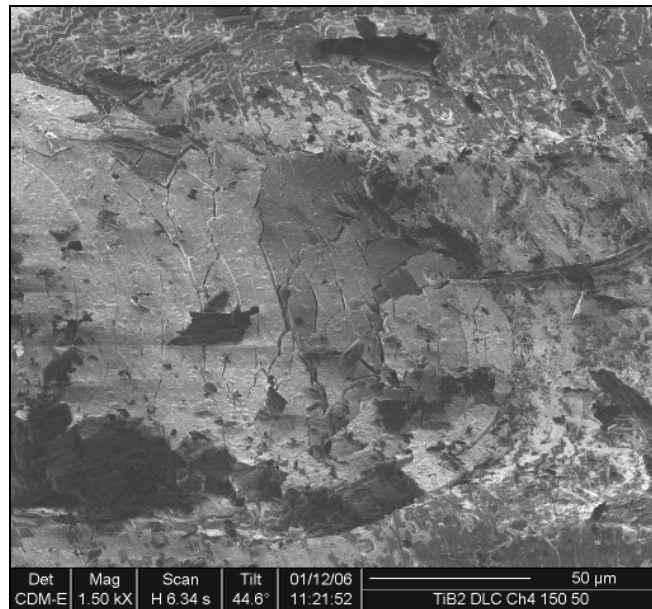


**Figure 160 – 15 N constant load scratch of 75 % ceramic where is possible to observe a transition zone where there is coating compressed to the substrate (left side) and coating removal (right side)**

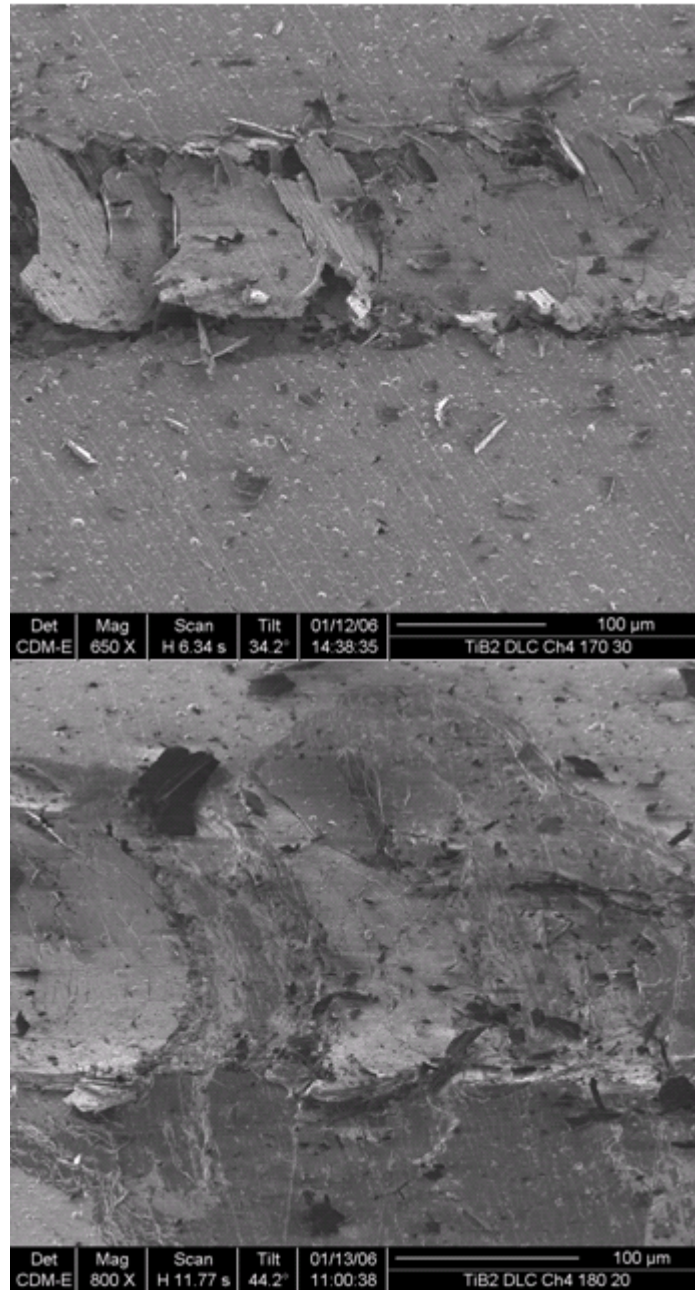


**Figure 161 – constant load scratch of 85% ceramic at 15N load where pieces of coating are detached along the scratch scar length**

Due to the high load (15N) in this test, these coatings show adhesive failure; they are loaded above the critical load which can be visualized in the form of semicircular cracks, and pieces with semicircular edges which propagate from the centre of the scratch line to the outside of the scar.

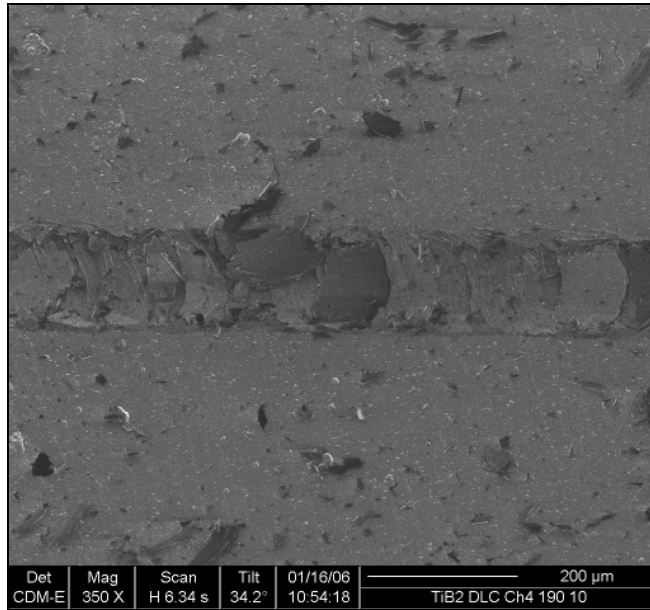


**Figure 162 – 15N constant load scratch where there are visible pieces detached from the substrate which remained on the surface of the scratch scar**

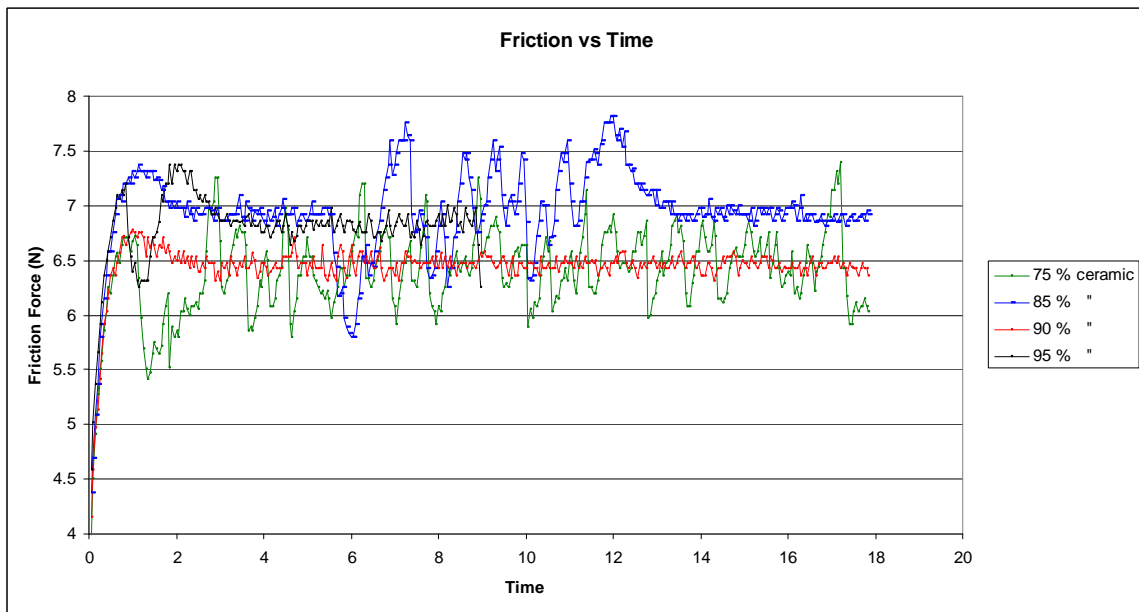


**Figure 163 – Friction curve of 20N constant load scratch where is visible variations of the friction curve indication severe failure as indicate in the micrograph visible in Figure 164**

In Figure 163 at 20N load, one can see that friction forces are very high (5.5-7.5). This is a clear indicator of coating failure due to the amount of stress generated during the test. These stresses caused delamination of the coating from the substrate.

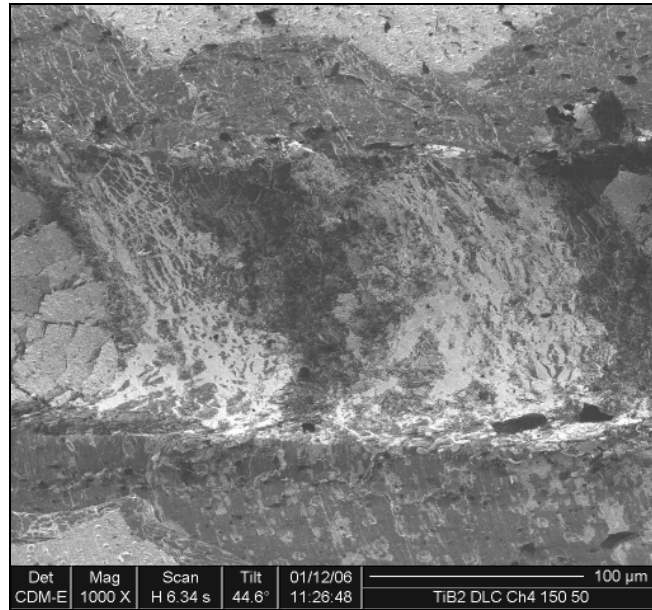


**Figure 164 – 20N constant load scratch where the coating is detached from the substrate and the damage is propagated to a region on the outside of the wear scar**

Spallation occurs when through-thickness cracks form in regions of high tensile stress within the coatings then these pre-cracked regions link together. Once a buckle has occurred ahead of the stylus, the scratch stylus passes over the failed region and can crush the coating into the surface of the scratch track formed in the substrate.

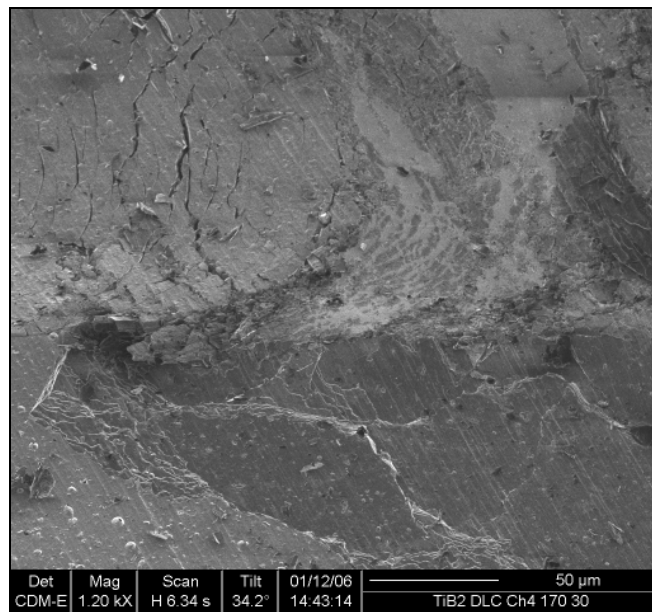


**Figure 165 – 20N constant load scratch of 85% ceramic where is visible two regions of failure, compressed coating (left side of the picture) and detached coating (right side of the picture)**

Coating removal can be enhanced at this point or the failure may no longer be visible, disappearing completely depending on its size and the toughness of the coating. This can be seen in Figure 164 -Figure 166.

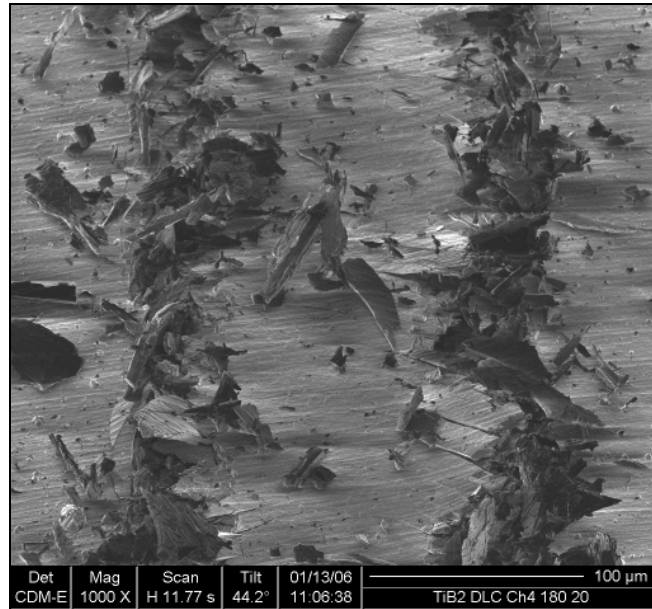


**Figure 166 – Failure on the edge of the scratch from a 20N constant load scratch where the amount of recovery spallation in the edge of the scar is visible**

### **8.5.2.3 Multilayer Wear Testing**

In Figure 167 it is possible to see the evolution of the friction coefficient, which is continuously monitored by the friction force between the WC ball and the sample. It can be seen that all the multilayers with different DLC contents have a similar friction coefficient.

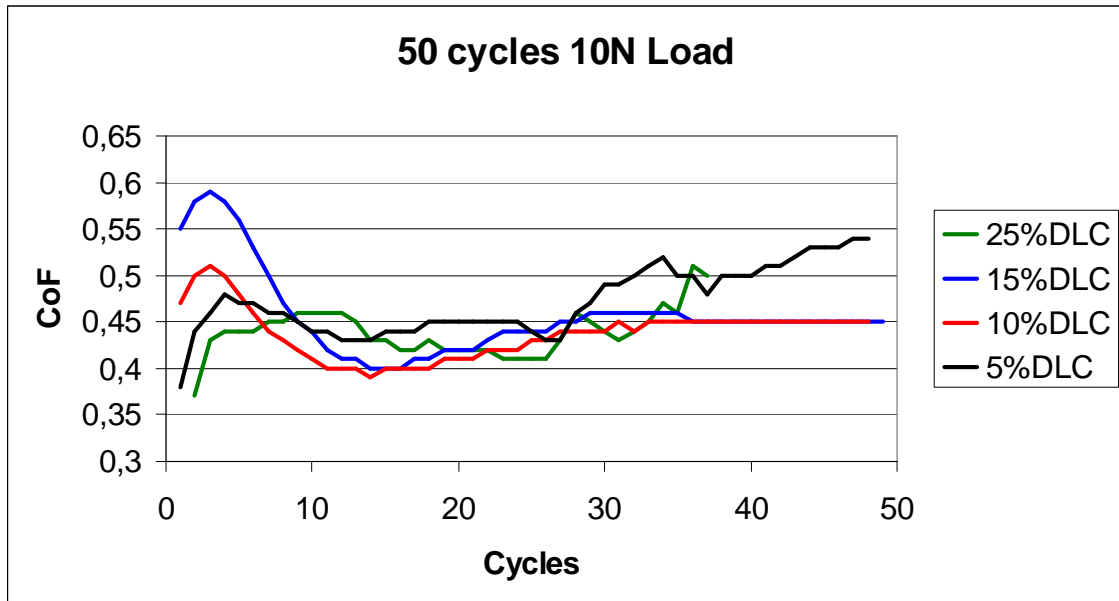
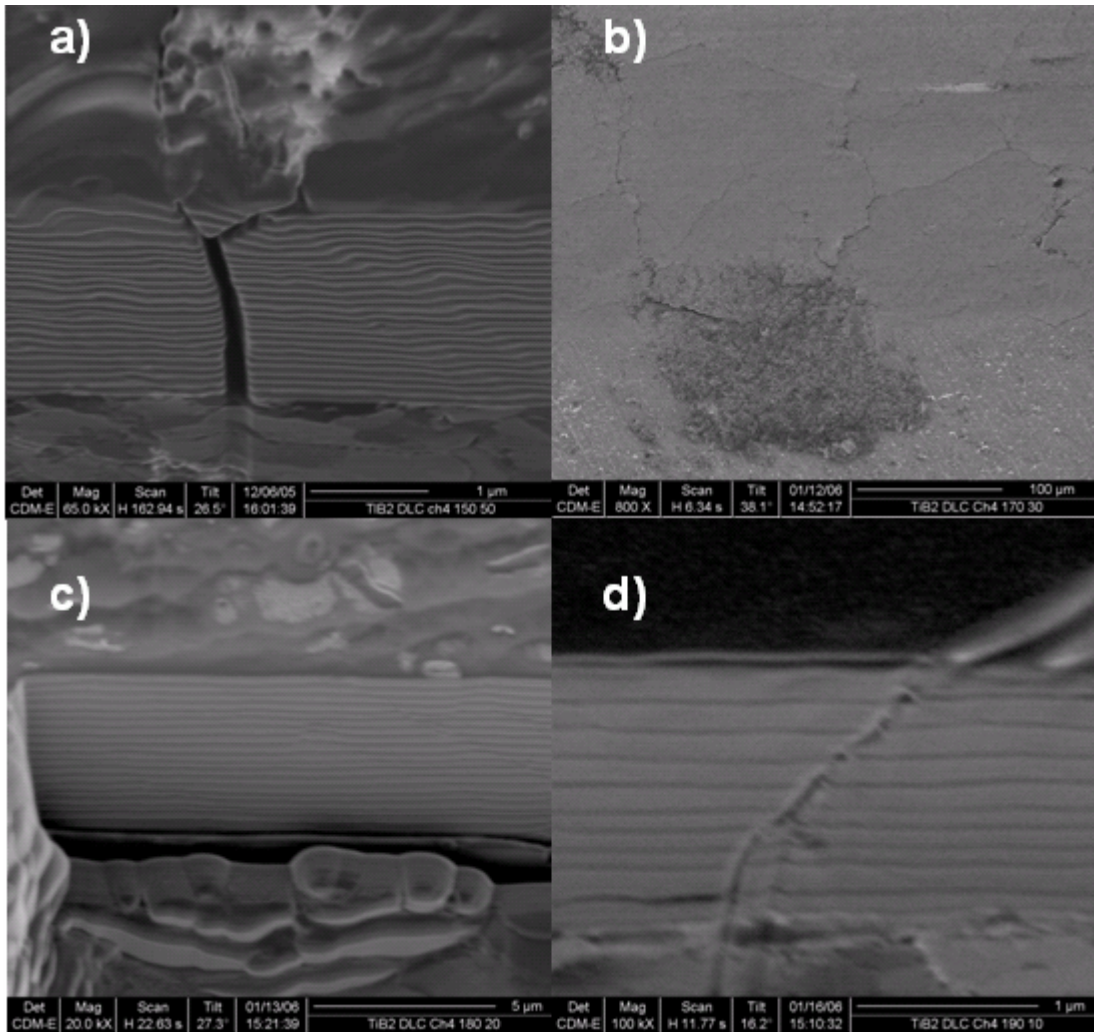


Figure 167 – Bidirectional Wear testing of 50 cycles at 10 N loads.

In Figure 168a) and d) It possible to see that cracking occurred from the surface to the substrate at a 10N load, caused by the deflection of the film as the indenter passes. As the indenter is dragged across the surface there is interaction between the surfaces in contact, causing debris to be detached, visible in Figure 168b). This has a direct influence in the friction values. Figure 168 c) presents a FIB cross section of the coating with a 10% volume fraction presented no cracking during the test.

In the literature, Podgornik [248] and Erdemir [244] have reported that the friction coefficients for DLC films varies form 0.01 to 0.5 depending how the DLC is deposited as well the type of test conditions used. Furthermore, Podgornik [248] and Qia [128] have reported that in DLC films, the friction coefficient is limited due to the formation of a transfer film at the interface, which is easily sheared. The friction coefficients values result form chemical or physical interactions, such as Van der Waals forces, electrostatic attractions and capillary forces.



**Figure 168 – FIB milling inside a 10N bidirectional friction test: a) 25 % DLC where through thickness cracking inside the wear scar propagated to the substrate; b) surface micrograph of surface cracking of 15 % DLC; c) cross section micrograph of 10 % DLC multilayer inside the wear scar with no visible damage on the layers; d) cross section of a 5 % DLC multilayer with crack propagated from surface to substrate.**

Donnet [236] has identified the origin of high friction coefficients for hydrogenated carbon films. It is due to the interaction between the counter surface and the dangling bonds of the carbon atoms. The deposition of DLC in a hydrocarbon atmosphere stops the interaction between the counter surface and these loose bonds, which are reduced by the reaction with hydrogen atoms present in the reactive gas. This leads to the passivation of the surface which, otherwise, would be likely to react with the atmosphere [124, 244, 245].

The worn coatings exhibit very smooth surface topography, Figure 169. The deformation of the substrate is significant due to the poor load-support capacity

of this aluminium alloy, thus the film deflects in relation to plastic damage to the substrate. The deformation of the substrate would as a result add either a ploughing or hysteresis effect to friction forces.

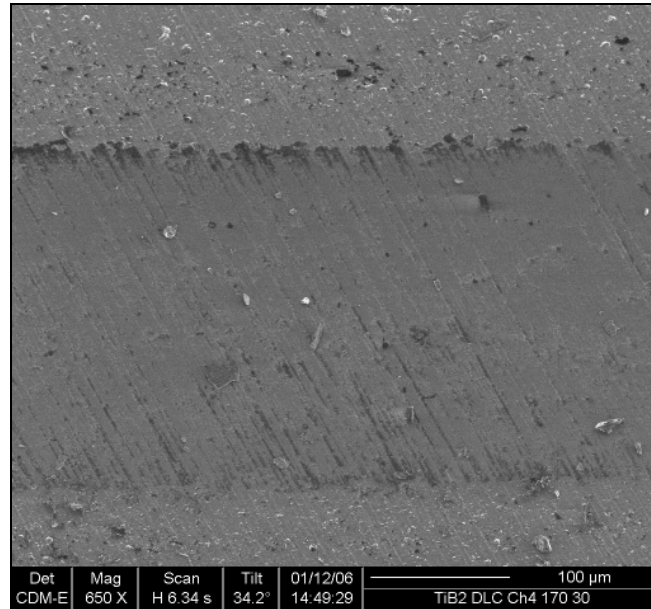


**Figure 169 – bidirectional wear scar of 85 % ceramic content at 10N load with sign of wear with some visible deformation inside the wear scar**

When the wear of the surface achieves a steady state during the test, this is due to the lubricant effect of the material released from the coating, when sometimes transfers to the WC ball, where it may work as a contact surface. At the edge of the scar some debris is deposited during the test. Such debris are pieces of detached coating and material transferred from the WC ball used during the test. As we can see from the EDX spectra Figure 170, for the sample 170 nm/ 30nm (85 % ceramic) TiB<sub>2</sub>/DLC coating material transfer occurs as evidenced by the presence of W on the edge of the wear scar.

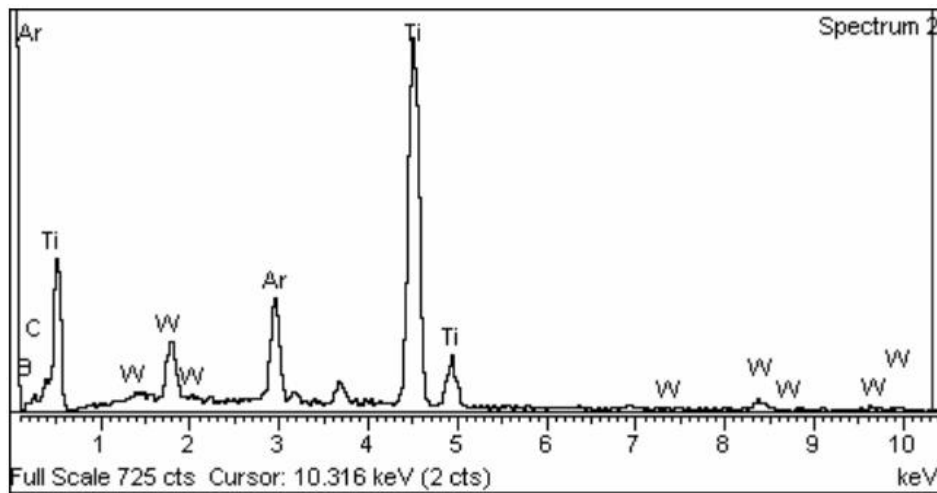
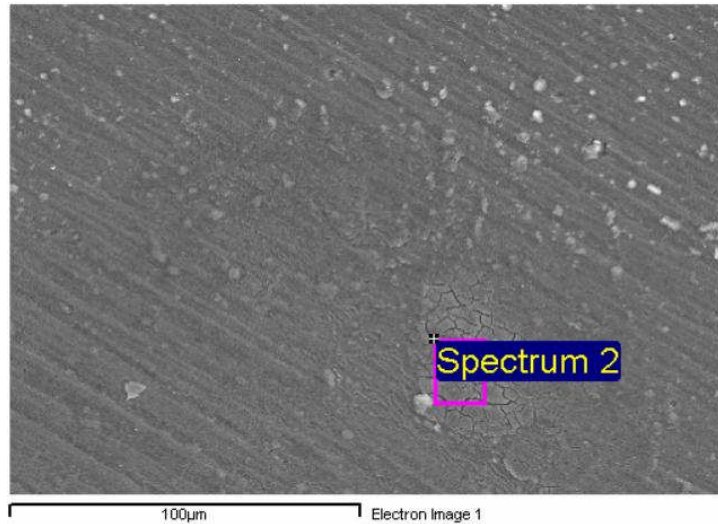


**Figure 170 – SEM micrograph and EDX spectra of wear scar in the multilayer with 85% ceramic content with presence of a W peak as a result of material transfer from the test apparatus**

From these tests Figure 171 shows that the high percentages of  $TiB_2$  ceramic in the  $TiB_2/DLC$  coatings, with 50%  $sp^3$  bonding in the DLC, gives a high wear scar volume; this is measured from the dimensions of the wear scar. It reveals that for a 20nm difference in layer thickness results in a large effect on the coating tribological performance. For the high percentages of ceramic the harder nature of the films is shown to result in a smaller wear scar volume.

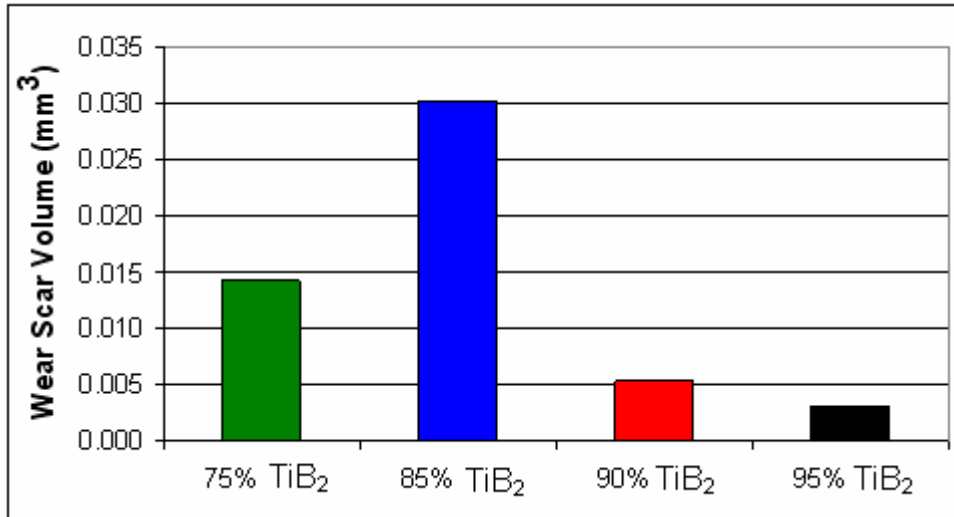


Figure 171 – Wear scar volume for during the bidirectional wear test at 10N load

### 8.5.3. Conclusions

- Multilayer coatings were fabricated with a TiB<sub>2</sub> ceramic fraction ranging from 75% to 95% and the DLC varied from 25% to 5% respectively. The bilayer thickness was kept constant at 200nm. Each coating had 25 individual layers of TiB<sub>2</sub> and DLC. The TiB<sub>2</sub> layer thickness varied from 150nm to 190nm and the DLC layer varied from 50nm to 10nm. The coatings were produced using pulsed-DC magnetron sputtering in a reactive atmosphere of Ar + 7.5% CH<sub>4</sub>.
- The thickness and quality of the DLC layer influences the mechanical properties of the multilayer stack. This effect on mechanical properties, hardness and reduced modulus is due to a change in the chemical bonding between the TiB<sub>2</sub> and the DLC, which forms an interfacial layer of Ti(B,C), and a possible depletion in the sp<sup>3</sup> diamond like bonding in the carbon layers within the multilayer stack.
- The hardness values were calculated from the loading portion of load-displacement curve and presented values of 21.7 GPa to 27.8 GPa for the 25 % and 5 % DLC containing coatings. The reduced modulus was calculated from the unloading portion of the curve and present values of 204 GPa to 279 GPa for 25 % and 5 % DLC content. The high ceramic

contents have a direct influence on the hardness which increases significantly for coatings with a DLC layers smaller than 20nm,

- The adhesion of the multilayers was evaluated by constant load scratch test, with loads ranging from 2N to 20N. Tensile cracking within the wear track was observed at 5N and 10N loads. The critical loads for delamination of the multilayers were around 15N, with signs of spallation and hertzian cracking.
- For the high ceramic content 95% the friction coefficient value was 0.47, while for the low ceramic content the friction coefficient was 0.43. These high friction coefficient are caused by the interaction of the loose carbon bonds with the counter surface, as explained in the work from Erdemir et al [244] and Donnet et al [245].

## 8.6. Summary Discussion

In Figure 172 the values of hardness for  $\text{TiB}_2/\text{C}$  multilayer films manufactured in pure Ar atmosphere are compared with earlier work from Silva Cruz [12]. Silva Cruz [12] multilayered  $\text{TiB}_2$  in a Ar atmosphere with a pure metals, Al, Ti and Hf. The composition wavelength ( $\lambda$ ) was kept constant at 200nm with a total of 50 layers and a total thickness of 5  $\mu\text{m}$ .

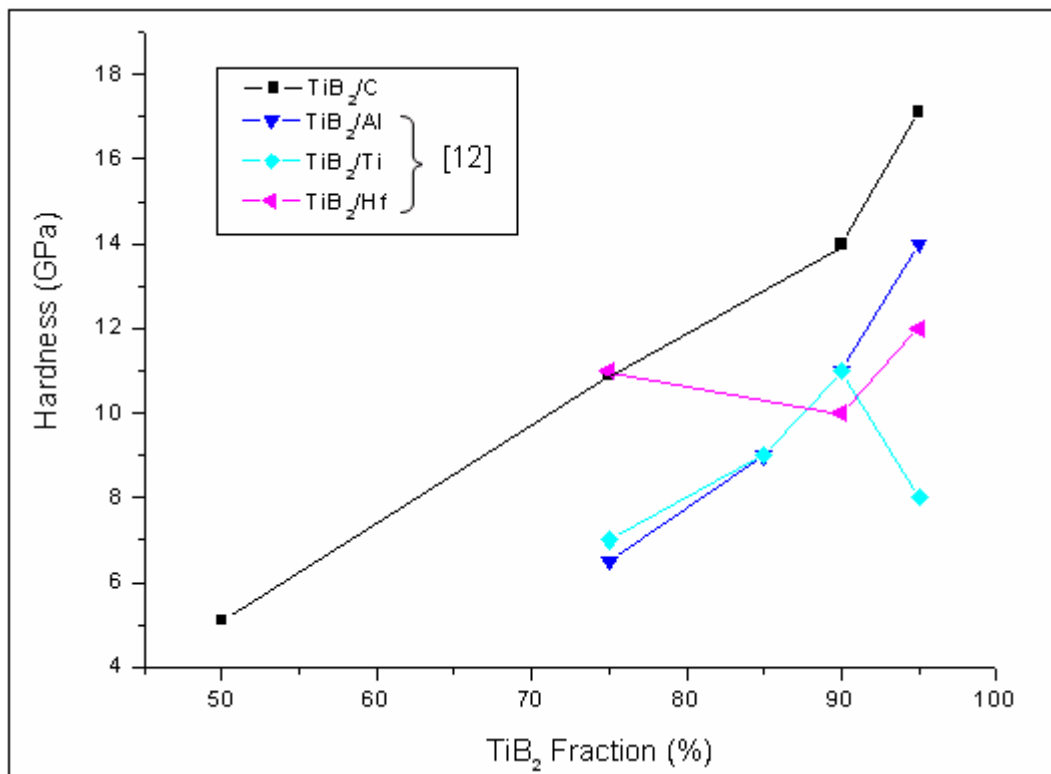
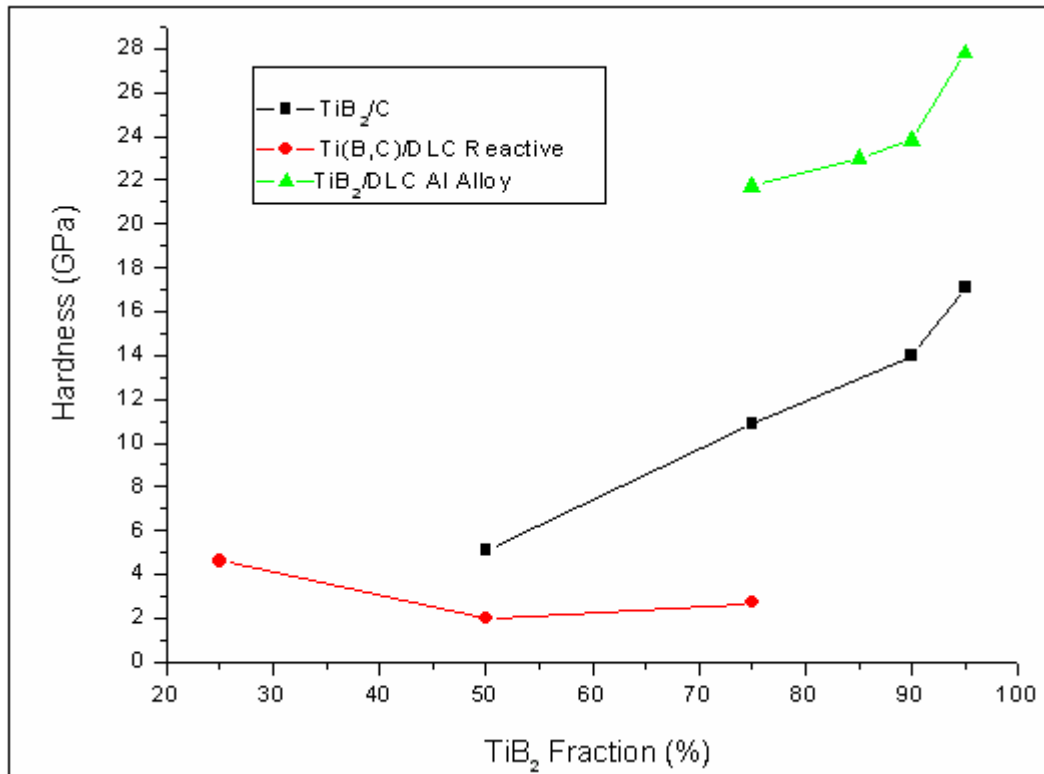


Figure 172 – Hardness comparison all the Multilayers produced in Ar atmosphere.

The  $\text{TiB}_2/\text{C}$  multilayers present a higher hardness ranging from 5.1 GPa for a 50% graphite layer to 17.1 for 5% graphite layer. While the hardness of the  $\text{TiB}_2$  multilayered with metal present lower hardness values ranging from 6.5 GPa to 14 GPa for  $\text{TiB}_2/\text{Al}$ .

In Figure 173 all the values of hardness for  $\text{TiB}_2$  multilayer with carbon (—■—) and DLC (—●—, —▲—) films are compared. The DLC manufactured in a reactive atmosphere of Ar + 7.5%  $\text{CH}_4$ , as discussed in 8.3, present the lowest hardness

values. This is due to the reduced ceramic fraction (25% - 75%), the nature of the Ti(B,C) layer formed, the reduction of the number of layers (20) and therefore the total coating thickness (2 $\mu$ m), similar effects are observed in the reduced modulus, Figure 174.



**Figure 173 - Hardness comparison between all the multilayers with carbon produced.**

These low hardness values are due to the coating design, highest carbon contents. The DLC layer is progressively replaced by an amorphous graphitic carbon as the carbon thickness is increased, thus the hardness and reduced modulus are increased due to increased sp<sup>3</sup> content in the carbon film. In low ceramic content films which have been deposited in a reactive atmosphere the Ti-B-C/DLC multilayers does not have a comparable performance to the other multilayers, TiB<sub>2</sub>/C and TiB<sub>2</sub>/DLC deposited on Al alloys. As observed in Figure 173 and Figure 174. The DLC multilayers have a good performance producing the higher hardness data and reduced modulus data in the high range of Figure 174. This is due to the high quality of the TiB<sub>2</sub> layers which were manufactured after the study of different methods of generating the plasma and thus

deposition. These were compared in section 8.1, and the high quality DLC layers manufactured in section 8.3. Some scatter is visible in the TiB<sub>2</sub>/DLC Al alloy (▲) results are visible and this is due to the very soft substrate used for coating, which has a reduced modulus of around 100 GPa and had an influence on the reduced modulus results.

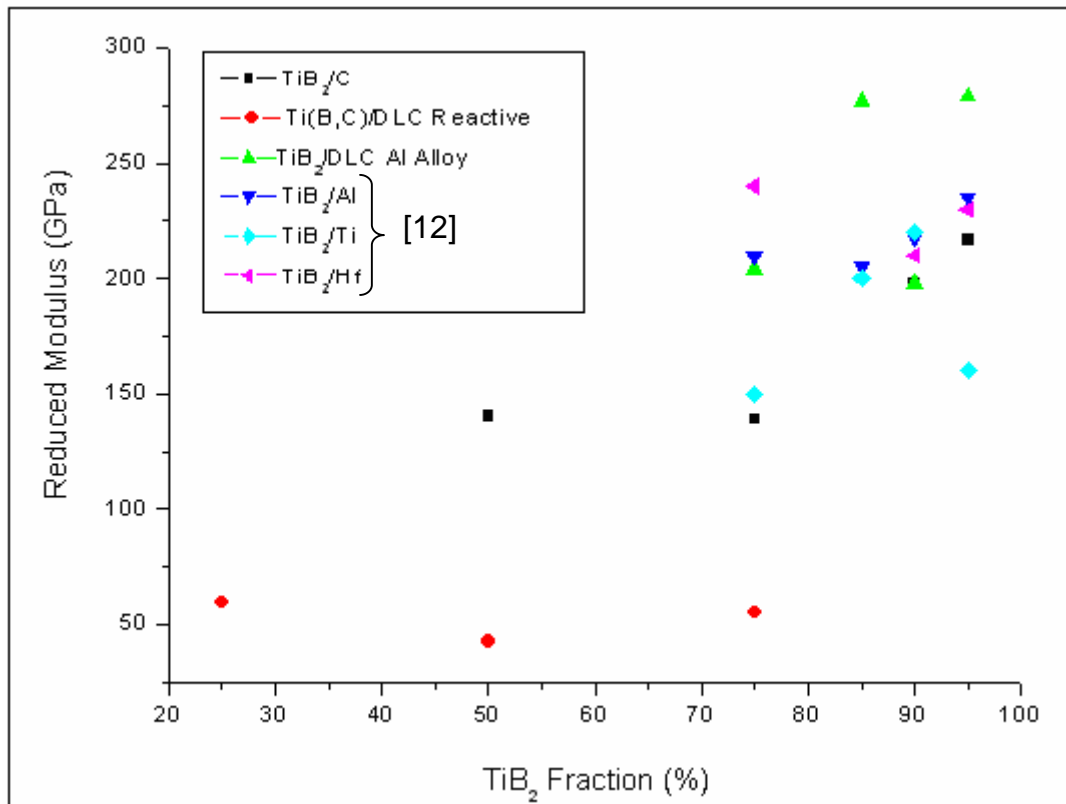


Figure 174 – Reduced modulus comparison of all the multilayers produced

In Figure 175 the  $H^3/E^2$  ratio for all the multilayers produced in this study are plotted together with the work done by Silva Cruz [12] where is possible to see graphitic carbon multilayers are not superior to metal multilayers in resistance to plastic deformation.

The DLC multilayers present by far the higher ratio, as visible in the figure above. This is due to the optimum deposition conditions of the DLC and TiB<sub>2</sub> layers deposited both using pulsed-DC.

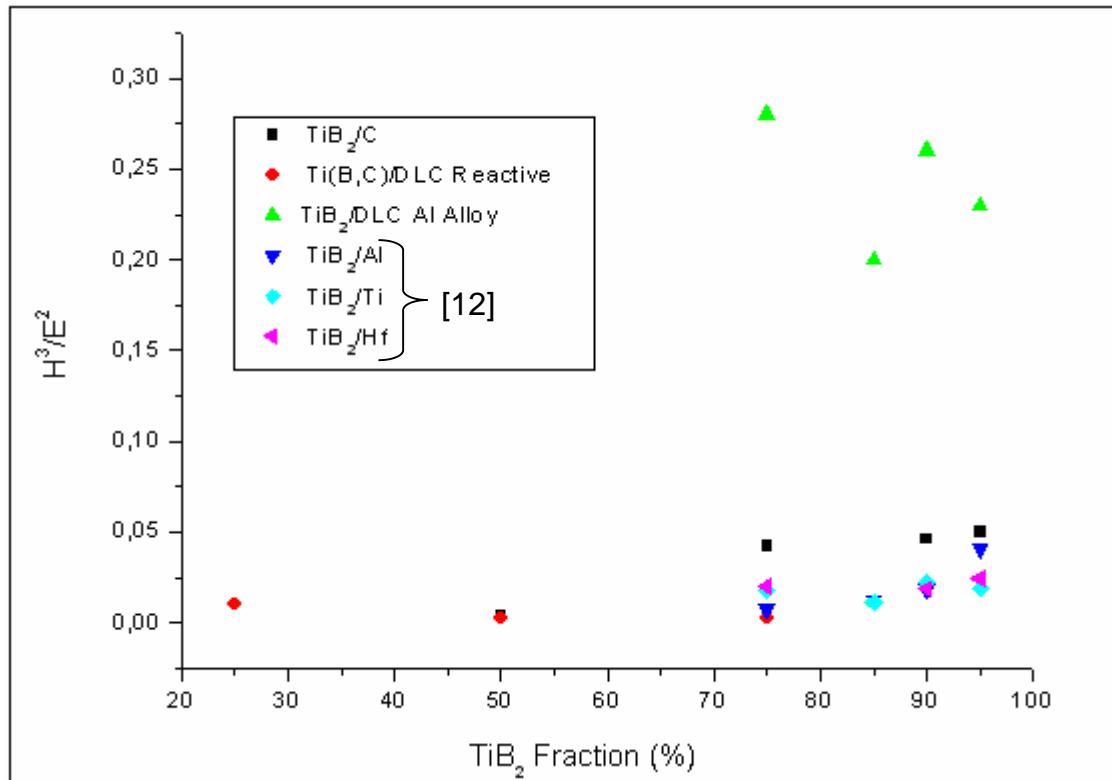
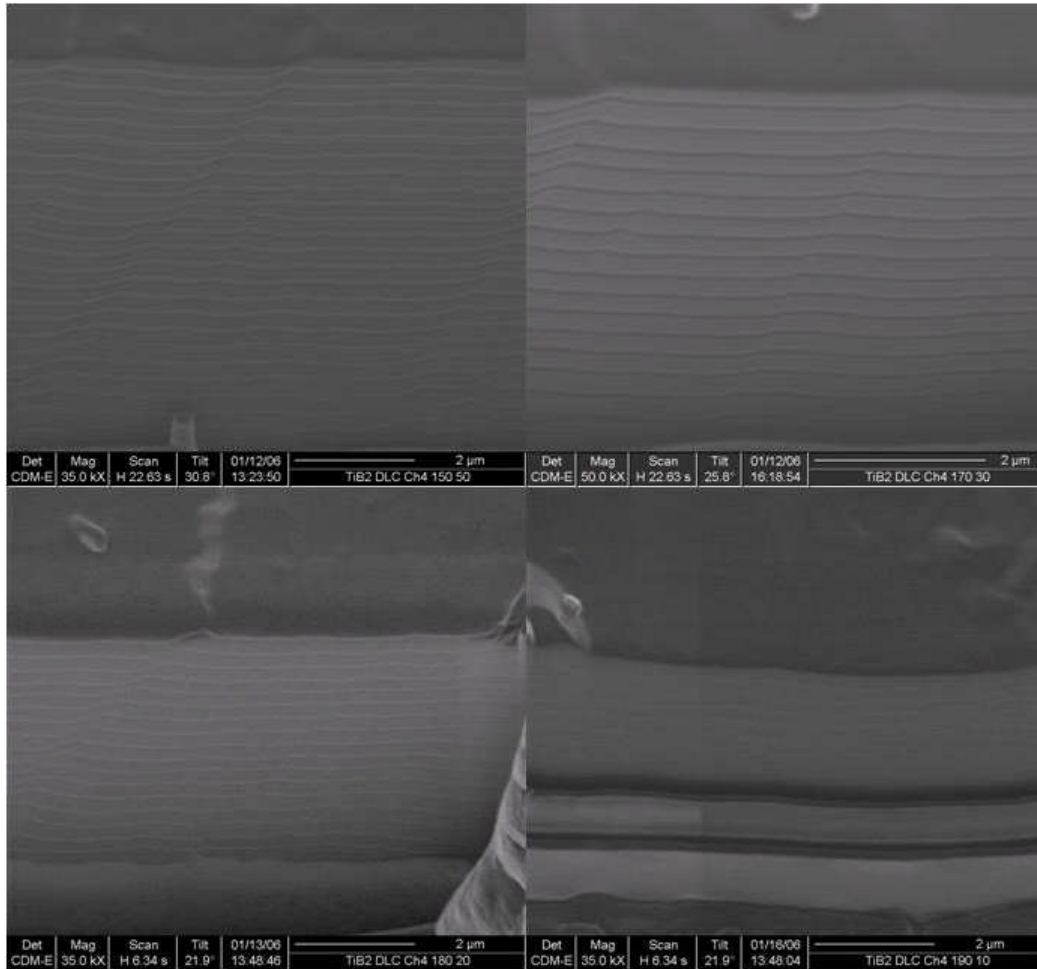


Figure 175 – Calculated  $H^3/E^2$  ratio from the Nanoindentation data

Visible in Figure 176 are the cross sections of the 4 multilayer stacks produced as discussed in section 8.5. The coatings microstructure is very dense and does not present any signs of delamination from the substrate surface any debonding in the layered structure. This is an indicator that the interface between the layers of DLC and TiB<sub>2</sub> is strong. Thus at the interface level Ti-B-C may form where it contributes to the load bearing capability and to an extent can provide lubrication.



**Figure 176 – FIB cross section of the multilayers manufactured in section 8.5**

The friction coefficients for all the multilayers produced in this thesis are plotted in Figure 177. The graphitic multilayers present a low friction coefficient, but as the ceramic content increases the CoF also increases. This is due to the loss of lubricant properties of the graphite layers below a thickness of 20nm through the formation of a Ti(B,C) interfacial layer. As the layers are deposited the bonding is preferentially done through the Ti component, as the incoming atoms saturate the interface. A similar effect was reported by Gilmore [113-115]. The TiB<sub>2</sub> phase is dominant, thus the multilayer stack loses its lubricant properties, but retains a high resistance to indentation.

The nature of the lubricant layer can be changed from graphitic to DLC as reported in sections 8.2 and 8.3, and this gives an increase in the friction coefficient. This increase in friction coefficient is caused by interactions at the

DLC interfaces, which may result from various combinations between chemical or physical interactions as was earlier discussed, before section 8.5. The high CoF (0.45) presented in these DLC films manufactured in a reactive atmosphere when a hydrogen rich gas is used. This results by the loose linking of carbon bonds with the counter surface due to the lack of energy during deposition. Similar effect was observed by Donnet [236] and Erdemir [244].

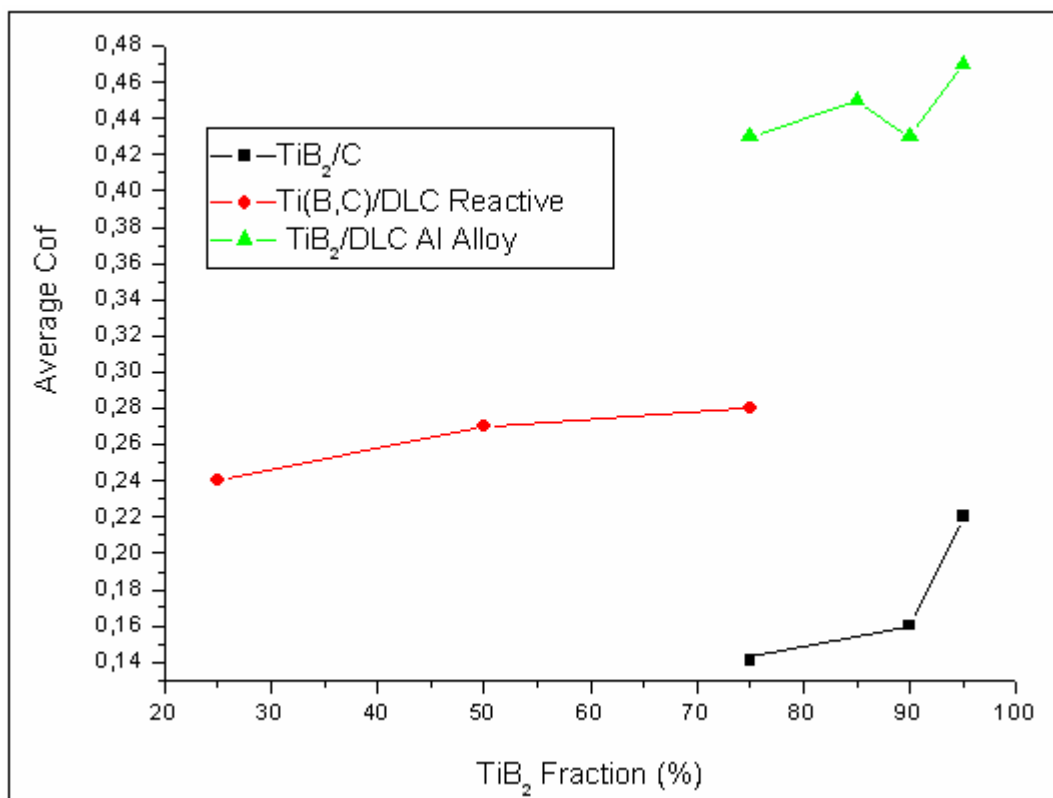


**Figure 177 – Average friction coefficient of the Multilayer coatings**

These high friction coefficients have a direct impact on the wear scar volume, Figure 178. Due to the high friction coefficient of the TiB<sub>2</sub>/DLC multilayers (~0.4) deposited onto Al alloys, the multilayers present a high wear scar volume, which is a function of depth of the indenter during the test. As a result the multilayer, although had a high friction coefficient, presented some signs of cracking but to an extent that was not sufficiently critical to cause surface delamination.

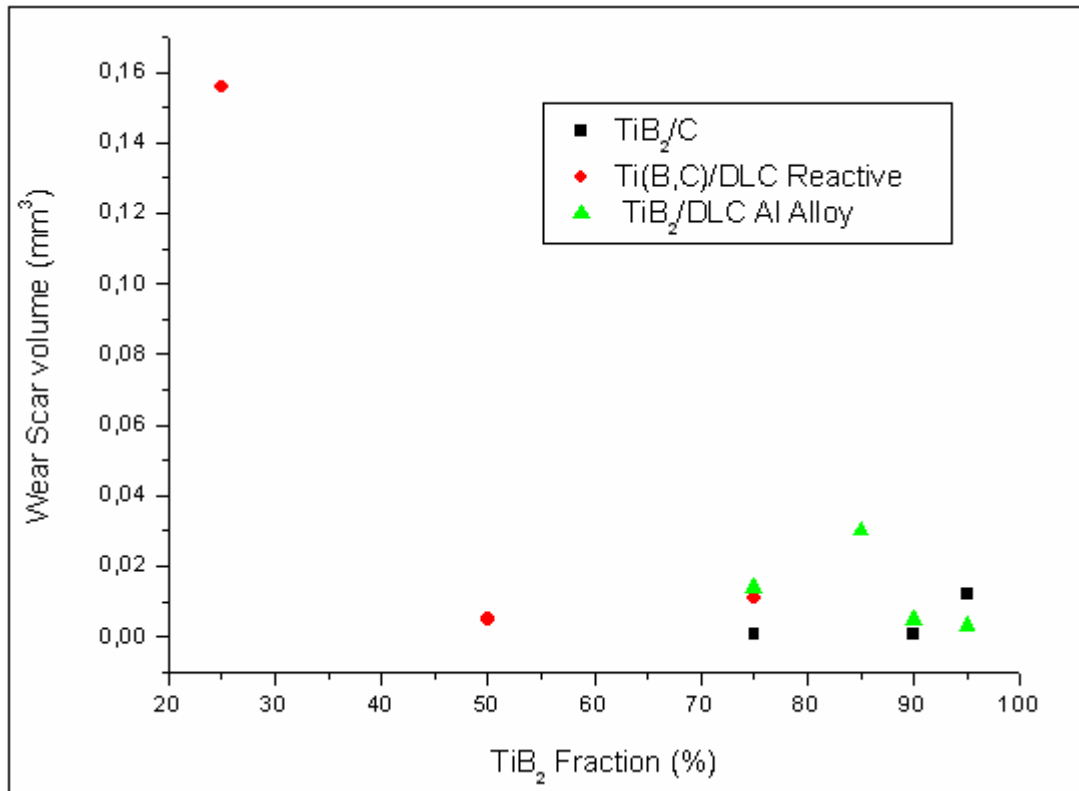


**Figure 178 – Calculated Wear Scar Volume of the Multilayer coatings.**

The wear scar volume of the graphitic multilayers is lower; this is due to the lubricant phase caused by the nature of the carbon layer. The multilayer coatings produced in Ar + 7.5% CH<sub>4</sub>, with the low ceramic content, presents a high wear scar volume, due to the damage sustained by the surface. This is an indicator that the coating is capable of sustaining damage without spalling, providing a lubricant surface.

The values from which the previous plots were made, from Figure 172 - Figure 178 are summarised in Table 11. From the table it is possible to compare the data according to the multilayer manufactured and the I<sub>D</sub>/I<sub>G</sub> ratio present in the DLC layer.

From the observation of Table 11 it is possible to see that there are some variations in hardness. The Ti(B,C)/DLC presented the lower hardness values due to the coating design configuration chosen for this multilayer, as seen in

section 7. As seen before in section 8.3 the deposition of TiB<sub>2</sub> in a Ar +7.5% CH<sub>4</sub> forms a Ti(B,C) layer as seen schematically in Figure 179 b).

Multilayer Coating	I <sub>D</sub> /I <sub>G</sub> ratio	Hardness (GPa)	Reduced Modulus (GPa)	H <sup>3</sup> /E <sup>2</sup> (Average)	Critical Load (N)	CoF (average)		Wear Scar Volume (mm <sup>3</sup> )	
						10N	20N	10N	20N
50% TiB <sub>2</sub> / 50%C	<50%	5,1	140,47	3.45E <sup>-3</sup>	-----	-----	-----	-----	-----
75% TiB <sub>2</sub> / 25%C		10.9	138,9922	4.2E <sup>-2</sup>	22.5 ± 1	0.141	0.133	6.3E <sup>-4</sup>	5.7E <sup>-4</sup>
90% TiB <sub>2</sub> / 10%C		14	197,4925	4.6E <sup>-2</sup>	15 ± 1	0.16	0.36	5.8E <sup>-4</sup>	1.0E <sup>-2</sup>
95% TiB <sub>2</sub> / 5%C		17.1	216,3917	5.0E <sup>-2</sup>	20 ± 1	0.22	0.5	1.2E <sup>-2</sup>	0.19
25% Ti(B,C)/ 75% DLC	>50%	4,6	68	0,01	15	24	-----	156	-----
50% Ti(B,C) /50% DLC		2	42,7718	0,0021	<15	0,27	-----	49	-----
75% Ti(B,C)/ 25% DLC		2,7	55,0022	0,0023	25	28	-----	108	-----
75% TiB <sub>2</sub> / 25%DLC		21,7	204,6418	0,28	15	0,43	-----	0,014	-----
85% TiB <sub>2</sub> / 15%DLC		23	277,2429	0,2	15	0,45	-----	0,03	-----
90% TiB <sub>2</sub> / 10%DLC		23,8	197,983	0,26	>20	0,43	-----	0,005	-----
95% TiB <sub>2</sub> / 5%DLC		27,8	279,0559	0,23	15-20	0,47	-----	0,003	-----

**Table 11 – Summary results of the different TiB<sub>2</sub> multilayers with DLC.**

As the sputter deposition of carbon occurs in Ar + 7.5% CH<sub>4</sub> atmosphere, which forms DLC, there is a reaction zone formed, which is rich in carbon agreeing with the findings of Prakash et al [232] and Knotek et al [233]. The carbon preferentially bonds with TiB<sub>2</sub> forming Ti(B,C)<sub>2</sub> in the presence of CH<sub>4</sub> and only DLC is formed when the Ti(B,C) phase is saturated. Also this Ti(B,C)/DLC multilayer had a the highest carbon content (75% -25%). The increasing carbon content provoke a decrease in hardness due to the incorporation of carbon atoms in the interface between the Ti(B,C) an TiB<sub>2</sub> as reported by Gilmore et al [113-115].

This can be seen as well in the TiB<sub>2</sub>/C multilayer, with the difference that in this case the DLC layer is replaced by a sputtered carbon layer in an Ar atmosphere. Forming a I<sub>D</sub>/I<sub>G</sub> ratio below 50% with preferential sp<sup>2</sup> bonding, due to the absence of hydrogen in the carrier gas which is known to preferentially etches the sp<sup>2</sup> component of DLC [225, 226]. As the ceramic content increases (TiB<sub>2</sub> layer reduced) and it reduces the proportion of carbon available to form a DLC layer (sp<sup>2</sup>+sp<sup>3</sup>), shown in Figure 179 a).

The TiB<sub>2</sub>/DLC deposited onto Al alloys present the higher hardness values, as we can see from Table 11. These optimum mechanical properties are thought to be due to the high quality TiB<sub>2</sub> layer deposited using pulsed DC sputtering, as reviewed in section 8.1, the high quality DLC layer with an I<sub>D</sub>/I<sub>G</sub> ratio above 50% and the thickness of the reaction zone between the DLC and the TiB<sub>2</sub> shown schematically in Figure 179 c).

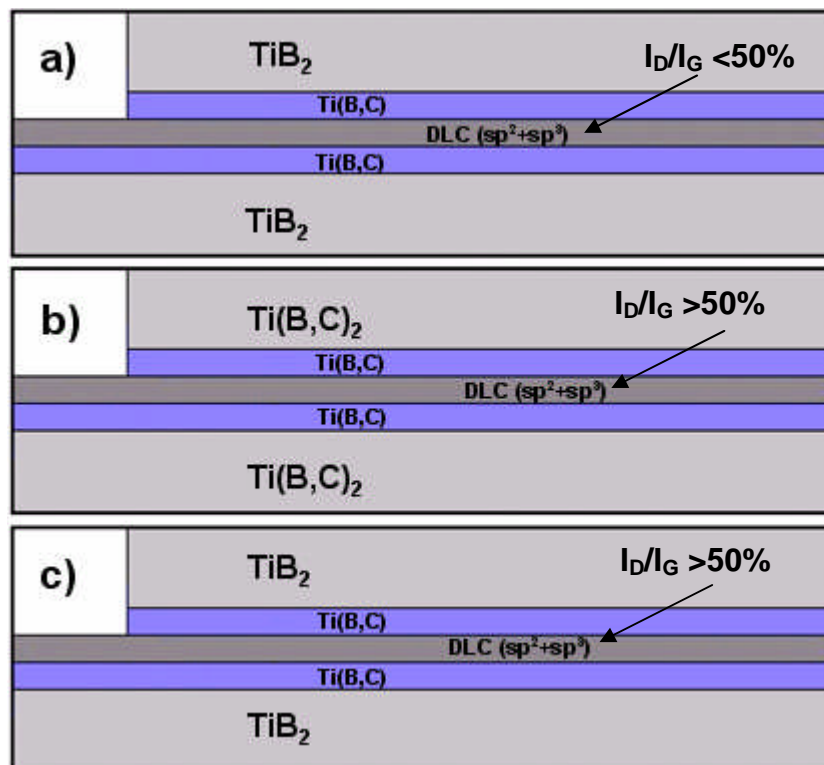


**Figure 179 – Nanolayer schematic of the reaction zones created by the deposition of DLC with TiB<sub>2</sub> ceramic, a) Multilayer manufactured in pure Ar, with a I<sub>D</sub>/I<sub>G</sub> ratio <math>< 50\%</math>. b) Multilayer manufactured in Ar + 7.5% CH<sub>4</sub> with I<sub>D</sub>/I<sub>G</sub> ratio <math>> 50\%</math>. c) Multilayer manufactured in pure Ar, with a I<sub>D</sub>/I<sub>G</sub> ratio <math>> 50\%</math> deposited onto Al alloy.**

These reaction zones have a crucial part on the overall performance of the multilayers. They are responsible for assuring a good adhesion between the TiB<sub>2</sub> and DLC layers. In Figure 180 it is possible to see a high resolution picture from the multilayers of TiB<sub>2</sub> and DLC deposited onto Al alloys. From the figures it is possible to see graded colouring between the layers. This is thought to be a Ti(B,C) layer formed during the DLC deposition. The formation of this layer is due to the preferential bonding between the TiB<sub>2</sub> with carbon, which preferentially forms Ti(B,C).

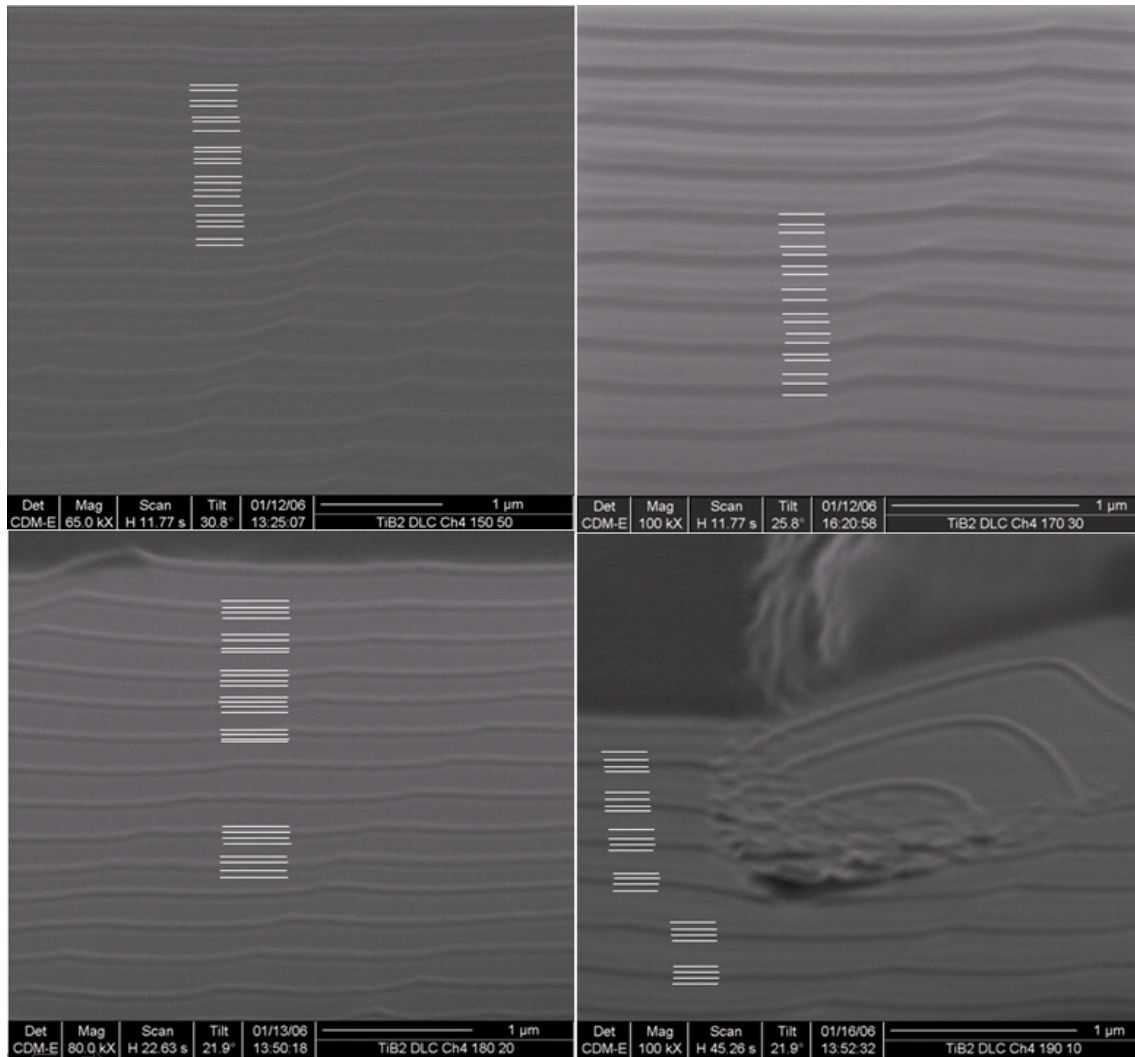


**Figure 180 – High resolution FIB micrograph of TiB<sub>2</sub>/DLC multilayers, highlighted in white are the reaction zones which the average thickness is calculated in Table 12, and shown schematically in Figure 181**

In Figure 180, the white lines represent the possible zones formed during deposition. In Figure 181 a) there is an illustration of the reaction zones, visible in Figure 180. With a careful analysis of figure above it is possible to measure the thickness of the reaction zones and the thickness of the individual layers.

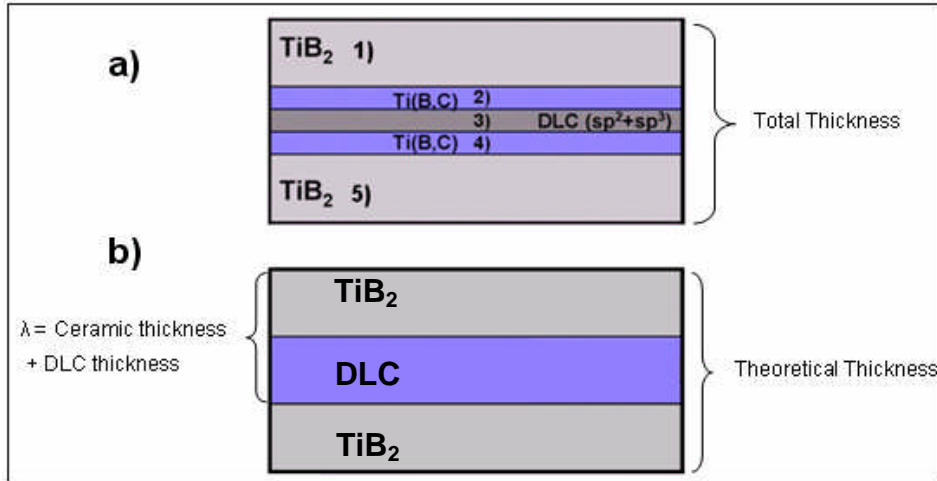


**Figure 181 – Illustration of the reaction zones by the observation of Figure 180.**

From the observation of Table 12 it is possible to see the calculated average thickness of the reaction zones (Ti(B,C) and adjacent layers). The average of the reaction zones is between 30 - 50nm, measured from high resolution FIB pictures in Figure 180.

TiB <sub>2</sub> /DLC Al Alloy	TiB <sub>2</sub> 1 (nm)	Ti(B,C) 2 (nm)	DLC 3 (nm)	Ti(B,C) 4 (nm)	TiB <sub>2</sub> 5 (nm)	Total thickness 1+2+3+4+5 (nm)	Theoretical thickness [Sum of λ + ceramic thickness (nm)]
75% TiB <sub>2</sub> 150nm+50nm	162	48	65	40	135	450	350
85% TiB <sub>2</sub> 170nm+30nm	83	33	70	30	80	296	370
90% TiB <sub>2</sub> 180nm+20nm	125	40	40	30	125	360	380
95% TiB <sub>2</sub> 190nm+10nm	125	30	40	50	135	380	390

**Table 12 – Average thickness of reaction zones calculated from Figure 180 a) and b).**

The total thickness values, Figure 181 a) and Table 12, present some scatter, which can be due to inaccuracies during the measurement from the high resolution pictures. When compared the total thickness against the theoretical thickness, Figure 181 b) and Table 12, it is possible to see that the highest difference between the total thickness and the theoretical thickness are in the high DLC content (70nm – 100nm). While for low DLC content, the difference is only (10nm – 20nm). This can be related with the availability of carbon at the interface and only DLC is formed when the Ti(B,C) layer is saturated with

carbon atoms, which can explain the high values for the DLC layer visible in Table 12, and the small variation of the Ti(B,C) values.

From observation of Figure 180, Figure 181, Table 12, and the observation of the nanoindentation results in Figure 173, the data indicates that as the TiB<sub>2</sub> content decreases there will be a threshold in which the deposition of TiB<sub>2</sub> multilayered with carbon will result in the formation of Ti(B,C).

In Table 12 it was possible to see that the reaction zone, Ti(B,C) was constant with values between 30nm – 50nm, with a average value  $37.6 \pm 8.1$ . In order to support the threshold of TiB<sub>2</sub> formation in the presence of carbon, Table 13 presents the values of the experimental composition wavelength ( $\lambda$ ), which is calculated from the thickness values measured from Figure 180 and presented in Table 12. The experimental composition wavelength is calculated by the sum of half of the TiB<sub>2</sub> layer the Ti(B,C) layer, the DLC layer and half of the remaining TiB<sub>2</sub> layer.

Experimental ceramic layer (nm)	Experimental composition wavelength $\lambda$ (nm)	Experimental ceramic fraction (%)	1 TiB <sub>2</sub> (nm)	TiB <sub>2</sub> /2 (nm)	2 Ti(B,C) (nm)	3 DLC (nm)	4 Ti(B,C) (nm)	TiB <sub>2</sub> /2 (nm)	5 TiB <sub>2</sub> (nm)
236,5	301	78,5	162	81	48	65	40	67,5	135
144,5	213	67,89	83	41,5	33	70	30	40	80
195	235	82,9	125	62,5	40	40	30	62,5	125
210	250	84	125	62,5	30	40	50	67,5	135

**Table 13 – Experimental ceramic layer, experimental composition wavelength ( $\lambda$ ) and Experimental ceramic fraction, calculated from data in Table 12.**

From the composition wavelength it is possible to calculate the experimental ceramic layer which is the sum of the half TiB<sub>2</sub> layer with Ti(B,C) layers and the remaining half of the TiB<sub>2</sub> layer. From these values it is possible to calculate the experimental ceramic fraction as visible in Table 13.

In Figure 182 is possible to see the experimental volume fraction calculated in Table 13, plotted with the theoretical volume fractions taken from sections: 8.2,

8.3 and 8.5. As discussed before, the reaction zone presents an average value of  $37.6 \pm 8.1$ . In Figure 182 the blue and black line are linear fitting to the data. From the fittings it is possible to see that the lines intersect with the Ti(B,C)/DLC, indicating that between the two points there is the possible formation of Ti(B,C)+TiB<sub>2</sub>.

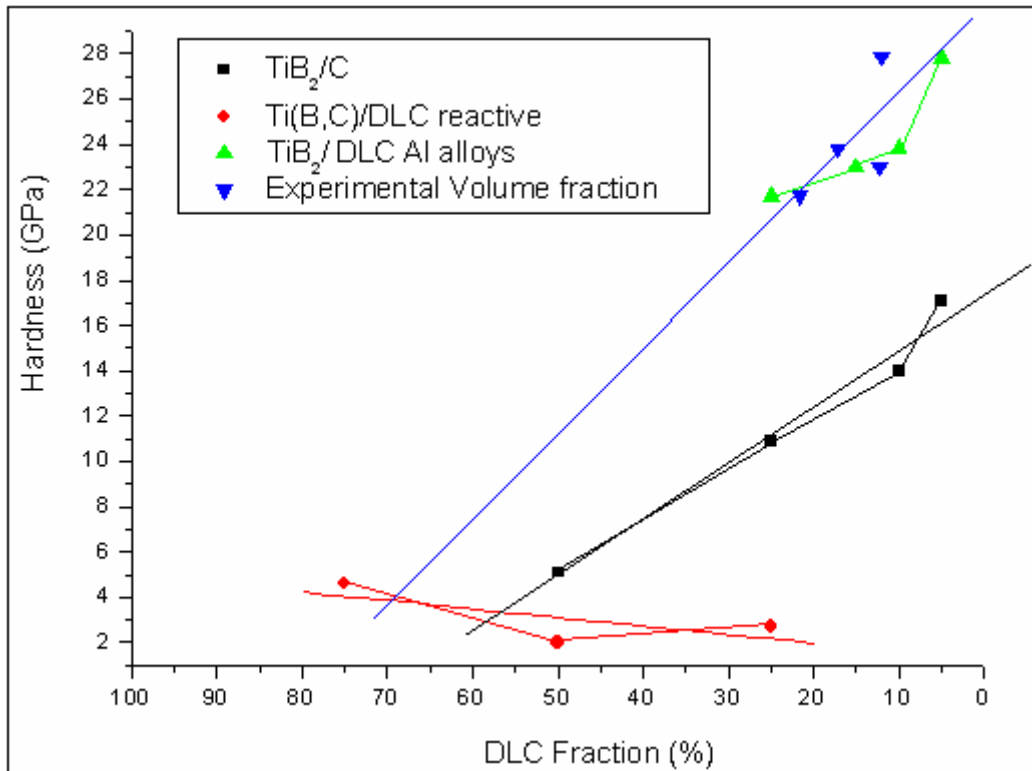


**Figure 182 - Hardness comparison between all the multilayers with carbon produced including the experimental volume fraction highlighting the formation threshold of TiB<sub>2</sub>.**

From the figure, as the DLC fraction is increased, above 70%, the deposited layer of TiB<sub>2</sub> will react with the carbon atoms forming Ti(B,C).

In the threshold zone, between 55% - 70% of DLC fraction, as the carbon content decreases the Ti(B,C) layer reaches saturation point allowing the formation of TiB<sub>2</sub>, therefore there is an increase in hardness.

Over the range of DLC and TiB<sub>2</sub> layers produced, even though the coatings presented an experimental composition wavelength and a theoretical wavelength the reaction zones were independent of the layer thickness with a thickness of around 40nm as possible to see in Figure 182 and Table 13.

## 9. Conclusions and Further work

### 9.1. Conclusions

The aim of this thesis was to expand the development of a new generation of multilayer coatings with a hard ceramic, TiB<sub>2</sub> and a solid lubricant, Diamond-like carbon to be applied on tool steels and soft substrates, which lack in surface hardness and lubricant properties.

The following conclusions can be drawn as a result of this study:

- The impact of the deposition technologies in the fabrication of TiB<sub>2</sub> based multilayer ceramic coatings has an extreme importance on the tribological performance of such coatings.
- TiB<sub>2</sub> films produced using Pulsed-DC magnetron technology have an optimum damage resilience, allowing the test loads to be distributed over a wide area, due to the dense and defect free nature of the films produced.
- The hardness values for TiB<sub>2</sub> ceramic are dependant on the deposition methodology used varied between 13GPa and 21GPa for 300W Pulsed DC, 9GPa and for RF 300W, and 10GPa and 12GPa for the DC, while the reduced modulus is constant at 200 GPa  $\pm$  10%.
- TiB<sub>2</sub> films deposited with Pulsed-DC plasma process presented good wear behaviour, small wear scar volumes and no signs of delamination. Under the same the same testing conditions the films deposited using RF and DC sputtering presented through thickness cracking and extensive plastic deformation of the coating and substrate.
- 3 multilayer stacks were produced in this study: The bi-layer thickness was kept constant at  $\lambda = 200\text{nm}$ .
  - TiB<sub>2</sub>/C deposited in an inert atmosphere with ceramic percentages ranging from 50% to 95% ceramic, with layer thicknesses ranging from 100nm to 190nm for the ceramic, and 50 individual layers.

- TiB<sub>2</sub>/DLC deposited in a reactive atmosphere of Ar+7.5% CH<sub>4</sub> with ceramic percentages ranging from 25% to 75%. With 20 individual layers for each component.
- TiB<sub>2</sub>/DLC, the ceramic was deposited in an inert atmosphere, and the DLC was deposited in Ar+7.5% CH<sub>4</sub>. The ceramic percentages were varied from 75% to 95% with 50 individual layers.
- The multilayer with the ceramic deposited in an inert atmosphere, and the DLC was deposited in Ar+7.5% CH<sub>4</sub> presented optimum hardness values between 21.7 to 27.8 GPa, while the other multilayers valued ranged for TiB<sub>2</sub>/C – 5GPa to 17GPa and the multilayer deposited in Ar+7.5% CH<sub>4</sub> presented hardness values between 3-5GPa.
- Raman spectroscopy was used to characterize the carbon and DLC films. The carbon films manufactured in an inert atmosphere presented an I<sub>D</sub>/I<sub>G</sub> ratio of 1.08. The carbon films sputtered in a reactive atmosphere with a CH<sub>4</sub> hydrocarbon gas presented a ratio of 1.25. The H component of the gas results in the etching of the graphite (sp<sup>2</sup>) bonds, therefore having a direct effect in film quality and increasing the sp<sup>3</sup>/sp<sup>2</sup> ratio.
- The hardness of TiB<sub>2</sub>/C multilayers varied from 5GPa for the 17GPa for the 95% ceramic, depending on the mode used for carbon deposition.
- The hardness values are dependant on the carbon content, and the allotropic form of carbon deposited. The graphitic nature of the layers does not act as load bearing but as a lubricant.
- Scratch adhesion testing from 10N to 60N presented values between 15N for the 90% ceramic to 22.5N for the 75% ceramic as the critical loads to coating failure. After testing the films presented a spallation failure mode due to the stress created ahead of the moving indenter.
- The wear testing revealed low friction coefficients of 0.14 for the 10N load for the 75% ceramic. In this case the friction coefficient increases as the ceramic content is increased. This coating has the highest carbon content of those tested.

- The wear testing conducted at low loads (10N), below the critical load for coating fracture did not showed any signs of coating delamination. The testing carried out at 20N above the critical load reveals signs of spallation.
- The multilayers manufactured in Ar + 7.5% CH<sub>4</sub> throughout the whole deposition process presented hardness values ranging from 3 to 5GPa for the 25% and 75% ceramic. These low values of hardness are associated with the formation of Ti(B,C) reaction zone rather than TiB<sub>2</sub> as the ceramic phase.
- The nature of the DLC produced gives the film load bearing properties, maintaining a friction coefficient comparable to a graphite layer.
- The multilayer coating deposition in a periodically switched environment produced significantly harder multilayers. The ceramic, TiB<sub>2</sub> was deposited in an inert atmosphere while the DLC was deposited in a reactive atmosphere of Ar + 7.5% CH<sub>4</sub>. The hardness values measured using nanoindentation presented values of 21.7 to 27.8 GPa for the 25% and 5% DLC containing coatings.
- In all multilayered coatings an interfacial layer of Ti(B,C) is formed at the interface between the TiB<sub>2</sub> ceramic and DLC layer. Its extent depends on the processing conditions used.
- On the powder processed Al alloy due to the soft nature of the substrate, a constant load scratch test had to be used with loads from 2N to 20N. Tensile cracking was observed in all the multilayers. The critical loads measured were still around 15N - 20N. Friction coefficients between 0.43 and 0.47 were measured, which is belived to be due the interaction of loose carbon bonds with the counter-surface. Hardness values depend on processing method but were up to 27.8 GPa.

## 9.2. Further work

The following investigations are suggested:

- The deposition of  $\text{TiB}_2$  films in a heated environment in order to produce crystalline films, hence changing the structure/mechanical properties.
- Annealing treatments of coatings deposited at low temperatures may improve the interface strength and crack propagation properties.
- As shown in literature the DLC produced by PVD is limited in thickness and mechanical properties. Research work has proven that the CVD process is a well known route to produce thick high quality DLC films.
- The multilayering of pulsed-DC sputtered  $\text{TiB}_2$  in a mixed PVD/CVD reactor as a production method of superior DLC properties, in the ceramic/DLC multilayers.
- $\text{TiB}_2$  has been employed as an erosion resistant coating multilayered with a variety of metals. No work has been done in the multilayering  $\text{TiB}_2$  and artificial Diamond as an erosion resistant coating.

## REFERENCE LIST

1. Cavaliere, P., *Mechanical properties of Friction Stir Processed 2618/Al<sub>2</sub>O<sub>3</sub>/20p metal matrix composite*. Composites Part A: Applied Science and Manufacturing, 2005. **36**(12): p. 1657-1665.
2. Fang, Q., Sidky, P., Hocking M., *Erosive wear behaviour of aluminium based composites*. Materials and Design, 1997. **18**(4-6): p. 389-393.
3. Krishna, S., *Thin Film Deposition - Process and Technology*. 2002, Norwich, N.Y: Material Science and Processing Technology Series.
4. Mattox, D.M., *Handbook of physical vapour deposition (PVD) processing*. 1998: William Andrew Publishing/Noyes
5. Mattox, D.M., *The foundations of vacuum coating technology*. 2003, Norwich, N.Y., USA: William Andrew Publishing.
6. Chapman, B., *Glow Discharge Processes, sputtering and plasma etching*. 1980: John Wiley & Sons.
7. Cuomo, J., Rossnagel, S., Kaufman, H., *Handbook of Ion Beam Processing Technology - Principles, Deposition, Film Modification and Synthesis*. 1989, NY: William Andrew Publishing/Noyes.
8. Smith, D., *Thin Film Deposition - Principles and Practice*. 1995, NY: McGraw Hill.
9. Vales Silva, M.F., *Multilayer TiB<sub>2</sub>/X hard coatings by sputtering deposition*, in SIMS. 1998, PhD Thesis, Cranfield University: Bedford.
10. Prengel, H., Jindal, P., Wendt, K., Santhanam, A., Hegde, P., Penich, R., *A new class of high performance PVD coatings for carbide cutting tools*. Surface and Coatings Technology, 2001. **139**(1): p. 25-34.
11. Venables, J.A., *Introduction to Surface and Thin Film Processes*. 2000: Cambridge University Press.
12. Silva Cruz, R., *Multilayered metal/ceramic nanostructure coatings*, in SIMS. 2003, MSc Thesis, Cranfield University: Bedford.
13. Mozhaev, P., Komissinki, P., Kukhata, N., Kuhle, A., *Comparison of High-Pressure DC-Sputtering and Pulsed Laser Deposition of Superconducting YBa<sub>2</sub>Cu<sub>3</sub>O<sub>x</sub> Thin Films*. Journal of Superconductivity, 1997. **10**(3): p. 1997.
14. Claeysens, F., *Fundamental Studies of Pulsed Laser Ablation*, in *Department of Chemistry*. 2001, University of Bristol: Bristol.
15. Ryeol Lee, K.E., K. Kim, I., *Design of W buffer layer for adhesion improvement of DLC films on tool steels*. Thin Solid Films, 2000. **377-378**: p. 261-268.
16. Wasa, K., Kitabatake, M., Adachi, H., *Thin Film Materials Technology - Sputtering of Compound Materials*, ed. Springer-Verlag. 2004: William Andrew Publishing/Noyes.
17. Bunshah, R.F., *Handbook of deposition technologies for films and coatings : science, technology, and applications* 2ed. 1994: Noyes Publications.
18. Rossnagel, S.M., *Handbook of plasma processing technology : fundamentals, etching, deposition, and surface interactions*. 1990, Park Ridge, N.J., USA: Noyes Publications.
19. Sanders, D., R. Boxman, and P. Martin, *Handbook of vacuum arc science and technology : fundamentals and applications*. 1995, Park Ridge, NJ, USA: Noyes Publications.
20. Holloway, P., McGuire, G., *Handbook of Compound Semiconductors - Growth, Processing, Characterization, and Devices*. 1995: William Andrew Publishing/Noyes.
21. <http://www.genco.com/tech/whatsputtering.html>.

22. Bunshah, R.F., *Handbook of hard coatings*. 2001: Noyes Publications.
23. <http://aultima.com/aultima/details.asp?itemid=11>.
24. Jonsson, L., Nyberg, T., Katardjiev, I., Berg, S., *Frequency response in pulsed DC reactive sputtering processes*. Thin Solid Films, 2000. **365**: p. 43-48.
25. Schiller, S., Goedicke, K., Reschke, J., Kirchoff, V., Schneider, S., Milde, F., *Pulsed magnetron sputter technology*. Surface and Coatings Technology, 1993. **61**: p. 331-337.
26. Safi, I., *Recent aspects concerning DC reactive magnetron sputtering of thin films: a review*. Surface and Coatings Technology, 2000. **127**: p. 203-219.
27. Sellers, J., *Assymmetric bipolar pulsed DC: The enabling technology for reactive PVD*. Surface and Coatings Technology, 1998. **98**: p. 1245-1250.
28. Hyungduk, K., Weon-Pil, T., Ki-Chul, K., Sang-Hyeob, K., Su-Jeong, S., Young-Sung, K., *Growth of Al-doped ZnO thin films by pulsed DC magnetron sputtering*. Journal of Crystal Growth, 2005. **277**(1-4): p. 352-358.
29. Cooke, K., Hamsphire, J., Southall, W., Teer, D., *The industrial application of pulsed DC bias power supplies in closed field unbalanced magnetron sputter ion plating*. Surface and Coatings Technology, 2004. **177-178**: p. 789-794.
30. Scholl, R.A., *Assymmetric bipolar pulsed power: A new power technology*. Surface and Coatings Technology, 1998. **98**: p. 823-827.
31. Bartzsh, H., Frach, P., Goedicke, K., *Anode effects on energetic particle bombardment of the substrate in pulsed magnetron sputtering* Surface and Coatings Technology, 2000. **132**(2-3): p. 244-250.
32. E. Martinez, J.R., A. Lousa. J. Esteve, *Mechanical strengthening in nanometric CrN/Cr multilayers measured by nanoindentation*. Journal of Applied Physics: D, 2002. **35** p. 1880-1883.
33. Batista, J., Joseph, M., Godoy, C., Matthews, A., *Micro-abrasion wear testing of PVD TiN coatings on untreated and plasma nitrided AISI H13 steel*. Wear, 2002. **249**(10-11): p. 971-979.
34. Samsonov, D., Goree, J., *Particle growth in a sputtering discharge*. Journal Vacuum Science Technollogy, 1999. **A-17**(5).
35. Mohammad, F., in SAS. 2006, PhD Thesis, Cranfield University: Bedford.
36. <http://www.testbourne.com>.
37. Jianhai, Q., *Corrosion and Non-Destructive Testing*. 2001, Nanyang Technological University Singapore.
38. Ratsch, C. and J.A. Venables, *Nucleation Theory and the Early Stages of Thin Film Growth*. Journal of Vacuum Science & Technology A: Vacuum, Surfaces, and Films, 2003. **21**(5): p. S96-S109.
39. Keudell, A.v., *Surface processes during thin-film growth*. Plasma Sources Science and Technollogy, 1999. **9**: p. 455-467.
40. Bauer, E., *Growth of thin films*. Journal of Physics: Condensed Matter, 1999. **11**: p. 9365-9385.
41. Wang, Z., Kang, Z., *Functional and Smart Materials - Structural Evolution and Structure Analysis*. 1998: Springer - Verlag.
42. Liu, H., Dandy, D., *Diamond chemical vapor deposition: nucleation and early growth stages* 1995, Park Ridge, N.J., USA: Noyes Publications.
43. Hyland, M. *RF Sputtering System*. 1998
44. Tryon, B., Cao, F., Murphy, K., Levi, C., Pollock, T., *Ruthenium-containing bond coats for thermal barrier coating systems*. The Journal of the Minerals, Metals & Materials Society, 2006. **58**(1): p. 53-59.
45. Davis, R.F., *Diamond films and coatings : development, properties, and applications* 1993, Park Ridge, N.J., USA: Noyes Publications.

46. Veprek, S., Nesládek, P., Niederhofer A., Glatz, F., *Search for superhard materials: Nanocrystalline composites with hardness exceeding 50 GPa.* Nanostructured Materials, 1998. **10**(5): p. 679-689.
47. Veprek, S., *New development in superhard coatings: the superhard nanocrystalline-amorphous composites.* Thin Solid Films, 1998. **317**(1-2): p. 449-454.
48. Veprek, S., Nesládek, P., Niederhofer, A., Glatz, F., Síma, M., *Recent progress in the superhard nanocrystalline composites: towards their industrialization and understanding of the origin of the superhardness.* Surface and Coatings Technology, 1998. **108-109**(1-3): p. 138-147.
49. Veprek, S., *The search for novel, superhard materials.* Journal Vacuum Science Technollogy, 1999. **A17**(5).(5): p. 2401-2420.
50. Helmersson U., T., S., Barnett, S., Sundgren, J., Markert, C., Greene, J., *Growth of single-crystal TiN/VN strained-layer superlattices with extremely high mechanical hardness.* Journal of Applied Physics, 1987. **62**(2): p. 481-484.
51. Mitchell T.E., Griffin A.J., Nastasi M., Kung H., *Microstructure/Properties Relations of Advanced Materials Structure and Mechanical Properties of Copper/Niobium Multilayers* Journal of the American Ceramic Society, 1997. **80**(7): p. 1673-1673.
52. Mirkarimi, P., Hultman, L., Barnett, S., *Enhanced hardness in lattice-matched single-crystal TiN/V<sub>0.6</sub>Nb<sub>0.4</sub>N superlattices.* Applied Physics Letters, 1990. **57**(25): p. 2654-2656.
53. Rutherford, K., Hatto, P., Davies, C., Hutchings, I., *Abrasive wear resistance of TiN/NbN multilayers: measurement and neural network modelling.* Surface and Coatings Technology, 1996. **86-87**: p. 472-479.
54. Lim, J., Lee, J., Ahn, H., Rie, K., *Mechanical properties of TiN/TiB<sub>2</sub> multilayers deposited by plasma enhanced chemical vapour deposition.* Surface and Coatings Technology, 2003. **174-175**: p. 720-724.
55. Martinez, E., Romero, J., Louisa.A., Esteve, J. , *Mechanical strengthening in nanometric CrN/Cr multilayers measured by nanoindentation.* Journal of Applied Physics: D, 2002. **35** p. 1880-1883.
56. Xu Junhua, L.G., Gu Mingyuan, , *The microstructure and mechanical properties of TaN/TiN and TaWN/TiN superlattice films* Thin Solid Films, 2000. **370**(1-2): p. 45-49
57. Veprek, S., *Conventional and new approaches towards the design of novel superhard materials.* Surface and Coatings Technology, 1997. **97**(1-3): p. 15-22.
58. Niederhofer, A., Nesládek, P. Männling, H., Moto, K., Veprek S., Jílek, M., *Structural properties, internal stress and thermal stability of nc-TiN/a-Si<sub>3</sub>N<sub>4</sub>, nc-TiN/TiSix and nc-(Ti<sub>1-y</sub>Al<sub>y</sub>Si<sub>6</sub>)N superhard nanocomposite coatings reaching the hardness of diamond.* Surface and Coatings Technology, 1999. **120-121**: p. 173-178.
59. Karvankova, P., Zindulka, O., Bergmaier, A., Veprek, S., *Superhard nc-TiN/a-BN and nc-TiN/a-TiB<sub>x</sub>/a-BN coatings prepared by plasma CVD and PVD: a comparative study of their properties.* Surface and Coatings Technology, 2003. **163-164**: p. 149-156.
60. Koehler, J., *Attempt to Design a Strong Solid.* Physics Review B, 1970. **2**(2): p. 547-551.
61. Lehoczy, S., *Strength enhancement in thin-layered Al-Cu laminates.* Journal of Applied Physics, 1978. **49**: p. 5479.
62. Lehoczy, S., *Retardation of dislocation generation and motion in thin-layered metal.* Physics Review Letters, 1978. **41**: p. 1814.

63. Saada, G., *Hall-Petch revisited*. Materials Science and Engineering A, 2005. **400-401**: p. 146-149.
64. Aldazabal, J., Sevillano, J. , *Hall-Petch behaviour induced by plastic strain gradients*. Materials Science and Engineering A, 2004. **365**(1-2): p. 186-190.
65. Embury, J., Hirth, J., *On dislocation storage and the mechanical response of fine scale microstructures*. Acta Metallurgica et Materialia, 1994. **42**(6): p. 2051-2056.
66. Sundgren, J., Birch, J., Håkansson, G.,Helmersson, U., *Growth, structural characterization and properties of hard and wear-protective layered materials*. Thin Solid Films, 1990. **193-194**(Part 2): p. 818-831.
67. Ducros, C., Sanchette, F. , *Multilayered and nanolayered hard nitride thin films deposited by cathodic arc evaporation. Part 2: Mechanical properties and cutting performances*. Surface and Coatings Technology, 2006. **201**(3-4): p. 1045-1052.
68. Springer, R., Catlett, D., *Structure and mechanical properties of Al/Al<sub>x</sub>O<sub>y</sub> vacuum deposited laminates*. Thin Solid Films, 1978. **54**: p. 197-205.
69. Springer, R., Harford, C., *Characterization of aluminium-aluminium nitride coatings sputter-deposited using the pulsed gas process*. Journal Vacuum Science Technollogy, 1982. **20**: p. 462-464.
70. Holleck, H., *Material selection for hard coatings*. Journal Vacuum Science Technollogy, 1986. **A4**: p. 2661-2669.
71. Leiste, H., Dambacher, U. , Holleck, H., *Microstructure and properties of multilayer coatings with covalent bonded hard materials*. Surface and Coatings Technology, 1999. **116-119**: p. 313-320.
72. Holleck, H., Lahres, M., Woll, P., *Multilayer coatings - Influence of fabrication parameters on constitution and properties*. Surface and Coatings Technology, 1990. **41**: p. 179-190.
73. Holleck, H., Schier, V., *Multilayer PVD coatings for wear protection*. Surface and Coatings Technology, 1995. **76-77**: p. 328-336.
74. Holleck H., L., M. , *Two-phase TiC/TiB<sub>2</sub> hard coatings*. Materials Science and Engineering A, 1991. **140**: p. 609-615.
75. Dimigen, H., Klages, C., *Microstructure and wear behaviour of metal-containing diamond-like coatings*. Surface and Coatings Technology, 1991. **49**(1-3): p. 543-547.
76. Bewilogua, K., Dimigen, H. , *Preparation of W-C-H coatings by reactive magnetron sputtering*. Surface and Coatings Technology, 1993. **61**(1-3): p. 144-150.
77. Donohue, L., Cawley, J., Lewis, D., Brooks, J., Munz, W. , *Investigation of superlattice coatings deposited by a combined steered-arc evaporation and unbalanced magnetron Sputtering Technique*. Surface and Coatings Technology, 1995. **76-77** (Part 1): p. 149-158.
78. Donohue, L., Munz, W. , Lewis, D. , Cawley, J., Hurkmans, T., Trinh, T., Petrov, I. Greene, J., *Large-scale fabrication of hard superlattice thin films by combined steered-arc evaporation and unbalanced magnetron sputtering*. Surface and Coatings Technology, 1997. **93**(1): p. 69-87.
79. Chu, X., Wong, M., Sproul, W., Rohde, S., Barnet. S., *Deposition and properties of polycrystalline TiN/NbN superlattice coatings*. Journal Vacuum Science Technollogy, 1992. **A10**(4 ) : p. 1604-1609.
80. Holmberg, K., Matthews, A., Ronkainen, H. , *Coatings tribology - contact mechanics and surface design*. Tribology International, 1998. **31**(1-3): p. 107-120.
81. Matthews, A., Leyland, A. , *Hybrid Techniques in Surface Engineering*. Surface and Coatings Technology, 1995. **71**(2): p. 88-92.

82. Matthews, A., Leyland, A., Holmberg, K., Ronkainen, H., *Design aspects for advanced tribological coatings*. Surface and Coatings Technology, 1998. **100-101**( 1): p. 1-6.
83. Goat, C., *Erosion resistance in metal - ceramic multilayer coatings for gas turbine compressor applications in SIMS*. 1994, PhD Thesis, Cranfield: Bedford.
84. Cadet, P., Pellerin, F., Rickerby, D., Quesnel, E. *Erosion, Corrosion and Foreign Object Damage Effects in Gas Turbines - - Revetments anti-erosion multicouches*. 1994: AGARD 558.
85. Kitamura, T., Hirakata, H., Itsuji, T., *Effect of residual stress on delamination from interface edge between nano-films*. Engineering Fracture Mechanics, 2003. **70**(2089-2101).
86. Voevodin, A., Bantle, R., Matthews, A. , *Dynamic impact wear of TiCxNy and Ti-DLC composite coatings*. Wear, 1995. **185**: p. 151-157.
87. Voevodin, A., Walck, S., Zabinski, J., *Architecture of multilayer nanocomposite coatings with super-hard diamond-like carbon layers for wear protection at high contact loads*. Wear, 1997. **203-204**: p. 516-527.
88. Mitterer, M., *Borides in Thin Film Technology*. Journal of Solid State Chemistry, 1997. **133**: p. 279-291.
89. Wang, K., Krstic, V., *Reaction Sintering of TiN-TiB<sub>2</sub> Ceramics*. Acta Materialia, 2003. **51**(6): p. 1809-1819.
90. Brinkman, H., Duszczuk, J., Katgerman, L., *In-situ formation of TiB<sub>2</sub> in a P/M aluminum matrix*. Scripta Materialia, 1997. **37**(3): p. 293-297.
91. Welman, N.J., *Formation of TiB<sub>2</sub> from Rutile by Room Temperature Ball Milling*. Materials Engineering, 1999. **12**(10): p. 1213-1224.
92. Lu, L., Lai, M., Chen, F. , *Al-4 wt% Cu composite reinforced with in-situ TiB<sub>2</sub> particles*. Acta Materialia, 1997. **45**(10): p. 4297-4309.
93. Feng, C., Froyen, L. , *Incorporation of Al into in TiB<sub>2</sub> Al matrix composites and Al-Ti-B master alloys*. Materials Letters, 1997. **32**: p. 275-279.
94. Gu, Y., Qian, Y., Chen, L., Zhou, F, *A Mild Solvothermal Route to Nanocrystalline Titanium Diboride*. Journal of Alloys and Compounds, 2003. **352**(1-2): p. 325-327.
95. Pierson, H.O., *Handbook of chemical vapor deposition* 1999, Norwich, N.Y.: Noyes Publications.
96. Karner, H., Lamer, J., Stori, H., *Preparation of TiB<sub>2</sub> and TiB<sub>x</sub>N<sub>y</sub> coatings by PACVD*. Surface and Coatings Technology, 1989. **39-40**: p. 293-300.
97. Shutou, A., Matsui, T., Tsuda, H., Mabuchi, H., Morii, K., *Structural and electric properties of TiB<sub>2</sub> thin films by RF sputtering*. Materials Letters 2000. **45**(3-4): p. 143-148.
98. Munro, R.G., *Material Properties of Titanium Diboride*. Journal of Research of the National Institute of Standards and Technology, 2000. **105**(5): p. 709-720.
99. Knotek, O., Moller, M., Lugscheider, E., Barimani, C., *Structure and Properties of PVD TiB<sub>2</sub> Coatings*. Journal of Solid State Chemistry, 1997. **133**(1): p. 117-121.
100. Tee, K., Lu, L., *Improvement in Mechanical Properties of in situ Al-TB<sub>2</sub> composite by Incorporation of Carbon*. Material Science and Engineering, 2003. **A-339**(1-2): p. 227-231.
101. Pfhol, C., Bulak, A., Rie, K., *Development of titanium diboride coatings deposited by PACVD*. Surface and Coatings Technology, 2000. **131**: p. 141-146.
102. Riviere, J., Miguet, S., Cahoreau, M., Chaumont J., Delafond, J., *Formation of TiB<sub>2</sub> coatings at room temperature by dynamic ion mixing*. Surface and Coatings Technology, 1996. **84**: p. 398-403.
103. <http://www.hwang.k.u-tokyo.ac.jp/research-e.html>.

104. Agarwal, A., Dahotre, N., *Comparative wear in titanium diboride coatings on steel using high energy density processes*. Wear, 2000. **240**(1-2): p. 144-151.
105. Agarwal, A., Dahotre, N., *The Functionality of Laser-Surface-Engineered Composite Titanium Diboride Coatings*. The Minerals, Metals & Materials Society, 2000. **51**(1).
106. Zergioti, I., Fotakis, C., Haidemenopoulos, G., *Growth of TiB<sub>2</sub> and TiC coatings using pulsed laser deposition*. Thin Solid Films, 1997. **303**(1-2): p. 39-46.
107. Berger, M., Hogmark, S., Karlsson, L., Larsson, M., *Low stress TiB<sub>2</sub> coatings with improved tribological properties*. Thin Solid Films, 2001. **401**(1-2): p. 179-186.
108. Berger, M., Wiklund, U., Eriksson, M., Engqvist H., Jacobson, S., *The multilayer effect in abrasion - optimising the combination of hard and tough phases*. Surface and Coatings Technology, 1999. **116-119**: p. 1138-1144.
109. Kustas, F., Mishra, B., Zhou, J., *Fabrication and characterization of TiB<sub>2</sub>/TiC and tungsten co-sputtered wear coatings*. Surface and Coatings Technology, 2001. **139**(1): p. 25-34.
110. Berger, M., Hogmark, S., *Tribological Properties of Selected PVD Coatings when slid against ductile materials*. Wear, 2002. **252**(7-8): p. 557-565.
111. Prakash, B., Celis, J., *Fretting Wear Behaviour of PVD TiB<sub>2</sub> Coatings*. Surface and Coatings Technology, 2002. **154**: p. 182-188.
112. Berger, M., Hogmark, S., Larson, M., *Evaluation of magnetron-sputtered TiB<sub>2</sub> intended for tribological applications*. Surface and Coatings Technology, 2000. **124**(2-3): p. 253-261.
113. Baker, M., Gilmore, R., Lenardi, C., Gibson, P., Gissler, W., *Microstructure and mechanical properties of multilayer TiB<sub>2</sub>/C and co-sputtered TiB<sub>2</sub>-C coatings for cutting tools*. Vacuum, 1999. **53**(1-2): p. 113-116.
114. Gilmore, R., Baker, M., Gibson, P., *Preparation and characterization of low-friction TiB<sub>2</sub> based coatings by incorporation of C or MoS<sub>2</sub>*. Surface and Coatings Technology, 1998. **105**: p. 45-50.
115. Gilmore, R., Baker, M., Gibson, P., *Comparative investigation of multilayer TiB<sub>2</sub>/C and co-sputtered TiB<sub>2</sub>/C coatings for low friction applications*. Surface and Coatings Technology, 1999. **116-119**: p. 1127-1132.
116. Wolfe, D., Singh J., Narasimhan, K., *Synthesis and characterization of multilayered TiC/TiB<sub>2</sub> coatings deposited by ion beam assisted electron beam-physical vapour deposition (EB-PVD)*. Surface and Coatings Technology, 2003. **165**: p. 8-25.
117. Robertson, J., *Diamond-like amorphous carbon*. Material Science and Engineering: R: Reports, 2002. **37**(4-6): p. 129-281.
118. Hazen, R.M., *The Diamond Makers* 1999: Cambridge University Press.
119. Kato, H., Yamasaki, S., Okushi, H. *N-type conductivity of phosphorus-doped homoepitaxial diamond on (001)substrate*. in ICNDST-10. 2005. Tsukuba, Japan.
120. Pierson, H.O., *Handbook of Carbon, Graphite, Diamond and Fullerenes - Properties, Processing and Applications*. 1993, NY: William Andrew Publishing/Noyes.
121. Nazare, M., Neves, A., *Properties, Growth and Applications of Diamond* 2001: Institution of Electrical Engineers.
122. Liu, H., Dandy, D, *Diamond Chemical Vapour Deposition*. 1995, NY: William Andrew Publishing/Noyes.
123. Robertson, J., *Amorphous carbon* Advances in Physics, 1986. **35**(4): p. 317-374.
124. Capote, G., Freire, F., Mariotto, G., *Amorphous hydrogenated carbon films deposited by PECVD in methane atmospheres highly diluted in argon: effect of*

- the substrate temperature*. Diamond and Related Materials, 2004. **13**(4-8): p. 1454-1458.
125. Capote, G., Prioli, R., Freire, F., *Amorphous hydrogenated carbon films deposited by PECVD: influence of the substrate temperature on film growth and microstructure*. Journal of Non-Crystalline Solids, 2004. **338-340**: p. 503-508.
  126. Yue, Q., Erkan, K., Ahmet, T. , *Atmospheric effects on the adhesion and friction between non-hydrogenated diamond-like carbon (DLC) coating and aluminum – A first principles investigation*. Surface Science 2006.
  127. Tamor, M., Wu, C., Carter, R., Lindsay, N., *Pendant benzene in hydrogenated diamond-like carbon*. Applied Physics Letters, 1989. **55**(14): p. 1388-1390.
  128. Yue Qia, E.K., Ahmet T. *Alpas Atmospheric effects on the adhesion and friction between non-hydrogenated diamond-like carbon (DLC) coating and aluminum – A first principles investigation*. Surface Science, 2006.
  129. Vandavelde, T., Vandierendonck, K., Van Stappen, M., Perremans, P., *Cutting applications of DLC, hard carbon and diamond films*. 1999. **113**(1-2): p. 80-85.
  130. Kim, D., Kim, Y., Chung, K., Lee, J., Kim, S., *Development of flying type head/slider for optical recording technology*. Tribology International, 2005. **38**(6-7): p. 578-587.
  131. Kuhr, M., Bauer, S., Rothhaar, U., Wolff, D., *Coatings on plastics with the PICVD technology*. Thin Solid Films, 2003. **442**(1-2): p. 107-116.
  132. Krawietz, R., Kämpfe, B., Brücher, M., *Raman spectroscopic and X-ray investigation of stressed states in diamond-like carbon films*. Crystal Research and Technology, 2005. **40**(1-2): p. 143-148.
  133. Dorner, A., Reisei, G., Irmer, G., Seidel, O., Muller, E., *Diamond-like carbon-coated TiAl<sub>6</sub>V<sub>4</sub>: influence of the coating thickness on the structure and the abrasive wear resistance*. Wear, 2001. **249**: p. 489-497.
  134. Sheeja, D., Tay, B., Leong, K., Lee, C., *Effect of film thickness on the stress and adhesion of diamond-like-carbon coatings*. Diamond and Related Materials, 2002. **11**: p. 1643-1647.
  135. Silva, S., Amaratunga, G., Salje, E., Knowles, K., *Evidence of hexagonal diamond in plasma-deposited films*. Journal of Materials Science, 1994. **29**: p. 4962-4966.
  136. Wang, D., Chang, C., Ho, W., *Characterization of hydrogen-free diamond-like carbon films deposited by pulsed plasma technology*. Thin Solid Films 1999. **355-356**: p. 246-251.
  137. Corbella, C., Pascual, E., Bertran, E., *Composition and morphology of metal-containing diamond-like carbon films obtained by reactive magnetron sputtering*. Thin Solid Films, 2005. **482**(1-2): p. 293-298
  138. Corbella, C., Gómez, M., Bertran, E., *Structure of diamond-like carbon films containing transition metals deposited by reactive magnetron sputtering*. Diamond and Related Materials, 2005. **14**(3-7): p. 1103-1107.
  139. Yang, S., Wiemann, E., Teer, D., *The properties and performance of Cr-based multilayer nitride hard coatings using unbalanced magnetron sputtering and elemental metal targets*. Surface and Coatings Technology, 2004. **188-189**: p. 662-668.
  140. Corbella, C., Canillas, A., Bertran, E., Andújar, J., *Visible and infrared ellipsometry applied to the study of metal-containing diamond-like carbon coatings*. Thin Solid Films, 2004. **455-456**: p. 370-375.
  141. Chen, C., Hong, F., *Interfacial studies for improving the adhesion of diamond-like carbon films on steel*. Applied Surface Science, 2005. **243**(1-4): p. 296-303.
  142. Hong, F., Chen, L., *Properties of diamond-like carbon films deposited by ion plating with a pulsed substrate bias*. Diamond and Related Materials, 1998. **7**(6): p. 884-891.

143. Yang, S., Renevier, N., Teer, D., *Tribological properties and wear mechanism of sputtered C/Cr coating*. Surface and Coatings Technology, 2001. **142-144**: p. 85-93.
144. Ahamd, I., Roy, S., McLaughlin, J., *Effect of substrate bias voltage and substrate on the structural properties of amorphous carbon films deposited by unbalanced magnetron sputtering*. Thin Solid Films, 2005. **482**(1-2): p. 45-49.
145. Ziebert, C., Stüber, M., Holleck, H., *Interfaces and temperature stability of stepwise graded DLC films studied by nanoindentation and Raman spectroscopy*. Surface and Coatings Technology, 2005. **200**(1-4): p. 1127-1131.
146. Zhang, S., Bui, X., Li, X., *Towards high adherent and tough a-C coatings*. Thin Solid Films, 2005. **482**(1-2): p. 138-144.
147. Zhang, S., Bui, X., Butler, D., *Bias-graded deposition of diamond-like carbon for tribological applications*. Diamond and Related Materials, 2004. **13**(4-8): p. 867-871.
148. Fischer-Cripps, A., *Nanoindentation*. 2002: Springer-Verlag.
149. Fischer-Cripps, A., *A review of analysis methods for sub-micron indentation testing*. Vacuum, 2000. **58**: p. 569-585.
150. Jönsson, B., Hogmark, *Hardness measurements of thin films*. Thin Solid Films, 1984. **114**(3): p. 257-269.
151. Burnett, P., Rickerby, D., *The Mechanical Properties of Wear-Resistant Coatings :I: Modelling of Hardness behaviour*. Thin Solid Films, 1987. **148**(1): p. 41-50.
152. Chicot, D., Lesage, J., *Absolute hardness of films and coatings*. Thin Solid Films, 1995. **254**(1-2): p. 123-130.
153. Burke, I., *Determination of Mechanical Properties of Multilayer Erosion Resistant Coatings*, in SIMS. 2000, MSc Thesis, Cranfield University: Bedford.
154. Page, T., Hainsworth, S., *Using nanoindentation techniques for the characterization of coated systems: a critique*. Surface and Coatings Technology, 1993. **61**: p. 201-208.
155. A. Niederhofer, P.N., H. -D. Männling, K. Moto, S. Veprek and M. Jílek, *Structural properties, internal stress and thermal stability of nc-TiN/a-Si<sub>3</sub>N<sub>4</sub>, nc-TiN/TiSi<sub>x</sub> and nc-(Ti<sub>1-y</sub>Al<sub>y</sub>Si<sub>x</sub>)N superhard nanocomposite coatings reaching the hardness of diamond*. Surface and Coatings Technology, 1999. **120-121**: p. 173-178.
156. Bulychev, S., Alekhin, V., Shorshorov, M., Ternovskii, A., *Mechanical properties of materials studied from kinetic diagrams of load versus depth of impression during microimpression*. Strength Material, 1976. **8**: p. 1084–1089.
157. Hertz, H., *On the contact of elastic bodies*. Journal fur die reine und angewandte Mathematic, 1881. **92**: p. 156-171.
158. Boussinesq, J., *Application des Potentiels a l'etude de equilibre et du mouvement des solides elastiques*, ed. Gautier-Villars. 1885, Paris.
159. Love, A., *The Stress Produced in a Semi-Infinite Solid by Pressure on Part of the Boundary*. Philosophical Transactions of the Royal Society of London. Series A, 1929. **228**: p. 377.
160. Harding, J., Sneddon, I., *The elastic stresses produced by the indentation of the plane surface of a semi-infinite elastic solid by a rigid punch*. Proceedings of the Cambridge Philosophical Society, 1945. **41**: p. 16-26.
161. Tabor, D., Stilwell, N., *Elastic Recovery of Conical Indentations*. Proceedings of the Physical Society, 1961. **78**(1): p. 169-179.
162. Olivier, W., Pharr, M., *An improved technique for determine hardness and elastic modulus using load and displacement sensing indentation experiments*. Journal Material Research, 1992. **7**(1564-1583).

163. Oliver, W., Pharr, G., Tsui, T., *Influences of stress on the measurement of mechanical properties using nanoindentation: Part I. Experimental studies in an aluminum alloy*. Journal of Materials Research, 1996. **11**(3): p. 752.
164. Oliver, W., Pharr, G., Bolshakov, A., *Influences of stress on the measurement of mechanical properties using nanoindentation: Part II. Finite element simulations*. Journal of Materials Research, 1996. **11**(3): p. 760.
165. Shan, Z., Sitaraman, S., *Elastic-plastic characterization of thin film using nanoindentation technique*. Thin Solid Films, 2003. **437**: p. 176-181.
166. Dorner, M.F. and W.D. Nix, *A method for interpreting the data from depth-sensing indentation instruments*. Journal Material Research, 1986. **1**(4): p. 601.
167. Nix, W.D., *Mechanical Properties of Thin Films*. Metallurgic Transactions, 1989. **20A**: p. 2217.
168. Loubet, J., Gorges, J., Marchesini, O., Meille, G. , *Vickers Indentation Curves of Magnesium Oxide*. Journal of Tribology, 1984. **106**: p. 43-48.
169. Hainsworth, S., McGurk, M., Page, T., *The effect of coating cracking on the indentation response of thin hard-coated systems*. Surface and Coatings Technology, 1998. **102**(1-2): p. 97-107.
170. Borodich, F., Keer, L., *Contact problems and depth-sensing nanoindentation for frictionless and frictional boundary conditions*. International Journal of Solids and Structures, 2004. **41**(9-10): p. 2479-2499.
171. J. Loubet, J.G., O. Marchesini, and G. Meille, *Vickers Indentation Curves of Magnesium Oxide*. Journal of Tribology, 1984. **106**: p. 43-48.
172. Li, X., Bhushan, B., *A review of nanoindentation continuous stiffness measurement technique and it's applications*. Materials Characterization, 2002. **48**: p. 11-36.
173. Pharr, M., *Measurement of mechanical properties by ultra-low load indentation*. Material Science and Engineering A, 1998. **253**(1-2): p. 151-159.
174. Ding, J., Meng, Y., Wen, S., *Mechanical properties and fracture toughness of multilayer hard coatings using nanoindentation*. Thin Solid Films, 2000. **371**: p. 178-182.
175. Chudoba, T., Richter, F., *Investigation of creep behaviour under load during indentation experiments and its influence on hardness and modulus results*. Surface and Coatings Technology, 2001. **148**: p. 191-198.
176. Herrmann, K., Jennet, N., Wegener, W., Meneve, J., Seemann, R., *Progress in determination of the area function of indenters used for nanoindentation*. Thin Solid Films, 2000. **377-400**: p. 394-400.
177. A. Bolshakov, G.P., *Influences of pileup on the measurement of mechanical properties by load and depth sensing indentation techniques*. Journal of Materials Research, 1998. **13**(4): p. 1049-1058.
178. Cekada, M., Panjan, P., *Evaluation of microhardness and elastic properties of multilayer hard coatings by microindentation*. Vaccum, 2001. **61**: p. 235-240.
179. Saha, R., Nix, W. D., *Soft films on hard substrates - nanoindentation of tungsten films on sapphire substrates*. Materials Science engineering A, 2001. **A319-321**(898-901).
180. Saha, R., Nix, W. D., *Effects of the substrate on the determination of thin film mechanical properties by nanoindentation*. Acta Materialia, 2002. **50**: p. 23-38.
181. Xu, Z., Rowcliffe, D., *Deriving mechanical properties of soft coatings using nanoindentation: an applications of mechanism-based strain gradient plasticity*. Surface and Coatings Technology, 2002. **157**: p. 231-237.
182. Nix, W.D., Gao, H., *Indentation size effects in crystalline materials: a law for strain gradient plasticity*. Journal of the Mechanics and Physics of Solids, 1998. **46**(3): p. 411-425.

183. Gao, H., Huang, Y., Nix, W. D., Hutchinson, J., *Mechanism-based strain gradient plasticity— I. Theory*. Journal of the Mechanics and Physics of Solids, 1999. **47**(6): p. 1239-1263.
184. Ohmura, T., Tanaka, K., Matsuoka, S., Yoshida, T., *Nanoindentation load-displacement behaviour of pure face centered cubic metal thin films on a hard substrate*. Thin Solid Films, 2001. **385**: p. 198-204.
185. Ohmura, T., Matsuoka, S., *Evaluation of mechanical properties of ceramic coatings on a metal substrate*. Surface and Coatings Technology, 2003. **169-170**: p. 728-731.
186. Sanchez, J., El-Mansy, S., Sun, B., Ford, W., Fuentes, M., Maiz, J., *Cross-sectional nanoindentation: a new technique for thin film interfacial adhesion characterization*. Acta Materialia, 1999. **47**(17): p. 4405-4413.
187. Archard, J., *Friction between metal surfaces*. Wear, 1986. **113**(1): p. 3-16.
188. Leyland, A., Matthews, A., *On the significance of the H/E ration in wear control: a nanocomposite coating approach to optimised tribological behaviour*. Wear, 2000. **246**(1-2): p. 1-11.
189. Galvan, D., Peia Y, Hosson, J., *Deformation and failure mechanism of nanocomposite coatings under nano-indentation*. Surface and Coatings Technology, 2006. **200**(24): p. 6718-6726.
190. Mayrhofer, P., Mitterer, C., Musil, J., *Structure–property relationships in single- and dual-phase nanocrystalline hard coatings*. Surface and Coatings Technology, 2003. **174-175** p. 725-731.
191. Rickerby, D.S., *A review of the methods for the measurement of the coating-substrate adhesion*. Surface and Coatings Technology, 1988. **36**: p. 541-557.
192. Burnett, P., Rickerby, D. , *The scratch adhesion test: An elastic-plastic indentation analysis*. Thin Solid Films, 1988. **157**(2 ): p. 233-254.
193. Bull, S., Rickerby, D., Matthews, A., Leyland, A., Valli, J., *The use of scratch adhesion testing for the determination of interfacial adhesion: The importance of frictional drag*. Surface and Coatings Technology, 1988. **36**(1-2): p. 503-517.
194. Thouless, M., *Some mechanics for the adhesion of thin films*. Thin Solid Films, 1989. **181**(1-2): p. 397-406.
195. Berg, J., *Adhesion science and engineering - Surfaces, chemistry and applications*. 1st ed, ed. A. Pocius. Vol. 2. 2002, Amsterdam: Elsevier.
196. Perry, A., *Scratch adhesion testing of hard coatings*. Thin Solid Films, 1983. **107**: p. 167-180.
197. Holmberg, K., Laukkanen, A., Ronkainen, H., Wallin, K., Varjus, S., Koskinen, J., *Tribological contact analysis of a rigid ball sliding on a hard coated surface: Part I: Modelling stresses and strains*. Surface and Coatings Technology, 2006. **200**(12-13): p. 3793-3809.
198. Bull, S., Berasetegui, E., *An overview of the potential of quantitative coating adhesion measurement by scratch testing*. Tribology International, 2006. **39**(2): p. 99-114.
199. Bull, S., Rickerby, D., *Multi-pass scratch testing as a model for abrasive wear*. Thin Solid Films, 1989. **181**: p. 545-553.
200. Sekler, J., Steinman, P., Hintermann, H., *The Scratch test: different critical load determination techniques*. Surface and Coatings Technology, 1988. **36**: p. 519-529.
201. Bull, S., *Failure modes in scratch adhesion testing*. Surface and Coatings Technology, 1991. **50**: p. 25-32.
202. Bull, S., *Failure Mode maps in the thin film scratch adhesion test*. Tribology International, 1997. **30**(7): p. 491-498.

203. Steinmann, P., Hintemann, H., *A review of the mechanical tests for the assessment of thin film adhesion*. Journal Vacuum Science Technology A, 1989. **7**(3): p. 2267-2272.
204. Shaginyan, L., Onoprienko, A., Britun, V., Smirnov, V., *Influence of different physical factors on microstructure and properties of magnetron sputtered amorphous carbon films*. Thin Solid Films. **397**(1-2): p. 288-295
205. Vales Silva, M., Nicholls, J.R, *A model for calculating the thickness profile TiB<sub>2</sub> of and AL multilayer coatings produced by planar magnetron sputtering*. Surface and Coatings Technology, 2001. **142-144**: p. 934-938.
206. <http://www.fibics.com/>. 2003
207. Phaneuf, M.W., *Applications of focused ion beam microscopy to materials science specimens*. Micron, 1999. **30**: p. 277-288.
208. Silva, M., *A new, low mass, bondcoat technology for thermal barrier coating, in SIMS*. 2005, Cranfield University: Bedford.
209. Abramo, M., Hrschbein, S. , *Focused-Ion-Beam Techniques Provide Circuit Modification Capability for Rapid Design Debug*. Micro News, 1999. **5**.
210. Ferraro, J.R., *Introductory raman spectroscopy*. 2nd ed. 2003, San Diego, CA Academic Press. 434.
211. Gunzler, H., *Handbook of analytical techniques*. . Vol. 1. 2001, Weinheim: Wiley-VCH.
212. Yu, P., Cardona, M., *Fundamentals of Semiconductors - Physics and Materials Properties*. 3rd ed. 2001: Springer - Verlag. 692.
213. Constable, C., Yarwood, J., Munz, W., *Raman microscopic studies of PVD hard coatings*. Surface and Coatings Technology 1999. **116-119**: p. 155-159.
214. Ferrari, A., Robertson, J., *Interpretation of Raman spectra of disordered and amorphous carbon*. Physics Review B, 2000. **61**(20): p. 14095.
215. Ferrari, A., Robertson, J., *Resonant Raman spectroscopy of disordered, amorphous and DLC carbon*. Physics Review B, 2001. **64**(7): p. 075414.
216. Kelesoglu, E., Mitterer, M., *Structure and Properties of TiB<sub>2</sub> Based Coatings Prepared by Unbalanced DC TiB<sub>2</sub> Magnetron Sputtering*. Surface and Coatings Technology, 1998. **98**(1-3): p. 1483-1489.
217. Deng, H., Chen, J., Inturi, R., Barnard, J., *Structure, mechanical and tribological properties of D.C. magnetron sputtered TiB<sub>2</sub> and TiB<sub>2</sub> (N) thin films*. Surface and Coatings Technology, 1995(76-77): p. 609-614.
218. Thornton, J., Hoffman, D., *Stress-related effects in thin films*. Thin Solid Films, 1989. **171**(1): p. 5-31.
219. Hyungduk Ko, W.-P.T., Ki-Chul Kim, Sang-Hyeob Kim, Su-Jeong Suh and Young-Sung Kim, *Growth of Al-doped ZnO thin films by pulsed DC magnetron sputtering*. Journal of Crystal Growth, 2005. **277**(1-4): p. 352-358.
220. Veprek, S., Karvankova, P., Mukherjee, S., Mannling, H., He, J., Moto, K. and A. Argon, *Hertzian analysis of the self-consistency and reliability of the indentation hardness measurements on superhard nanocomposite coatings*. Thin Solid Films, 2003. **436**(220-231).
221. S. Kadlec, C.Q., G. Knuyt and L. M. Stals, *Energy-resolved mass spectrometry and Monte Carlo simulation of atomic transport in magnetron sputtering*. Surface and Coatings Technology, 1997. **97**(1-3): p. 633-641.
222. Calendoncia, G., Krech, R. *Proc. Of the 4th European Symp. On Spacecraft Materials in Space Environment*. 1988.
223. Bunshah, R., *Chemical, mechanical and tribological characterization of ultra-thin and hard amorphous carbon coatings as thin as 3.5 nm: recent developments*. Diamond and Related Materials, 1999. **8**(11): p. 1985-2015.
224. Robertson, J., O'Reilly, E., *Electronic and atomic structure of amorphous carbon*. Physics Review B, 1987. **35**(6): p. 2946.

225. Wänstrand, O., Larssona, M., Hedenqvist P., *Mechanical and tribological evaluation of PVD WC/C coatings*. Surface and Coatings Technology, 1999. **111**(2-3): p. 247-254.
226. Uglov, V., Kuleshova, K., Rusalskya, D., Onateb, J., Yang, S., *Wear-resistant metal-carbon composite coating*. Surface and Coatings Technology, 2000. **128-129**: p. 150-155.
227. Podgornik, B., Hren, D., Vižintin, J., *Low-friction behaviour of boundary-lubricated diamond-like carbon coatings containing tungsten*. Thin Solid Films, 2005. **476**(1): p. 92-100.
228. Bradley, J., Bäckera, H., Kelly, P., Arnell, R., *Time-resolved Langmuir probe measurements at the substrate position in a pulsed mid-frequency DC magnetron plasma*. Surface and Coatings Technology, 2001. **135**(2-3): p. 221-228.
229. Glocker, D., *Influence of the plasma on substrate heating during low-frequency reactive sputtering of AlN*. Journal of Vacuum Science and Technology A, 1999. **11**(6): p. 2989-2993.
230. Jacobsohn, L., Capote, G., Cruz, N., Freire, F., *Plasma deposition of amorphous carbon films from CH<sub>4</sub> atmospheres highly diluted in Ar* Thin Solid Films, 2002. **419**(1-2): p. 46-53.
231. Teii, K., *Structure changes in a-C:H films in inductive CH<sub>4</sub>/Ar plasma deposition*. Thin Solid Films, 2000(333): p. 103-107.
232. Prakash, B., Richter, E., Celis, J., *Ti-B and Ti-B-C coatings deposited by plasma immersion ion implantation and their fretting behavior*. Surface and Coatings Technology, 2003. **173**(2-3): p. 150-160.
233. Knotek, O., Jungblut, F., Breidenbach, R., *Magnetron-sputtered superhard coatings within the system Ti-B-C-N*. Vacuum, 1990. **41**(7-9): p. 2184-2186.
234. Liu, Y., Meletis, E., *Evidence of graphitization of diamond-like carbon films during sliding wear*. Journal of Materials Science, 1997. **32**(13): p. 3491-3495.
235. Enke, K., Dimigen, H., Hübsch, H., *Frictional properties of diamondlike carbon layers*. Applied Physics Letters, 1980. **36**(4): p. 291-292.
236. Donnet, C., *Recent progress on the tribology of doped diamond-like and carbon alloy coatings: a review*. Surface and Coatings Technology, 1998. **100-101**: p. 180-186.
237. Yue Qia, E.K., Ahmet T. Alpas *Atmospheric effects on the adhesion and friction between non-hydrogenated diamond-like carbon (DLC) coating and aluminum – A first principles investigation*. Surface Science 2006.
238. W. Choi, I.C., Y. Lee, B. Hong, *Characterization of diamond-like carbon thin films prepared by a microwave plasma enhanced chemical vapor deposition method*. Surface and Coatings Technology, 2004. **180-181**: p. 254-258.
239. G. Abadias, *Nanoindentation hardness and structure of ion beam sputtered TiN, W and TiN/W multilayer hard coatings* Surface and Coatings Technology, 2006. **220**(22-23): p. 6538-6543.
240. J. Aldazabal, J.S., *Hall-Petch behaviour induced by plastic strain gradients*. Materials Science and Engineering A, 2004. **365**(1-2): p. 186-190.
241. Gouldstone, A., Zeng, K., Suresh, S., *Discrete and continuous deformation during nanoindentation of thin films*. Acta Materialia, 2000. **48**(9): p. 2277-2295.
242. Suresh, S., Giannakopoulos, K., *A new method for estimating residual stresses by instrumented sharp indentation*. Acta Materialia, 1998. **46**(16): p. 5755-5767.
243. Mata, M., Casals, O., Alcalá, J., *The plastic zone size in indentation experiments: The analogy with the expansion of a spherical cavity*. International Journal of Solids and Structures, 2006. **43**(20): p. 5994-6013.
244. Erdemir, A., *The role of hydrogen in tribological properties of diamond-like carbon films*. Surface and Coatings Technology, 2001. **146-147**: p. 292-297.

245. J. Fontaine, C.D., A. Grill and T. LeMogne, *Tribochemistry between hydrogen and diamond-like carbon films*. Surface and Coatings Technology, 2001. **146-147**: p. 286-291.
246. Burnett, P., Rickerby, D., *The relationship between hardness and scratch adhesion*. Thin Solid Films, 1987. **154**(1-2): p. 403-416.
247. Chalker, P., Bull, S., Rickerby, D. , *A review of the methods for the evaluation of coating-substrate adhesion*. Materials Science and Engineering A, 1991. **140**(7): p. 583-592.
248. B. Podgornik, D.H., J. Vižintin, *Low-friction behaviour of boundary-lubricated diamond-like carbon coatings containing tungsten*. Thin Solid Films, 2005. **476**(1): p. 92-100.